

Institut für Angewandte Photophysik - Fachrichtung Physik
Fakultät Mathematik und Naturwissenschaften
Technische Universität Dresden

Top-Emitting OLEDs

-

Improvement of the Light Extraction Efficiency and Optimization of Microcavity Effects for White Emission

**Dissertation zur Erlangung des akademischen Grades
Doctor rerum naturalium**

vorgelegt von
Tobias Schwab
geboren am 06. Mai 1986 in Dresden

Dresden, 28. Mai 2014

Eingereicht am: 28.05.2014

Verteidigt am: 03.11.2014

1. Gutachter: Prof. Dr. Karl Leo
2. Gutachter: Prof. Dr. Wolfgang Brütting

Contents

Abstract	V
List of Publications	IX
1 Introduction	1
2 Organic Semiconductors	5
2.1 Molecular Orbitals	5
2.2 Optical Properties of Organic Semiconductors	8
2.3 Inter-Molecular Energy Transfer	11
2.4 Charge Carrier Transport in Amorphous Organic Semiconductors	14
2.5 Charge Injection and Material Interfaces	18
3 Organic Light-Emitting Diodes	21
3.1 External Quantum Efficiency of OLEDs	21
3.2 Optimization of the Internal Quantum Efficiency	23
3.3 Highly Efficient Organic Light-Emitting Diodes	28
3.4 Human Perception of Electromagnetic Radiation	35
4 Optics of Top-Emitting OLEDs	41
4.1 Light Propagation in Thin Film Structures	41
4.2 Optical Optimization of Top-Emitting OLEDs	45
4.3 Outcoupling of Internally Trapped Light Modes	53
5 Experimental Methods	67
5.1 Sample Fabrication	67
5.2 Investigated Materials	70
5.3 Characterization Methods	72
6 Highly Transparent Metal Top Electrodes	79
6.1 Au/Ag Top Electrodes on N-Doped Layers	81
6.2 MoO ₃ /Au/Ag Top Electrodes on P-Doped Layers	85
7 White Top-Emitting OLEDs with Optimized Microcavity Effects	91
7.1 Hybrid White Top-Emitting OLEDs	92
7.1.1 Optimization of the Silver Thickness	92
7.1.2 Gold Wetting Layer for Ultra-Thin Metal Top Electrodes	95
7.1.3 Comparison to Bottom-Emitting Reference OLEDs	98
7.2 Stacked Inverted White Top-Emitting OLEDs	102
7.3 ITO-Free Transparent White OLEDs	108

7.3.1	Total Transmittance of ITO-Free Transparent OLEDs	108
7.3.2	Performance of Transparent OLEDs with Fixed Top Electrode . .	110
8	Extraction of Internally Trapped Light Modes	119
8.1	Preparation of a Periodically Corrugated Top-Emitting OLED	120
8.1.1	Fabrication and Characterization of Photoresist Gratings	120
8.1.2	Corrugation of the Organic Layer Sequence	122
8.2	Extraction of Internal Light Modes from Corrugated Top-Emitting OLEDs	124
8.2.1	Efficiency Enhancement of Corrugated Top-Emitting OLEDs . . .	125
8.2.2	Identification of Bragg Scattered Modes	128
8.3	Coherent Mode Coupling in Strongly Corrugated Microcavities	134
8.3.1	OLED Performance on Strongly Corrugated Substrates	134
8.3.2	Analysis of Bragg Scattered Modes	138
8.3.3	Mode-Coupling Effects in Strongly Corrugated OLEDs	140
9	Optimization of the Grating-OLED System	147
9.1	Microcavity Optimization for Constructive Mode Interference	148
9.1.1	Variation of the Top Electrode Thickness	148
9.1.2	Variation of the Capping Layer to Optimize the Microcavity . . .	152
9.2	White Top-Emitting OLEDs on Periodically Corrugated Substrates . . .	155
9.2.1	Application of Highly Transparent Wetting Layer Electrodes . . .	156
9.2.2	Variation of the Corrugation Period	162
10	Conclusions and Outlook	167
	Appendix A: OLED Optimization for Warm White Emission	173
	Appendix B: Thermal Annealing of Inverted OLEDs	179
	Appendix C: Top-Emitting OLEDs on Metal Gratings	181
	Bibliography	189
	List of Abbreviations	209
	Acknowledgements	211

Abstract

In the last decades, investigations of organic light-emitting diodes (OLEDs) have tackled several key challenges of this lighting technology and have brought the electron to photon conversion efficiency close to unity. However, currently only 20% to 30% of the photons can typically be extracted from OLED structures, as total internal reflection traps the major amount of the generated light inside the devices.

This work focuses on the optimization of the optical properties of top-emitting OLEDs, in which the emission is directed away from the substrate. In this case, opaque materials, e.g. a metal foil or a display backplane can be used as substrate as well. Even though top-emitting OLEDs are often preferred for applications such as displays, two main challenges remain: the application of light extraction structures and the deposition of highly transparent materials as top electrode, without harming the organic layers below. Both issues are addressed in this work.

First, top-emitting OLEDs are deposited on top of periodically corrugated light outcoupling structures, in order to extract internally trapped light modes by Bragg scattering and to investigate the basic scattering mechanisms in these devices. It is shown for the first time that the electrical performance is maintained in corrugated top-emitting OLEDs deposited on top of light extraction structures. Furthermore, as no adverse effects to the internal quantum efficiency have been observed, the additional emission from previously trapped light modes directly increases the device efficiency. It has been proven that the spectral emission of corrugated OLEDs is determined by the interference of all light modes inside the air light-cone, including the observation of destructive interference and anti-crossing phenomena. The formation of a coherently coupled mode pair of the initial radiative cavity mode and a Bragg scattered mode has been first observed, when grating structures with an aspect ratio > 0.2 are applied. There, the radiative cavity mode partially vanishes. The observation and analysis of such new emission phenomena in corrugated top-emitting OLEDs has been essential in obtaining a detailed insight on fundamental scattering processes as well as for the optimization and control of the spectral emission by light extraction structures.

Second, the adverse impact of using only moderately transparent silver electrodes in white top-emitting OLEDs has been compensated improving the metal film morphology, as the organic materials often prevent a replacement by state-of-the-art electrodes, like Indium-tin-oxide (ITO). A high surface energy Au wetting layer, also in combination with MoO_3 , deposited underneath the Ag leads to smooth, homogeneous, and closed films. This allows to decrease the silver thickness from the state-of-the-art 15 nm to 3 nm, which has the advantage of increasing the transmittance significantly while maintaining a high conductivity. Thereby, a transmittance comparable to the ITO benchmark has been reached in the wavelength regime of the emitters.

White top-emitting OLEDs using the wetting layer electrodes outperform state-of-the-art top-emitting devices with neat Ag top electrodes, by improving the angular color stability, the color rendering, and the device efficiency, further reaching slightly improved characteristics compared to references with ITO bottom electrode. The enormous potential of wetting layer metal electrodes in improving the performance of OLEDs has been further validated in inverted top-emitting devices, which are preferred for display applications, as well as transparent OLEDs, in which the brittle ITO electrode is replaced by a wetting layer electrode.

Abstract

Combining both concepts, wetting layer electrodes and light extraction structures, allows for the optimization of the grating-OLED system. The impact of destructive mode interference has been reduced and thus the efficiency increased by a decrease of the top electrode thickness, which would have not been achieved without a wetting layer. The optimization of corrugated white top-emitting OLEDs with a top electrode of only 2 nm gold and 7 nm silver on top of a grating with depth of 150 nm and period of 0.8 μm have yielded a reliable device performance and increased efficiency by a factor of 1.85 compared to a planar reference (5.0 % to 9.1 % EQE at 1000 cd/m^2). This enhancement is comparable to common light extraction structures, such as half-sphere lenses or microlens foils, which are typically restricted to bottom-emitting devices. Overall, the deposition of top-emitting OLEDs on top of light extraction structures finally allow for an efficient extraction of internally trapped light modes from these devices, while maintaining a high device yield.

Finally, the investigations have resulted in a significant efficiency improvement of top-emitting OLEDs and the compensation of drawbacks (optimization of the white light emission and the extraction of internal light modes) in comparison to the bottom-emitting devices. The investigated concepts are beneficial for OLEDs in general, since the replacement of the brittle ITO electrodes and the fabrication of roll-to-roll processing compatible light extraction structures are also desirable for bottom-emitting, or transparent OLEDs.

Kurzfassung

Die Entwicklung organischer Leuchtdioden (OLEDs) ermöglicht heute die Erzeugung von Licht mit nahezu idealer Umwandlungseffizienz von elektrischen Ladungsträgern in Photonen. Jedoch können auf Grund der optischen Eigenschaften der verwendeten Materialien meist nur 20 % bis 30 % des erzeugten Lichtes das Bauteil auch verlassen, während der Großteil des Lichtes total reflektiert wird und im Bauteil verbleibt.

Diese Arbeit untersucht die Optimierung der Optik von top-emittierenden OLEDs, welche Licht vom Trägersubstrat weg abstrahlen und somit auch die Nutzung lichtundurchlässiger Substrate, z.B. Metallfolien, ermöglichen. Trotz dieses entscheidenden Vorteils gegenüber OLEDs, die durch ein transparentes Substrat hindurch emittieren (bottom-OLEDs), ist die Nutzung der meisten transparenten Elektroden sowie die Verwendung von Lichtauskopplungsstrukturen durch die darunter liegenden organischen Schichten stark begrenzt. Die Forschungsschwerpunkte dieser Arbeit richten sich somit auf die Erforschung hochtransparenter Elektroden, sowie die Entwicklung und Integration von Lichtauskopplungsstrukturen für die Extraktion interner Lichtmoden in top-emittierenden OLEDs. Die Abscheidung top-emittierender OLEDs auf periodisch strukturierten Substraten ermöglichte die Extraktion interner Lichtmoden mittels Bragg-Streuung sowie die detaillierte Untersuchung der auftretenden Streueffekte und der zugrunde liegenden Mechanismen mit Einfluss auf die Emission. Durch die Verwendung von Strukturen mit geringer Oberflächenrauigkeit konnte die Erhaltung der elektrischen Eigenschaften in den nun strukturierten top-emittierenden OLEDs erstmals gezeigt werden. Auf Grund der vergleichbaren elektrischen Charakteristik sowie der erhaltenen Lichterzeugungseffizienz kann die Effizienzsteigerung von strukturierten top-emittierenden OLEDs direkt auf eine erhöhte Lichtauskopplungseffizienz zurück geführt werden. Dies ermöglicht die Evaluierung geeigneter Struktur- und OLED-Parameter zur Steigerung der Lichtauskopplung. Untersuchungen der Streueffekte zeigen, dass die Emission periodisch strukturierter OLEDs durch die Interferenz aller Fernfeldlichtmoden bestimmt ist, wobei destruktive Interferenz und eine vermiedene Kreuzung von Lichtmoden (Anti-Crossing) beobachtet werden konnte. Weiterhin wurde die Bildung einer kohärent gekoppelten Lichtmode aus der Überlagerung der ursprünglichen Kavitätsmode und einer gestreuten Wellenleitermode in top-OLEDs auf Gitterstrukturen mit einem Aspektverhältnis $> 0,2$ beobachtet, wobei die fundamentale Kavitätsmode teilweise verschwand. Dieser erstmals in periodisch strukturierten OLEDs beobachtete Effekt hat nicht nur einen entscheidenden Einfluss auf die Emission, sondern muss ebenfalls für die Modellierung und Optimierung geeigneter Strukturen berücksichtigt werden.

Auf Grund der Empfindlichkeit organischer Schichten gegenüber der Abscheidung hochtransparenter Elektrodenmaterialien wie z.B. Indiumzinnoxid (ITO) ist die Optimierung top-emittierender OLEDs durch die zu nutzenden semitransparenten Metallelektroden begrenzt. Besonders in Hinblick auf effiziente, farbstabile und qualitativ hochwertige Weißlichtemission ergeben sich schlechtere Eigenschaften im Vergleich zu bottom-OLEDs, die diese Einschränkung hinsichtlich der transparenten Elektrode nicht aufweisen.

In dieser Arbeit konnte die Transmission von Silber-Topielektroden durch die Verwendung von dünnen Gold sowie Molybdäntrioxid Aufwachsschichten deutlich gesteigert werden. Die Aufwachsschichten führen zur Bildung glatter und geschlossener Silberfilme, die es ermöglichen, die Schichtdicke von derzeit 15 nm auf bis zu 3 nm zu reduzieren, während die elektrische Leitfähigkeit bei erheblich erhöhter Transmission vergleichbar bleibt. Die

hochtransparenten Metallelektroden erreichen eine zum Referenzmaterial ITO vergleichbare Transmission im Spektralbereich der verwendeten Emitter.

Die Anwendung der hochtransparenten Aufwachsschichtelektroden auf weißen top-emittierenden OLEDs ermöglichte eine deutliche Steigerung der Effizienz sowie eine Verbesserung der Winkelstabilität und der Farbqualität gegenüber bisherigen Ergebnissen zu top-emittierenden OLEDs. Des Weiteren wurden erstmals vergleichbare Eigenschaften hinsichtlich der Winkelstabilität, Farbqualität und Effizienz weißer top-emittierender OLEDs zu bottom-emittierenden Referenzbauteilen erreicht. Diese Untersuchungen zeigen, dass die Nachteile top-emittierender OLEDs hinsichtlich der Weißlichtemission mit der Verwendung hochtransparenter Metallelektroden überwunden werden können. Das Konzept der hochtransparenten Aufwachsschichtelektroden wurde erfolgreich für die Verbesserung weiterer OLED Architekturen angewandt, z.B. in invertierten top-emittierenden OLEDs mit zusätzlich verbesserten elektrischen Eigenschaften und in transparenten OLEDs ohne das spröde Elektrodenmaterial ITO, welche somit besonders für flexible Anwendungen geeignet sind.

Für die Optimierung von periodisch strukturierten OLEDs erwiesen sich Aufwachsschichtelektroden ebenfalls als unabdingbar. Der Einfluss destruktiver Interferenzen konnte durch die Reduktion der Metalldicke sowie Schichtdickenanpassung auf besonders spektral breite Emission verringert und der Effizienzzuwachs gesteigert werden. Die Verwendung von Aufwachsschichtelektroden mit Dicken von 2 nm Gold und 7 nm Silber in strukturierten weißen OLEDs mit Höhenvariationen von 150 nm und Gitterperioden von $0,8 \mu\text{m}$ ermöglichte eine Steigerung der Bauteileffizienz um einen Faktor von 1,85 (von 5,0 % EQE auf 9,1 % bei 1000 cd/m^2) durch extrahierte interne Lichtmoden. Hierbei blieb die elektrische Charakteristik der OLEDs im Vergleich zu unstrukturierten weißen top-OLEDs unverändert. Die erreichte Effizienzsteigerung entspricht der von konventionellen Auskoppelstrukturen, wie z.B. Halbkugeln oder Mikrolinsenfolien, die meist nur in bottom-emittierenden Strukturen verwendet werden können. Die Kombination der Aufwachsschichtelektroden mit Lichtauskoppelstrukturen unterhalb der organischen Schichten ermöglichte erstmals die effiziente Extraktion interner Lichtmoden aus top-emittierenden OLEDs unter Bewahrung einer hohen Bauteilausbeute.

Die erforschten Konzepte ermöglichen eine maßgebliche Verbesserung der optischen Eigenschaften top-emittierender OLEDs und die Beseitigung vieler bisherigen Nachteile (hinsichtlich der Weißlichtemission und der Lichtauskopplung) im Vergleich zu bottom OLEDs. Des Weiteren besteht in der Anwendung der Konzepte weder eine Bindung an spezifische organische Materialien noch sind diese auf top-emittierende OLEDs beschränkt. Besonders die gezeigte Kompatibilität der integrierten Lichtauskopplungsstrukturen mit der elektrischen Charakteristik von OLEDs, sowie der Verwendung von Aufwachsschichtelektroden anstatt des spröden ITOs ist interessant für jegliche OLED Architekturen, auch mit Blick auf die zukünftige Herstellung von OLEDs im Rolle-zu-Rolle Verfahren.

List of Publications

Articles

- [A1] T. Schwab, M. Thomschke, S. Hofmann, M. Furno, K. Leo, and B. Lüssem, “Efficiency enhancement of top-emitting organic light-emitting diodes using conversion dyes”, *Journal of Applied Physics* **110**, 083118 (2011).
- [A2] C. Fuchs, T. Schwab, R. Scholz, T. Roch, A. Lasagni, S. Hofmann, B. Lüssem, L. Müller-Meskamp, K. Leo, and M. C. Gather, “Quantitative description of the scattering angles in electrically-driven OLEDs fabricated on periodically corrugated substrates”, *Renewable Energy and the Environment, OSA Technical Digest LT2B*, LT2B.6 (2012).
- [A3] M. Fröbel, A. Perumal, T. Schwab, M. C. Gather, B. Lüssem, and K. Leo, “Enhancing the efficiency of alternating current driven organic light-emitting devices by optimizing the operation frequency”, *Organic Electronics* **14**, 809 (2013).
- [A4] T. Schwab, S. Schubert, M. Thomschke, M. Fröbel, L. Müller-Meskamp, K. Leo, and M. C. Gather, “43.3: Inverted Top-Emitting White OLEDs with Improved Optical and Electrical Characteristics”, *SID Symposium Digest of Technical Papers* **44**, 600 (2013).
- [A5] T. Schwab, S. Schubert, S. Hofmann, M. Fröbel, C. Fuchs, M. Thomschke, L. Müller-Meskamp, K. Leo, and M. C. Gather, “Highly Efficient Color Stable Inverted White Top-Emitting OLEDs with Ultra-Thin Wetting Layer Top Electrodes“, *Advanced Optical Materials* **1**, 707 (2013).
- [A6] M. Fröbel, A. Perumal, T. Schwab, C. Fuchs, K. Leo, and M. C. Gather, “White light emission from alternating current organic light-emitting devices using high frequency color-mixing”, *Phys. Status Solidi A* **210**, 2439 (2013).
- [A7] C. Fuchs[†], T. Schwab[†], T. Roch, S. Eckardt, A. Lasagni, S. Hofmann, B. Lüssem, L. Müller-Meskamp, K. Leo, M. C. Gather, and R. Scholz, “Quantitative allocation of Bragg scattering effects in highly efficient OLEDs fabricated on periodically corrugated substrates”, *Optics Express* **21**, 16319 (2013).

[†] These authors contributed equally to this work.

- [A8] T. Schwab, C. Fuchs, R. Scholz, X. Li, F. Xie, W. Choy, K. Leo, and M. C. Gather, “Improved light outcoupling and mode analysis of top-emitting OLEDs on periodically corrugated substrates”, *Proceedings of SPIE* **8829**, 88291I (2013).
(Awarded with the “Best Student Paper Award” of the SPIE Optics & Photonics Conference.)
- [A9] J. Lee, H. Cho, T.-W. Koh, S. Hofmann, Y.H. Kim, C. Yun, T. Schwab, S. Reineke, B. Lüssem, J.-I. Lee, S. Yoo, K. Leo, and M.C. Gather, “Straight-forward control of the degree of micro-cavity effects in organic light-emitting diodes based on a thin striped metal layer”, *Organic Electronics* **14**, 2444 (2013).
- [A10] T. Schwab, S. Schubert, L. Müller-Meskamp, K. Leo, and M. C. Gather, “Eliminating Micro-Cavity Effects in White Top-Emitting OLEDs by Ultra-Thin Metallic Top Electrodes”, *Advanced Optical Materials* **1**, 921 (2013).
- [A11] T. Schwab[†], C. Fuchs[†], R. Scholz, A. Zakhidov, K. Leo, and M. C. Gather, “Coherent mode coupling in highly efficient top-emitting OLEDs on periodically corrugated substrates”, *Optics Express* **22**, 7524 (2014).
- [A12] J. Lee, T.-W. Koh, H. Cho, T. Schwab, J.-H. Lee, S. Hofmann, J.-I. Lee, S. Yoo, K. Leo, and M. C. Gather, “Transparent organic light-emitting diodes with different bi-directional emission colors using color-conversion capping layers”, *in preparation*.
- [A13] M. Fröbel, T. Schwab, M. Kliem, S. Hofmann, K. Leo, and M. C. Gather, “AC/DC OLEDs: A new Concept for Color-tunable and White Light Sources”, *in preparation*.
- [A14] T. Schaefer, T. Schwab, S. Hofmann, K. Leo, and M. C. Gather, “White top-emitting OLEDs with nanoparticle scattering layers”, *in preparation*.
- [A15] C. Fuchs, T. Schwab, M. Wiczorek, M. C. Gather, S Hofmann, K. Leo, and R. Scholz: “Surface plasmon polariton modification within top-emitting organic light-emitting diodes for enhanced light outcoupling”, *in preparation*.

Book

- [B1] T. Schwab, B. Lüssem, M. Furno, M. C. Gather, and K. Leo, “Organic light-emitting diodes (OLEDs)”, Chapter 18, “Handbook of organic materials for optical and (opto)electronic devices: Properties and Applications”, Editor: Oksana Ostroverkhova, *Woodhead Publishing Ltd. (Cambridge)*, 2013.

[†] These authors contributed equally to this work.

Patents

- [P1] T. Hoheisel, T. Schwab, S. Schubert, M. Riede, and K. Leo, "Verfahren zur Erzeugung von Metallpartikeln auf organischen Schichten, mit Hilfe einer Zwischenschicht Divanadiumpentoxid", DE 10 2012 113 030.2 *submitted*.
- [P2] T. Schaefer, T. Schwab, S. Hofmann, and M. C. Gather, "Lichtauskopplung in top-emittierenden organischen Leuchtdioden (OLED) durch Streuschichten mit Titandioxid-Nanopartikeln in orthogonaler Polymermatrix", DE 10 2013 112 200.0 *submitted*.
- [P3] M. Fröbel, T. Schwab, S. Hofmann, K. Leo, and M. C. Gather, "Über Wechselspannung farbsteuerbares organisches lichtemittierendes Bauelement", *in preparation*.

Oral Conference Contributions

- [C1] T. Schwab, S. Hofmann, M. Thomschke, K. Leo, and B. Lüssem: "Efficiency Improvement in Top-Emitting Organic Light Emitting Diodes Using Color Conversion Layer", Solid State and Organic Lighting, Austin (TX, USA), 2011.
- [C2] C. Fuchs, T. Schwab, R. Scholz, T. Roch, A. Lasagni, S. Hofmann, B. Lüssem, L. Müller-Meskamp, K. Leo, and M. C. Gather: "Quantitative description of the scattering angles in electrically-driven OLEDs fabricated on periodically corrugated substrates", Solid State and Organic Lighting, Eindhoven (NED), 2012.
- [C3] T. Schwab, S. Schubert, M. Thomschke, M. Fröbel, L. Müller-Meskamp, K. Leo, and M. C. Gather: "Inverted Top-Emitting White OLEDs with Improved Optical and Electrical Characteristics", SID Displayweek, Vancouver (BC, CA), 2013.
- [C4] T. Schwab, C. Fuchs, R. Scholz, X. Li, F. Xie, W. Choy, K. Leo, and M. C. Gather: "Improved light outcoupling and mode analysis of top-emitting OLEDs on periodically corrugated substrates", SPIE Optics and Photonics, San Diego (CA, USA), 2013.
- [C5] L. Müller-Meskamp, S. Schubert, C. Sachse, Y.H. Kim, L. Bormann, F. Selzer, T. Schwab, S. Hofmann, M. C. Gather, and K. Leo: "Alternative Transparent Electrode Technologies for Organic Optoelectronic Devices", 2014 MRS Spring Meeting & Exhibit, San Francisco (CA, USA), 2014.

List of Publications

1 Introduction

In the late 1990s, scientists intended to investigate in various socioeconomic and research fields effects of the urbanization on the global scale, e.g. the climate change, land transformation, and ecologic sustainability.[1, 2] To account for the rapid growth in the earth's population and to observe effects on these large scales, satellite images were evaluated. Even though satellite images included all the necessary information, the enormous challenge of identifying urbanized areas without a detailed evaluation of the respective region on a square-foot-scale remained.

The impressive solution for this challenge was found in night-light images of the earth [1, 2], as an analogy of the accumulation of humans in urbanized areas and the amount of dissipated light was observed. Night-light images of Europe from 1992 and 2010 are shown in Fig. 1.1, in which the increasing light emission alongside the progressing urbanization is visualized. In addition, it confirms that nowadays, artificial light sources are a fundamental part of our daily life!

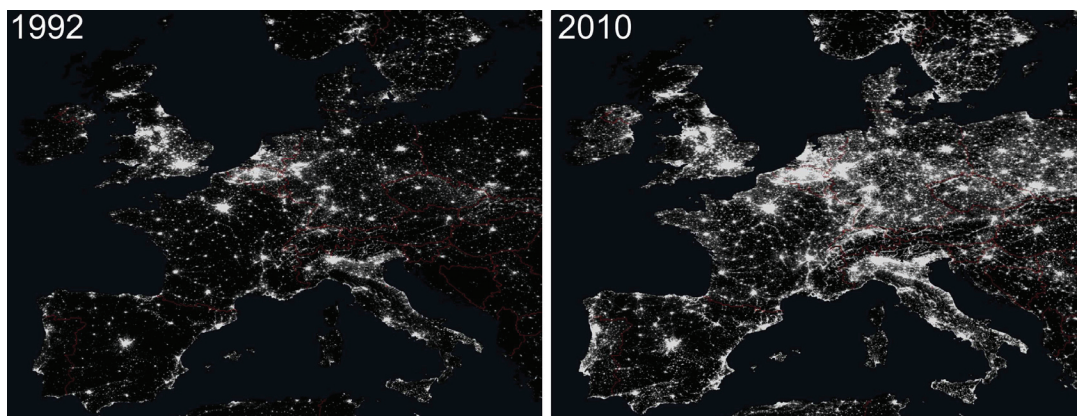


Figure 1.1: Satellite night-light images of Europe showing a significant increase in the light dissipation of the urbanized areas from 1992 to 2010. [3]

Although the distribution of artificial light sources has been increasing with urbanization, there has been only a comparatively slow development in lighting technology. In the end of the 2000's, either light-bulbs that dissipate 95 % of their consumed power as heat or mercury containing fluorescent tube lamps have been used almost exclusively. Highly efficient light-emitting diodes (LEDs) have only just started to revolutionize the lighting market.[4]

LEDs represent a new state-of-the-art technology which generates emission more efficiently than other light sources, as their charge-to-photon conversion efficiencies approaching unity.[4] Since 1987, another lighting technology has made its progress in research, the organic LED (OLED).[5] Even though OLEDs have had the shortest development time, intensive research have also led to charge-to-photon conversion efficiencies close to unity [6] and efficiencies compatible with fluorescent tubes [7].

Introduction

In addition, OLEDs are already commercially used for display applications, mainly in smartphones, and are to be used in upcoming designs for large area and curved TV screens (Fig. 1.2(a)). In Fig. 1.2(b), an OLED design study illustrating two unique features of this technology is shown: area emission and transparency. Furthermore, OLEDs allow for flexible device designs and roll-to-roll fabrication. Especially for lighting applications, OLEDs have various benefits in comparison to LEDs. The broad spectral emission is advantageous for high quality white light emission with excellent color rendering, whereas LEDs require conversion layers to obtain broad emission. As an area emitter, OLED emission is perceived as more pleasant, in contrast to LED point light sources with directed emission and high brightness, which are often preferred in spot light applications. However, the organic materials in OLEDs are sensitive to oxygen and moisture and must be encapsulated within an inert atmosphere to avoid chemical decomposition as well as to achieve device lifetimes similar to other lighting technologies.

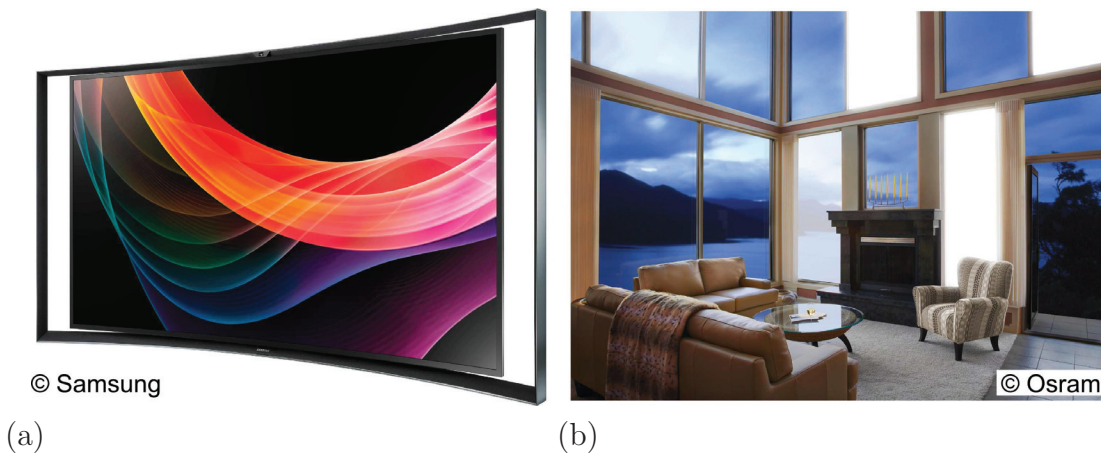


Figure 1.2: Photograph of OLED applications in a large area curved OLED-TV [8] (a) and a design study of transparent white OLEDs for solid-state lighting applications [9] (b).

Motivation

Although LEDs and OLEDs can already be found in various products, researchers still focus on their optimization. For both devices, the major efficiency limitation is based on the trapping of generated emission inside the devices, as total internal reflection occurs at a critical propagation angle in the emissive medium. In OLEDs, only 20 % to 30 % of the emission can be extracted from the typically planar devices. [10, 11]

For point light sources such as LEDs, this problem is solved, e.g. by attaching a half-sphere on top. The successful application of light extraction structures to LEDs has been one fundamental basis to the development of highly efficient LEDs, which represent currently the most efficient light sources. However, the application of half-spheres on top of OLEDs with significantly larger emitting areas is unfavorable and thus large area compatible, flat light extraction structures have to be developed. This work tackles the remaining key challenge of the OLED technology in increasing the device efficiency, which is the extraction of internally trapped light modes. In order to extract the inter-

nal light modes, periodically corrugated grating structures are applied to OLEDs, which introduces Bragg scattering. In contrast to random scattering layers, which are often preferred in product applications, periodic structures do not suffer from an averaging of the scattering effects due to the structural randomness. Hence, they allow the detection and analysis of the scattering mechanisms in detail.

In this work, top-emitting OLED architectures are investigated, in which the emission is directed away from the carrier substrate. Hence, these devices do not require a transparent substrate as it is the case for bottom-emitting OLEDs, which emit through the substrate and can therefore be deposited on opaque materials, e.g. metal foils and display back planes. Top-emitting OLEDs are preferred in device applications, such as displays, where the non-transparent TFT-backplane can be integrated underneath the OLEDs. This improves the fill factor and also reduces driving currents at a comparable brightness in comparison to bottom-emitting OLED displays.

However, the organic layers, deposited prior to the transparent top electrode in top-emitting devices, hinder the application of most state-of-the-art transparent electrode materials. Hence, metal films with only moderate transmittance have often been applied, resulting in a pronounced angular emission dependency, narrowed emission spectra, and lower efficiency of white top-emitting OLEDs in comparison to their bottom-emitting counterparts. Therefore, the application of highly transparent electrodes is one focus of this research work. Furthermore, the sensitivity of the deposited organic layers typically impedes the application of common light extraction structures on top of top-emitting OLEDs, as mechanical damage is introduced. In contrast, bottom-emitting devices are protected against damage by the substrate. The development and integration of periodic light extraction structures underneath top-emitting OLEDs is a further point of interest in this work, with the aim to extract the internal light modes, while the electrical performance and the charge-to-photon conversion efficiency is maintained. As such, large area compatible processes for the preparation of the light extraction structures are investigated in advance.

The basics of organic semiconductors (Chapter 2), OLEDs (Chapter 3), and the light propagation in a multi-layer structure (Chapter 4) are described preliminary to the experimental results. Details on the sample preparation and the device characterization are provided in Chapter 5. In Chapter 6, the investigation of highly transparent metal top electrodes, using wetting layers to improve the film growth is presented, increasing the transmittance of the electrodes while maintaining the conductivity. Their application to white top-emitting OLEDs is shown in Chapter 7, which compensate the present limitations of top-emitting OLEDs regarding white emission. The extraction of internally trapped light modes is presented in Chapter 8 & 9. First, a detailed analysis of the Bragg scattering effects in periodically corrugated top-emitting OLEDs are provided. Then, the optimization of the grating-OLED system is shown in Chapter 9. Finally, corrugated white top-emitting OLEDs have been prepared, in order to combine the benefits from the application of wetting layer electrodes and light extraction structures.

2 Organic Semiconductors

The following chapter discusses the fundamental properties of organic molecules and molecular solids. The electronic structure of the molecules are the main determiner of the optical, electrical, and chemical properties of organic solids. By evaluating molecular orbitals, excitation and decay mechanisms of molecules are investigated and the energy transfer between molecules is analyzed. Furthermore, non-radiative decay paths of excited molecules are discussed, as they limit the efficiency of OLEDs. The last part of this chapter illustrates the basics of charge carrier transport in molecular solids.

Organic semiconductors offer unique properties suitable for applications in electronics, lighting, as well as photovoltaics. The fundamental building blocks of an organic solid are molecules which are bound by van der Waals forces. [12] As the binding energies are low compared to covalent bonds and the molecular interaction is weak, the optical and electrical properties of the organic semiconductor are primarily determined by the properties of the single molecules. Knowledge about the single molecule is therefore essential for the understanding of processes in organic solids. Two electronic states mainly determine the chemical and photo-physical characteristics, namely the highest occupied molecular orbital (HOMO) and the lowest unoccupied molecular orbital (LUMO), both forming the frontier orbitals of the molecule. The implementation of an emitter molecule is fundamental for OLED applications as it has a major impact on the device efficiency, the spectral emission, and the device lifetime. To emit light in the visible spectral range, the energy gap which is mainly determined by the difference of HOMO and LUMO as well as the exciton binding energies [13], has to range from 1.6 to 3.5 eV.

2.1 Molecular Orbitals

In theory, the properties of micro- and macroscopic systems can be calculated from the wave function Ψ of the investigated system. This wave function can be obtained from the Schrödinger equation [14, 15]. For time-independent Hamiltonian \hat{H} , it is sufficient to solve the time-independent Schrödinger equation:

$$\hat{H}\Psi = E\Psi. \quad (2.1)$$

A certain set of wave functions, the eigenfunctions Ψ_n , can be used to solve this time-independent Schrödinger equation for the Hamiltonian \hat{H} . The corresponding eigenvalues E_n represent the stationary state energies of the system investigated.

However, even for such small systems as the molecules used in this work, there is often no analytical solution for Eq. 2.1 due to complicated many-body aspects. Nevertheless, it is possible to obtain suitable eigenenergies of the organic molecules by the application of the

Hartree Fock method (HF) and through the use of several approximations. The Born-Oppenheimer approximation [14, 16] separates the total molecular wave function $\Psi(\vec{r}, \vec{R})$ into an electronic $\phi(\vec{r}, \vec{R})$ and a nuclear $\chi(\vec{R})$ part, based on the assumption that the heavy nuclei are much slower than the electrons and that the electrons will adiabatically react to a configuration change of the nuclei. Therefore, the electrons ($\vec{r} = \{r_1, r_2, \dots, r_N\}$) move in a quasi static nuclei configuration $\vec{R} = \{R_1, R_2, \dots, R_M\}$:

$$\Psi_n = \phi_n^{\vec{R}}(\vec{r}) \cdot \chi_n(\vec{R}) . \quad (2.2)$$

This separation ansatz of the wave function reduces the complexity of the calculation by separately solving the Schrödinger equation for the electronic part and the nuclear part. The resulting electronic eigenenergies ϵ_n^{el} depend on the nuclei configuration \vec{R} . While solving the Schrödinger equation for the nuclear part $\chi_n(\vec{R})$, the obtained electronic eigenvalues ϵ_n^{el} for each configuration (\vec{R}) are respected. The eigenvalues of the nuclei represent the vibrational and rotational states for the given nuclei configuration. The eigenvalues of the total molecular state can be written as the sum of the electronic and nuclear eigenvalues:

$$E_n = \epsilon_n^{el} + \epsilon_n^{\text{vib}} + \epsilon_n^{\text{rot}} . \quad (2.3)$$

For the calculation of the molecular eigenvalues, e.g. the HOMO and LUMO energies or transition dipole moments between two stationary eigenstates, the corresponding molecular wave functions have to be investigated. In addition to this, approximations can be made to obtain the electronic molecular wave function ($\phi_n^{\vec{R}}(\vec{r})$). A well-known method is the so-called molecular orbital theory. This method simplifies the interaction between the electrons which allows the Schrödinger equation to be solved separately for each electron in an effective potential arising from the nuclei and the other electrons.[14] The total electron wave function in the configuration can thus be expressed as a product of the single electron molecular orbitals ξ_j :

$$\phi_n^{\vec{R}}(\vec{r}) = \left[\prod_j \xi_j(\vec{r}_j) \right]_{\vec{R}}^{\vec{R}} \quad (2.4)$$

To deduce the molecular orbitals ξ_j , a further approximation can be made. Following the argument of Hund and Mulliken, the molecular orbitals can be built from a linear combination of atomic orbitals ζ_i (LCAO) [13, 15], in which the electron is only affected by the potential of a single and isolated nucleus:

$$\xi_j = \sum_i c_{i,j} \cdot \zeta_i \quad (2.5)$$

Compared to the atomic orbital configuration, the resulting molecular orbitals can either have an increased amplitude between adjacent atoms, which is called a “binding” orbital, or a reduced amplitude, “anti-binding” orbital. The fermionic nature of electrons demands certain requirements for the occupation of the molecular orbitals and the form of the electronic wave functions. The Pauli principle [14, 17] excludes that two electrons can simultaneously occupy the same state with identical quantum numbers. Respecting the two different electronic spin configurations, “up” and “down”, each molecular orbital ξ_j

can be occupied by two electrons with opposite spin orientations. Furthermore, the wave function of fermions has to be anti-symmetric under the exchange of the coordinates of two electrons:

$$\phi(1, \dots, i, j, \dots n) = -\phi(1, \dots, j, i, \dots n) \quad (2.6)$$

In a further approximation of the Hartree Fock method, the electronic wave function $\phi(1, \dots, i, j, \dots n)$ for a given configuration of n electrons is constructed as a determinant of single electron states:

$$\phi(1, \dots, i, j, \dots n) = \frac{1}{\sqrt{n!}} \begin{vmatrix} \xi_1(1) & \xi_1(2) & \dots & \xi_1(n) \\ \xi_2(1) & \xi_2(2) & \dots & \xi_2(n) \\ \vdots & \vdots & \ddots & \vdots \\ \xi_n(1) & \xi_n(2) & \dots & \xi_n(n) \end{vmatrix}, \quad (2.7)$$

where $\xi_1(1)$ denotes the molecular orbital of electron 1 at position \vec{r}_1 abbreviated as "1", $\xi_1(2)$ of electron 1 at position 2, ... This Slater determinant of the molecular orbitals automatically fulfills the requirements of the Pauli principle.

To accurately describe the energy levels and transition moments of a multi electron system, e.g. the excitation of a molecule, two contributions to the interaction between electrons have to be included. First, the Coulomb repulsion between the electrons:

$$J = \frac{e^2}{4\pi\epsilon_0} \int \int \xi_1^*(\vec{r}_1)\xi_2^*(\vec{r}_2) \frac{1}{r_{12}} \xi_1(\vec{r}_1)\xi_2(\vec{r}_2) d^3\vec{r}_1 d^3\vec{r}_2, \quad (2.8)$$

including the elementary charge e , the permittivity in free space ϵ_0 , and the conjugated molecular orbitals ξ_j^* . Second, as a direct consequence of the quantum-mechanical nature of electrons, being indistinguishable fermionic particles, the exchange interaction:

$$K = \frac{e^2}{4\pi\epsilon_0} \int \int \xi_1^*(\vec{r}_1)\xi_2^*(\vec{r}_2) \frac{1}{r_{12}} \xi_2(\vec{r}_1)\xi_1(\vec{r}_2) d^3\vec{r}_1 d^3\vec{r}_2. \quad (2.9)$$

The contributions of those two corrections to the eigenenergies are dependent on the symmetry of the molecular orbitals ξ_j . As mentioned before, they have to be anti-symmetric with respect to the exchange of two electron coordinates. This is achieved either by a symmetric spin-function and an anti-symmetric spatial wave function or an anti-symmetric spin-function and a symmetric spatial wave function. For a symmetric spatial wave function and $|\vec{S}| = 0$ (singlet state), these terms contribute as:

$$E_S^{\text{HF}} = J + K, \quad (2.10)$$

while for an anti-symmetric spatial wave function and $|\vec{S}| = 1$ (triplet state):

$$E_T^{\text{HF}} = J - K \quad (2.11)$$

is found.[13] As a consequence, the triplet levels of the molecule will have a lower energy than the singlet states ($E_S^{\text{HF}} - E_T^{\text{HF}} = 2K$, *singlet-triplet splitting*). While the Coulomb repulsion J only depends on the distance between the electrons, which are mainly confined on a single molecule, the exchange interaction K further depends on the overlap of the molecular orbitals. One interpretation states that electrons with parallel spin orien-

tation (triplet state) try to avoid one another according to the Pauli principle, whereas electrons with an anti-parallel spin configuration in a singlet state tend to approach each other. As consequence, the Coulomb repulsion of the singlet state increases, while it decreases for the triplet state.

2.2 Optical Properties of Organic Semiconductors

All materials used in this work are conjugated hydro-carbons with alternating single and double bonds between the carbon atoms. The valence electrons of the carbon atoms either contribute to the strong σ -bonds, by the sp^2 hybridized electrons, or to π -bonds by the residual $2p_z$ valence electron.[18] The π -electrons are considered to be delocalized, as the probability density of these electrons is spread over the whole molecule in the π -orbital. The electrons in the σ -bonds have a higher binding energy compared to the weakly bound π -electrons. This leads to a larger energetic splitting between binding (σ) and anti-binding (σ^*) state. As a consequence, the HOMO and LUMO orbitals of conjugated molecules are formed by the π -orbitals as shown in Fig. 2.1(a). The lowest energy transition of such molecules from the ground to an excited state occurs from the binding π to the anti-binding π^* orbitals.[12] Since the HOMO is completely occupied and the LUMO completely unoccupied, most organic solids are considered to be either semiconductors or insulators. The attractive force in the molecular solids is based on the rather weak van der Waals interaction between the molecules.[19]

Interaction of Organic Molecules with Electromagnetic Radiation

The optical spectra of organic molecular solids are closely related to the electronic and vibrational states of the single molecules discussed in the previous section. The interaction of a molecule with the electromagnetic fields of a light wave can cause dipole transitions between two molecular eigenstates Ψ_i , e.g. from the ground state and to the first excited singlet state by photon absorption. The dipole transition probability P can be obtained by calculating the corresponding matrix elements (*Fermis Golden Rule*) [15]:

$$P_{n,m} \propto \left| \langle \Psi_m^* | \hat{M} | \Psi_n \rangle \right|^2, \quad (2.12)$$

where \hat{M} is the dipole operator and the subscripts refer to the initial and final state. According to the Born-Oppenheimer approximation, the molecular wave function can be written as:

$$\Psi_n = \phi_n \cdot \chi_n = \phi_n^i S_n \cdot \chi_n^{\text{vib}} \chi_n^{\text{rot}} \quad (2.13)$$

and finally the matrix element:

$$P_{n,m} \propto |\langle \phi_m^i | \hat{M} | \phi_n^i \rangle|^2 |\langle S_m^* | S_n \rangle|^2 |\langle \chi_m^{\text{vib}*} | \chi_n^{\text{vib}} \rangle|^2 |\langle \chi_m^{\text{rot}*} | \chi_n^{\text{rot}} \rangle|^2, \quad (2.14)$$

with ϕ_n^i as spatial electronic molecular orbital, S_n spin-function, χ_n^{vib} vibronic wave function, and χ_n^{rot} rotational wave function. A dipole transition is called “*forbidden*” if the matrix element is zero. For all “*allowed*” transitions, the transition probability and therefore the transition rate is proportional to the matrix element. In the following, the single factors of Eq. 2.14 will be described in detail. The first factors represents the

interaction of the spatial electronic molecular orbitals with the dipole operator and is mainly determining the probability of a transition. The second factor is only non-zero for eigenstates with the same spin-multiplicity, which forbids a transition between singlet and triplet states. In molecules containing heavy metal atoms, e.g. iridium, this selection rule is no longer valid as spin-orbit coupling effects have a major impact on the quantum mechanics of the molecules and allow transitions between singlet and triplet states, as well as radiative emission from excited triplet levels into the singlet ground state. The third factor is called *Franck-Condon factor* and refers to the overlap of the vibronic wave functions of the initial and final state. For most transitions, the rotational factors can be assumed to be one as the rotational configuration is not changing for embedded molecules.

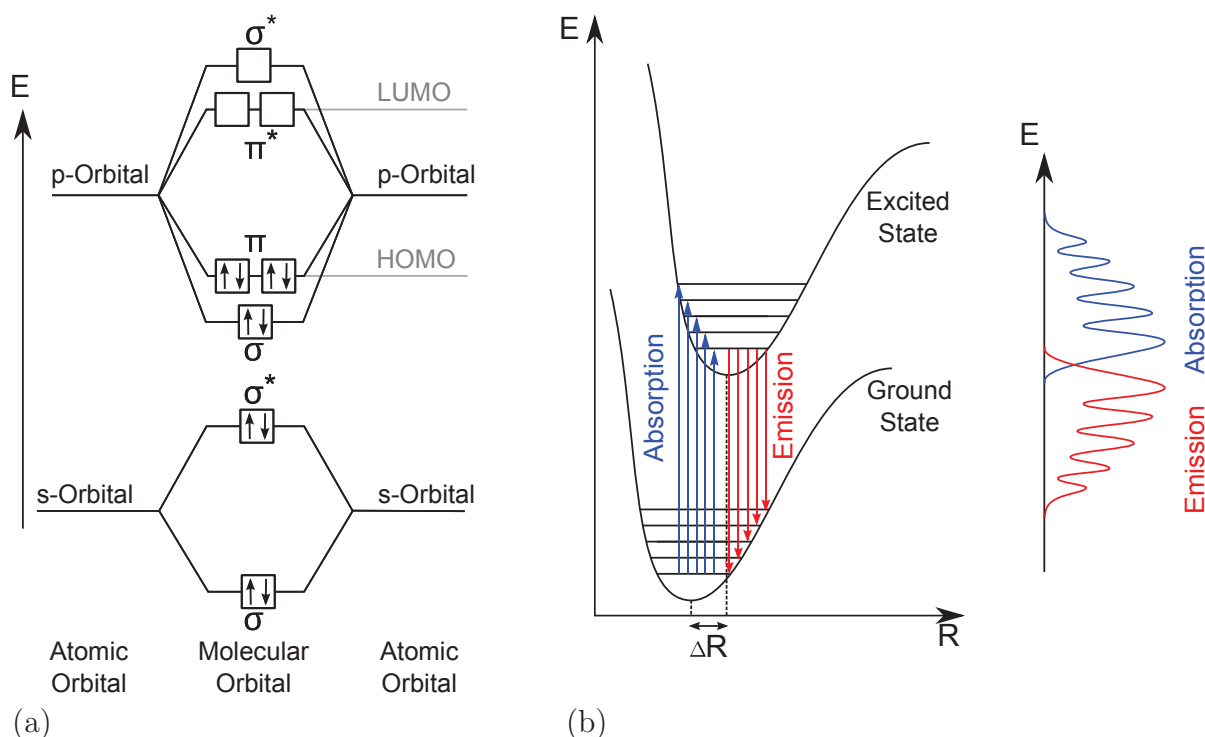


Figure 2.1: Simplified energy level scheme of molecules based on the linear combination of atomic orbitals (a).[18] The frontier orbitals, HOMO & LUMO, of conjugated organic compounds are formed by the π -orbitals. Absorption and emission of photons by an organic compound (b).[12] Non-radiative vibronic relaxations to the respective ground level of the electronic eigenstates result in an energetic shift between absorption and emission spectra (*Stokes shift*).

Figure 2.1(b) shows a scheme of the absorption and emission of photons by an organic molecule. As stated in the Born-Oppenheimer approximation, the nuclei are quasi static during a change of the electronic configuration. Thus, the nuclei positions are not significantly altered during the absorption / emission of a photon. As a consequence, the equilibrium configuration of each electronic state is only reached after non-radiative internal conversion processes (*Franck-Condon principle*). According to the *Kasha rule* [16], non-radiative conversion between the energetically close vibronic levels occurs on a much shorter time scale than photon emission / absorption. The non-radiative vibronic transitions cause a so-called *Stokes shift* between absorption and emission spectra. As illus-

trated in Fig. 2.1(b), the observed emission and absorption spectra do not show distinct monochromatic spectral lines, but a continuous spectrum with broadened and smoothed peaks. The limited lifetime τ of the dipole transition leads to an energy uncertainty responsible for the *natural line width*.^[18] The organic solids investigated in this thesis are amorphous solids which have no long-range order like a crystal.^[20] Disorder of the spatial distribution, molecule orientation, as well as deformation introduced e.g. by polarization effects causes the *inhomogeneous broadening*, resulting in a Gaussian shaped, broadened line.^[21] Figure 2.2 summarizes the most important radiative and non-radiative processes in a *Jablonski diagram* ^[15]. Optical excitation of a molecular solid is obtained by absorption of a photon with an energy compensating the energy level difference of initial and final state. Radiative transitions to the ground state occur either as *fluorescence*, from an excited singlet level, or as *phosphorescence* from an excited triplet state. The non-radiative inter system crossing (ISC) and the reverse process (RISC) transfer the molecule from an excited singlet to a triplet level or vice versa. As discussed previously, the singlet-triplet splitting leads to a higher energetic fluorescence emission compared to the phosphorescence of a molecule.

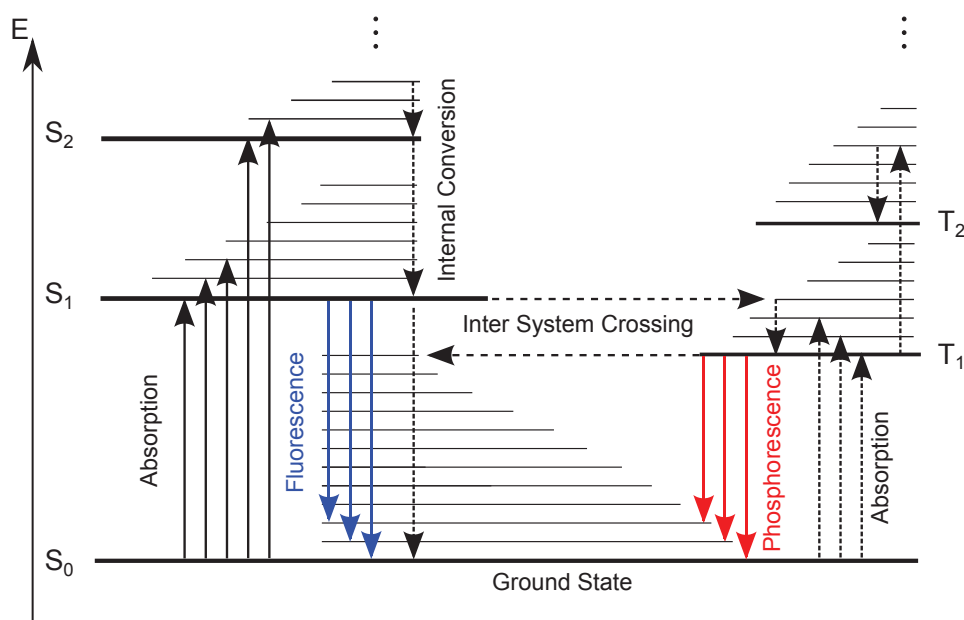


Figure 2.2: The optical transitions of a molecule are depicted in a Jablonski diagram ^[15]. Non-radiative processes like internal conversion and inter system crossing are shown as dashed lines. The radiative emission of a photon can occur from excited singlet states as fluorescence or from excited triplet states as phosphorescence (solid arrows downwards).

Excitons in Organic Semiconductors

The excitation of a molecule by photon absorption can be illustrated by a transfer of an electron from the HOMO into the LUMO level of the molecule, leaving a positively charged *hole* in the HOMO level. The localization of electron and hole on a molecule causes Coulomb attraction forces and (bound) electron-hole pairs are formed, which are called *excitons*.^[16] In organic solids, the binding energy of excitons is in the range of

0.1 to 1.0 eV [12], and therefore much larger than $k_B T$ at room temperature. Localized, *tightly-bound* excitons are called *Frenkel excitons*. *Charge-transfer excitons* (CT), where electron and hole are distributed on neighboring molecules, are also observed in organic semiconductors. For spatially distributed electron-hole pairs like in inorganic semiconductors (*Wannier-Mott excitons*), the binding energies can be in the range of 0.01 eV. Therefore, Wannier-Mott excitons can only be observed at low temperatures. Figure 2.3 illustrates the different types of excitons. Excitons cannot only be formed by direct optical excitation of the molecule, but also by charge carrier recombination.[16] As the formation of an exciton is energetically preferred by the Coulomb attraction compared to separated electron and hole, the optical band gap is smaller than the electrical band gap.[19] The exciton formation from the separate charge carriers as they come close to each other often builds a precursor state to the intra-molecular radiative decay on emitter molecules in OLEDs.

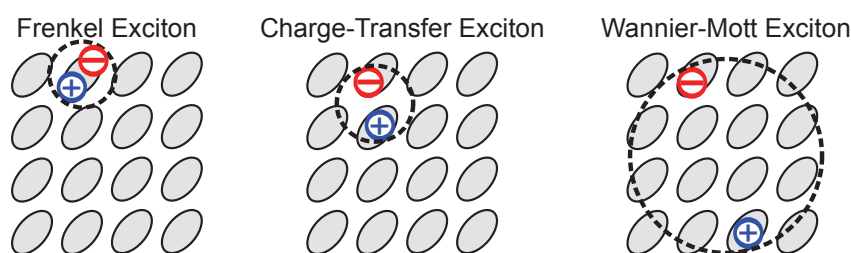


Figure 2.3: Scheme of the different exciton types.[12] Frenkel and charge-transfer excitons can be observed in organic semiconductors at room temperature as their binding energies are larger than the thermal energy. Wannier-Mott excitons can mostly be found in inorganic semiconductors.

2.3 Inter-Molecular Energy Transfer

In addition to the intra-molecular energy transfer discussed previously, inter-molecular energy transfer mechanisms such as radiative transfer by re-absorption of an emitted photon, non-radiative processes as Förster and Dexter transfer, and the diffusion and quenching of excitons have to be considered as well. Energy donating molecules are referred to donors (D) while energy accepting molecules are referred to acceptors (A). An asterisk marks the excited molecule, respectively.

Re-Absorption of Emitted Light

The re-absorption of a photon represents a two-step radiative energy transfer process. In the first step, the excited donor relaxes to the ground state via the emission of a photon, which in the second step is absorbed by the acceptor:



For the realization of efficient OLEDs, re-absorption of emitted light has to be strictly avoided, as it reduces the overall radiative efficiency of the device.

According to the *Lambert-Beer law*:

$$A(d) = \frac{I(0) - I(d)}{I(0)} = 1 - e^{-\alpha d} , \quad (2.16)$$

the absorption $A(d)$ in an organic layer with finite thickness d is given by the absorption coefficient α , which is determined by the dipole matrix elements discussed previously. For an organic material, the self-absorption of emitted light is small due to the Stokes shift between absorption and emission spectra.

Förster Resonant Energy Transfer

The *Förster resonant energy transfer* (FRET) represents a non-radiative single step energy transfer mechanism based on the Coulomb interaction between molecules, primarily the dipole-dipole-interaction[15]. This mechanism is widely used for the realization of efficient *host-guest* emitter systems in OLEDs.[22] During the energy transfer, the electrons remain on the molecules and the spin eigenstates have to be conserved:



The efficiency of the FRET strongly depends ($\propto r^{-6}$) on the distance between the contributing molecules. Furthermore, the spectral overlap of emission spectra of the donor and the absorption spectra of the acceptor, as well as the according dipole orientation are crucial parameters.[15] The sensitivity on short length scales in the nanometer regime can be used, e.g. to monitor molecular dynamics.[23] Even though the FRET rate is strongly dependent on the donator-acceptor distance, FRET still occurs for distances up to 10 nm.

Dexter Energy Transfer

In contrast to FRET, Dexter energy transfer is based on the exchange interaction between molecules. For efficient electron exchange, the corresponding molecular orbitals have to overlap. As they are mainly confined to a single molecule, the Dexter transfer rate exponentially depends on the distance between donor and acceptor. Dexter energy transfer represents a short range energy transfer [22, 24] with typical distances in the range of 1 nm. Furthermore, only the total spin of the contributing molecules has to be conserved, and thus triplet transfer between molecules can be realized:



Figure 2.4 illustrates FRET and Dexter type energy transfer mechanisms.

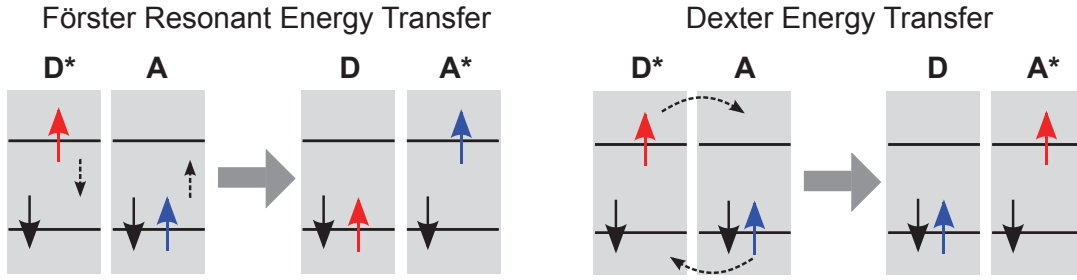


Figure 2.4: Förster and Dexter type energy transfer between an energy donating (D) and an accepting molecule (A). Förster resonant energy transfer occurs on typical distances up to 10 nm, while Dexter transfer is often limited to ≈ 1 nm.

Exciton Diffusion

Diffusion of excitons in the organic solid is based on a gradient of the exciton density ($n(\vec{r}, t)$). The diffusion process itself can be assumed as several uncorrelated Förster and Dexter energy transfer processes, transferring the exciton from one molecule to another and can be described by *Fick's second law*:

$$\frac{\partial n(\vec{r}, t)}{\partial t} = G(\vec{r}, t) - \frac{n(\vec{r}, t)}{\tau} + D\Delta n(\vec{r}, t) . \quad (2.19)$$

The time dependent evolution of the exciton density in the medium is dependent on three factors: exciton generation $G(\vec{r}, t)$, exciton decay within their lifetime τ , and diffusion according to the diffusion constant D .

This equation can be solved using a separation ansatz. Furthermore, the isotropic properties of the used amorphous materials result in isotropic solutions of the separated equations in all directions; without lack of generality one can focus on the one-dimensional solution in x-direction. In addition, the exciton generation zone is often localized close to a certain interface or layer and can be approximated by a delta-distribution $G(x, t) = G \cdot \delta(x = x_0, t)$. A steady state solution ($\partial n(x, t)/\partial t = 0$) to Eq. 2.19 can be found:

$$n(x, t) = n_0 \cdot e^{-x/L_x} \quad \text{with} \quad L_x = \sqrt{D\tau} \quad (2.20)$$

defining the diffusion length L_x . In dependence on the diffusion constants and the lifetimes of singlet and triplet excitons, diffusion lengths can range from a few to more than 10 nm.[25, 26] Moreover, specific organic compounds yield strong differences between the diffusion lengths of singlet and triplet excitons, which can be used in specific emission layer designs.

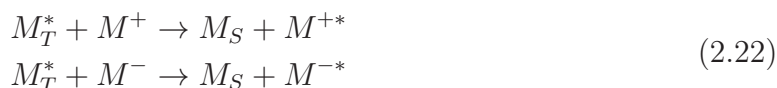
Exciton Quenching

Quenching mechanisms reduce the amount of excitons which can contribute to radiative decay compared to the initially generated ones. For typical operating conditions of OLEDs, singlet exciton quenching plays only a minor role compared to triplet exciton quenching.[27] For fluorescent OLEDs, in which the triplet excitons do not contribute to the radiative decay, singlet quenching processes are of course relevant, but not the focus of

this work. The longer lifetime of triplet excitons supports quenching effects which lower the OLED performance under normal operation conditions.[28] Two processes are mainly determining the observed efficiency decrease in phosphorescent OLEDs with increasing brightness (*roll-off*): *Triplet-Triplet-Annihilation* (TTA) and *Triplet-Polaron-Quenching* (TPQ).[16, 29, 30] The most prominent quenching mechanism is TTA, as its contribution scales with the second order of the exciton density.[29] The following decay paths are present in TTA:



Here, M_T^* represents the excited triplet state of the molecule, M_S singlet ground state, M_S^{**} and M_T^{**} a higher excited singlet or triplet states. For the first TTA quenching path, *delayed fluorescence* emission from the higher excited M_S^{**} can be observed. TPQ results from the interaction of triplet excitons with single charge carriers / charged molecules (M^\pm) and is linearly dependent on the exciton density.[29] Its decay paths can be visualized as:



In order to reduce quenching processes in phosphorescent OLEDs, the exciton density has to be reduced, e.g. by broadening the exciton generation and recombination zone.[31, 32]

2.4 Charge Carrier Transport in Amorphous Organic Semiconductors

The investigation of charge carrier transport and injection phenomena in the organic layers allows to understand the electrical properties of OLEDs. In the following, basic considerations on the charge carrier transport in amorphous organic solids are provided. It should be noted that the complexity of the topic as well as an ongoing research on the details of the charge transport does not allow a too detailed description of all occurring phenomena in respect to the focus of this work.

An additional charge injected to the HOMO or LUMO level of a molecule causes a feedback from the residual electrons and nuclei of the molecule, e.g. as deformation of the molecular shape or charge carrier redistribution. This so-called *self-polarization* or reorganization energy leads to a reduction of the energetic gap between HOMO and LUMO of the molecule.[16] The injected charge also interacts with the molecular orbitals of neighboring molecules as well as polarizing and deforming its surroundings while moving through the solid.[16] It can be described as a quasi-particle called *polaron* and the transport of charge through an organic semiconductor is based on the transport of these polarons.[16] In the following, the transport states of the charge carriers are denoted as E_+ for holes and E_- for electrons. They result from the HOMO and LUMO levels of the single molecules respecting the interactions in the molecular solid and the polarization energies of the charge carrier. When used to describe the transport of electrons and holes in the organic solid, it becomes a simplification of an electron (hole) polaron.

For the light generation in OLEDs, the macroscopic current flow j resulting from an applied electric field F is of importance. For the most simple case, the semiconductor shows only a linear response to the electric field F and the current is given by [17]:

$$j = \sigma F = e(n\mu_n + p\mu_p)F \quad , \quad (2.23)$$

where σ is the conductivity of the semiconductor. The conductivity σ is determined by the mobilities of electrons (μ_n) and holes (μ_p), as well as the charge carrier densities n , and p , which in the case of organic solids can show a dependency on the electric field.[33] Thereby, the mobilities of the charge carriers and the charge carrier densities mainly determine the current flow. The intrinsic charge carrier density of a semiconductor can be calculated according to [33, 34]:

$$n_i = N_0 \exp(-E_g/2k_B T) \quad . \quad (2.24)$$

By assuming a comparable effective density of states N_0 , the comparison of the intrinsic charge carrier density for an arbitrary organic semiconductor ($E_g = 2.5$ eV) and silicon ($E_g = 1.12$ eV) shows that organic semiconductors have a rather low amount of intrinsic charge carriers. This finding holds for other state-of-the-art inorganic semiconductors, such as Ge ($E_g = 0.67$ eV) and GaAs ($E_g = 1.42$ eV), as well.

The mobility of charge carriers depends on the transport through the semiconductor. For inorganic materials, the solid can often be approximated to be strictly periodic, and the electrons to be *quasi-free* in a periodic potential of the nuclei.[17] Band transport with mobilities higher than 10^3 cm²/Vs can be found for (crystalline) Si and other inorganic materials. For organic crystals with a high purity, band transport can also be observed. However, lower bandwidths as well as a weak electron delocalization result in lower mobilities than for inorganic semiconductors [33], typically reaching values in the range of 10^1 - 10^3 cm²/Vs. In contrast, the amorphous organic compounds investigated in this thesis show a prominent spatial disorder and locally varying polarization in the solid. This results in a broadened distribution of the transport states and can be described by a Gaussian *density of states* (DOS) [35]:

$$n(E) = (2\pi\sigma^2)^{-1/2} \exp\left[\frac{(E - E_0)^2}{2\sigma^2}\right] \quad , \quad (2.25)$$

where E_0 represents the energy of the center of the DOS. The disorder in amorphous solids hinders the formation of conductive transport bands and *hopping transport* of the charge carriers through the amorphous solid is present. For hopping transport, mobilities far lower than 1 cm²/Vs [16] are typically detected. Both, the lower intrinsic charge carrier densities and the lower mobilities rise challenges on the device concepts of organic electronics to overcome these intrinsic limitations in comparison to inorganic materials.

Hopping Transport

The transport of charge carriers in amorphous molecular solids is considered to be realized by a series of separate uncorrelated hopping transfers between the localized orbitals of the molecules (see Fig. 2.5(a)).[35]

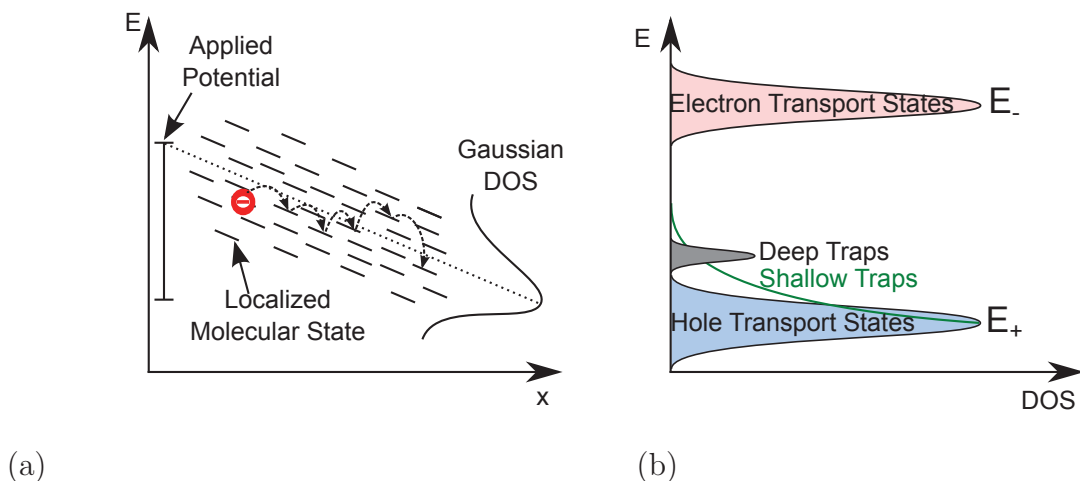


Figure 2.5: Illustration of the hopping transport of an electron between the different localized molecular states driven by an external applied potential (a).[36] Schematic image of the density of states (DOS) distribution of an organic semiconductor including the Gaussian shaped DOS of the transport levels, as well as the gap states by deep and shallow traps (b).

The hopping process between the localized molecular orbitals is thermally activated and the transfer probability increases with increasing temperature.[16, 35] A description of phonon assisted hopping transport of electrons and the corresponding hopping rates were given by *Miller and Abrahams* using a percolation network approach.[37] From their investigations, it follows that the hopping rate in organics is not only dependent on the distance between the molecules, but further on the energetic positions and molecular orbital overlap of the initial and final state.[35] *Bässler* introduced the *Gaussian Disorder Model* which describes the hopping transport in disordered organic solids by a Gaussian shaped density of states. The charge carrier mobility $\mu(T)$ can be written as [35]:

$$\mu(T) = \mu_0 \cdot \exp\left(-\frac{2}{3} \left(\frac{\sigma}{k_B T}\right)^2\right), \quad (2.26)$$

where μ_0 represents the mobility extrapolated for temperatures $T \rightarrow \infty$. [35] The charge carrier mobility in organic solids is further dependent on externally applied fields, as the energetic differences between the localized molecular states are reduced in field direction.[35, 38] The transport of charge carriers under an external field is described by the *Poole-Frenkel effect*. [38] A formulation of the field dependency of the mobility is given by [35, 38]:

$$\mu(F, T) = \mu(0, T) \cdot \exp\left[\gamma(T)\sqrt{F}\right] \quad (2.27)$$

including the field activation factor $\gamma(T)$, which represents the lowering of the hopping barriers in direction of the external field.[38, 39] In addition to the observed dependence on the temperature and external fields, *Tanase et al.* [40] provided evidence for the dependency of the mobility from the charge carrier density n .

They showed that for an increased charge carrier density, the mobility of holes is significantly increased in the devices. In addition to the Gaussian distributed states of the

transport levels, trap states representing additional states in the gap between the transport levels, are present in most semiconductors. Traps are generated, e.g. by impurities, dopant molecules or during grain and interface formation. If a charge carrier occupies such a molecular trap state, it does not longer contribute to charge transport and the probability of a release to the transport levels is significantly reduced.[33] The trapped charges contribute to the electric field distribution inside the organic solid, and thus influence the transport of the other charges. Trap states between the transport levels are often characterized by the distance to the transport states, either as *deep* or *shallow traps* (tail states of the DOS) (see Fig. 2.5(b)). The latter are mostly considered with an exponential DOS ($n_t(E)$) in relation to the center of the transport levels (E_{\pm}):

$$n_t(E) = \left(\frac{N_t}{k_B T_t} \right) \exp \left[\frac{E - E_{\pm}}{k_B T_t} \right] , \quad (2.28)$$

where N_t is the total density of traps, and T_t as trap distribution parameter.[41, 42]

Current-Voltage Dependence

In the case of a steady current flow with a linear response to an applied potential V , Ohmic charge carrier transport within a device is realized [43]:

$$j_{\text{Ohmic}} = en_0\mu \frac{V}{d} , \quad (2.29)$$

with the electron density n_0 , and the layer thickness d . However, the population and emission from trap states can influence the charge carrier transport while charge carriers can also accumulate inside the organic layer at a certain voltage, due to the low mobility, and build up a space charge. The space charge repulses further charge carriers, hindering the injection and limiting the current flow through the device.[41] In the *space charge limited current* (SCLC) regime, the current density can be described by:

$$j_{\text{SCLC}} = \frac{9}{8} \mu \epsilon_0 \epsilon_r \frac{V^2}{d^3} \quad (2.30)$$

including the relative permittivity ϵ_r . [16, 39] The SCLC model assumes Ohmic charge injection at the electrodes, unipolar charge transport, as well as the absence of trap states and diffusion currents. Although the SCLC-voltage dependency ($j \propto V^2$) is found for strong simplifications, it describes the conditions for certain regimes in real device operation. The dependency of the current on the 3rd order of the reciprocal thickness leads to a reasonable current in amorphous organic semiconductors if they are thin enough (tens of nanometers), obtaining bright emission from OLEDs at applied potentials of only a few volt.[33] For certain potentials, it is often not possible to describe the current-voltage dependency according to Eq. 2.30 as effects like population and emission from trap states [41, 42], as well as charge carrier density and field dependencies of the mobility have to be taken into account.[16, 39, 40] In this regime, the current-voltage characteristics can be often described by *trap limited currents*. [44, 45]

In order to determine the charge carrier mobility, analysis of the SCLC [46], time-of-flight [47, 48], and field-effect mobility measurements [34, 49, 50] are commonly performed. For more detailed investigations on the mobility, the current transport, and

the current density in real devices, the reader is referred to the work of Pope *et al.* [16], Blom *et al.* [39, 46], and Burrows *et al.* [51].

2.5 Charge Injection and Material Interfaces

So far, the charge carrier transport has been discussed for a single organic layer without focus on the charge injection from the electrodes. In OLEDs, it is desirable to realize efficient charge carrier injection without energetic barriers. In addition, sufficient charge transport in the organic layers has to be achieved to avoid the generation of space charges. Energetic barriers in multi organic layer structures can also cause the accumulation of charges at organic/organic interfaces and therefore should also be minimized.

Metal-Organic Interfaces

The injection of charge carriers into an OLED is determined by the interface formed between the electrode and the organic layer. The *Mott-Schottky* theory predicts that the vacuum levels of the metal and the organic semiconductor align in contact.[34] An occurring *zero-field* injection barrier Φ_B is defined by the difference of the work function of the metal (Φ_M) and the vacuum transport levels of the charge carriers in the organic (E_+ and E_-).[52, 53] Even though vacuum level alignment is not always observed, the height of the charge injection barrier Φ_B is the crucial parameter which quantifies, whether a contact is a non-rectifying (*Ohmic*), or a rectifying contact (*Schottky diode*).[34] In most devices, Ohmic contacts are preferred, as charges can be injected for small applied potentials and charge accumulation can mostly be neglected.

In the case of a rectifying Schottky contact, the charge injection can be described by a field assisted *thermionic emission* [54] of electrons in accordance to the *Schottky effect* [55]:

$$j_{\text{thermal}} = AT^2 \exp \left[\frac{-(\Phi_B - \sqrt{\beta F})}{k_B T} \right], \quad (2.31)$$

including the field induced lowered injection barrier according to $\beta = e^3/4\pi\epsilon\epsilon_0$ and the Richardson constant $A = 4\pi em_e^* k_B^2/h^3$, containing the effective mass of the electrons m_e^* . The formulation of the Schottky effect was obtained from a modification of the thermionic emission of electrons from metals into vacuum according to *Richardson*. [56] The electric field lowers the emission barrier (see Fig. 2.6) and increases the emission current in comparison to the vacuum case. Furthermore, the injection into localized organic states and the contribution of the hopping transport had to be considered for organic layers. The injection barrier Φ_B can be strongly modified by the formation of interface dipoles as the energy levels including the vacuum level are affected. This can be desired to reduce injection barriers. Interface dipoles can intrinsically be formed by chemisorption and physisorption effects, e.g.: charge redistribution at the surface, occupation of interface and trap states, chemical interaction, due to permanent dipoles in the organic material, charge transfer between metal and organic, or explicitly introduced by doping.[52, 57, 58] The interface dipole formation causes an inhomogeneous redistribution of mobile charge carriers in the organic material, which leads to the formation of a *depletion zone* and the bending of the transport levels.

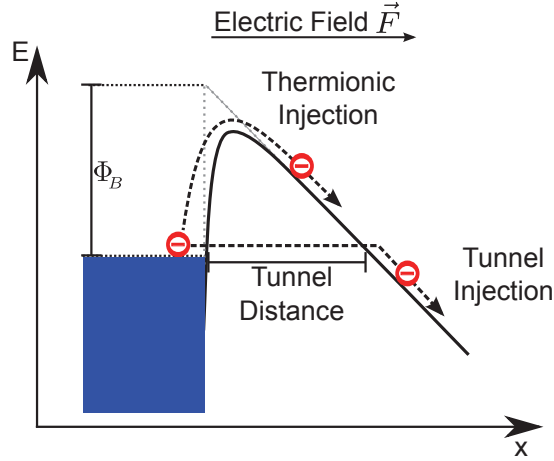


Figure 2.6: Illustration of charge injection by thermionic and tunnel injection into organic semiconductors. The electric field \vec{F} lowers the injection barrier Φ_B in field direction. Field assisted thermionic injection, described by the Schottky effect, demands the pass of the injection barrier. Tunnel injection instead allows for injection of charge carriers without the pass of the injection barrier. The probability of the tunnel injection process is strongly dependent on the thickness of the injection barrier (tunnel distance) and typically occurs for barriers in the nm range.[18]

In intrinsic organic semiconductors, the number of mobile charge carriers is small and depletion zones are formed which can reach dimensions of the layer thickness. The method of controlled doping of organic semiconductors and the certain properties of those layers will be investigated in detail in Section 3.2.3.

In the case that the injection barrier is narrow, either by strong electric fields, or the generation of a thin depletion layer, a further charge injection process based on the tunneling injection is enabled (see Fig. 2.6). According to *Fowler and Nordheim*, the current provided via the tunneling mechanism is defined by [34, 59, 60]:

$$j_{\text{tunnel}} = \frac{A}{\Phi_B} \left(\frac{eF}{\alpha k_B} \right) \exp \left[-\frac{2\alpha\Phi_B^{3/2}}{3eF} \right], \quad (2.32)$$

including the constant $\alpha = 4\pi\sqrt{2m_e^*/\hbar}$. The current flow according to the tunnel process is temperature independent, but strongly related to the electric field F . The tunnel injection mechanism allows for the formation of a non-rectifying, Ohmic contact for thin injection barriers.[54, 58]

For certain values of the metal work function, charge carrier transfer between metal and organic is energetically preferred. For $\Phi_M > E_+$, electrons are transferred from the organic to the metal and the Fermi level will be pinned at E_+ . For $\Phi_M < E_-$, electrons are transferred from the metal to the organic and the Fermi level is pinned at E_- . [52] In such cases the formation of Ohmic contacts is likely as only negligible injection barriers can be formed.[52] However, this would require a sensitive selection of electrode materials to realize Ohmic contacts, certainly for low E_- and high E_+ energies of the organic materials. The doping concept enables the formation of Ohmic contacts between metal and organics almost independently from the explicit work function of the materials and is the

favored method to generate Ohmic contacts [19, 61] (see Section 3.2.3). An important fact to mention here is that the interface dipole formation between metal/organic and organic/metal interfaces can yield strong deviations.[57] While most organic molecules evaporated on a metal surface do not tend to diffuse into the metal or undergo chemisorption effects, metal atoms evaporated on organics can diffuse into the organic layers and introduce strongly metal doped interfaces.[62, 63] This difference in the interface formation is a crucial fact to mention when the performance of OLED structures is compared where the deposition sequence was altered (*inverted OLEDs*).[63, 64] According results will be presented in Section 7.2.

Organic-Organic Interfaces

Intrinsic organic layers have a lower amount of mobile charge carriers than metal layers, which often results in weaker interface dipoles, rather negligible band bending, and small offsets in the vacuum energies are found.[65–67] However, those interface dipoles introduce further energetic barriers in multi-layer devices and their investigation is crucial to analyze and to understand the electrical characteristics of an OLED, as the hopping transport is affected at the material interfaces by a change of the DOS (position, width).[55, 68] The interface dipole formation at organic/organic interfaces can also be sensitive to the sequence of the layer deposition, as mixed interfaces, spatial- and dipole orientation disorder of the molecules, as well as the formation of interface states have a major impact, even though the comparably large organic molecule species do not tend to diffuse into each other.[57]

Experimental access to the energy level formation is often enabled by *UPS* (ultraviolet photon spectroscopy).[64, 66] The energy of the UV radiation allows to monitor the energy of the HOMO orbitals of organics and to determine the ionization potential and Fermi level position.[69, 70]

3 Organic Light-Emitting Diodes

This chapter introduces fundamental designs and highly efficient operation concepts of OLEDs, based on the optimization of the external quantum efficiency. Furthermore, the molecular doping of charge transport layers is investigated as it allows to optimize the optics of OLEDs without affecting the electrical properties, as well as providing superior electrical device performance. Finally, the perception of electromagnetic radiation by the human observer, and the impression of color are discussed.

The most simple concept to realize an electrically driven organic light-emitting device is a single emissive organic layer sandwiched between two electrodes. Bernanose *et al.* firstly reported on electroluminescence of organic compounds used as dielectric in a capacitor, when applying alternating current potentials of up to 2000 V.[71] In the early 1960's, investigations by Pope *et al.* [72] on the electroluminescence of crystalline organic materials have demonstrated DC electroluminescence with a threshold voltage of approximately 400 V.

While the efficiencies of the first single organic layer electroluminescent devices were considerably low, tremendous improvements were achieved in the late 1980's, where a bi-layer structure of small molecule materials between two electrodes was introduced. This first "real" OLED by Tang and van Slyke [73] incorporated a fluorescent emitter and achieved operational voltages below 10 V.

To realize efficient OLEDs, all processes regarding the injection of charge carriers and their transport to the emitters, the formation of excitons inside the emitting layer, the radiative decay of the excitons, and finally the extraction of the generated photons have to be optimized.

3.1 External Quantum Efficiency of OLEDs

The most important parameter to quantify the efficiency of an OLED is the *external quantum efficiency* (EQE), which is defined as the ratio of the number of extracted photons (n_{ph}) to the number of injected charge carriers (n_{el}):

$$\eta_{\text{EQE}} = \frac{n_{\text{ph}}}{n_{\text{el}}} . \quad (3.1)$$

In the ideal case, the EQE reaches unity, if every injected charge carrier couple forms an exciton which decays radiatively and the photon is subsequently extracted from the OLED structure. Taking the *light extraction efficiency* η_{out} and the *internal quantum efficiency* (IQE) into account, the EQE can be written as follows:

$$\eta_{\text{EQE}} = \eta_{\text{IQE}} \cdot \eta_{\text{out}} = \gamma \eta_{\text{rad}} \eta_{\text{ST}} \cdot \eta_{\text{out}} . \quad (3.2)$$

The IQE is determined by the charge carrier balance γ , the radiative efficiency of the emitter material η_{rad} , and the singlet-triplet ratio η_{ST} . The charge carrier balance γ describes the ratio of generated excitons to injected charge carriers. The radiative efficiency of an emitter material η_{rad} is determined by the ratio of emitted photons to generated excitons. The singlet-triplet ratio η_{ST} describes the ratio excitons which contribute to the radiative decay to the total amount of excitons. A rough approximation of the light outcoupling efficiency can be made, considering ray optics based on the refractive index mismatch of the light-emitting organic layer, the substrate, and the external media (air).[74] For a planar OLED the outcoupling efficiency is only in the range of 20-30%.[10, 11, 74] Approaches to enhance the outcoupling efficiency will be discussed in detail in Section 4.3. The optimization of the factors contributing to the internal quantum efficiency will be shown in the following.

Singlet-Triplet Ratio

According to the selection rules for dipole transitions, radiative decay can only occur from an excited singlet state into the singlet ground state of the molecules (fluorescence) (see Section 2.2). The charge carriers injected from the electrodes carry statistically distributed spin orientations, which results in approximately 25% singlet excitons and 75% triplet excitons.[19] Therefore, fluorescent OLEDs can only reach maximum IQEs of 25% ($\eta_{\text{ST}} = 0.25$), and EQEs of 5%, assuming $\eta_{\text{out}} \approx 20\%$.

Radiative emission from a triplet level (phosphorescence) is allowed if spin-orbit coupling effects are present in the emitter materials. Efficient phosphorescent emitter materials show radiative decay from an excited triplet level and further reasonable ISC transfer rates, transferring singlet excitons to the triplet states.[6, 75] In this case, the singlet-triplet ratio η_{ST} can become approximately 100% and all excitons can contribute to radiative decay.[6, 19, 75] OLEDs using phosphorescent emitters can therefore reach IQEs up to 100%, whereas only the light extraction efficiency limits the EQE.

Radiative Efficiency of the Emitter

Without influences from the surrounding media, the intrinsic radiative efficiency of the emitter material (η_{PL}) is determined by radiative Γ_{rad} and non-radiative $\Gamma_{\text{n-rad}}$ decay rates according to [76, 77]:

$$\eta_{\text{PL}} = \frac{\Gamma_{\text{rad}}}{\Gamma_{\text{rad}} + \Gamma_{\text{n-rad}}} . \quad (3.3)$$

In order to obtain highly efficient emitters, the radiative rate has to be significantly higher than the non-radiative rate. In OLEDs, the optical environment can have a significant influence on the efficiency of the emitter material.[78, 79] The *Purcell factor* F accounts for the influence of the optical environment on the radiative and non-radiative decay rates of the emitter.[77, 80] The effective radiative efficiency is defined by [80]:

$$\eta_{\text{rad}} = \frac{F \cdot \eta_{\text{PL}}}{1 - \eta_{\text{PL}} + F \cdot \eta_{\text{PL}}} , \quad (3.4)$$

while the intrinsic emitter efficiency in free space is obtained for $F = 1$. Optimization of the optical environment of the emitting layer can yield a Purcell factor which increases

η_{rad} compared to η_{PL} . [77, 80] The increase of the radiative efficiency of the emitter by the Purcell effect will consequently increase the EQE. [80]

Charge Carrier Balance

In order to obtain an optimized charge balance, electrons and holes have to reach the emission layer (EML) in an equal amount. This requires sufficient charge injection of both carrier types at the electrodes and transport through the device without prominent loss channels for one charge carrier type. Furthermore, a simple pass of the charge carriers through the device has to be avoided.

3.2 Optimization of the Internal Quantum Efficiency

The realization of highly efficient OLEDs with an electron to photon conversion efficiency close to unity will be discussed in the following. The single parameters contributing to the IQE are optimized by specifically designed layers, which are later incorporated in the complete OLED designs.

3.2.1 Emitting Layer Concepts

An efficient emitting layer combines a high radiative efficiency (η_{rad}) with a high singlet-triplet ratio (η_{ST}). In the following, three concepts which fulfill these efforts are introduced: Host-guest, triplet-harvesting, and TADF (*thermally activated delayed fluorescence*) emitter systems (see Fig. 3.1).

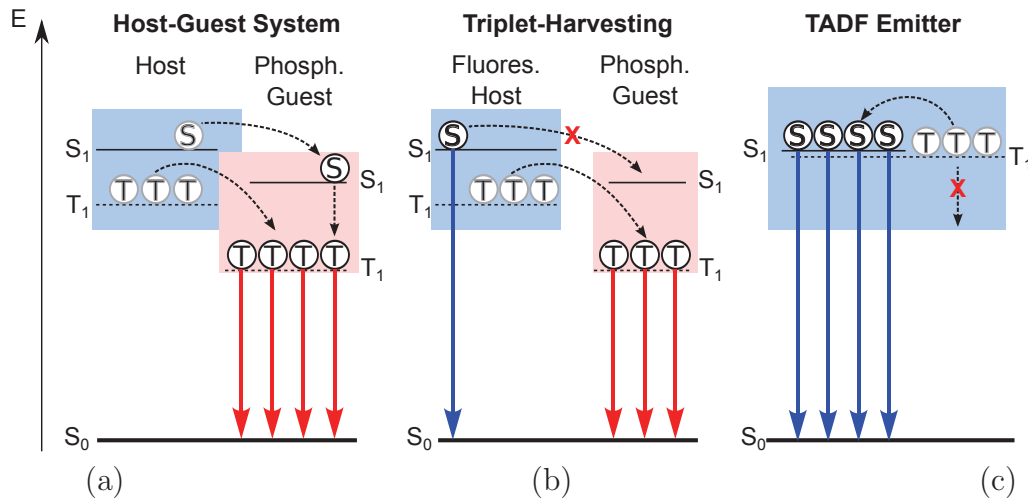


Figure 3.1: Comparison of different emitter systems regarding the radiative decay paths of singlet (S) and triplet (T) excitons. In all emitter systems, the excitons are generated at the host material. In a host-guest system only the phosphorescent guest is emissive, as singlets and triplets are transferred to the guest (a). [75] In the triplet-harvesting concept only triplets are transferred to the guest (b). [81] TADF emitters show only fluorescent emission either by a directly generated singlet or an "up-converted" triplet exciton (c). [82]

Host-Guest Emitter Systems

Phosphorescent emitters are often preferred as emitters in OLEDs, due to their singlet triplet ratio of approximately one. Deposited as a neat *emitter layer* (EML), the radiative efficiency significantly decreases as quenching effects become prominent.[83, 84] The co-deposition of a matrix material (host) with a few weight percent (1-10 wt.%) of a phosphorescent emitter (guest) reduces the impact of the so-called *aggregation quenching* effects.[83, 84]

In most host-guest systems, the emission of the host material is an unwanted side-effect, even though the excitons are generated at the host. Therefore, certain requirements to realize efficient energy transfer from the host to the guest material and further to avoid the host emission have to be fulfilled. Singlet excitons are transferred via Förster transfer to the phosphor while triplet excitons are transferred via the Dexter transfer mechanism (see Fig. 3.1(a)). The fundamentals for both transfer mechanisms have been given in Section 2.3. As soon as the excitons are transferred to the guest, a transfer to other materials has to be strictly avoided. This can be achieved by using organic materials with higher triplet level energies than the guest.[85] Optimized host-guest systems have already reached radiative efficiencies of almost 100 %.[6, 75]

Triplet-Harvesting Emitter Systems

Another highly efficient emitter system concept is based on a fluorescent host material which transfers only triplet excitons to a phosphorescent guest.[86, 87] This so-called *triplet-harvesting* concept is often applied in white OLEDs, as the generation of long-term stable deep blue emission by a phosphor is still challenging.[87] On the one hand, such phosphors suffer from chemical stability issues and significantly lower lifetimes in comparison to phosphorescent green or red emitters. On the other hand, a suitable host material would require an even higher energy gap, which could imply further chemical stability issues, but also drawbacks concerning the introduction of energy barriers in the layer structures.

Here, a fluorescent blue emitter with larger diffusion length of the triplets than the singlets is applied, to spatially separate the singlet and triplet excitons.[26, 88] A layer with a larger thickness than the singlet diffusion length, which can be a neat layer of the fluorescent host material, is deposited to ensure that no singlet excitons can reach the phosphorescent guest.[89] Hence, the singlet excitons decay on the fluorescent host, while the triplets diffuse to the phosphorescent guest in order to decay radiatively (see Fig. 3.1(b)). The triplet-harvesting concept can also reach a singlet-triplet ratio of approximately unity.[86, 87]

Thermally Activated Delayed Fluorescence

The TADF concept recycles triplet excitons via a thermally activated RISC process to singlet excitons (see Fig. 3.1(c)).[82, 90] Therefore, the singlet-triplet splitting ($E_S^{\text{HF}} - E_T^{\text{HF}} = 2K$), which is determined by the exchange interaction K (see Section 2.1), has to be in the range of the thermal energy. Most organic semiconductors do not fulfill this requirement ($\Delta E_{\text{ST}} \approx 0.5 - 1.0 \text{ eV}$) [82], demanding "low- K " molecule designs. This can be realized by a spatial separation of HOMO and LUMO level of the molecule. The separation of

the orbitals can be achieved by the introduction of electron donating and electron accepting groups to the molecular structure, where the donating group confines the HOMO level and the accepting group the LUMO level, respectively. Recently, Adachi *et al.* [82] showed that an OLED using a green TADF emitter ($\Delta E_{ST} < 0.1$ eV) achieved EQEs of 19.3%, comparable to phosphorescent OLEDs. Assuming again an outcoupling efficiency for bottom-emitting OLEDs in the range of 20%, the singlet-triplet ratio of the TADF concept has to reach values close to $\eta_{ST} \approx 100\%$. As the TADF emitters do not contain heavy metal atoms and often provide a simplified molecule synthesis they are considered as a future low budget alternative for highly efficient OLEDs.

3.2.2 Exciton Blocking Layers

A further important parameter for the realization of efficient OLEDs is the migration control of the generated excitons. To confine the generated excitons and to avoid non-radiative decay in other layers, intrinsic *blocking layers* are deposited on both sides of the EML. Suitable blocker materials should therefore have higher singlet and triplet energies than the emitter material. In order to avoid a simple pass of charge carriers through the device, the blockers are chosen to introduce energetic barriers for one charge carrier type, electrons or holes, respectively.[77, 91] In the case of an *electron blocking layer* (EBL), a potential step compared to the LUMO level of the EML is introduced, while the HOMO levels are aligned. For the *hole blocking layer* (HBL) an energetic barrier between the HOMO levels of EML and HBL is set, while the LUMO levels are aligned. The single charge carriers accumulate on the EML/blocker interfaces and are enforced to form excitons in the EML enabling charge carrier balance factors of almost unity.

3.2.3 Charge Injection and Charge Transport Layers

As discussed in Section 2.4, the charge carrier transport in organics is mainly determined by the hopping transport rate, which results in a rather low mobility of the charge carriers in comparison to most conductive inorganic solids. Moreover, the low intrinsic charge carrier density leads to a low overall conductivity of the organics. Hence, space charge effects are widely determining the current-voltage dependency of intrinsic OLEDs which results in a high sensitivity to the thickness of the organic layers.

Electrical Doping of Organic Semiconductors

In order to enhance the conductivity of organic semiconductors, mobile charge carriers have to be generated. This is achieved by co-deposition of a small amount of *dopants* into an organic *matrix* material (M). Through the electron exchange between matrix molecules and the dopants, which occur in dependence of the energy level positions of the dopants, a super-linear increase of the conductivity can be achieved.[58] This increase is based on the enhanced charge carrier density, which can range over several orders of magnitude [58, 61] and an increase of the charge carrier mobility with the charge carrier density [40]. Figure 3.2 illustrates the doping concept for molecular dopants which either act as electron donator (D) or acceptor (A). For the realization of a *p-doped* organic layer (hole transport layer, HTL), the matrix material has to transfer an electron from its completely occupied HOMO level into the empty LUMO level of the acceptor.[58, 61]

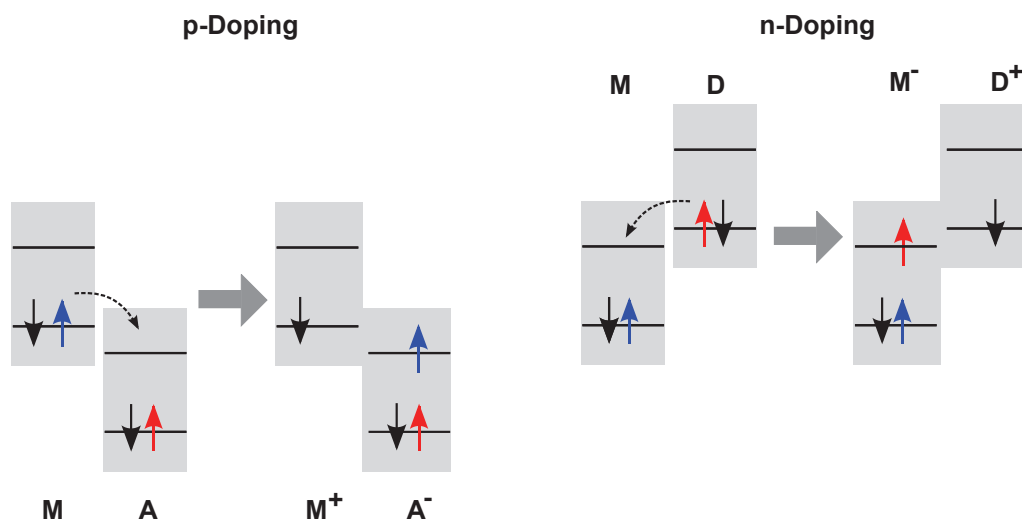


Figure 3.2: Illustration of *p*- and *n*-doping in organic semiconductors.[61] The conductivity is strongly increased by suitable donor (*D*) or acceptor (*A*) molecules which are co-evaporated into the matrix material (*M*). Mobile charge carriers are generated by electron transfer between dopant and matrix which results in partially occupied HOMO and LUMO levels.

This transfer is preferred when the LUMO energy of the dopant is lower than the HOMO energy of the matrix material.[19] A common dopant material class which fulfills this requirement is based on fluorinated molecules, as the fluorine atoms have a large affinity to accept further electrons.[91, 92] For an *n-doped* organic semiconductor (electron transport layer, ETL), the dopant has to donate an electron from its HOMO level into the LUMO level of the matrix material.[61] Even though molecular dopants with corresponding energy levels have been designed, they tend to be extremely reactive and can be decomposed in a chemical reaction, e.g. with oxygen or water. Inorganic *n*-dopants are usually based on alkali metals, e.g. LiF [91], Cs [77], Cs₂CO₃ [93] with a low electron affinity and are therefore extremely reactive, too.

Charge Injection from Electrodes into Doped Organic Semiconductors

In OLEDs, the formation of Ohmic contacts is preferred, as injection barriers and accumulated charge carriers at Schottky contact negatively influence the device operation. In Section 2.4, the formation of Ohmic contacts, e.g. by a careful choice of the metal work function, as well as the formation of Schottky contacts have been briefly discussed. Figure 3.3 illustrates the formation of metal/*p*-doped organic interfaces in equilibrium without an externally applied potential. The *p*-doping concept can be adapted to metal/*n*-doped organics interfaces, as well. *P*-doping of an organic layer induces a Fermi level shift (E_F^{Org}) from the center of the band gap closer to the HOMO level.[34, 61]

The redistribution or extraction of the generated mobile charge carriers leads to the formation of a *depletion zone* at the interface, and bending of the charge transport levels occurs.[34] The width w of the depletion zone is given by:

$$w = \sqrt{\frac{2\epsilon\epsilon_0 V_{\text{bi}}}{eN_{\text{D}}}}, \quad (3.5)$$

where V_{bi} is the *built-in potential* and N_D the ionized dopant density. The built-in potential is generated from the difference of the work function of the metal Φ_M and the organic semiconductor Φ_O ($V_{bi} = \Phi_M - \Phi_O$). Equation 3.5 shows that a low ionized dopant/molecule density leads to extended depletion layer thickness. Intrinsic organic semiconductors typically have only a few mobile charge carriers, which results in broad depletion zones and weak band bending. The case of "weak p-doping" in Fig. 3.3 represents the Schottky contact formation for mobile charge carriers present in the organic. The injection barrier of height Φ_B is too broad to allow for tunnel injection of charge carriers and can only be passed by field assisted thermionic injection (see Section 2.5). For a "highly p-doped" layer, the increased mobile charge carrier density and ionized molecular dopant density, respectively lead to the formation of narrow depletion zones at the metal interface, often smaller than 5 nm.[61, 94] For such thin energetic barriers, Ohmic charge injection by charge carrier tunneling from the metal electrode into the hole transport level E_+ of a p-doped organic layer is observed with negligible potential drop between the transport level and the Fermi level.[19, 58]

The doping concept provides Ohmic contacts even though the work function of the metal is not perfectly aligned to the energy levels of the organic material. Therefore, metals with a higher work function (e.g. Al instead of Ba) and consequently a higher resistivity against reaction with oxygen and water can be used as cathode. Furthermore, Ohmic anodes can be realized with less noble metals (e.g. Al instead of Au), which is often a low-cost alternative.

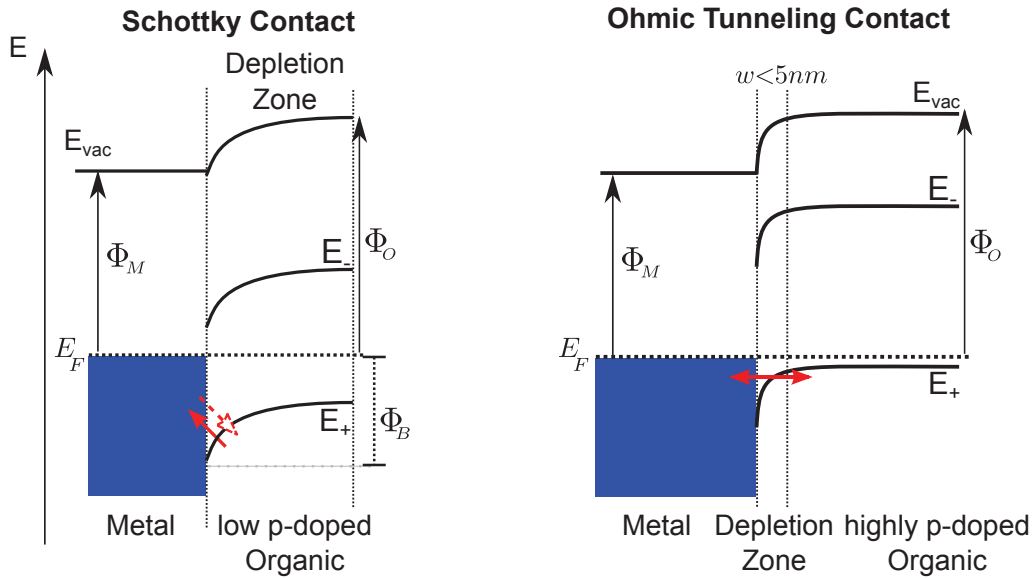


Figure 3.3: Schematic illustration of the formation of metal-organic contacts, with different work functions ($\Phi_M > \Phi_O$) for: (a) weakly p-doped organic material, and (b) a strongly p-doped organic layer. Fermi level E_F alignment of the materials is obtained by the diffusion of mobile charges. Thereby a depleted layer is formed inside the organic material. In the case of the weakly p-doped layer, a broad depletion zone and a rectifying Schottky contact with injection barrier Φ_B is formed. In contrast, the strongly doped organic layer forms a narrow depletion zone of only a few nanometer thickness. Thus, ohmic contacts are obtained as charge carriers are injected via a tunnel process.[19, 94]

Ultra-Thin Inorganic Charge Injection Layers

Efficient charge carrier injection into organic layers can be further realized by deposition of thin, sub-nm thick inorganic charge injection layers in combination with intrinsic charge transport layers. For hole injection, metal oxide layers, e.g. *molybdenumtrioxide* (MoO_3) [95–97] are widely used, whereas LiF is a prominent material for electron injection [6, 91, 98]. The metal oxides used for hole injection have conduction band energies in the range of the HOMO level of the organics.[96, 97] In the specific case of MoO_3 , which is strongly n-doped by oxygen vacancies even for high-vacuum deposition conditions, the Fermi energy is located close to the conduction band.[96] In the organic/ MoO_3 heterojunction, an interface dipole is formed as the organic layer transfers electrons to the injection layer. The resulting shift in Fermi level of the organic layer enables the injection of holes by efficient electron extraction via the conduction band of the charge injection layer.[95–97]

3.3 Highly Efficient Organic Light-Emitting Diodes

In state-of-the-art OLEDs, several functional organic layers are incorporated in order to benefit from all optimizations of the single layers, in order to reach a high IQE. These device concepts can then be introduced to several OLED architectures, where the extraction of the generated light through a transparent electrode is the particular focus.

3.3.1 OLED Device Concepts

PIN-Concept

The most common device concept is called *pin-concept*. *p*- and *n*-doped charge transport layers assure Ohmic charge injection and efficient charge transport, while intrinsic (*i*) blocking layers embed the emission layer to confine the charge carriers and excitons. The blockers also avoid quenching of excitons at the doped charge transport layers. Thereby, the intrinsic layer thickness is reduced to a minimum, in order to avoid an increased voltage drop on the intrinsic layers. Figure 3.4 schematically shows the energy level alignment of a five organic layer pin-OLED under a forward bias U . Similar to a *pn-junction*, a pin-OLED is a rectifying device which ideally passes the current in only one direction (forward direction).[17, 34] For reverse bias operation, the charge carriers are driven towards the electrodes and wide depletion zones are formed. Under forward bias operation, charges are driven into the depletion zone, decreasing its thickness. For potentials smaller than the built-in potential mainly charge carrier diffusion generates a current flow.[17] As the built-in potential is reached, charges are injected from the electrodes and migrate through the device, forming excitons which decay in the EML. The current-voltage dependence (*jV-curve*) of a pn-junction can be described by the *Shockley equation* [34]:

$$j(V) = j_0 \cdot \left[\exp \frac{eV}{nk_B T} - 1 \right] , \quad (3.6)$$

where n is the ideality factor of the diode.

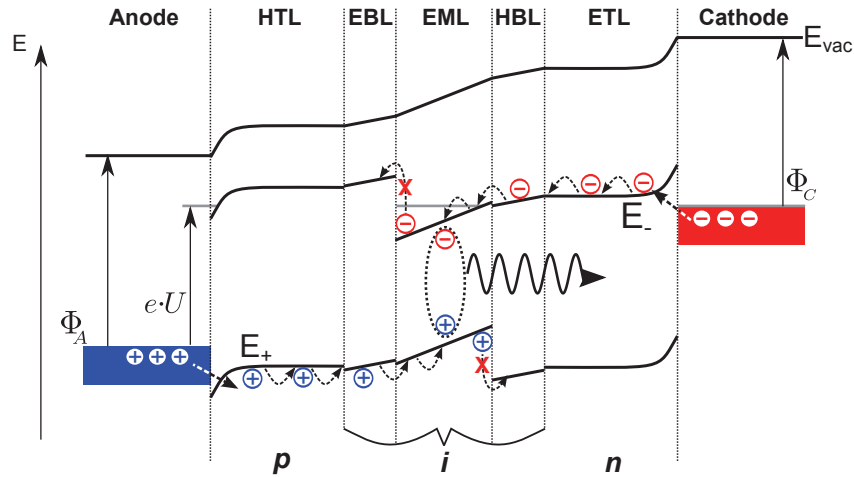


Figure 3.4: Schematic illustration of an energy level diagram of a five organic layer pin-OLED under a forward bias U . Electrically doped charge transport layers (p , n) are deposited next to the electrodes for ohmic charge injection and sufficient charge transport (ETL, HTL). The intrinsic (i) blocking layers (EBL, HBL), enclosing the emitting layer (EML) confine the formed excitons which are supposed to decay radiatively in the EML.

Its measure is an indicator for effects like emissive recombination, as well as non-radiative processes in the device.[99] For most pin-OLEDs, the Shockley equation gives an accurate description of the current-voltage characteristic and ideality factors in the range of 1 to 2 are typically found.[99]

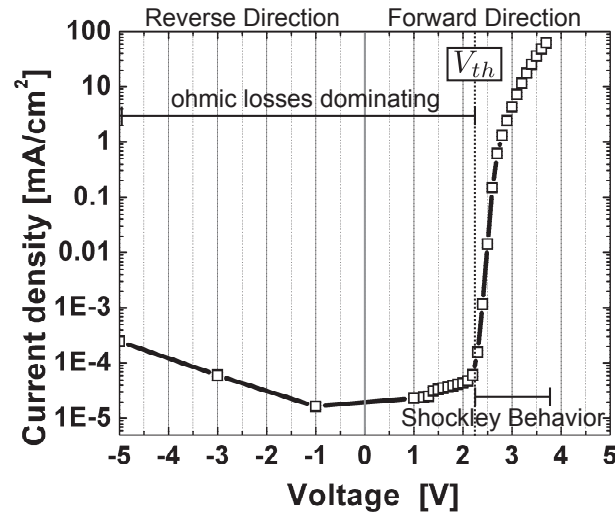


Figure 3.5: Current-voltage characteristics of a red phosphorescent pin-OLED. Ohmic losses dominate the current flow in reverse direction, whereas the forward direction shows a Shockley behavior as soon as the threshold voltage V_{th} is passed. It is noteworthy that the Ohmic leakage currents contribute symmetrically in forward and reverse direction.

It is worth to note than an ideality factor of 1 represents a pure drift current through the device, while a factor of 2 would be found for a pure recombination current.[34] Deviations from the Shockley equation are observed if the contributions of exciton quenching processes as well as the emission and population of trap states increase. A parasitic Ohmic current contribution to the jV -curve can be found in most OLEDs, originating from local electrical shorts. The contribution of the Ohmic leakage currents is independent from the direction of the applied potential.

The pin-concept shows major benefits based on the usage of doped charge transport layers:

- Ohmic contacts by tunnel injection of charges from the electrodes
- Ohmic contacts without exact match of the electrode workfunction and the charge transport level of the adjacent organic material
- Negligible voltage drop on the doped layers
- Operational voltage close to the thermal equilibrium energy of the emitter for thin intrinsic layers [87, 91]
- Optimization of the optical properties of pin-OLEDs without affecting the electrical properties

Homojunction OLEDs

In most pin-OLEDs, the functional layers comprises individual organic compounds which leads a large variety of used materials in a device. In order to reduce the number of materials, homojunction OLEDs are of interest. In an ideal case, a single organic layer is desirable to provide ambipolar charge carrier injection and transport as well as efficient light emission.[100, 101] However, a single material efficiently fulfilling all requirements has not been found so far. Furthermore, the beneficial effects of the pin-concept previously mentioned would not be applicable.

The doping concept can be expanded to realize homojunction pin-OLEDs. In those devices, a single organic matrix material is deposited and sequentially doped by guest molecules. The intrinsic material serves as blocking layers while electrical doping leads to formation of charge transport layers. Doping of an emissive guest defines the emission zone.[102] Even though the requirements on the matrix material are quite high, homojunction pin-OLEDs reaching 15% EQE for monochrome OLEDs have been reported recently.[102]

OLEDs using Ultra-thin Injection Layers

An alternative for simplified OLED processing can be achieved by the replacement of the doped transport layers by ultra-thin charge injection layers in combination with intrinsic organic compounds for charge carrier transport. Recently, Wang *et al.* demonstrated extraordinarily high EQEs of 24.5% using a simplified OLED structure using a phosphorescent green emitter.[98, 103] Compared to a pin-device, the optimization of simplified OLED structures with intrinsic charge transport layers is often more challenging, as small perturbations like impurities can have a significant impact on the device performance and the electrical characteristics depend on the thickness of the intrinsic transport layers.

3.3.2 OLED Architectures

The device concepts discussed can be implemented in different OLED architectures which can be distinguished concerning the emission direction, the number of OLED units, and even more specified concerning the substrate, and the applied light extraction technique. Figure 3.6 illustrates the architectures of bottom- and top-emitting OLEDs, as well as transparent, and stacked devices. Bottom-emitting OLEDs (Fig. 3.6(a)) are built on a transparent substrate, while the emission is directed through the transparent electrode and the substrate, respectively. As the transparent electrode is deposited prior to the organic layers, there are no restrictions regarding the use of transparent electrode materials, which will be discussed in detail in the next section. Typically, they comprise a transparent conductive oxide (TCO) as transparent electrode, while an opaque metal electrode deposited on top of the organic layers and reflects the light. Currently, TCO materials represent the benchmark regarding a high transmittance while showing a low resistance, but are typically brittle. This limits a R2R fabrication or the application in flexible devices. Monochrome bottom-emitting OLEDs already achieve EQEs of 20-30% [6, 10] which clearly verifies that the IQE in such OLEDs has to be close to unity, as the outcoupling efficiency for bottom-emitting OLEDs is in the range of the EQE.[6, 86] Furthermore, the high transmittance of the transparent electrode enables an efficient, high color-quality, and angularly color-stable white emission of bottom-emitting OLEDs. In addition, macroscopic light extraction structures can be attached to the outer side of the transparent substrate without harming the organic layers, which has already resulted in remarkable efficiencies of white bottom-emitting OLEDs, being competitive to conventional light sources.[7, 87, 104]

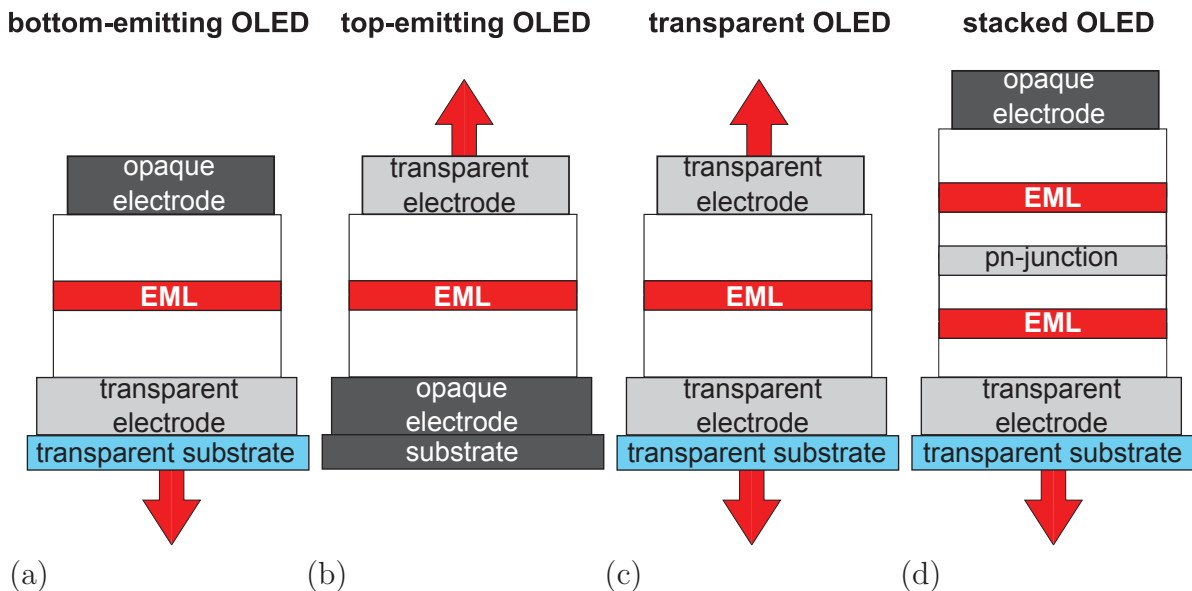


Figure 3.6: Comparison of (a) bottom- and (b) top-emitting, (c) transparent, and (d) stacked device architecture. In contrast to top-emitting OLEDs, where the emission is directed away from the carrier substrate, bottom-emitting OLEDs emit through the substrate. Transparent OLEDs provide emission through both electrodes. The series connection of several functional OLEDs, e.g. by a pn-junction, yields a stacked device.

In contrast, top-emitting OLEDs can be deposited on all kind of substrates which allow for a reliable electrical operation, including opaque substrates (metal foils, backplane electronics) (Fig. 3.6(b)). However, the transparent electrode has to be deposited on top of the organic layer stack, which dramatically reduces the choice of suitable materials, often restricted to metal films with only moderate transmittance. As a consequence, the optical properties of white top-emitting OLEDs are adversely affected from the poor optical performance of the top electrode, rising challenges to reach a comparable performance for white light emission in comparison to bottom-emitting devices. A benefit of metal electrodes in comparison to TCO materials is their compatibility for flexible device applications. Common light extraction structures have to be attached on top of top-emitting OLEDs, where the organic layers are not protected from a substrate and thus typically harm the devices. Hence, light extraction techniques can typically not be applied to top-emitting devices, maintaining a high device yield. Nevertheless, planar monochrome top-emitting OLEDs often outperform their bottom-emitting counterparts and have also reached EQEs of up to 30% [11], while the unique compatibility with opaque substrates qualifies them as suitable candidate, e.g. for display applications. In order to unlock the full potential of top-emitting OLEDs, the realization and application of highly transparent top electrodes and light extraction structures to top-emitting OLEDs have been in the focus of this work.

Transparent devices (Fig. 3.6(c)) contain two transparent electrodes and require a transparent substrate like a bottom-emitting OLED. They represent an interesting device concept due to their emission to both sides, being transparent in the off-state, while showing a bright emission for electrical operation and have also been investigated in this work. Stacked device architectures (Fig. 3.6(d)) provide several benefits concerning solid-state lighting applications in comparison to single unit OLEDs. There, several OLEDs are connected in series, e.g. via pn-junctions. In addition to the injected charge carriers from the outer electrodes, further charge carrier couples are generated at each pn-junction inside the device.[81, 105] Due to the internally generated charge carriers, each sub-unit generates a photon which contributes to the EQE. Furthermore, the lifetime of stacked devices is increased, as higher brightness levels are obtained for a lower current density. On the other hand, the different emitters contributing to the white light generation can be optimized in single sub-units for maximum efficiency.

It is worth to note that each of the above mentioned OLED architectures can yield IQEs of approximately unity. However, for all OLEDs most of the photons are trapped inside the organic layers, the metal electrodes, or for some architectures also in the substrate, typically resulting in EQEs lower than 30%. This emphasizes the essential need to improve the light extraction efficiency for OLEDs, which is a major part of this work.

3.3.3 Transparent Electrode Materials

In general, suitable transparent electrode materials require a high transmittance T and a high conductivity, low sheet resistance R_S [Ω/\square]. However, a high conductivity σ of the electrode leads to a rather low transmittance if the thickness cannot be kept thin enough to avoid prominent absorption or reflection, which will be shown in Section 4.1. Consequently, the realization of highly transparent electrodes is challenging, as an optimized trade-off between high transmittance, but low conductivity (e.g. glass) and high conductivity, but low transmittance (e.g. metals) has to be achieved.

Transparent electrodes can be roughly categorized concerning the applied material class into:

- Transparent Conductive Oxides
- Conductive Polymers
- Carbon Nanotubes and Graphene
- Metals

In contrast to bottom-emitting OLEDs, the transparent electrode of top-emitting OLEDs is deposited after the organic layers. Hence, deposition techniques which introduce damage to the organic layers cannot be applied. This processability requirement strictly limits the choice of suitable electrode materials for top-emitting OLEDs, which is discussed in the following. TCO materials, like ITO and aluminum doped zinc-oxide (Al:ZnO), with transmittances larger than 90% and R_S in the range of 10 - 100 Ω/\square currently represent the benchmark for transparent electrodes, with various applications, such as large area screens.[106, 107] Even though typical electrode thicknesses are in the range of 100 nm, these TCOs have a high transmittance in the visible spectral range due to a large band gap ($E_{\text{gap}} > 3 \text{ eV}$). The conductivity of these layers is the result of a Fermi level located closely to the conduction band, which can be realized by specific doping of the oxides with metals (e.g. Sn, Al) and oxygen vacancies.[106] TCOs are typically prepared by sputtering or chemical vapor deposition [108–110] and treated by post thermal annealing procedures at several hundred degree Celsius [111–113] to improve the electrode characteristics. Due to this processing and post-treatment conditions, TCOs are often not suitable for top-emitting OLEDs, as the organic layer sequence underneath would be harmed.

Kanno *et al.* [114] realized top-emitting OLEDs using ITO as top electrode, which reached comparable performances as bottom-emitting reference OLEDs. However, the application of ITO as top electrode remains challenging and is only rarely applied. Furthermore, the brittle character of TCO layers limits the application for desired R2R processing and future flexible devices.

Transparent electrodes have also been prepared from conductive polymers like PEDOT:PSS (poly(3,4-ethylenedioxythiophene):poly(styrenesulfonate)), providing a transmittance $> 85\%$ and a sheet resistance in the range of 100 Ω/\square . [115] The deposition of conductive polymer electrodes is realized by printing or coating from aqueous or organic solutions. However, such polymer electrodes are also not applicable for top-emitting OLEDs, as the organic layers underneath could be resolved or chemically decomposed by reactions with the solvent.

Recently, carbon based transparent electrodes of carbon nanotube (CNT) networks [116, 117] or graphene sheets [118–120] have been prepared. Graphene represents an only one atom thick layer of graphite, where the sp^2 -hybridized carbon atoms form a 2D honeycomb plane.[121] A transparent electrode of four graphene layers reached a transmittance of 90% and a sheet resistance of $\approx 30 \Omega/\square$, which is comparable to state-of-the-art TCO materials.[119] The high mechanical strength and flexibility of graphene, as well as the impermeability of the carbon mesh even for gases [122] emphasize the potential of graphene as electrode material for future electrode applications.

Even though the unique characteristics are beneficial for several applications, the production of graphene sheets remains challenging. CNTs represent a rolled up form of graphene, while single and multi-walled CNTs, as well as metallic and semiconducting nanotubes are often simultaneously formed during fabrication via CVD.[123] For many applications, only a single type of CNTs is desired, to control the properties of the devices, which can be achieved by post-processing sorting.[123] For an application as a transparent electrode, an area coverage is required, which is often achieved by the deposition of CNT networks from solution via spin- or spray-coating. Such electrodes show a comparably high sheet resistance in the range of 60 to 200 Ω/\square due to a poor charge transfer between the single CNTs.[117] Furthermore, the reported transmittance in the range of 60 to 80 % can also not completely compete with TCO or graphene electrodes, whereas Again the solution processing of CNTs limits an application for top-emitting OLEDs.

State-of-the-art transparent electrodes for top-emitting OLEDs are thin metal films of silver or aluminum with thickness in the range of 15 to 20 nm, prepared by thermal evaporation.[124, 125] Even though diffusion of the condensating metal atoms into the organic layers has been shown, the thermal evaporation does not harm the organic layers. The large material availability and bendability of metal films demonstrate the applicability for R2R processing. However, metals have a comparably low transmittance, but a high conductivity. In order to reach the performance benchmark of TCO electrodes, the transmittance of metal thin film electrodes has to be significantly increased, which is one particular focus of this work.

A summary of the transparent electrode materials, comparing transmittance, sheet resistance, and applicability as electrode on top of organics is shown in Table 3.1

Table 3.1: Comparison of transparent electrode materials regarding reported transmittance and sheet resistance values. In addition, the applicability as electrode on organics is mentioned.

Material	Transmittance [%]	Sheet Resistance [Ω/\square]	Application on Organics
TCOs	> 90	10 - 100	no*
Conductive Polymers	> 85	\approx 100	no*
CNTs & Graphene	\approx 90	30 - 200	(yes)*
Metal Electrodes	\ll 80	< 10	yes

* Most wet chemical deposition and post thermal annealing procedures are not applicable on organics.

3.4 Human Perception of Electromagnetic Radiation

An interesting point which has not been discussed in this work so far is the symbolism of the word *light*, even though it has been extensively used. In this section, the focus will be on the correlation between electromagnetic radiation, light, and the perception of color.

Perception of the Human Eye

Radiation is a general description of an electromagnetic wave propagating in space or in a medium. Light instead is electromagnetic radiation which can be perceived by the human eye. The wavelength regime of visible light ranges from 380 nm to 780 nm.[43] Incident light passes the iris of the human eye, is focused by the lens, and then projected on the retina. Rod and cone cells inside the retina get stimulated and provide a neurotransmitter impulse which is evaluated by the brain.[43]

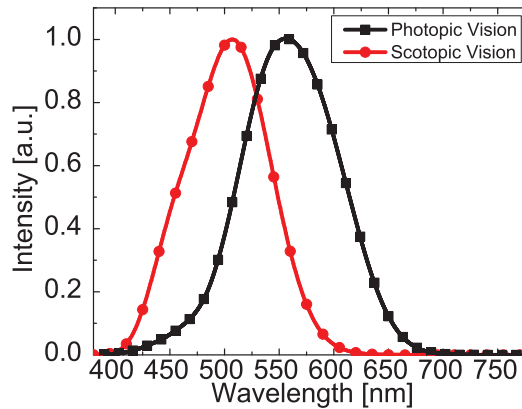


Figure 3.7: Spectral sensitivity curve to visible electromagnetic radiation of the human eye for a CIE standard observer at 2° . The photopic curve is observed for bright light, while the scotopic curve represents the dim light vision.[126]

The sensitivity of the rod and cone cells to the incident light is strongly wavelength dependent.[127] The photopic luminosity function $V(\lambda)$ which was determined by the *Commission Internationale l'Éclairage* (CIE) describes the stimulation feedback of the human eye caused from incident visible light for a *standard observer at 2°* (see Fig. 3.7).[126] The scotopic luminosity function was determined for low brightness and is shifted to smaller wavelengths compared to the photopic function. Differences between the photopic and scotopic function are caused by the altered contributions of cone and rod cell signals to the neurotransmitter impulse, depending on the intensity of the incident light.

3.4.1 Radiometry and Photometry

The characterization and evaluation of electromagnetic radiation is the scope of *radiometry*, while *photometry* describes the characterization of light perceived by the eye. A specific measure of a radiative light source is its *radiant flux* Φ_R , which describes the total radiated energy of an emitter in form of electromagnetic waves per time. Based on the radiant flux, further radiometric parameters of a light source can be determined,

e.g. the *radiant intensity* I_R , which describes the radiant flux per solid angle $d\Omega$, and the *radiance* L_R evaluating the radiant flux in a solid angle, per projected area $A_S(\theta)$ of the light source ($A_S(\theta) = A_S \cdot \cos \theta$).

Considering a so-called *Lambertian light source*, the observed radiant intensity obeys a cosine law ($I_R^{\text{Lambert}} = I_R(0) \cdot \cos \theta$) regarding the observation angle θ and the direction perpendicular to the surface is determined by $\theta = 0^\circ$. For the radiance of a Lambertian emitter it is found [128]:

$$L_R^{\text{Lambert}}(\theta) = \frac{d^2\Phi_R^{\text{Lambert}}(\theta)}{d\Omega dA_S(\theta)} = \frac{dI_R^{\text{Lambert}}(\theta)}{dA_S \cdot \cos \theta} = \frac{dI_R(0) \cdot \cos \theta}{dA_S \cdot \cos \theta} = L_R^{\text{Lambert}}(0) = \text{const.} \quad (3.7)$$

The radiance of a Lambertian emitter is therefore constant regarding the observation angle.[129] Diffusive and area light sources, especially bottom-emitting OLEDs often show Lambertian emission characteristics. In contrast, a light bulb does not obey a cosine law of the radiant intensity, but has an isotropic distribution, while lasers as well as inorganic LEDs have strongly directed emission. The *irradiance* E_R characterizes the amount of radiated flux which reaches the surface of a detector/observer (A_D) and is often the parameter which is measured by a spectrometer.

The irradiance can be correlated to the initial radiant flux as well as to the other radiometric parameters according to:

$$E_R = \frac{d\Phi_R}{dA_D} = \frac{I_R d\Omega}{dA_D} = \frac{L_R d\Omega dA_S}{dA_D} . \quad (3.8)$$

In order to determine efficiency parameters in context of light instead of radiation, the luminosity function $V(\lambda)$ has to be respected. The photometric quantities X_P can be derived from the according radiometric quantity X_R (X represents the respective quantity: Φ , I , L , or E) by:

$$X_P = K_m \int_{\text{vis}} X_R(\lambda) V(\lambda) d\lambda , \quad (3.9)$$

including the maximum luminous efficacy $K_m = 683 \text{ lm/W}$. The photonic quantity *Luminance* L_P corresponds to the brightness of a light source and is often used to characterize OLEDs. It is worth to note that, an OLED which emits in the more sensitive region of the $V(\lambda)$ curve reaches a higher luminance L_P compared to OLEDs which emit in the less sensitive regions, even though both devices have an identical radiance L_R . Table 3.2 summarizes and compares the radiometric and photometric quantities which have been introduced.

Table 3.2: Summary and comparison of the most important parameters of radiometry and photometry.

Radiometry			Photometry		
Parameter	Symbol	Unit	Parameter	Symbol	Unit
Radiant Flux	Φ_R	W	Luminous Flux	Φ_P	lm
Radiant Intensity	I_R	W/sr	Luminous Intensity	I_P	cd=lm/sr
Radiance	L_R	W/sr m ²	Luminance	L_P	cd/m ²
Irradiance	E_R	W/m ²	Illuminance	E_P	lx=lm/m ²

3.4.2 Color Stimulus

The human eye further provides the impression of *color*, as the three cone cell types (s, m, and l) have a specific spectral response to incident light. In order to define a color standard for all human beings, the CIE introduced the *CIE 1931*, or CIE_{xy} color space which visualizes all color impressions in a two-dimensional plane (see Fig. 3.8(a)).[126]

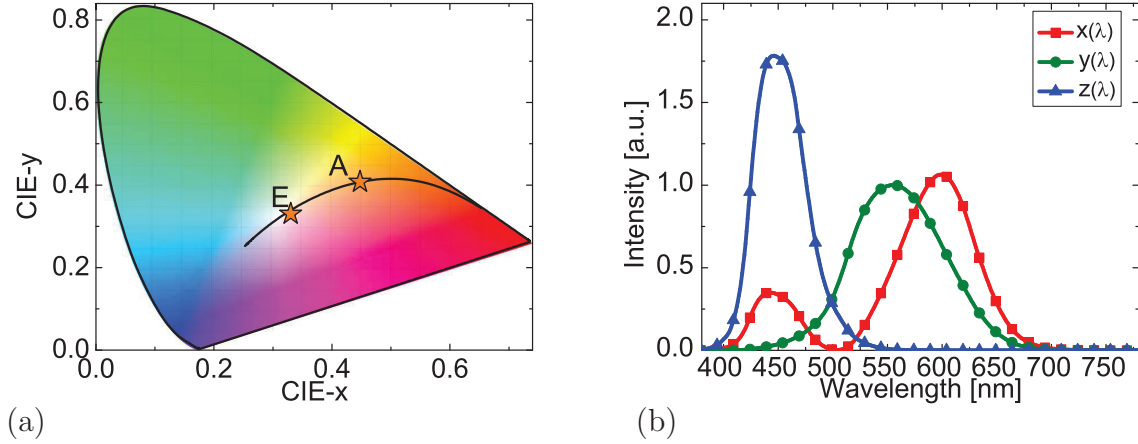


Figure 3.8: *CIE 1931 color space including the Planckian locus (black solid line), the color reference point E, which is the point of equal energy, and the color standard A for warm white emission (a). The color matching functions of the CIE 1931 standard observer[130] are used to calculate the CIE(x,y) color values (b).*

The color coordinates CIE(x,y) of a light source can be calculated from the radiated spectrum $I(\lambda)$ respecting the three *color matching functions* $x'(\lambda)$, $y'(\lambda)$, and $z'(\lambda)$ [130] (see Fig. 3.8(b)) according to [127]:

$$X = \int_{\text{vis}} I(\lambda)x'(\lambda)d\lambda \quad Y = \int_{\text{vis}} I(\lambda)y'(\lambda)d\lambda \quad Z = \int_{\text{vis}} I(\lambda)z'(\lambda)d\lambda \quad (3.10)$$

$$x = \frac{X}{X + Y + Z} \quad y = \frac{Y}{X + Y + Z} \quad z = \frac{Z}{X + Y + Z}$$

Monochromatic, *pure* emission spectra have color points which can be found on the edge of the CIE diagram. For non-monochromatic emission, the color coordinates are located in the inner part of the CIE diagram.

A light source is called *white* if its color coordinates are close to the *Planckian Locus*, determined from the emission of ideal Planckian radiators (black body radiators) in the temperature range from 1000 K to ∞ . The spectrum of a Planckian radiator is defined by [43]:

$$I_{\text{Planck}}(\lambda, T) = \frac{2hc^2}{\lambda^5} \cdot \frac{1}{\exp\left(\frac{hc}{\lambda k_B T}\right) - 1} \quad (3.11)$$

A white light source can be characterized by the *correlated color temperature* (CCT) of the black body radiator which has color coordinates closest to the light source.[127] The calculation of the distance to the Planckian Locus cannot be applied in the CIE 1931 color space, as this space is not uniform regarding the perception of color differences.

The non-uniformity of the CIE 1931 color space is validated by investigations of small color differences in the CIE space by Wright [131], as well as the different sizes of the *Mac Adams ellipses* [132], which are regions in the color space where all light sources appear to have an identical color to the observer. The *CIE1960 UCS* color space was introduced to improve the uniformity of the color space regarding the perception of color differences, and is typically applied to calculate the distance between two close color points. The CIE 1960 UCS coordinates (u,v) result from a transformation of the CIE(x,y) coordinates according to [133]:

$$u = \frac{4x}{-2x + 12y + 3} \quad v = \frac{6y}{-2x + 12y + 3} \quad (3.12)$$

In order to obtain the CCT of a light source, the *Euclidean distance* between the color of the source and the Planckian Locus is calculated:

$$\Delta uv = \sqrt{(u - u_{\text{Planck}})^2 + (v - v_{\text{Planck}})^2} \quad (3.13)$$

Based on the CCT, white light sources can be classified as warm (2000-3300 K), neutral (3300-5000 K), or cold (5000-7500 K) white light sources. Two important color reference points which are desired for many white light applications are: *E* which marks the point of equal energy, or cold white point, with coordinates (0.33, 0.33), and *A* which is correlated to the emission of a Planckian radiator of T=2856 K (light bulb), and is often referred to as the color point for warm white emission (0.448, 0.407).

3.4.3 Color Rendering

The perception of color by the human eye allows an infinite amount of spectra to be perceived as identical color (cf. Eq. 3.10). This so-called *metamerism* of the eye is beneficial when a certain CIE color point has to be achieved, as there is no strict requirement to the spectral composition. However, even more crucial than the direct perception of the light source is the perception of the environment illuminated by the light source.

A quantity to measure the color reproduction of the environment is the *color rendering index* (CRI). The accurate calculation of the CRI requires a light source with color coordinates close to the Planckian Locus, so the light source has to be approximately white ($\Delta uv < 5.4 \cdot 10^{-3}$). [127, 134]

The CRI of a light source is calculated in comparison to the black body radiator at the same CCT, which reaches per definition the maximum CRI of 100. According to the reproduction of the reflectivity of eight reference samples, the general CRI (CRI_a) is calculated. [127] If the CCT of the light source is larger than 5000 K, the standard illuminant D has to be used as reference instead of the according black body radiator. [127] In dependence on the spectrum of the light source, a CRI ranging from 0 to 100 can be obtained, while a light bulb also reaches the maximum value per definition. For solid-state lighting applications, a CRI higher than 80 is desired, while for most general applications it is sufficient to reach a CRI larger than 60. Often, a broad spectrum almost covering the entire visible spectral range is required to reach the demanded CRI for solid-state lighting application, but also fluorescent tubes or inorganic LEDs, which still have gaps in their spectra can obtain high CRIs > 80.

There are still vivid discussions on the demand of a new calculation method or an extension of the actual method, in order to accurately evaluate the color rendering of a light source.[135] First, only eight color references are used to calculate CRI_a which might not be enough to characterize the color-quality, and the extension to 14 color references is already in discussion. Second, the color-quality can only be calculated for approximately white light sources, while for all others a CRI value is not defined. In addition, the CIE 1960 UCS color space is still not completely uniform and does not allow to precisely calculate the distance of the color between two arbitrary light sources.[135]

3.4.4 CIELAB Space

In order to calculate the distance between two arbitrary color points, a uniform color space is required. The *CIELAB* or *CIE 1976* (L^*, a^*, b^*) space is obtained from the CIE_{xy} space by non-linear conversion, to exactly reproduce the perception of color differences by the human eye.[127] In comparison to the CIE_{xy} space, where colors are displayed in a two-dimensional plane according to the CIE(x,y) coordinates, the CIELAB space is three-dimensional determined from the coordinates L^*, a^*, b^* .

The coordinate L^* represents the *lightness* of a color and ranges between 0 (black) to 100 (diffuse white). The value a^* describes the position of the color point between green and the magenta region, whereas b^* gives the position between yellow and blue. For visualization, the according a^*, b^* -color planes can be illustrated for a fixed *lightness* L^* (see Fig. 3.9). The perception of different colors is strongly dependent on the lightness L^* , represented by the size of the a^*, b^* -color planes. Introducing polar color coordinates, the *hue* (polar angle) and the *chroma* (radial coordinate) of a color is obtained.

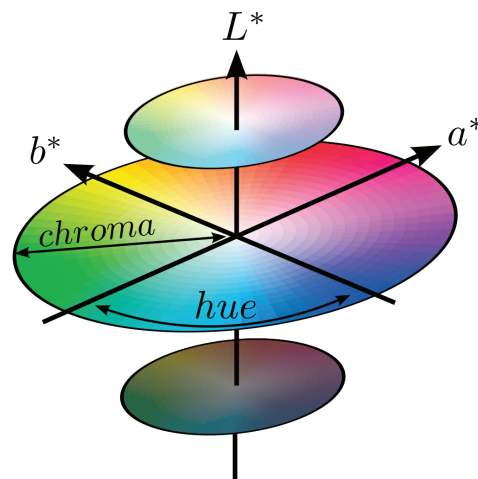


Figure 3.9: Schematic illustration of the three-dimensional CIELAB space. Colors are represented by the coordinates L^*, a^*, b^* . The perception of colors is strongly dependent on the lightness L^* , represented by the size of the a^*, b^* -color planes. The transformation of the a^*, b^* -color coordinates into polar coordinates results in the *chroma* and the *hue* of a color.[127]

The transformation from the CIE_xy to the CIE_{LAB} space is defined by [127, 136]:

$$L^* = 116 \cdot F\left(\frac{Y}{Y_n}\right) - 16; \quad \frac{a^*}{500} = F\left(\frac{X}{X_n}\right) - F\left(\frac{Y}{Y_n}\right); \quad \frac{b^*}{200} = F\left(\frac{Y}{Y_n}\right) - F\left(\frac{Z}{Z_n}\right) \quad (3.14)$$

$$F\left(\frac{i}{i_n}\right) = \begin{cases} \left(\frac{i}{i_n}\right)^{1/3} & \frac{i}{i_n} > \left(\frac{6}{29}\right)^3 \\ \frac{1}{3} \left(\frac{29}{6}\right)^2 \cdot \left(\frac{i}{i_n}\right) + \frac{4}{29} & \text{otherwise} \end{cases} \quad i = X, Y, Z \quad (3.15)$$

which is related to a reference color point with the coordinates (X_n, Y_n, Z_n) . In Section 5.3.1, the calculation of the angular color-stability of OLEDs in the CIE_{LAB} space will be described in detail.

4 Optics of Top-Emitting OLEDs

This chapter analyzes the optical properties of top-emitting OLEDs and introduces several approaches to improve the light extraction efficiency. The state-of-the-art capping layer concept is investigated and the essential need for highly transparent thin-film metal top contacts to realize efficient white emission is emphasized. Furthermore, the improvement of the light extraction efficiency by means of light outcoupling structures is discussed.

In the previous chapter, the realization of efficient OLEDs has been discussed in the context of layer designs and OLED architectures. Top-emitting OLED structures are in the focus of this work. Their potential fabrication on surfaces of large area, flexible substrates in roll-to-roll production [7, 137] for solid-state lighting, as well as the direct fabrication on opaque backplane electronics [138–140] for display applications favor them in comparison to bottom-emitting devices, which are so far mostly deposited on rigid glass substrates.

However, top-emitting OLEDs exhibit certain differences of the optical properties in comparison to bottom-emitting devices, rising challenges in the realization of highly efficient devices. Especially white top-emitting OLEDs have not yet reached the performance of their bottom-emitting counterparts, which are currently the benchmark for efficiency, color-quality, and angular color-stability.

This chapter describes the propagation of light in a multi-layer OLED structure (Section 4.1). Section 4.2 emphasizes the improvement of white top-emitting OLEDs using highly transparent and ultra-thin metal top electrodes while also the capping layer concept is discussed. To enhance the efficiency of OLEDs, the extraction of internally trapped light modes, e.g. by Bragg scattering at periodically corrugated structures, is investigated in Section 4.3.

4.1 Light Propagation in Thin Film Structures

In order to describe the optical properties of OLED architectures, the propagation of the light dissipated from the emitter molecules has to be evaluated. This classic electrodynamic problem of electromagnetic waves propagating in a medium is described by the four *Maxwell equations* [43, 141, 142]:

$$\vec{\nabla} \cdot \vec{D} = \rho_f \quad \vec{\nabla} \cdot \vec{B} = 0 \quad \vec{\nabla} \times \vec{E} = -\frac{\partial \vec{B}}{\partial t} \quad \vec{\nabla} \times \vec{H} = \vec{j}_f + \frac{\partial \vec{D}}{\partial t} \quad (4.1)$$

introducing the electric field \vec{E} , magnetic flux density \vec{B} , charge density (ρ_f) and current density (\vec{j}_f) of free charges, as well as the electric displacement field \vec{D} , and the magnetic field \vec{H} . The four fields are linked via the interaction of the electromagnetic waves with

the medium of propagation, which can result in *polarization* \vec{P} and *magnetization* \vec{M} . [141] In the following, the investigations are restricted to linear responding, non-magnetic ($\vec{M} = \vec{0}$, $\mu_r = 1$), and isotropic media. In that case, two material relations can be found:

$$\vec{D} = \epsilon_0 \vec{E} + \vec{P} = \epsilon_0 \epsilon_r \vec{E} \quad \vec{B} = \mu_0 (\vec{H} + \underbrace{\vec{M}}_{=\vec{0}}) = \mu_0 \vec{H} \quad (4.2)$$

defining the dielectric constant ϵ_r . In order to describe the propagation of the emitted light, the spatial and time dependent development of the electric and the magnetic field has to be determined. The combination of both curl equations of the Maxwell equations (Eq. 4.1) results in the *wave equation* [142]:

$$\vec{\nabla} \times (\vec{\nabla} \times \vec{E}) = \vec{\nabla}(\vec{\nabla} \cdot \vec{E}) - \vec{\nabla}^2 \vec{E} = -\mu_0 \frac{\partial \vec{j}_f}{\partial t} - \mu_0 \epsilon_0 \epsilon_r \frac{\partial^2 \vec{E}}{\partial t^2} \quad (4.3)$$

This general form of the wave equation can often be simplified in dependence on the propagation medium. In case of non-conductive media ($j_f = 0$, $\rho_f = 0$, and $\sigma = 0$), the *homogeneous* wave equation is obtained:

$$\vec{\nabla}^2 \vec{E} - \underbrace{\mu_0 \epsilon_0 \epsilon_r}_{=\epsilon_r/c^2} \frac{\partial^2 \vec{E}}{\partial t^2} = 0 \quad (4.4)$$

introducing the speed of light in vacuum c . Solutions for the homogeneous wave equation are plane waves given by:

$$\vec{E}(\vec{r}, t) = \vec{E}_0 e^{i(\vec{k} \cdot \vec{r} - \omega t)} \quad \text{with} \quad \omega = \frac{c}{\sqrt{\epsilon_r}} \cdot |\vec{k}| = \frac{c}{n} \cdot |\vec{k}| \quad (4.5)$$

with the wavenumber $|\vec{k}|$, the electric field amplitude \vec{E}_0 , and the refractive index $n = \sqrt{\epsilon_r}$. It is noteworthy that the magnetic flux density \vec{B} holds an analogous solution as the electric field \vec{E} . From the Maxwell equations, the transversal character of these electromagnetic waves can be deduced. [142] For conductive ($\sigma \neq 0$) uncharged materials ($\vec{\nabla} \cdot \vec{E} = 0$) with linear current response to external electric fields ($\vec{j}_f = \sigma \vec{E}$), the wave equation (Eq. 4.3) yields [142]:

$$\vec{\nabla}^2 \vec{E} - \mu_0 \sigma \frac{\partial \vec{E}}{\partial t} - \mu_0 \epsilon_0 \epsilon_r \frac{\partial^2 \vec{E}}{\partial t^2} = 0 \quad (4.6)$$

which can also be solved by harmonically time dependent planar waves of the type:

$$\vec{E}(\vec{r}, t) = \vec{E}_0(\vec{r}) e^{-i\omega t} \quad (4.7)$$

From Eq. 4.6, the spatial term of the field $\vec{E}_0(\vec{r})$ can be determined, leading to an expression comparable to the homogeneous wave equation:

$$\vec{\nabla}^2 \vec{E}_0(\vec{r}) + \tilde{\epsilon}_r(\omega) \frac{\omega^2}{c^2} \vec{E}_0(\vec{r}) = 0 \quad \text{with} \quad \tilde{\epsilon}_r(\omega) = \epsilon_r + i \frac{\sigma}{\epsilon_0 \omega} \quad (4.8)$$

Consequently, the wave equation in conductive media can also be solved by harmonic waves as for non-conductive media.

From the conductivity of the propagation medium, several consequences arise. First, the refractive index n is now a complex value \tilde{n} , based on the complex character of the dielectric constant $\tilde{\epsilon}_r$:

$$(n(\omega) + i\kappa(\omega))^2 = \tilde{\epsilon}_r(\omega) \quad \text{and} \quad \kappa(\omega) = \frac{\sigma}{2\epsilon_0\omega n(\omega)} \quad (4.9)$$

Second, the imaginary part of the refractive index $\kappa(\omega)$, which is proportional to the conductivity of the medium, leads to a damped electromagnetic wave and thus a reduction of the amplitude/intensity for ongoing propagation through the medium:

$$\vec{E}(\vec{r}, t) = \vec{E}_0 e^{i(\vec{k}\cdot\vec{r} - \omega t)} = \vec{E}_0 e^{-(\kappa(\omega)\omega c^{-1}\vec{e}_k\vec{r})} e^{i(n(\omega)\omega c^{-1}\vec{e}_k\vec{r} - \omega t)} \quad (4.10)$$

Hence, highly conductive electrodes should be as thin as possible, in order to minimize the damping of the incident light and thus to reach a high transmittance.

The optical properties of multi-layer OLED architectures are determined by the refractive index ($\tilde{n}(\omega) = n(\omega) + i\kappa(\omega)$) and the thickness d of the layers. Therefore, differences in the optics of bottom- and top-emitting architectures are associated to differences in the applied materials and their dimensions.

In most cases, OLEDs comprise planar layers with almost infinite extension in two dimensions in comparison to the wavelength in the medium.[78] The total thickness of the OLED layer structures is often below the spatial coherence length of the emitted light, requiring a coherent treatment of electromagnetic radiation inside the multi-layer structure and thus the consideration of interference effects to determine the optical properties.[78, 80]

Before the light generated within the EML is extracted to air, several material interfaces have to be passed. At each material interface (\tilde{n}_1/\tilde{n}_2), an incident electromagnetic wave (i) can be either reflected (r) or refracted (t). While the reflected wave keeps propagating in the incident medium, the refracted wave is transmitted into the adjacent medium. From the continuity conditions of the field components, obtained from the Maxwell equations, several relations can be deduced [142]:

- Conservation of the frequency: $\omega_i = \omega_r = \omega_t$
- Reflection law: $|\vec{k}_i| = |\vec{k}_r|$ ($\theta_i = \theta_r$)
- Snell's refraction law: $\frac{|\vec{k}_i|}{|\vec{k}_t|} = \frac{\tilde{n}_1}{\tilde{n}_2} \left(\frac{\tilde{n}_1}{\tilde{n}_2} = \frac{\sin\theta_2}{\sin\theta_1} \right)$

At planar interfaces, reflection and transmittance of incident light can be described by the *Fresnel coefficients* $r_{i,j}$ and $t_{i,j}$ according to [43]:

$$\begin{aligned} r_{12}^s &= \frac{\tilde{n}_1 \cos \theta_1 - \tilde{n}_2 \cos \theta_2}{\tilde{n}_1 \cos \theta_1 + \tilde{n}_2 \cos \theta_2} & \text{and} & & r_{12}^p &= \frac{\tilde{n}_2 \cos \theta_1 - \tilde{n}_1 \cos \theta_2}{\tilde{n}_2 \cos \theta_1 + \tilde{n}_1 \cos \theta_2} \\ t_{12}^s &= \frac{2\tilde{n}_1 \cos \theta_1}{\tilde{n}_1 \cos \theta_1 + \tilde{n}_2 \cos \theta_2} & \text{and} & & t_{12}^p &= \frac{2\tilde{n}_1 \cos \theta_1}{\tilde{n}_2 \cos \theta_1 + \tilde{n}_1 \cos \theta_2} \end{aligned} \quad (4.11)$$

with respect to the polarization of the electromagnetic wave (*s*- or *p*-polarized, cf. Fig. 4.1(a)), the incident angle θ_1 , the angle of refraction θ_2 , as well as the complex refractive indices \tilde{n}_i of the materials. The correlation between the incident angle θ_1 and the refraction angle θ_2 is given by *Snell's law* [43]. The calculation of reflectance and transmittance of an arbitrarily polarized wave is also given by Eq. 4.11, as such waves can be decomposed into a *s*- and *p*-polarized component.[43]

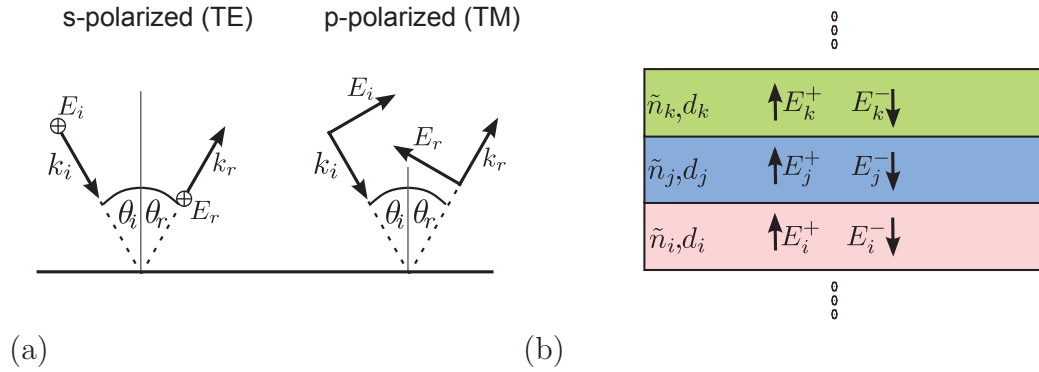


Figure 4.1: Illustration of *s*- (TE) and *p*-polarized (TM) waves according to Neyts et al. [78] (a). Representation of a multi-layer structure of refractive indices \tilde{n}_i and thicknesses d_i (b). A transfer matrix formalism can be used to evaluate the propagation of electromagnetic waves in the structure, describing an up (+) and down (-) propagating wave in each layer, which are connected via the Maxwell and Fresnel equations.

For normal incident light, the reflectance R of a non-absorptive dielectric/metal (n_D/\tilde{n}_M) interface is given by [43]:

$$R = |r|^2 = \left| \frac{\tilde{n}_M - n_D}{\tilde{n}_M + n_D} \right|^2, \quad (4.12)$$

representing the ratio of the electric field intensities of incident and reflected wave. For thick metal layers, the reflectance approaches 100% (mirror), as the imaginary part of the refractive index (κ_m) of most metals is much larger than the real refractive index of dielectrics.

The reflectance and transmittance of a multi-layer stack has to be calculated from the coherent superposition of all possible light paths, regarding reflection and transmittance at the single interfaces and their interference inside the layer structure. An elegant method which accounts for all possible light paths in the layer structure is the *transfer matrix method*. [143] For each layer, two waves are considered, one propagating “up” (+), and one propagating “down” (-) through the layer (cf. Fig. 4.1(b)). [79] Each side of an interface is represented by a *dynamical matrix* \mathbf{D} , accounting for reflectance $r_{i,j}$ and transmittance $t_{i,j}$ determined by the Fresnel equations. The propagation through a single layer is represented by a *propagation matrix* \mathbf{P} . The electric field amplitudes E_i^+ , E_i^- in the i -th layer are connected to the electric field amplitudes in the j -th layer via the matrices according to [143]:

$$\begin{pmatrix} E_i^+ \\ E_i^- \end{pmatrix} = \mathbf{D}_i^{-1} \mathbf{D}_j \begin{pmatrix} E_j^+ \\ E_j^- \end{pmatrix} = \frac{1}{t_{i,j}} \begin{bmatrix} 1 & r_{i,j} \\ r_{i,j} & 1 \end{bmatrix} \begin{pmatrix} E_j^+ \\ E_j^- \end{pmatrix}, \quad (4.13)$$

$$\begin{pmatrix} E_j'^+ \\ E_j'^- \end{pmatrix} = \mathbf{P}_j \begin{pmatrix} E_j^+ \\ E_j^- \end{pmatrix} = \begin{bmatrix} \exp(i\delta_j) & 0 \\ 0 & \exp(-i\delta_j) \end{bmatrix} \begin{pmatrix} E_j^+ \\ E_j^- \end{pmatrix}, \quad (4.14)$$

including the phase of the light gathered during the pass of one cycle through the j -th layer $\delta_j = 2\pi kn_j d_j$. [143] In order to calculate the transmission (t) and reflection (r) coefficients of a complete N layer device, an electromagnetic wave E_0^+ incident from the outside (0 -th layer) is investigated. The reflected or transmitted light from the structure is given by the transfer matrix formalism according to:

$$\begin{pmatrix} E_0^+ \\ E_0^- \end{pmatrix} = \mathbf{T} \begin{pmatrix} E_{N+1}'^+ \\ E_{N+1}'^- \end{pmatrix} = \mathbf{D}_0^{-1} \left[\prod_{m=1}^N \mathbf{D}_m \mathbf{P}_m \mathbf{D}_m^{-1} \right] \mathbf{D}_{N+1} \begin{pmatrix} E_{N+1}'^+ \\ E_{N+1}'^- \end{pmatrix} = \begin{bmatrix} T_{11} & T_{12} \\ T_{21} & T_{22} \end{bmatrix} \begin{pmatrix} E_{N+1}'^+ \\ E_{N+1}'^- \end{pmatrix}, \quad (4.15)$$

introducing the system transfer matrix \mathbf{T} , in which all dynamical and propagation matrices are linearly combined. The reflection r and transmission t coefficients of the N layer structure result from the matrix elements of the system matrix according to [143]:

$$r = \left. \frac{E_0^-}{E_0^+} \right|_{E_{N+1}'^- = 0} = \frac{T_{21}}{T_{11}} \quad \text{and} \quad t = \left. \frac{E_{N+1}'^+}{E_0^+} \right|_{E_{N+1}'^- = 0} = \frac{1}{T_{11}} \quad (4.16)$$

The reflection coefficient r is defined as the ratio of the incident electric field magnitude E_0^+ to the reflected field magnitude E_0^- in the incident medium, without an incident wave from the other side of the structure ($E_{N+1}'^- = 0$). The transmission coefficient t is calculated from the ratio of the field magnitude $E_{N+1}'^+$ penetrating the adjacent medium on the other side of the structure to the incident light E_0^+ , while again no incident wave from the other side is expected.

4.2 Optical Optimization of Top-Emitting OLEDs

In this section, the optimization of top-emitting OLED structures regarding their spectral emission and efficiency is investigated. The application of a thin metal film as a transparent electrode introduces prominent microcavity effects, which strongly influence the spectral emission. With focus on white top-emitting OLEDs, it is emphasized that a broad spectral emission can be achieved by the application of the *capping layer* concept and highly transparent ultra-thin metal films.

4.2.1 Microcavity Effects Introduced by Reflective Electrodes

Top-emitting OLEDs employing two metal electrodes are often described as a micro-resonator with parallel mirrors, or *Fabry Pérot interferometer*. [43] The spectral emission of top-emitting OLEDs and further the spontaneous emission rate of the emitting dipoles are determined by the properties of the resonator. [144] The propagating electromagnetic waves inside the microcavity are reflected at the metallic mirrors, causing interference between the incident and the reflected waves. Constructive interference is observed if the phase difference $\Delta\Phi$ after a full light cycle is a multiple of 2π . [144]

These modes represent *resonator modes* of the microcavity and the phase difference is given by:

$$\Delta\Phi = 2\pi \cdot m = \Phi_b + \Phi_t + \sum_i \phi_i = \Phi_b + \Phi_t + \frac{4\pi}{\lambda_{\text{res}}} \sum_i n_i d_i \cos \theta_i , \quad (4.17)$$

with contributions from the phase difference ϕ_i in the single layers i , depending on the layer thickness d_i and reflective index n_i , the propagation angle θ_i , and the resonance wavelength λ_{res} , as well as the phase shift at the metallic bottom (Φ_b) and top (Φ_t) electrode. The phase shift at a dielectric/metal interface (n_D/\tilde{n}_M) for normal incident light is given by [145]:

$$\Phi_m = \arctan \left(\frac{2n_D \kappa_M}{n_D^2 - n_M^2 - \kappa_M^2} \right) . \quad (4.18)$$

Equation 4.18 clearly shows that the specific electrode material strongly affects the phase shift of electromagnetic waves at the interface and therefore the resonance condition of the microcavity.[145] An analogue expression of the resonance condition in Eq. 4.17 is given by the path difference ΔL of the light waves [146]:

$$\Delta L = m \cdot \lambda_{\text{res}} = 2 \left(\sum_i n_i d_i \cos \theta_i + L_{\text{pen},b} + L_{\text{pen},t} \right) , \quad (4.19)$$

taking the penetration depth L_{pen} in the top and bottom metal electrode into account. For normal incident light ($\theta_i = 0$), Eq. 4.19 can be transformed to:

$$\frac{m}{2} \lambda_{\text{res}} = \sum_i n_i d_i + L_{\text{pen},b} + L_{\text{pen},t} = L_{\text{cav}} , \quad (4.20)$$

and the first resonator mode ($m=1$) is observed for a cavity length $L_{\text{cav}} = \frac{1}{2} \lambda_{\text{res}}$, while higher modes are obtained for multiples of $\frac{1}{2} \lambda_{\text{res}}$. For an ideal conductor, the penetration depth is $L_{\text{pen}} = 0$, as the damping constant would be infinite.[43, 146] In real metals, the damping is not that strong, so 15 nm of silver, which is often referred to as standard transparent electrode for top-emitting OLEDs [124, 125], still allow an average transmittance in the range of 50 %.[77]

From the description of a planar micro-resonator, the spectral emission properties of top-emitting OLEDs can be deduced. The spectrum $I_{\text{cav}}(\lambda, \theta)$ which is emitted from the microcavity can be described by [124, 147]:

$$I_{\text{cav}}(\lambda, \theta) = T_t \frac{1 + R_b + 2\sqrt{R_b} \cos \left(-\Phi_b + \frac{4\pi n_{\text{org}} z_0 \cos(\theta_{\text{EML}})}{\lambda} \right)}{(1 - \sqrt{R_t R_b})^2 + 4\sqrt{R_b R_t} \sin^2 \left(\frac{\Delta\Phi}{2} \right)} \cdot I_0(\lambda) \quad (4.21)$$

$$I_{\text{cav}}(\lambda, \theta) = C(\lambda, \theta) \cdot I_0(\lambda) ,$$

introducing the distance z_0 of the emitting dipoles to the highly reflective bottom electrode and the emission angle θ_{EML} of the dipoles inside the EML. The *emission affinity* $C(\lambda, \theta)$ represents a feedback function of the microcavity, where the observed emission $I_{\text{cav}}(\lambda, \theta)$ results from convolution of the emission affinity and the emission of the emitter material $I_0(\lambda)$ in free space.

The FWHM of the emission from a microcavity ($\Delta\lambda_{\text{FWHM}}$) can be approximated by [148]:

$$\Delta\lambda_{\text{FWHM}} = \frac{\lambda^2}{2\pi L_{\text{cav}}} \frac{1 - \sqrt{R_t R_b}}{(R_t R_b)^{\frac{1}{4}}}, \quad (4.22)$$

considering the uncertainty relation and the photon lifetime inside the microcavity. Equations 4.21 and 4.22 show the dependence of the emission properties on the reflectivity of the metal electrodes R_b and R_t , and further on the cavity length L_{cav} . If both metal electrodes would be highly reflective ($R \approx 1$), the spectral width of the emission would narrow to an infinitely small value ($\Delta\lambda_{\text{FWHM}} \approx 0$). Note that also an increase in cavity length narrows the emission spectrum.

In the context of white top-emitting OLEDs, both parameters have to be carefully controlled to avoid spectral narrowing, which would lead to low efficiencies and poor color rendering. Furthermore, a high reflectivity of the metal electrodes introduces a pronounced angular dependency of the spectral emission, as described by Eq. 4.21.[124]

4.2.2 Optimization of the Microcavity by Optical Simulation

In order to optimize OLEDs without major effort in performing experiments and to analyze data obtained through experimental studies, the software tools “*Simoled*” and “*OLED-Power*” by Mauro Furno have been used. Both rely on the planar wave expansion of the emission generated from the emitter molecules, which are described as a set of radiative point dipole sources embedded in the OLED structure.[80, 149] Details of the implementation of the radiative dipole sources in multi-layer systems and the calculation of their radiation close to metal interfaces have been intensively investigated in literature.[78–80]

In contrast to dipoles surrounded by an infinite medium, the OLED structure influences the decay rates of the emitting dipoles via the Purcell effect. Furthermore, the dissipated power is distributed into specific supported modes due to the coherent superposition of light modes inside the OLED structure.[150]

The required input parameter for the simulation include: the layer characteristics (thickness d_i , refractive index \tilde{n}_i), the emission spectrum of the emitter $I_0(\lambda)$, its radiative efficiency η_{PL} , the dipole orientation in the emission layer θ_{Dipole} , and the distance of the dipoles to the reflective bottom electrodes z_0 . The EML itself is considered to be a loss-free media ($\kappa = 0$). The simulation tool allows to calculate several parameter, e.g. the angular resolved spectral emission of the top-emitting OLED $I_{\text{cav}}(\lambda, \theta)$, the emission affinity $C(\lambda, \theta)$, the electric field distribution inside the device, as well as the *photon flux*. The simulated photon flux is a measure equivalent to the EQE, as the emission intensity $I_{\text{cav}}(\lambda, \theta)$ is evaluated in the full solid angle. In order to obtain highly efficient top-emitting OLEDs, the microcavity has to be optimized for maximum photon flux of the incorporated emitter(s). In the following, the optimization of top-emitting OLEDs is shown for a red emitter by using two state-of-the-art concepts. On the one hand, an organic *capping layer* is introduced on top of the transparent metal electrode.[124, 151] On the other hand, the influence of the transparent thin-film metal top electrode is investigated.[152–154] The optimization process requires a simultaneous variation of several layer thicknesses, while the figure of merit, e.g. high efficiency or broad emission can be optimized. In order to visualize the influence of the thickness variations on the

emission properties and efficiency of top-emitting OLEDs, only two simultaneous layer variations can be shown. It is worth noting that for the devices used in this work, a parallel optimization of up to six layers has been performed.

Figure 4.2 visualizes the optimization of a red top-emitting OLED with a 15 nm thick silver standard top electrode [124, 125] for varied transport layer thicknesses. According to the pin-concept, the thickness of the transport layers can be used to optimize the optics of the OLED without drawbacks on the electrical performance (see Section 3.3.1). The EML consists of a preferably hole conductive matrix (NPB), doped with the red phosphorescent emitter Ir(MDQ)₂(acac). Therefore, the exciton formation for OLEDs containing such an EML is expected to be close to the EML/HBL interface. In the simulation, this is modeled by locating the emissive dipoles in an infinitely thin layer (δ -function) at this interface (see Fig. 4.2). The simulated OLED architecture, starting from the substrate, is defined as follows:

Al (40)/Ag (40)/**HTL (Y)**/EBL (10)/EML (20)/HBL (10)/**ETL (X)**/Ag (15)

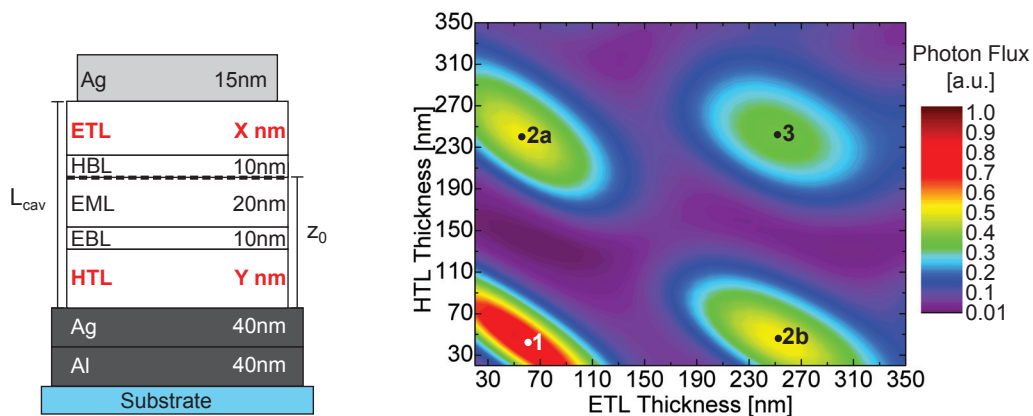


Figure 4.2: Simulated photon flux of a red top-emitting OLED for varied ETL and HTL thickness, assuming a δ -shaped emitting dipole distribution at the EML/HBL interface. Local maxima of the photon flux are found (**1**, **2a**, **2b**, **3**), which can be associated to the resonant modes of the microcavity. The most efficient device (highest photon flux) is obtained for 65 nm ETL and 40 nm HTL (**1**).

Maxima of the photon flux are formed for several ETL and HTL combinations, according to the resulting cavity length L_{cav} and the distance z_0 of the emitting dipoles to the bottom electrode.[80] Four local maxima (**1**, **2a**, **2b**, **3**) of the photon flux are found in the thickness range investigated, where the thinnest device (**1**) yields the highest photon flux. Meerheim *et al.* [76] investigated the EQE dependency of top-emitting OLEDs with the thickness of the ETL layer. In accordance to the results in Fig. 4.2, they observed a lower efficiency of higher order cavity devices, caused by a lower Purcell effect and an increased power dissipation of the emissive dipoles into fundamental light modes which do not contribute to the far-field emission.

In Fig. 4.3, the electric field intensities for the four local maxima devices from Fig. 4.2 are shown in normal emission direction for the peak wavelength of the emitter material ($\lambda_{max} = 610$ nm). Resonator modes having multiples of $m \cdot \lambda_{max}/2$ of the peak emission

wavelength are formed inside the optimized microcavities of the four devices, corresponding to local photon flux maxima. For each maximum device, the emitting dipoles are positioned close to an antinode of the electric field intensity of λ_{\max} . For dipoles positioned in the antinodes of the resonator modes, constructive interference inside the microcavity is given, which results in maximum stimuli and power dissipation of the dipoles.[79] Therefore, the optimization of the cavity length and the positioning of the emitting dipoles close to an antinode of the electric field intensity of the emitter spectrum are crucial parameters to achieve an intense power dissipation and thus efficient OLEDs, respectively.

For a 1st order cavity, only one combination of EML and HTL thicknesses (ETL: 65 nm, HTL: 40 nm) gives an optimized device (**1**), where the dipoles are positioned in the field antinode. In comparison, for a 2nd order ($2 \cdot \lambda_{\max}/2$) microcavity, two efficient OLEDs can be realized, depending on the position of the dipoles in the field antinode close to the transparent metal electrode (**2a**) or close to the opaque electrode (**2b**). Consequently, for a 3rd order cavity, three devices with local maxima of the photon flux could be designed. Furthermore, the penetration of the electric field into the metal electrodes is clearly verified in Fig. 4.3.

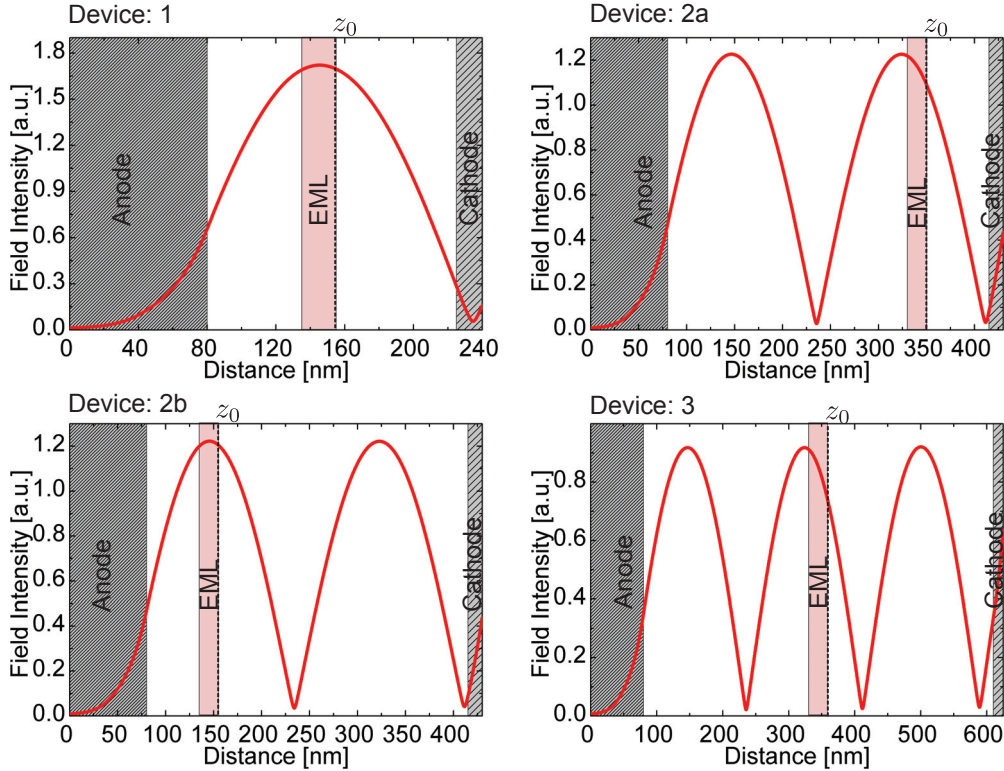


Figure 4.3: Simulated electric field intensities of the local maxima of the photon flux in normal direction at the peak emission wavelength of 610 nm. The different thicknesses of the organic layers form 1st (**1**), 2nd (**2a**, **2b**), and 3rd order (**3**) $\lambda_{\max}/2$ resonant modes. For all devices, the photon flux optimization yields an emitting dipole position close to the antinodes of the electric field.

Organic Capping Layer Concept

In order to improve the efficiency and to optimize the emission properties, the capping layer concept is often applied to top-emitting OLEDs.[124, 125, 151, 155] It introduces an additional (organic) layer on top of the transparent metal contact of the top-emitting OLED. On the one hand, the capping layer can enhance the transmittance of the top contact, determined by the Fresnel coefficients.[124, 151] On the other hand, the resonance conditions within the microcavity change and the emission affinity $C(\lambda, \theta)$ as well as the device efficiency are strongly affected.[124, 156] Riel *et al.*[156] have shown that a maximum transmittance of the top electrode does not necessarily lead to the highest efficiency of monochrome top-emitting OLEDs, but that optimized resonant conditions by a tailored capping layer thickness can enhance the efficiency up to a factor of 1.7.

Figure 4.4(a) shows the simulated photon flux for a thickness variation of the HTL and an organic capping layer with a refractive index of $n=1.8$. The simulated OLED architecture, starting from the substrate, is given by:

Al (40)/Ag (40)/**HTL (Y)**/EBL (10)/EML (20)/HBL (10)/ETL (65)/Ag (15)/**CAP (X)**.

Introducing the capping layer, the photon flux is significantly enhanced. It is found that the deposition of a capping layer with 100 nm thickness increases the photon flux by 14 % in comparison to the pre-optimized device without capping layer (**1'** compared to **1**), at a fixed HTL thickness of 40 nm. Figure 4.4(b) shows a contour plot of the emission affinity $C(\lambda, 0)$ in normal direction, for a fixed HTL thickness of 40 nm, while wavelength (vertical-axis) and capping layer thickness (horizontal-axis) are varied. Each vertical slice in Fig. 4.4(b) represents the emission affinity of a single device with a fixed capping layer thickness. Without a capping layer ($x=0$), the FWHM of the emission affinity is $\lambda_{\text{FWHM}}=71$ nm, which is sufficiently broad for the red emitter.

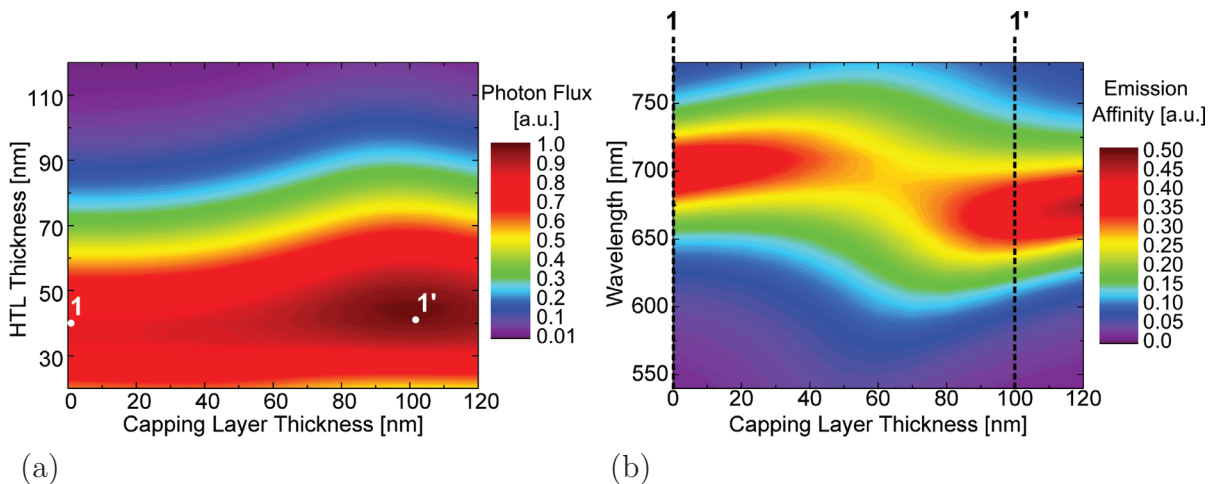


Figure 4.4: Photon flux of a red top-emitting OLED with an organic capping layer ($n=1.8$), for different HTL and capping layer thicknesses (a). Emission affinity in normal direction ($C(\lambda, 0)$) for different wavelengths and capping layer thicknesses, and a fixed HTL at 40 nm (b). Introducing a capping layer results in an enhancement of the photon flux (**1** compared to **1'**). The width and intensity of $C(\lambda, 0)$ can be controlled with the capping layer thickness.

For increasing capping layer thickness, the peak intensity decreases, while the width of the emission affinity increases. The broadest FWHM of the emission affinity ($\lambda_{\text{FWHM}} = 152 \text{ nm}$) is found for a capping layer thickness of 60 nm, while the photon flux remains comparable to Device **1** (cf. Fig.4.4(a)). This demonstrates the potential of the capping layer in the context of white top-emitting OLEDs, modifying the emission affinity for broader emission while maintaining the efficiency.[124] For an increased capping layer thickness, the emission affinity confines again, correlated with an increase of the peak intensity. Device **1'**, which reaches the highest photon flux, shows a λ_{FWHM} of 92 nm, only slightly increased compared to Device **1**.

Although the introduction of a capping layer broadens the emission affinity by more than a factor of two, a λ_{FWHM} of 152 nm is still not sufficient to realize a white emitting device with a broad spectrum and high CRI. Reports on white top-emitting OLEDs using a capping layer and semitransparent silver electrodes with thicknesses in the range of 15 nm [125, 157, 158] still show lower efficiency, narrowed spectra, and stronger angular color-shift compared to their bottom-emitting counterparts.

Ultra-Thin Metal Top Electrodes

In contrast to the application of an additional organic capping layer, the optical properties of the microcavity can also be optimized by a variation of the metal thickness. Figure 4.5(a) emphasizes the dependence of the photon flux and the emission affinity as a function of the top electrode thickness, assuming homogeneously closed bulk metal films. For this simulation, the ETL and HTL layer thickness obtained from the preliminarily optimization (Device **1'**) have been kept constant, and the OLED structure, starting from the substrate, is given by:

Al (40)/Ag (40)/HTL(40)/EBL (10)/EML (20)/HBL (10)/ETL (65)/**Ag (X)**/**CAP (Y)**.

Figure 4.5(a) shows a strong dependency of the photon flux on the combination of the capping layer and the top electrode thickness. In comparison to the quite uniform dependency of the photon flux on the capping layer/HTL optimization (see Fig. 4.4(a)), the silver thickness has a complex influence, by significantly changing the reflectivity (transmittance) and resonance condition of the microcavity. An increase of the metal layer thickness from 15 to 21 nm, by simultaneous adjustment of the capping layer to 80 nm, leads to a photon flux enhancement by 17% (**1*** compared to **1'**).

A careful adjustment of the capping layer thickness conserves a high photon flux for reduced top electrode thicknesses down to 5 nm. Figure 4.5(b) verifies the beneficial effect of the reduced top electrode thickness regarding the realization of broad spectral emission from microcavity OLEDs, as the FWHM of the emission affinity strongly increases. For a fixed capping layer thickness of 80 nm, the FWHM of the emission affinity increases from $\lambda_{\text{FWHM}} = 64 \text{ nm}$ (**1***) to a maximum of $\lambda_{\text{FWHM}} = 193 \text{ nm}$ (**1[†]**) at a silver thickness of 10 nm. For the realization of highly efficient, angularly color-stable white top-emitting OLEDs, ultra-thin top electrodes combined with rather thick capping layers show promising results. Even though the benefits of a reduction of the metal electrode thickness for broad cavity emission seem quite reasonable from the simulation, major problems occur in the experimental realization of such thin metal films due to unfavorable agglomerate growth of silver on most underlying organic layers.

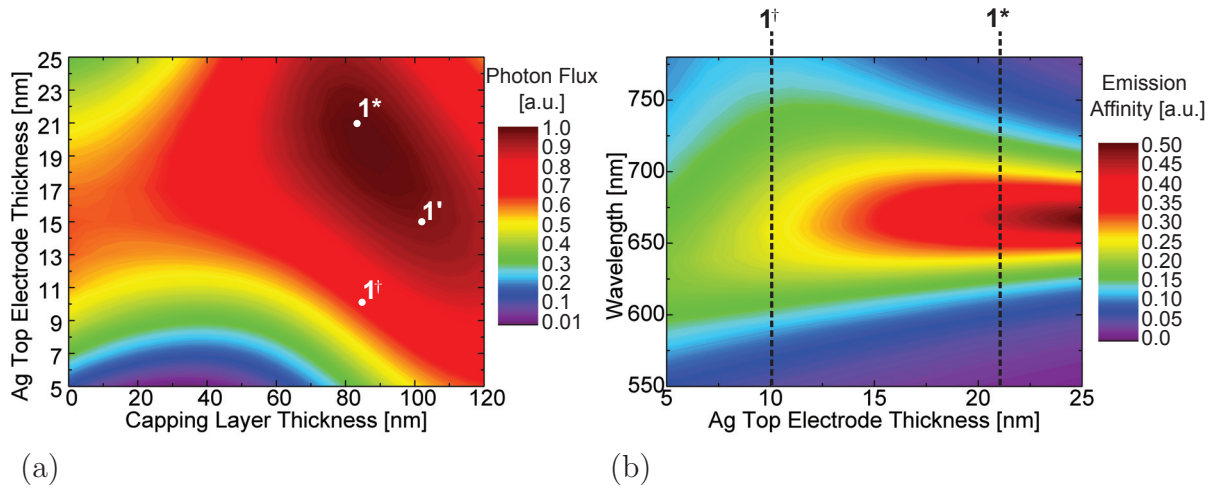


Figure 4.5: Photon flux of a red top-emitting OLED with an organic capping layer ($n=1.8$), for different top electrode and capping layer thicknesses (a). Emission affinity in normal direction ($C(\lambda, 0)$) for different wavelengths and top electrode thicknesses with a fixed capping layer thickness of 80 nm (b). The optimization of the capping layer and the top electrode thickness results in a further enhanced photon flux of OLED structure (1*) compared to (1'). The width of the emission affinity strongly increases with decreasing metal top electrode thickness, proving beneficial for the realization of efficient white emission.

It is worth to note that simulation results and experiments can strongly diverge if not the expected bulk, but agglomerate metal films are present, due to a change of the refractive index.[159] Details on the metal film growth and optical properties of ultra-thin metal electrodes on organics will be shown in the following Chapters.

4.2.3 State-of-the-art top-emitting OLEDs

In state-of-the-art top-emitting OLEDs, the capping layer concept [151, 160, 161] as well as transparent electrodes [162–165] have been successfully applied to realize highly efficient monochrome emission. Hofmann *et al.* [11] reported an EQE of 29% for red top-emitting OLEDs, using a 21 nm thick silver top contact and an optimized capping layer. In bottom-emitting OLEDs, the cavity effect has been achieved by deposition of a 23 nm thick silver layer on top of the ITO electrode, leading to a remarkable increase in EQE from 17 to 25.5%. Nevertheless, monochrome top-emitting OLEDs usually outperform bottom-emitting reference devices, benefiting from the enhanced emission intensity of the microcavity and the Purcell effect.[166] However, the angular dependency of the emission of microcavity OLEDs is not suitable for most applications.

White top-emitting OLEDs also apply capping layers and optimized top electrodes to achieve efficient and broad emission. However, white top-emitting OLEDs reported so far still lack in efficiency, angular color-stability, and color rendering compared to bottom-emitting OLEDs. Table 4.1 summarizes the achieved efficiencies with respect to the applied top electrode and capping layer.

Table 4.1: Literature review on white top-emitting OLEDs without additional light extraction techniques. The achieved efficiency, applied top electrode and capping layer are given.

Publication	Year	Efficiency		Top Electrode	Capping Layer
		EQE [%]	LE [lm/W]		
Feng[157]	2001	1.8*	1.9*	–	none
Hsu[158]	2005	–	9.6*	5 nm Ca/ 15 nm Ag	SnO ₂
Kanno[114]	2005	10.5*	9.8*	ITO	none
Zhu[167]	2007	9.1*	12.8*	6 nm Ca/ 15 nm Au	Alq ₃
Thomschke[124]	2009	7.8*	13.3*	1 nm Al/ 15 nm Ag	NPB
Freitag[125]	2010	4.9 ⁰	13.3 ⁰	1 nm Al/ 15 nm Ag	NPB
Xie[168]	2010	–	17.6*	2 nm Al/ 18 nm Ag	m-MTDATA
Chen[155]	2011	–	10.5 ⁰	5 nm Al/ 15 nm Ag	MoO ₃
Wang[169]	2012	16.9*	–	1 nm Al/ 18 nm Ag	TCTA

Symbols: ⁰ at 1000 cd/m², * peak value, – not reported

In summary, highly transparent top electrodes which are compatible with the organic layers have to be introduced to top-emitting OLEDs, in order to obtain an efficient and angularly color-stable white emission, compensating the present drawbacks of these devices in comparison to their bottom-emitting counterparts. While Chapter 6 focuses on the realization of such electrodes on organics, the application to white top-emitting OLEDs and the optical optimization of the devices will be shown in Chapter 7.

4.3 Outcoupling of Internally Trapped Light Modes

Although the optimization of the optical properties of OLEDs and the application of highly transparent electrodes allows for efficient and angularly color-stable white emission, this cannot solve a general limitation of OLEDs, which is the trapping of light modes inside the planar device structures.

The investigations in Chapter 3 have shown that state-of-the-art OLEDs already reach IQEs close to unity. However, the EQE is typically below 30 %, limited from the light extraction efficiency η_{out} . Here, the dissipation of radiated power by the emitter molecules is investigated in detail, analyzing the optical losses of an OLED. Furthermore, approaches to extract the internally trapped emission are provided.

4.3.1 Internally Trapped Light Modes

According to Snell's law, the critical angle for total internal reflection of light at the interface between the organics and the external medium (air) ($\sin(\theta_{\text{org}}^{\text{crit}})$) is given by:

$$\sin(\theta_{\text{air}}) = 1 = \frac{n_{\text{air}}}{n_{\text{org}}} \sin(\theta_{\text{org}}^{\text{crit}}) . \quad (4.23)$$

For a given refractive index of the organic layers ($n_{\text{org}} = 1.8$), light waves propagating with angles larger than $\theta_{\text{org}}^{\text{crit}} = 33.7^\circ$ cannot be transferred to air and instead are trapped inside the organic layers (see Fig. 4.6). These waveguided modes (WG) do not contribute to the far-field emission and thus the EQE, representing a prominent efficiency loss.[80]

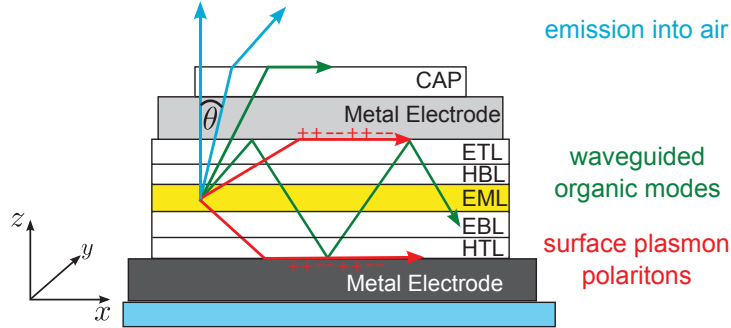


Figure 4.6: Illustration of the emission from a top-emitting OLED structure. Total internal reflection of light and the excitation of SPP modes at the metal electrodes limit the EQE of OLEDs in general.

A further loss channel is introduced by the metal electrodes, as the radiating molecules can dissipate power into the excitation of coherent electron gas oscillations in the metal electrodes (see Fig. 4.6).[80, 170] These surface plasmon polariton modes are hybrid modes of longitudinal electron gas oscillations and an electromagnetic wave propagating at the metal/dielectric interface, evanescently decaying in both adjacent media.[150, 171] The dispersion relation $\omega_{\text{SPP}}(k_x)$ of the bulk SPP mode can be determined by solving the Maxwell equations for the electric and magnetic field, assuming plane waves with evanescent decay perpendicular to the interface.[141, 171, 172] Note that for TE-modes, only a trivial solution would fulfill the continuity conditions for the fields at the interface.[141] Therefore, and in contrast to waveguided modes, guided SPP modes are exclusively TM (p-polarized) light modes.[141] For a TM-mode, the following continuity conditions have to be fulfilled at the metal/dielectric interface:

$$(1) \quad E_{M,x} = E_{D,x} \quad (2) \quad H_{M,y} = H_{D,y} \quad (3) \quad \epsilon_M E_{M,z} = \epsilon_D E_{D,x} \quad . \quad (4.24)$$

To fulfill the condition of an evanescent decay in both adjacent media around the interface ($z=0$), planar TM electromagnetic waves of the following type are analyzed:

$$\vec{E} = \begin{pmatrix} E_x \\ 0 \\ E_z \end{pmatrix} \cdot e^{-\kappa_z |z|} e^{i(k_x x - \omega t)} \quad \text{and} \quad \vec{H} = \begin{pmatrix} 0 \\ H_y \\ 0 \end{pmatrix} \cdot e^{-\kappa_z |z|} e^{i(k_x x - \omega t)} \quad . \quad (4.25)$$

Figure 4.7(a) schematically shows a bulk metal/dielectric (ϵ_M/ϵ_D) interface illustrating a spatially confined SPP mode, its evanescent decay into the adjacent media, and its propagation along the interface. Solving the Maxwell equations, the following relations for the wavenumbers are found [172]:

$$k_{M,x} = k_{D,x} \quad \text{and} \quad \frac{\kappa_{M,z}}{\epsilon_M} + \frac{\kappa_{D,z}}{\epsilon_D} = 0 \quad . \quad (4.26)$$

4.3 Outcoupling of Internally Trapped Light Modes

From the wave equation (Eq. 4.3), the following dispersion relation of the SPP mode is obtained [171, 172]:

$$\omega_{\text{SPP}}(k_x) = k_x \frac{c}{\sqrt{\epsilon_D}} \sqrt{\frac{\epsilon_M + \epsilon_D}{\epsilon_M}} . \quad (4.27)$$

For a confined SPP mode propagating with real k_x at the interface, $\text{Re}(\epsilon_M) < 0$, $\epsilon_D > 0$, and $|\text{Re}(\epsilon_M)| > \epsilon_D$ are required.[171] Consequently, the dispersion of the bulk SPP mode

$$\omega_{\text{SPP}}(k_x) = k_x \frac{c}{\sqrt{\epsilon_D}} \sqrt{\frac{\epsilon_M + \epsilon_D}{\epsilon_M}} < k_x \frac{c}{\sqrt{\epsilon_D}} = \omega_{\text{Ph}}(k_x) \quad (4.28)$$

is shifted to lower frequencies compared to the photon dispersion in the dielectric media $\omega_{\text{Ph}}(k_x)$. [141, 171] For some metals, a sufficient approximation of the dielectric constant within the visible spectral range is given by the Drude model. Strong simplifications are introduced by the assumption of quasi-free electrons moving through the solid while colliding with the ion lattice, generating a momentum relaxation rate Γ [141]:

$$\epsilon_M^{\text{Drude}}(\omega) = \epsilon_\infty - \frac{\omega_P^2}{\omega(\omega + i\Gamma)} , \quad (4.29)$$

with the plasma frequency of the metal ω_P and the material specific constant ϵ_∞ . Introducing the dielectric constant $\epsilon_M^{\text{Drude}}$ according to Eq. 4.29 into Eq. 4.27, it is found that the SPP dispersion approaches the photon dispersion for small k_x , while for large wavenumbers, the dispersion of the SPP modes tends asymptotically to the value $\omega_{\text{sp}} = \omega_P/\sqrt{1 + \epsilon_D}$. [141] For all wavenumbers, the SPP dispersion remains at lower frequencies compared to the light-line and no intersection between the light-line and the plasmon dispersion is found (Fig. 4.7(b)). Therefore, bulk SPP modes propagating along planar interfaces are non-radiative and cannot be excited by photons.[171]

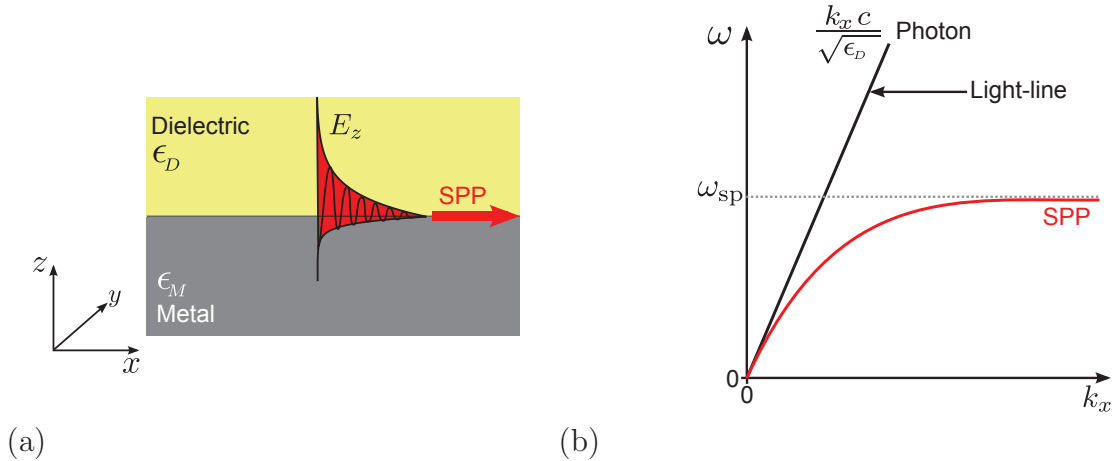


Figure 4.7: Schematic illustration of a surface plasmon polariton (SPP) mode propagating along the metal/dielectric interface with evanescent decay into both adjacent media (a). Dispersion relation of a bulk SPP mode and a photon propagating in the dielectric medium (b). The SPP dispersion is shifted to higher k_x compared to the photon dispersion, which avoids an optical SPP excitation at planar interfaces.

Note that the dispersion of a SPP mode is sensitive to the dielectric constants of the adjacent metal and organic materials, while the relation to the photon dispersion remains. Top-emitting OLEDs show prominent dissipation of energy into SPPs modes [80, 166], as the emitting dipoles can couple to the evanescently decaying fields of the SPP modes [171]. Furthermore, SPP modes can be generated at both metal/dielectric interfaces of the thin transparent metal electrode and SPP mode coupling in dependence on the film thickness is observed.[171, 173, 174]

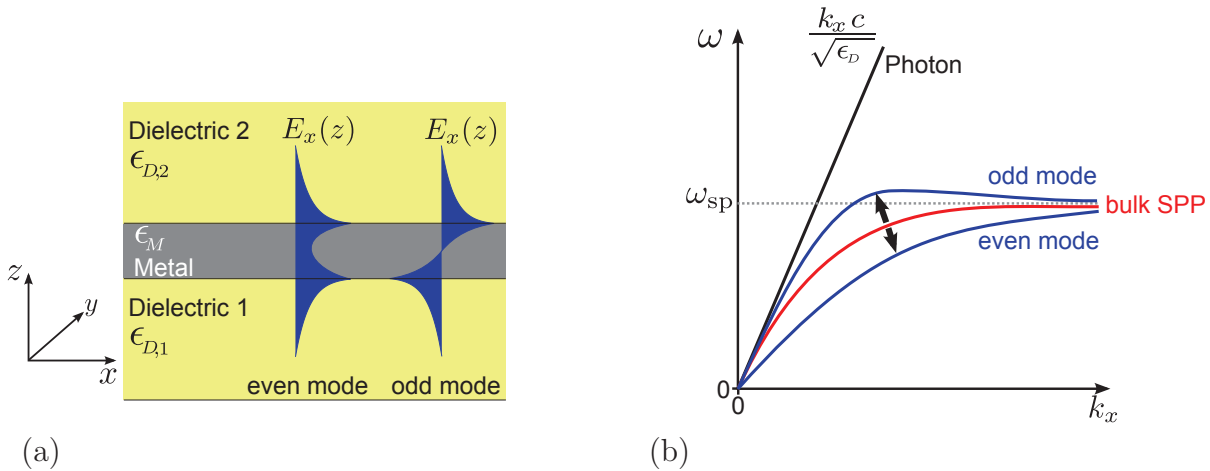


Figure 4.8: Illustration of the electric field distribution $E_x(z)$ perpendicular to the interfaces for bound even and odd surface plasmon polaritons (SPP) at a thin metal layer between two dielectric media (a). Schematic dispersion relation for the coupled SPP modes in comparison to the bulk SPP (b). For the even SPP, the dispersion is shifted to lower frequencies, while the odd SPP is shifted to higher energies with respect to an assumed bulk SPP.[141, 173, 174]

For a dielectric/metal/dielectric system, two confined modes with either even or odd in-plane field distribution perpendicular to the interface ($E_x(z)$) are found (see Fig. 4.8(a)). [173–175] In comparison to the bulk SPP mode at a single metal/dielectric interface, the coupling of the top- and bottom SPP mode at a thin metal film leads to a dispersion splitting. While the dispersion of the odd coupled state is shifted to higher energies, the even coupled SPP mode shows an energy reduction.[173] However, the dispersion of both bound modes still show no intersection with the light-line (see Fig. 4.8(b), for $\epsilon_{D,1} = \epsilon_{D,2}$), so that both modes are non-radiative.

In addition to bound, non-radiative SPP modes, radiative SPP modes can be formed at thin metal films.[173, 174] Such modes are only confined at one metal/dielectric interface and for finite distances they show an increasing perpendicular field component in the second dielectric medium.[173] These modes are able to transfer energy via the SPP formation from the first to the second dielectric. This can be used to transfer energy through comparably thick metal films, e.g. to excite emitters in the other dielectric medium.[176]

In discontinuous metal films like metal nano-structures, isolated metal nano-particles, or granular metal films, localized surface plasmon modes (LSP modes) can be excited.[177] In contrast to SPP modes propagating along extended metal/dielectric interfaces, LSP modes are spatially confined on the metal nano-particle.[178] Their dispersion/excitation is strongly dependent on the dielectric constants of the adjacent materials as well as the

shape, the composition, and the size of the metallic structures.[178, 179] Hence, an optimization of the nano-structures allows to tune the excitation frequency. However, for most LSP modes the excitation frequency is within the visible spectral range, introducing significant absorption of the incident light.[179, 180]

Thus, the formation of metal nano-particles and isolated metal grains, allowing the excitation of LSP modes, should be strictly avoided. Therefore, the realization of highly transparent and smooth thin-film metal electrodes will be in the focus of this work.

4.3.2 Power Dissipation Spectra of Top-Emitting OLEDs

In order to analyze the dissipated power of the emitter molecules, the OLED-Power tool mentioned previously is used. The power dissipation is calculated for the three fundamental dipole types in OLEDs: $\vec{p}_{\parallel, TM}$, $\vec{p}_{\perp, TM}$, and $\vec{p}_{\perp, TE}$, according to orientation (parallel or perpendicular to the interface) and polarization of their emission (TE or TM).[78, 79] Note that each arbitrary dipole orientation (\vec{p}) in the EML can be represented by a linear combination of these components.

In Fig. 4.9, the power dissipation spectra for s- and p-polarized emission is exemplary shown for a red monochrome top-emitting OLED of a second order cavity. Again, the red phosphorescent emitter system investigated in Section 4.2.2 is used. A dipole orientation factor of $\theta_{\text{Dipole}}=0.24$ ($\theta_{\text{Dipole}}=0$, completely horizontal) has been assumed, according to a literature report from Schmidt *et al.*[181] The OLED architecture, starting from the substrate, is given by:

Al (40)/Ag (40)/HTL (251)/EBL (10)/EML (20)/HBL (10)/ETL (91)/Ag (20)/CAP (60).

The air light-line and the organic light-line (dash-dotted lines) are obtained from the dispersion relation of photons $E(k_x) = \hbar ck_0/n$ and added in order to emphasize the propagation medium. Black lines in Fig. 4.9 highlight the maximum intensity of the modes, as a guide to the eye.

In the air light-cone, the radiative cavity mode is observed, dissipating power to the far-field and showing a parabola-like dispersion relation. The thick organic layer sequence leads to the formation of two waveguided modes (WG1, WG2), propagating inside the organic layers. For thinner OLEDs, the number of waveguided modes and the amount of energy dissipated into the organics decreases.[150] Furthermore, two SPP modes are observed in p-polarization (Fig. 4.9(a)). The SPP at the thick metal electrode (SPP1) is located close to the organic light-line and is strongly confined. In contrast, the SPP mode at the thin metal electrode (short-dashed line) is shifted to larger in-plane wavenumbers and has a much broader intensity distribution. For s-polarized emission (Fig. 4.9(b)), only the radiative cavity mode propagates inside the air light-cone, while two waveguided modes (WG1s, WG2s) are propagating inside the organics.

The polarization dependency of the Fresnel coefficients leads to a trade-off between the s- and p-polarized cavity mode, becoming is most prominent for large in-plane wavenumbers. In order to analyze the amount of dissipated power into air, waveguided, and SPP modes, power dissipation profiles from Fig. 4.9 have been extracted at the peak wavelength ($\lambda_{\text{max}}=610$ nm) of the PL emitter spectrum (see Fig. 4.10).

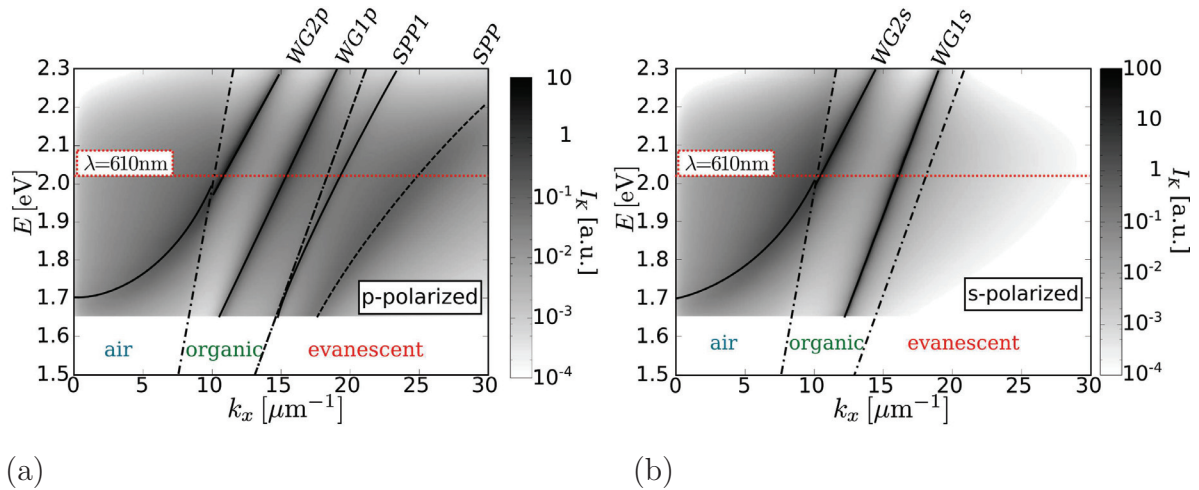


Figure 4.9: Power dissipation spectra I_K of a red top-emitting OLED as a function of the in-plane wavenumber k_x for p-polarized (a) and s-polarized emission (b). The radiating molecules dissipate energy either into the external medium (air), waveguided modes inside the organic layers (WG), or into evanescently decaying SPP modes at the metal interfaces. Black lines serve as a guide to the eye for the dispersion of the intensity maxima of the modes. Dash-dotted lines represent the air and organic light-line, emphasizing the corresponding media in which the mode propagates.

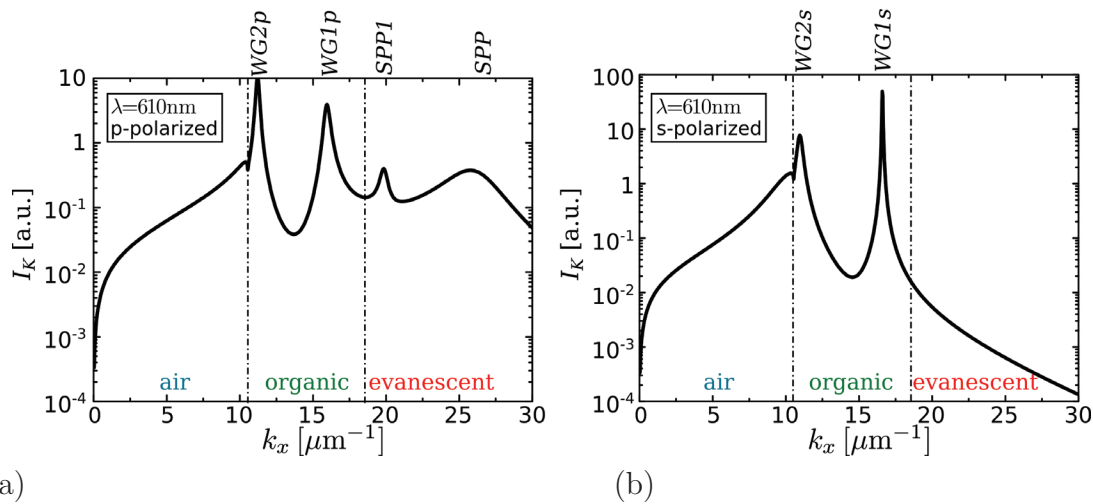


Figure 4.10: Power dissipation spectra I_K as a function of the in-plane wavenumber k_x for p-polarized (a) and s-polarized (b) emission at the peak emitter wavelength ($\lambda_{\text{max}} = 610\text{nm}$). In comparison to the broad, but less intense emission into the external media, intense and confined waveguided modes (WG) are found, together with SPP modes at organic/metal interfaces for p-polarization. Dash-dotted lines represent the air- and organic light-line, emphasizing the corresponding media in which the mode propagates.

Integration of the dissipated power in the three different regimes (air, organics, evanescent) shows that the majority of the dipole power is either dissipated into waveguided modes, or to SPP modes.[80, 150] For the given device architecture, only 15.6 % of the dissipated power is emitted to air (organics: 73.6 %, evanescent: 10.7 %). Even though the power dissipation into waveguided organic modes would decrease for a first cavity order OLED, further analysis have shown that the light extraction into the far-field will remain around 30 % at maximum, assuming isotropically oriented emitters, as the contribution of SPP modes increases.[76, 80] In the following, different techniques to increase the amount of dissipated power into the far-field will be discussed.

4.3.3 Light Outcoupling Techniques

The light extraction efficiency of an OLED structure can be significantly enhanced by extracting or by hindering the excitation of trapped waveguided and SPP modes. Therefore, different light extraction techniques can be applied:

- Macroscopic outcoupling structures
- Random scattering layers
- Periodic scattering layers
- Oriented emitter molecules
- Refractive index modulation

The application of macroscopic outcoupling structures, such as a half-sphere lens [7], microlens foils [7, 182], or pyramidal structures [7, 81] to extract internally trapped light modes, have already been reported, but almost exclusively for bottom-emitting devices. In order to guarantee the penetration of all waveguided organic modes into the outcoupling structure, its refractive index should be at least equal to the refractive index of the organic layers. Hence, total reflection at the interface between the OLED and the structure is avoided. Furthermore, the outer surface of the structure should be shaped in a way that prevents total reflection at the interface to air. Figure 4.11(a) shows a top-emitting OLEDs with an index matched half-sphere lens. Half-sphere lenses are ideal candidates, as all incident light waves propagate perpendicular to the surface, so that no total reflection can occur at the interface to air. Therefore, all light modes which have been previously trapped inside the organic layers can be transferred to air (see Fig. 4.11(b)), while the evanescent SPP modes remain unaffected. In accordance to the previous results, of the OLED structure in Section 4.3.2, the light extraction efficiency η_{out} would reach 89.3 %, as only the SPP modes remain trapped (10.7 %).

However, for top-emitting OLEDs the attachment of such structures requires an enormous experimental effort and often introduces damage to the organic layers. Thus, this method is not preferred for a reliable top-emitting OLED preparation, whereas it is a common technique in bottom-emitting devices which are protected from damage by the substrate.

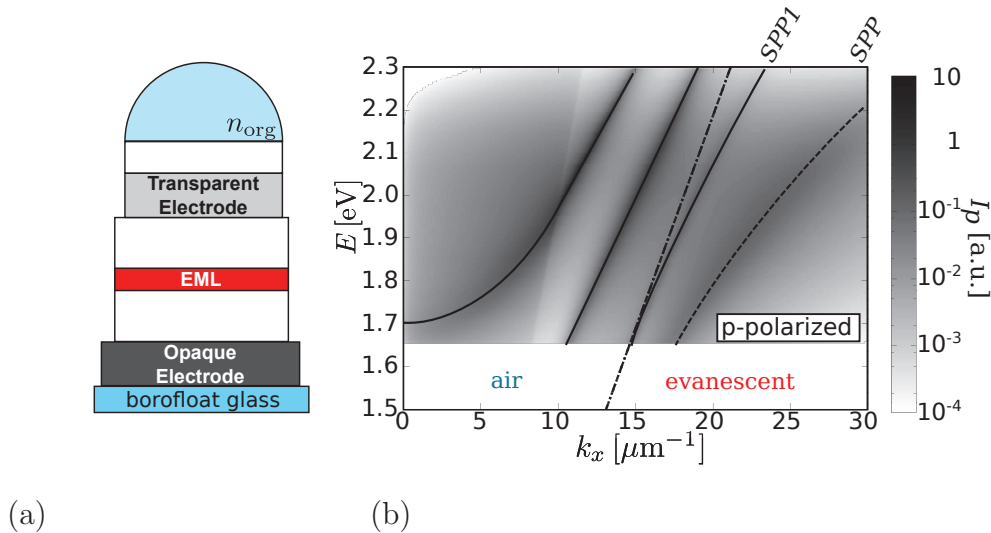


Figure 4.11: Illustration of a top-emitting OLED with an additional half-sphere outcoupling structure, assuming identical refractive index as for the organic layers (a). Power dissipation spectra of a top-emitting OLED with an index matched outcoupling structure (b). As total internal reflection is circumvented at the organic/structure and structure/air interface, no light is trapped in the organic layers and the light extraction efficiency is significantly increased.

The application of scattering structures provides the redistribution of the light modes, according to a modified in-plane wavenumber during the scattering process. This allows to extract light modes from the waveguided or the evanescent regime. Detailed investigations on the scattering process and periodic structures will be given in Section 4.3.4. Random scattering layers, are often preferred for white light applications, as the structural randomness leads to an averaging of the scattering events and the spectral emission, resulting in an angularly color-stable emission. Such scattering layers mostly contain metal oxide nano-particles of significantly higher refractive index than the embedding polymer matrix material, are almost exclusively deposited by wet chemical techniques.[183] Aqueous or organic solvents harm the organic layers, inhibiting an application for top-emitting OLEDs. In addition to this, the polymer matrix materials are often non-conductive, which is unfavorable for an application in the electrically active part of the OLED, e.g. directly on the opaque bottom electrode. Concepts like the deposition of organic materials forming nano-crystalline layers after deposition [184] as well as the application of highly fluorinated, orthogonal solvents [185], which do not resolve the organic layers, hold great promise as new methods to apply random scattering layers to top-emitting OLEDs.

Even without scattering layers or additional outcoupling structures, the light extraction efficiency can be significantly enhanced. Reports on preferentially horizontally aligned emitter molecules have shown that external quantum efficiencies of up to 46.0% can be reached for a planar bottom-emitting OLED, without the need for expensive light extraction structures.[10] The stated EQEs are significantly higher compared to results for isotropically oriented emitters and can be attributed to an avoided excitation of SPP modes. Since SPP modes represent a prominent loss channel in top-emitting OLEDs, this approach can yield significant benefits for these devices, as well. The application of

oriented emitters has an enormous potential in OLEDs, as it is entirely compatible with all OLED architectures and organic materials. Furthermore, the combination of oriented emitters with light extraction structures is supposed to yield in high device efficiencies, as only SPP modes which are then excited in a minor portion will remain inside the devices. Even though, a controlled deposition horizontally aligned highly efficient phosphorescent emitter layers has not been achieved so far, some interesting material candidates have been suggested.[10, 181, 186] Detailed investigations on the orientation of the highly efficient phosphorescent red emitter Ir(MDQ)₂(acac) in an alpha-NPD matrix by Schmidt *et al.* [181] and Flämmich *et al.* [187] have validated a preferential horizontal orientation for this material. Recently, Kim *et al.* [10] showed that the phosphorescent green emitter Ir(ppy)₂(acac) in a TCTA:B3PYMPM matrix is also preferentially horizontally aligned, reaching 30% EQE in a planar bottom-emitting OLED without further light extraction techniques, surpassing the EQE which could be achieved with an isotropically oriented emitter material for this layer stack. Alternatively, a reduction of the refractive index of the organic materials from typically $n \approx 1.8$ is also desirable to increase the amount of extractable light, but has so far often been restricted from insufficient electrical characteristics of such films.[78] For detailed reviews on light extraction techniques, the reader is referred to Brütting *et al.* [150] and Saxena *et al.* [188].

4.3.4 Scattering at Periodic Structures

The application of random scattering layers results in statistically distributed scattering events. Thus, only an averaged convolute of randomly scattered modes would be detected, while the details on the physics of the scattering process are obscured. In contrast, Bragg scattering of light modes at periodic structures allows for a more detailed investigation of the scattering mechanism.

In order to achieve coherent interference of the modes within an OLED, the grating period has to be smaller than the spatial coherence length of the emitted light.[43] The spatial coherence length l_{coh} of a broad emission spectrum can be estimated from the uncertainty principle ($\Delta E \cdot \Delta t \geq \hbar/2$) as:

$$l_{\text{coh}} \geq \frac{1}{2} \frac{\lambda_0^2}{\Delta\lambda} , \quad (4.30)$$

with λ_0 the center, and $\Delta\lambda$ the FWHM of the spectrum. For typical OLED emitters, the PL spectral widths are in the range of 100 nm, which results in coherence lengths of several μm .

Diffraction of light at gratings has been intensively investigated in the past.[43] Based on the *Fresnel-Huygens-principle*, each point of the grating serves as an initial source for new waves, which interfere coherently.[43] In general, the intensity I of two planar electromagnetic waves (\vec{E}_1, \vec{E}_2) interfering with each other is determined by:

$$I = \langle (\vec{E}_1 + \vec{E}_2) \cdot (\vec{E}_1 + \vec{E}_2)^* \rangle = I_1 + I_2 + \langle \vec{E}_1 \vec{E}_2^* + \vec{E}_2 \vec{E}_1^* \rangle \quad (4.31)$$

Assuming planar waves of the type $\vec{E}_i = \vec{E}_{0,i} \exp \left[i(\vec{k}_i \cdot \vec{r} - \omega t + \Delta\varphi_i) \right]$, the expression can be written as:

$$I = I_1 + I_2 + 2\sqrt{I_1 I_2} \cos \left[\underbrace{r(k_1 - k_2)}_{\Delta\Phi} - \Delta\varphi \right]. \quad (4.32)$$

While the simple addition of the initial mode intensities describes the superposition of two non-interfering modes, the third term represents the interference term, determined by the phase difference of both modes. Destructive interference ($\cos[\Delta\Phi] = (2n + 1)\pi$, with integer n) decreases the total intensity or even results in total extinction. Constructive interference ($\cos[\Delta\Phi] = 2n\pi$, with integer n) significantly increases the intensity, even compared to the incoherent superposition of the single modes.

Interference patterns of light diffracted at grating show maximum and minimum intensities according to the path difference of the interfering light waves. For a normal incident electromagnetic wave diffracted at a grating with a period Λ , intensity maxima corresponding to path differences of multiple wavelengths can be found at angles θ_m :

$$\sin(\theta_m) = \frac{m \cdot \lambda}{\Lambda}, \quad (4.33)$$

where m is the diffraction order. In general, the intensity distribution of a planar wave scattered at an object can be calculated from the *Kirchoff diffraction equation*. [43] As the emission spectra of the OLEDs in this work are always measured far away from the diffracting object (*Fraunhofer diffraction*), several simplifications can be made. [43] In the Fraunhofer diffraction limit, the intensity distribution is determined by the multiplication of the initial intensity of the light wave I_0 with the Fourier transformed (FT) representation of the diffracting object. [43] For example, a grating consisting of N rectangularly shaped openings in real space can be represented by a convolution of a single rectangle with a *Dirac comb* (see Fig. 4.12(a)).

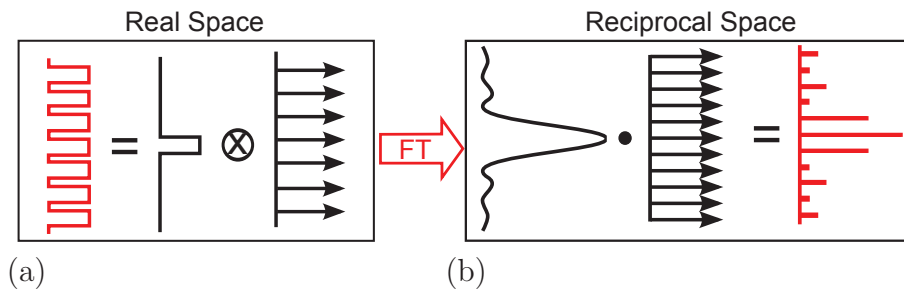


Figure 4.12: Intensity distribution of a light wave diffracted at a rectangular grating in the Fraunhofer diffraction limit. The intensity pattern of the diffracted light wave in reciprocal space is determined by the Fourier transformation of the scattering object.

The Fourier transformed representation of the grating is given by the product of the FT rectangle and the FT Dirac comb (see Fig. 4.12(b)). The FT of the rectangle of width b is given by:

$$F[\text{rect}_b(x)](k) = b \cdot \frac{\sin(\frac{b}{2}k)}{(\frac{b}{2}k)}, \quad (4.34)$$

while the FT of the Dirac comb with a separation Λ again yields a Dirac comb:

$$F[\Delta_{\Lambda}(x)](k) = \frac{1}{\Lambda} \Delta_{1/\Lambda}(k) . \quad (4.35)$$

The reciprocal space intensity distribution of light diffracted at the grating is determined by the product:

$$I(k) = I_0 \cdot [F[\text{rect}_b(x)](k) \cdot F[\Delta_{\Lambda}(x)](k)]^2 = I_0 \cdot \left[b \cdot \frac{\sin(\frac{b}{2}k)}{(\frac{b}{2}k)} \cdot \frac{1}{\Lambda} \Delta_{1/\Lambda}(k) \right]^2 , \quad (4.36)$$

which is schematically shown in Fig. 4.12(b). Note that the dimensions and shape of the grating determine its Fourier transformed representation and therefore the intensity distribution of the scattered light. The FT of a 1D line grating oriented in x-direction is schematically shown in Fig. 4.13.

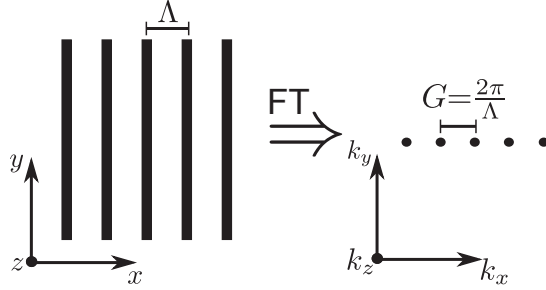


Figure 4.13: 1D grating in real space with a period Λ in x-direction and the Fourier transformed representation of the grating (restricted to 5 points).

Von Laue, who investigated elastic electron scattering at a crystal lattice, described the scattering process by a change of the initial lattice vector \vec{k} by multiples of the reciprocal lattice vector \vec{G} ($|\vec{G}| = 2\pi/\Lambda$) [189]. In analogy to the *Bragg law* [189], scattering processes can be described by the *Laue equation*:

$$\vec{k}' = \vec{k} - m \cdot \vec{G} . \quad (4.37)$$

For a 1D grating with period Λ in x-direction, the equation simplifies to the in-plane wavenumbers k_x of the Bragg scattered modes:

$$k'_x = k_x - m \cdot |\vec{G}| , \quad (4.38)$$

where k'_x is the in-plane wavenumber after the scattering event and m the scattering order. The scattering order m can be any real number, which also includes the scattering into higher in-plane wavenumbers, which is undesirable for light extraction. The Laue equation (Eq. 4.38) indicates that for sufficiently large reciprocal lattice numbers G or sufficiently high scattering orders m , internally trapped light modes of a planar device ($k_x > k_0$), can be outcoupled by Bragg scattering ($k'_x < k_0$). Using the analogue relation of k_x to the propagation angle θ ($k_x = |\vec{k}| \cdot \sin(\theta)$), scattered light modes propagating at angles smaller than the angle of total internal reflection ($\sin(\theta') < \sin(\theta_{\text{org}}^{\text{crit}})$) are extracted into air.

Rigneault *et al.* [190] have shown that for a small perturbation of weak microcavities by a shallow grating, where the grating depth h_Λ is much smaller than the optical thickness of the device d_{opt} , that the positions and dispersions of Bragg scattered modes can be determined from a planar unperturbed reference device with identical layer architecture. As long as the prediction of a weak perturbation is fulfilled, Bragg scattered modes in corrugated OLEDs can be identified using the power dissipation spectrum of the planar reference, whereas the Bragg scattered modes are obtained from the Laue equation according to:

$$k'_{x,\text{corrugated}} = k_{x,\text{planar}} - m \cdot G \quad (4.39)$$

In Fig. 4.14, the determination of the Bragg scattered mode positions in the wave vector diagram is shown for a 1D grating in x-direction and with a reciprocal lattice vector $|\vec{G}| = 2\pi/\Lambda = 2\pi/0.8\mu\text{m}$ for the top-emitting OLED structure investigated in Section 4.3.2.

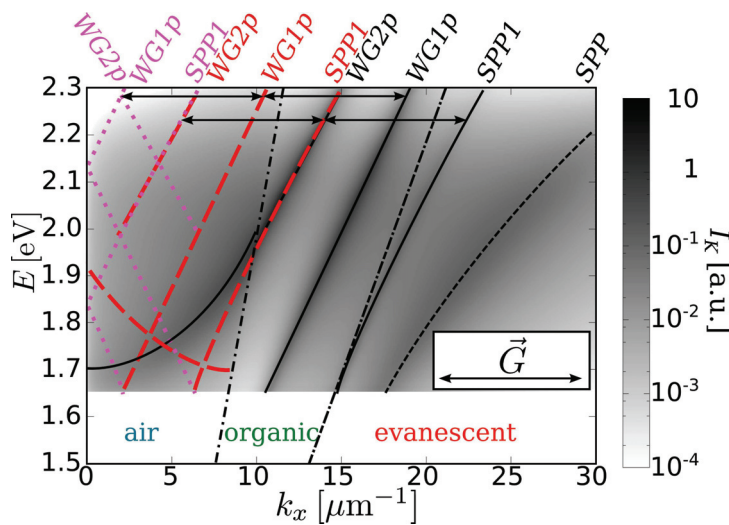


Figure 4.14: Determination of Bragg scattered modes in a corrugated red top-emitting OLEDs on a periodic 1D grating with a reciprocal lattice vector \vec{G} for the 1st (red compact lines) and the 2nd (purple dotted lines) scattering order. According to Rigneault *et al.* [190], the scattered light modes can be obtained from a planar reference, applying the Laue equation. Internal light modes can be scattered into the air light-cone, increasing the light extraction efficiency.

For the 1st Bragg scattering order $m = 1$ (Fig. 4.14), the scattered WG and SPP1 modes are partially scattered into the air light-cone, which allows to extract light from these modes. For higher Bragg scattering orders, e.g. the second order, additional modes are transferred into the air light-cone. For better visualization, neither higher scattering orders, nor scattering to higher in-plane wavenumbers are included in Fig. 4.14. The spatial symmetry of the system allows to limit the investigations exclusively to positive in-plane wavenumbers and implies a mirroring of propagating modes at the $k_x = 0$ axis. In order to calculate the efficiency enhancement from the Bragg scattered modes, the dissipated power of all modes inside the air light-cone has to be determined.

As already discussed for the intensity distribution of a light wave diffracted at an object, the dissipated power of the modes is strongly dependent on the grating itself as well as on

the interference of the contributing modes. For top-emitting OLEDs under investigation in this thesis, an *a priori* prediction of the dissipated power by the Bragg scattered modes inside the air light-cone is challenging. This is due to uncertainties of device parameters as well as the lack of a suitable model to calculate the power dissipation spectra of corrugated OLEDs, e.g. the intensities of the scattered modes, respecting all effects of the corrugation on the emitting dipoles inside the microcavity. Furthermore, the prediction for a weakly perturbed device by Rigneault *et al.* [190] has been found for a dielectric waveguide with weak cavity effects, which might not be given for top-emitting OLEDs. The validity of this assumption has to be tested with planar reference devices produced together with the corrugated top-emitting OLEDs.

4.3.5 State-of-the-art Corrugated OLEDs

The application of outcoupling techniques, e.g. macroscopic outcoupling structures [7, 81, 191] or nano-particle scattering layers [192, 193] are widely established for bottom-emitting OLEDs. There, the outcoupling structures are either placed on the other side of the glass substrate [194–196] or between substrate and the transparent conductive electrode [183, 192, 197], often over-coated with a planarization layer. In these cases, the preparation of the outcoupling layer does not affect the OLED processing or the electrical performance compared to devices without outcoupling layer.

The application of periodical gratings or photonic crystals with periodicities in a range of several hundred nanometer to a few μm have also been reported. Periodically corrugated bottom-emitting OLEDs on top of corrugated photoresist layers showed efficiency enhancements by approximately a factor of 2 to 4, compared to a non-corrugated reference device.[198–200] Even though the reported enhancement factors of corrugated bottom-emitting OLEDs are impressive, the overall device efficiency often remains lower than for state-of-the-art planar devices.[193, 199, 201] Compared to bottom-emitting OLEDs, corrugated top-emitting OLEDs could further benefit from a stronger contribution of outcoupled SPP modes.[202–204]

However, reports on top-emitting OLEDs, either on corrugated substrates [201, 205] or with attached outcoupling structures [182, 206, 207], are rare. On the one hand, no planarization layer can be used for an outcoupling structure underneath the opaque metal electrode, when its scattering properties shall be exploited. This often implies critical electrical operation conditions due to local electrical shorts. On the other hand, potential mechanical damage or material resolving limits the application most outcoupling techniques after the organic layer deposition.

In most reports on corrugated OLEDs, a strong change of the electrical characteristics is observed when the corrugation is introduced.[193, 199, 200] This suggests that not only the light extraction efficiency, but also the internal quantum efficiency is affected. Therefore, the observed efficiency enhancements might be caused by an enhanced internal quantum efficiency and do not necessarily originate from an improved light outcoupling. Table 4.1 summarizes published work concerning white top-emitting OLEDs with additional light outcoupling structures. Canzler *et al.* [184] successfully used an organic ETL material with a tendency to crystallize after evaporation, in order to extract the internal light modes. Scattering at these irregular micro-crystals enhances the efficiency and luminous efficacies higher than 30 lm/W have been achieved. Freitag *et al.* [137] exchanged the metallic top electrode by a CNT sheet to increase the angular stability of the emission

and to enhance the efficiency by light scattering. Unfortunately, parasitic resistances between the electrode and the organics reduce the overall device efficiency. Thomschke *et al.* [182] managed to attach a microlens foil on a top-emitting OLED, which successfully improved the angular color-stability and the device efficiency, surpass 30 lm/W. Unfortunately, the device yield was dramatically low.

Table 4.2: Literature review on white top-emitting OLEDs with additional light outcoupling techniques.

1st Author	Year	Efficiency		Technique
		EQE [%]	LE [lm/W]	
Canzler[184]	2011	28.8*	36.5*	organic scattering material
Freitag[137]	2012	1.46*	0.2*	carbon nanotube top electrode
Thomschke[182]	2012	26.8 ⁰	30.1 ⁰	laminated microlens foil

Symbols: ⁰ at 1000 cd/m², * peak value

In summary, the main challenges for realizing highly efficient corrugated top-emitting OLEDs are:

- Prevent damage to the organic layers
- Maintain a stable electrical operation
- Conserve the internal quantum efficiency
- Optimize the top-emitting OLED ↔ grating system

While the conservation of the mechanical and electrical stability of the top-emitting OLEDs is obvious, the maintaining of the internal quantum efficiency is crucial in order to evaluate the enhancement of the light extraction efficiency η_{out} , as only the EQE of the top-emitting OLED can be measured.

In Chapter 8 and 9 investigations on the light extraction enhancement of state-of-the-art top-emitting OLEDs, which accomplish the challenges of corrugated devices, are shown.

5 Experimental Methods

This chapter provides details about the OLED and light outcoupling structure fabrication, including the applied materials. Furthermore, the experimental setups are described, which are used to characterize OLEDs and electrodes. Finally, the investigation of the surface topography of the light outcoupling structures with atomic force microscopy is discussed.

5.1 Sample Fabrication

This section describes the fabrication of the different sample types. *Physical vapor deposition* (PVD) of the materials from a crucible is used for the fabrication of small molecule organic- and thin-film metal electrode layers. Corrugated light outcoupling structures are produced by *photolithography* or *nanoimprint lithography* of *photoresist* layers.

5.1.1 OLED and Electrode Fabrication

All organic materials used in this work are based on small molecules. In contrast to polymers, which are typically deposited by wet chemical techniques, these materials are deposited by PVD at ultra high vacuum (UHV) conditions with base pressures in the range from 10^{-5} to 10^{-10} mbar. The metal electrodes are also thermally evaporated. Co-evaporation of materials is used for the preparation of doped layers, e.g. EML, ETL, and HTL. In Fig. 5.1 a very simple OLED preparation setup is shown, which incorporates all necessary components for OLED manufacturing. In order to prepare layers with thickness precision on the nanometer scale, quartz crystal monitors control the layer thickness and deposition rate (0.1 to 2 Å/s). Shutter blades prevent unwanted material deposition on the substrate. Shadow masks are applied to define the active area of the OLEDs ($A = 6.76 \text{ mm}^2$) as well as the shape of the electrodes. Here, a sample layout with 4 OLED pixels on a 1×1 inch substrate is used (see Fig. 5.2).

All samples are fabricated in a single chamber tool (Kurt J. Lesker Company), allowing to fabricate 36 1×1 inch substrates in parallel. Furthermore, adjustable blades can be used to vary thicknesses of specific layers, in order to perform systematic investigations of layer thickness dependencies on the OLED performance, while all further parameters remain comparable. To protect the devices from oxygen, moisture, and mechanical damage, the OLEDs are encapsulated with a glass lid, glued by an epoxy resin (XNR5590, Nagase Europa GmbH) directly after the layer deposition in a nitrogen atmosphere. Hence, the complete layer deposition and encapsulation process is handled without oxygen or water contamination.

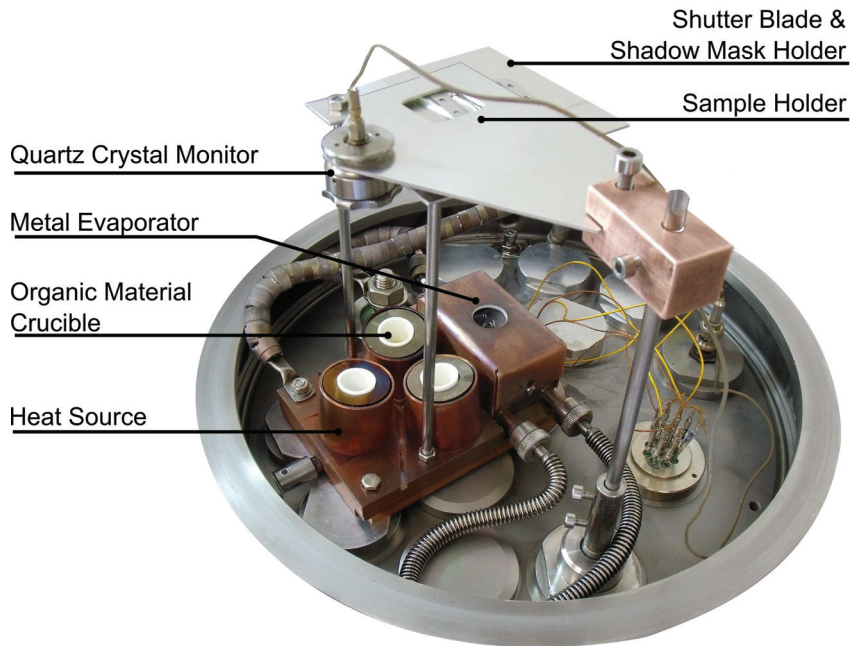


Figure 5.1: Custom-built PVD deposition tool for OLEDs*. Materials in the crucibles are thermally evaporated and deposit on a substrate. Deposition rate and thickness are detected by quartz crystal monitors. Shutter blades and shadow masks are used to prevent unintended material deposition and to define the layout. * “Die Sendung mit der Maus” TV broadcast setup (IAPP, 2011).

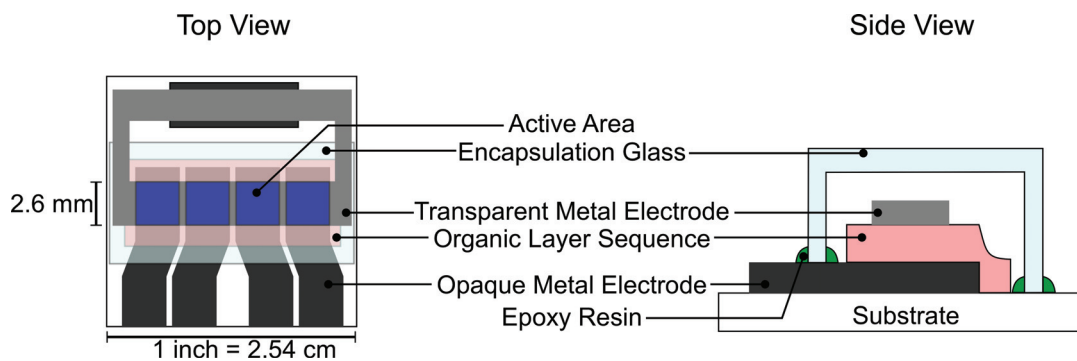


Figure 5.2: Sample layout of the 1×1 inch substrates, defined by shadow masks. Four identical OLED pixels per substrate allow for statistical data evaluation.

5.1.2 Light Outcoupling Structure Preparation

Investigations on the extraction of trapped light modes are performed on periodically corrugated substrates. In principle, all techniques which are able to generate strictly periodic surfaces with low roughness, covering the active area A of the OLEDs can be applied, as the OLED processing is completely independent from the structure preparation.

In this work, different techniques based on the treatment of photoresist layers, which are sensitive to the exposure with blue or UV light, are applied. On the one hand, photolithography is used to transfer the desired grating pattern by light exposure from a photomask into the photoresist. On the other hand, nanoimprint lithography with a master stamp carrying the corrugation pattern is applied to transfer the corrugation into a wet pristine photoresist layer.

In Fig. 5.3, the fabrication steps to create a pattern by photolithography are shown. After spin coating and pre-baking of the photoresist on a hot plate for 1 min at 110 °C, the photomask is aligned with the substrate. The photomask carries the desired corrugation pattern in form of opaque and non-opaque regions for the exposure light, comparable to a shadow mask. In this work, the maskless UV exposure system *SF-100 Extreme* (Intelligent Micro Patterning LLC) with a mercury lamp as light source is used. The exposed regions of the resist are chemically modified and form either soluble (*positive*) or insoluble (*negative*) compounds for a *developer* solution. After a post-bake procedure at a hot plate for 1 min at 110 °C, the exposed photoresist is developed and the soluble regions are removed.

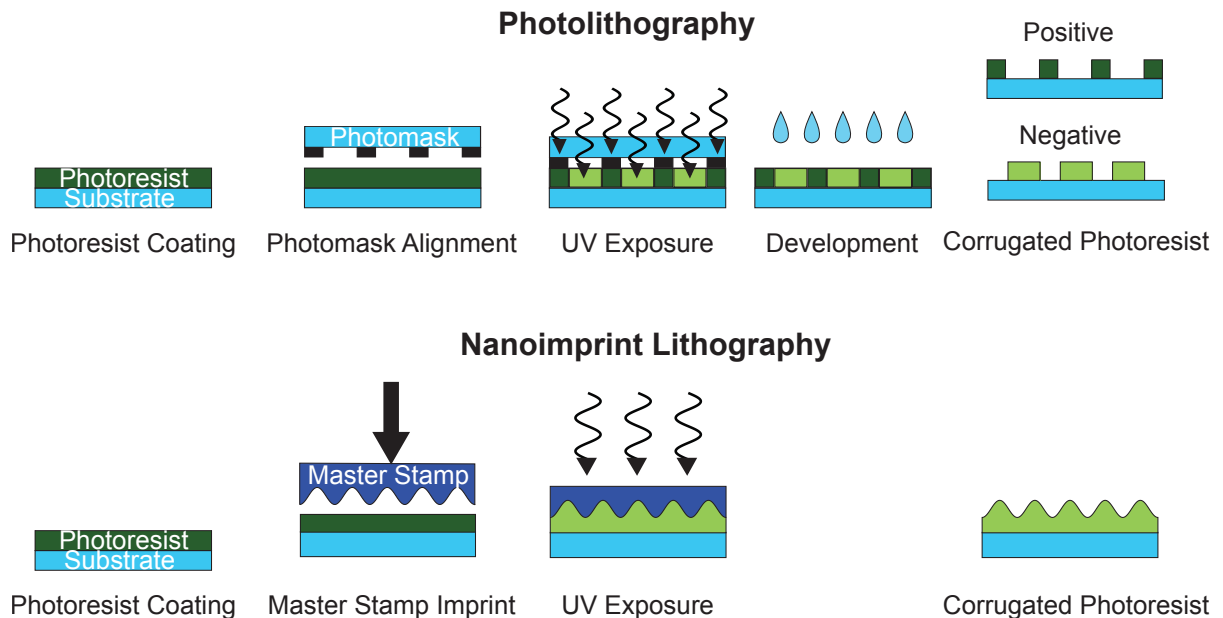


Figure 5.3: Fabrication sequences of corrugated photoresist layers for photolithography and nanoimprint lithography. Photolithography yields corrugated layers after the exposure and development of a photoresist layer. Nanoimprint lithography instead introduces the corrugation by a master stamp, which is pressed into a pristine photoresist layer. Light exposure of the resist preserves the corrugation.

Hence, a positive resist produces a perfect copy of the photomask, while a negative resist gives the negative image. Often, the structured photoresist layer is only used to transfer the structure from the photomask to a target material, which is then finally structured by *etching* or *lift-off* procedures. An etching procedure removes the regions of the target material, which are not covered with photoresist, whereas lift-off removes the photoresist layer after the deposition of the target material on top, which is then withdrawn. Even though photolithography is applied for decades in micro-electronics, many parameters have a significant influence on the patterning of the resist, as well as on the lift-off or etching quality of the target material.

The fabrication of corrugated structures by nanoimprint lithography is also shown in Fig. 5.3. A master stamp carrying the desired corrugation is pressed into a spin coated photoresist layer. With the attached master stamp on top, the photoresist is cured with light from a high pressure mercury lamp (Solimed GmbH). There, the photoresist forms a solid layer, which conserves the corrugation. Compared to photolithography, nanoimprint is simple and demands fewer processing steps. Furthermore, the requirements on the experimental setup in order to obtain high quality sub- μm corrugation patterns are less strict. Experimental results on the different patterning techniques are presented in Section 8.1.

5.2 Investigated Materials

In the following, the materials used for OLED and corrugation fabrication are provided. Note that in the body text only abbreviations are used, while the chemical names of the organic compounds are given in the List of Abbreviations.

5.2.1 Organic Small Molecule Compounds

All OLEDs in this work are build according to the pin-concept described in Section 3.3.1. Therefore, doped charge transport layers, charge blocking layers, and emission layers are incorporated in the devices. In Table 5.1, all applied organic compounds are listed regarding their functionality. Furthermore, the energy levels of HOMO and LUMO are given.

For hole transport layers (HTLs), the matrix materials MeO-TPD and Spiro-TTB are co-evaporated with the organic p-dopant F6-TCNNQ. Electron transport (ETL) is guaranteed by a cesium (Cs) doped BPhen layer. To reach desired transport layer conductivities in the range of 10^{-5} S/cm, 2-4 wt.% of F6-TCNNQ, but almost 50 mol.% of Cs are required [208]. Blocker materials are applied to confine the charge carriers and excitons in the EML. Hole blocking materials (HBL) are Spiro-TAD, NPB, and TCTA, while TPBi, BAlq₂, and BPhen are used as electron blockers (EBL).

For white emission, up to four different emitters are used, almost covering the entire visible spectral range. Blue emission is generated from the fluorescent emitter systems MADN doped with TBPe (1 wt.%), and the bulk emitter 4P-NPD. Green, yellow, and red emission is generated by host-guest systems with Ir-based phosphorescent dopants. For red emission, Ir(MDQ)₂(acac) is doped with 10 wt.% into NPB. Ir(dhfp_y)₂(acac) (yellow) and Ir(ppy)₃ (green) are doped into TCTA and TPBi with doping concentrations in the range of 1-8 wt.%.

Table 5.1: Summary of the organic compounds and the according energies of HOMO and LUMO level*. All compounds have been thermally evaporated.

Material Type	Short Name	HOMO [eV]	LUMO [eV]	Comment
Hole Transporter	MeO-TPD	-5.1	-1.9	matrix
	Spiro-TTB	-5.0	-1.9	matrix
	F6-TCNNQ	-7.8	-5.4	organic p-dopant
Electron Blocker	Spiro-TAD	-5.4	-2.3	-
	NPB	-5.4	-2.6	also red host
	TCTA	-5.3	-2.7	also green & yellow host
Fluorescent Emitter	4P-NPD	-5.7	-2.3	bulk blue emitter
	MADN	-5.6	-2.6	blue host
	TBPe	-5.3	-2.3	blue dopant
Phosphorescent Emitter	Ir(ppy) ₃	-5.1	-2.4	green dopant
	Ir(dhfpv) ₂ (acac)	-5.1	-2.4	yellow dopant
	Ir(MDQ) ₂ (acac)	-5.4	-2.8	red dopant
Hole Blocker	TPBi	-6.3	-2.8	also green & yellow host
	BPhen	-6.5	-2.9	-
	BAIq ₂	-6.1	-3.2	-
Electron Transporter	BPhen	-6.5	-2.9	matrix, cesium doped

* HOMO and LUMO values taken from Hofmann [88] and Thomschke [209].

5.2.2 Electrode Materials

The opaque bottom electrode of top-emitting devices consists of 40 nm Ag on top of 40 nm Al, directly deposited on the substrate. In bottom-emitting reference devices, 100 nm of Al are used as opaque top electrode. Transparent top electrodes are formed by thin metal films of Ag. For the optimization of the Ag top electrode performance wetting layers of Au or MoO₃/Au are applied (see Chapter 7). A 90 nm thick ITO layer on a 1.1 mm thick borofloat glass substrate (Thin Film Devices Inc.) is applied as transparent bottom electrode in bottom-emitting reference devices. The work functions of all investigated electrode materials are summarized in Table 5.2.

Table 5.2: Summary of the electrode materials and their work functions. Except for ITO, all materials have been thermally evaporated.

Material	Work function [eV]	Comment
Al	4.3 [209]	opaque electrodes
Ag	4.3 [209]	opaque and transparent electrode
Au	5.1 [209]	Ag wetting layer
MoO ₃	5.4 [165]	Ag wetting layer
ITO	3.7 - 4.7 [209]	TCO, bottom electrode

Even though top-emitting OLEDs do not require a transparent or stiff substrate, borofloat glasses (Thin Film Devices Inc. and Corning Inc.) are used as laboratory standard substrate, here.

5.2.3 Lithography Materials

Light outcoupling structures are fabricated from spin coated photoresist layers. The positive photoresist ma-P 1210 (Micro Resist Technology GmbH) as well as the negative resist AZ nLOF 2020 (Micro Chemicals GmbH) have been investigated in photolithography. In order to vary the photoresist thickness, PGMEA (Sigma Aldrich Co.) is used as diluter for both resists. Photoresist developer materials are either based on TMAH or NaOH, in order to remove the soluble resist after exposure.

The obtained structure in the photoresist can be transferred into metal films either by etching or lift-off procedures. For wet chemical etching of Al and Ag films, often mixtures of different acids are applied. Here, HNO₃:HCl diluted in de-ionized water (1:1:1) has been used. The HNO₃ oxidizes the metal surface, while HCl dissolves the oxidized material. Gold films have been etched with a selective gold etchant provided by Sigma Aldrich Co. After the etching procedure, the residual photoresist has been removed with acetone. Nanoimprint lithography has also been applied for both photoresists. All materials used for the lithography processing are summarized in Table 5.3.

Table 5.3: Materials for light outcoupling structure fabrication via photolithography.

Material Class	Short Name	Comment
Photoresist	AZ nLOF 2020	negative resist
	ma-P 1210	positive resist
	PGMEA	diluter for both photoresists
Developer	TMAH	for AZ nLOF 2020
	ma-D 331	for positive resist, contains NaOH
	ma-D 533s	for positive resist, contains TMAH
Remover/Stripper	Acetone	for both photoresists
Etchants	Gold Etchant	selective gold etchant (Sigma Aldrich Co.)
	HNO ₃ :HCl:H ₂ O	aluminum and silver etchant

5.3 Characterization Methods

In order to comprehensively characterize OLEDs, the electrical and the emission characteristics have to be investigated (Section 5.3.1). Transparent thin-film metal electrodes are evaluated regarding transmittance, sheet resistance, and metal growth (Section 5.3.2). Light outcoupling structures are mainly characterized regarding the surface topography. Therefore, *atomic force microscopy* (AFM) measurements have been performed (Section 5.3.3).

5.3.1 Characterization of OLEDs

Current-Voltage-Luminance Measurement

The electrical performance of OLEDs is characterized with a source measure unit (SMU-2400, Keithley Instruments Inc.), which supplies a defined voltage V and detects the current I through the device. Simultaneously, the electroluminescence signal in normal direction to the sample surface ($\theta = 0^\circ$) is detected with a Si-photodiode. Intensity and wavelength calibrated spectral radiance $L_R(\lambda, 0)$ is measured for fixed currents with a CCD spectrometer (CAS 140 CT, Instrument Systems GmbH). Furthermore, the CCD spectrometer is used to calibrate the photodiode signal, which allows for the calculation of the forward luminance $L_P(0)$ for each applied voltage and yields the current-voltage-luminance (I-V-L) curve of the OLEDs.

This characterization is performed at a measurement robot (IVL-robot) with a movable sample tray, which provides a software controlled characterization of up to 36 1×1 inch samples.

Angular Dependent Emission Characterization

The angular dependent emission characteristics are determined with a software controlled spectro-goniometer custom-made by Simone Hofmann at the IAPP (see Fig. 5.4). There, the OLED is mounted on a tray, which rotates the sample in front of a fixed optical fiber connected to a CCD spectrometer (USB4000, Ocean Optics). For OLED power supply, a SMU-2400 is used. It is worth to mention that a calibration laser is used to align the rotating OLED on the optical axis with the spectrometer.

The angular resolved spectral irradiance $E_R(\lambda, \theta)$ of planar samples is measured with a step width $d\theta$ of 5° and covers the angular range θ from 0° to 90° . OLEDs containing a light outcoupling structure are additionally characterized with a step width $d\theta$ of 1° in s- and p-polarization, including a polarization filter (PGT 5010, Casix Inc.) in front of the optical fiber. If not stated otherwise, light outcoupling structures are oriented perpendicular to the rotation plane (cf. Fig. 5.4) to investigate the scattering effects on the emission.

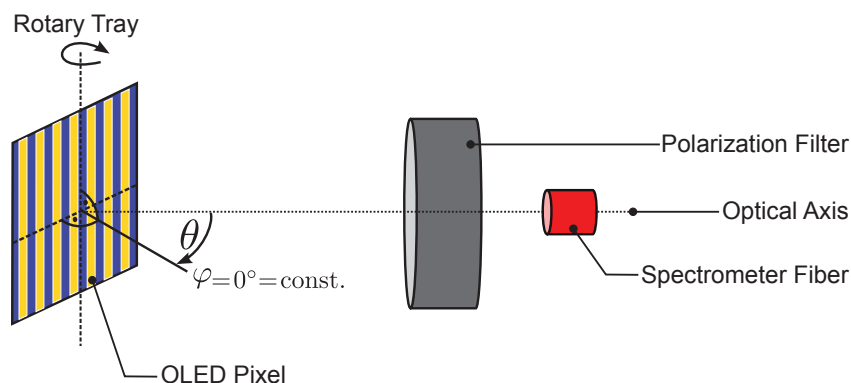


Figure 5.4: Schematic illustration of the spectro-goniometer, which is used to characterize the angular resolved emission of OLEDs $E_R(\lambda, \theta)$. Polarization dependent measurements are performed for corrugated substrates, where 1D gratings are aligned perpendicular to the rotational plane.

Efficiency Measurement

The OLED efficiency is evaluated regarding the external quantum efficiency η_{EQE} and the luminous efficacy η_{LE} . While the EQE is defined as the ratio between the number of extracted photons n_{Ph} to the number of injected electrons n_e , the LE gives the ratio between the emitted luminous flux Φ_{P} and the consumed electrical power P_{el} of the OLED in the solid angle Ω .

For the calculation of the EQE, the number of photons can be deduced from the spectral radiance $L_R(\lambda, \theta)$, or spectral radiant intensity $I_R(\lambda, \Omega)$ divided by the photon energy. Furthermore, the number of injected electrons is correlated to the injected current I , which yields:

$$\eta_{\text{EQE}} = \frac{n_{\text{Ph}}}{n_e} = \frac{e}{I} \int_{\lambda} \int_{\Omega} \frac{\lambda}{hc} I_R(\lambda, \Omega) d\lambda d\Omega \quad (5.1)$$

The luminous flux Φ_{P} of the OLED can also be calculate from the spectral radiant intensity $I_R(\lambda, \Omega)$, according to the correlation between radiometric and photometric parameters (see Section 3.4.1). The consumed power is given by the product of the injected current I and the applied potential V . Therefore, the LE can be calculated by:

$$\eta_{\text{LE}} = \frac{\Phi_{\text{P}}}{P_{\text{el}}} = \frac{1}{VI} \int_{\lambda} \int_{\Omega} K_m V(\lambda) I_R(\lambda, \Omega) d\lambda d\Omega \quad (5.2)$$

The efficiency of OLEDs can be accurately determined with an *integrating sphere* setup (LMS-100, Labsphere Inc.). There, the OLED is mounted inside a completely white coated sphere (see Fig. 5.5). Diffuse diffraction of the emitted light at the white surface allows to detect the full solid angle emission of the sample with an attached spectrometer (CDS-600, Labsphere Inc.). Emission from substrate edges and the backside has to be shielded, e.g. by a sample holder, to neglect a contribution to the detected emission.

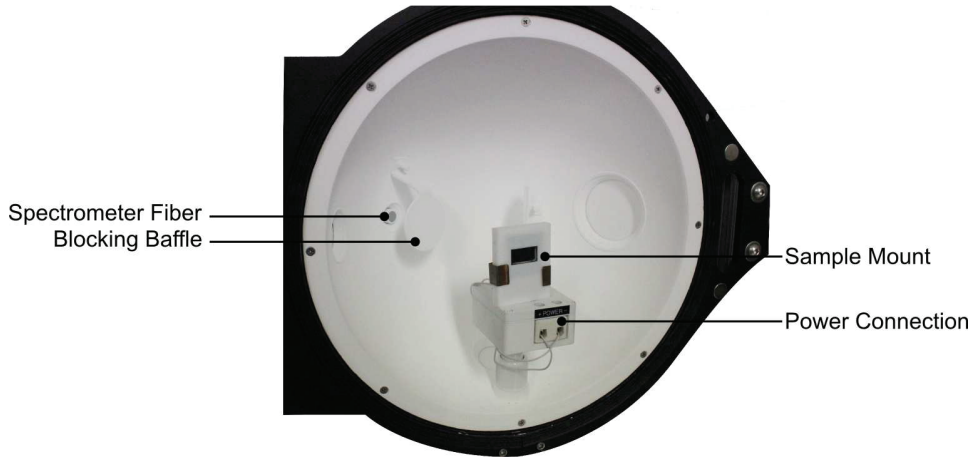


Figure 5.5: Image of the integration sphere setup to measure the efficiency of OLEDs. The OLED emission is diffracted at the white surface, and the full solid angle emission is detected with an attached spectrometer in a single measurement.

A SMU-2400 is used as power supply for the OLED. For the investigations of light out-coupling structures, all devices are characterized using the integrating sphere. Another distinct method to calculate the efficiency of planar OLEDs is based on the evaluation

of the angular dependent emission spectra from the goniometer setup. For planar samples without any preferred orientation, symmetry considerations simplify the efficiency calculation regarding the solid angle integration $d\Omega$, especially in spherical coordinates. On the one hand, the OLED emission is assumed to be independent of the polar angle φ (cf. Fig. 5.4). On the other hand, the emission with respect to the azimuthal angle θ is symmetric ($I_R(\theta) = I_R(-\theta)$), which reduces the azimuthal integration from 0 to $\pi/2$. Therefore, the EQE and LE can be calculated from the measured angular irradiance spectra $E_R(\lambda, \theta)$ according to:

$$\begin{aligned}\eta_{\text{EQE}} &= \frac{2\pi e}{hcI} \int_{\lambda} \int_0^{\pi/2} \lambda F(\lambda) E_R(\lambda, \theta) \sin \theta d\lambda d\theta \\ \eta_{\text{LE}} &= \frac{2\pi K_m}{VI} \int_{\lambda} \int_0^{\pi/2} V(\lambda) F(\lambda) E_R(\lambda, \theta) \sin \theta d\lambda d\theta \\ F(\lambda) &= \frac{I_R(\lambda, 0)}{E_R(\lambda, 0)}\end{aligned}\tag{5.3}$$

introducing the calibration factor $F(\lambda)$ for the goniometer spectra. The current dependent efficiency can either be directly calculated from respective spectral emission measurements for each current, or from the I-V-L characteristics. The latter can only be applied if the angular dependent emission does not alter for different currents and if the spectral shape is preserved. Especially for white light emitting OLEDs, the second requirement is not always fulfilled, as a shift of the recombination zone with the current and differential quenching of the emitters could induce a change of the spectral shape. In this work, the efficiency-current dependencies are determined from the I-V-L curve, as prominent shifts of the spectral emission with the current have not been detected.

Calculation of the Angular Color-Stability in the CIELAB Space

As discussed previously, microcavity effects lead to an angularly dependent spectral emission from top-emitting OLEDs and therefore to a change of the perceived color with the observation angle θ (see Section 4.2.1). Figure 5.6 illustrates the angular color-shift of a white top-emitting OLED employing a 15 nm thick standard silver top electrode in the CIExy space. The angular color-shift of an OLED is calculated in the CIELAB space, as it provides the highest homogeneity of all color spaces regarding the perception of color differences (see Section 3.4.4).

The distance between two points can be easily determined from the *Euclidean distance*. However, the *CIE-DE2000* metric provides a more reliable calculation metric of the color distance and is applied here, as further corrections enhancing the uniformity of the CIELAB space are introduced.[136, 210] For further details on the implementation of lightness, chroma, hue and hue rotation corrections by the CIE-DE2000 metric, the reader is referred to Sharma *et al.*[210] and Luo *et al.*[136].

In order to calculate the angular color-shift ΔCIE of an OLED, the distance between the initial color point in normal direction $\theta = 0^\circ$ ($\vec{v}(0)$) and the color point at each observation angle θ ($\vec{v}(\theta)$) is evaluated. Furthermore, the velocity of the color change, calculated from the numerical derivative for a single angular step $d\theta$, is taken into account.[211]

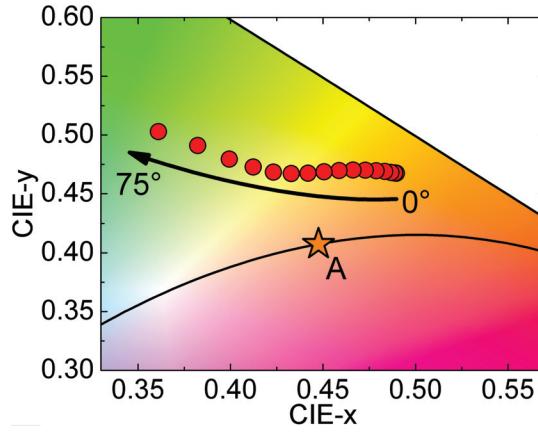


Figure 5.6: Angular dependency of the color coordinates of a white top-emitting OLED in the CIE xy space.

Finally, the angular color-shift ΔCIE is given by [154]:

$$\begin{aligned} \Delta CIE &= \int_{\theta} f[\vec{v}(\theta)] d\vec{v}(\theta) = \int_{\theta} f[L^*(\theta), a^*(\theta), b^*(\theta)] d\vec{v}(\theta) \\ &= \int_{\theta} \|(\vec{v}(\theta) - \vec{v}(0))\| \cdot \left\| \frac{d\vec{v}(\theta)}{d\theta} \right\| d\theta \end{aligned} \quad (5.4)$$

The first term represents the distance between the color points, while the second term represents the velocity of the color-shift. The obtained measure of ΔCIE cannot be threatened as an absolute number, as the angular step size $d\theta$ as well as the integration range of θ have a significant influence on the absolute number. Instead, the relative angular color-shift in comparison to a reference device, which has been evaluated for identical step size $d\theta$ and integration range, will be given.

5.3.2 Transparent Metal Electrode Characterization

Transmittance and Reflection Characterization

The transparent thin-film metal electrodes are characterized regarding spectral transmittance $T(\lambda)$ and reflection $R(\lambda)$. Therefore, a white light source (Ava-Light-DH-S-Bal, Avantes BV) with an attached optical fiber illuminates the electrodes under normal angle. Transmitted and reflected light are also detected under normal angle by optical fibers attached to CCD spectrometers (CAS 140 CT, Instrument Systems GmbH and Reflection-Measurement-System, Optische Messtechnik GmbH). The spectral transmittance $T(\lambda)$ is calculated from the ratio between the spectra without ($I_0(\lambda)$) and with the sample in the light path ($I(\lambda)$):

$$T(\lambda) = \frac{I(\lambda)}{I_0(\lambda)} \quad (5.5)$$

For the spectral reflection $R(\lambda)$, an opaque aluminum sample with precisely characterized reflection is used as reference and $R(\lambda)$ is calculated in analogy to the spectral transmittance.

Sheet Resistance Measurements

The sheet resistance R_S of the electrodes is measured with a four-point-probe measurement stand (S 302-4, LucasLabs). In the four-point-probe layout, separated source and sensing probe pairs are used.[212] This allows to neglect the influence of the parasitic probe and spreading resistances on the measurement, which improves the accuracy especially for low sheet resistances.

A current I is supplied through the outer source probe pair and a voltage drop occurs in the electrode according to Ohm's law ($V = RI$). The sensing electrodes are linearly positioned between the source electrodes. They measure the voltage drop V in the sample with a high impedance voltmeter. Hence, an almost current free voltage measurement with negligible contributions of the parasitic resistances is performed. The sheet resistance R_S is calculated, respecting a stated geometry factor F depending on the probe layout [213], according to:

$$R_S = F \cdot \frac{V}{I} \quad (5.6)$$

Here, the supplier states a geometry factor of $F = 4.4$ for the $20 \times 20 \text{ mm}^2$ sample size used in the experiments.

Metal Growth Investigations by Scanning Electron Microscopy

The transparent metal electrodes are further characterized by scanning electron microscopy (SEM) to investigate the metal growth and film coverage on organics and wetting layers (Ultra 40 & Ultra 55, Carl Zeiss AG). Here, a focused electron beam is scanned over the sample, which yields resolutions down to 1 nm.[214]

Primary electrons (PE) are emitted from a filament and accelerated by electric potentials in the kV-regime. The incident PE beam interacts with the sample, e.g. leading to the emission of Auger electrons and *secondary electrons* (SE) from the sample material. Elastic and inelastic scattering of the PE (reflected electrons, RE) can occur as well, resulting in a teardrop shaped interaction volume of the PE beam in the sample.[215] Furthermore, luminescence and X-ray emission of the sample can also be generated.[215] In this work, SE signals ($E_{SE} < 50 \text{ eV}$) are investigated, as they have a high surface sensitivity, determined by a low mean escape depth of approximately 1 nm in metals, and a high resolution of the signal, as most of the SEs are generated at the impact point of the PE beam.[214]

5.3.3 Corrugation Characterization via Atomic Force Microscopy

Preliminary characterizations of the fabricated light outcoupling structures are performed with an optical microscope (Jenaval, Carl Zeiss AG), which has a sufficient solution to distinguish separated line structures with periods in the desired μm range. The topography of the surface is determined from AFM measurements (Combiscope 1000, Aist-Nt Co.).[216] AFM provides spatial resolutions in the nanometer range, while accessing scan areas of several μm^2 . Furthermore, also non-conductive materials can be imaged without further treatment, in contrast to SEM measurements. Here, a cantilever containing a tip with a radius of only a few nanometer is scanned over the sample surface to sense the

surface topography. In order to minimize a potential tip induced damage to the light out-coupling structure, the measurements in this work are performed in *tapping mode*. [217] There, the cantilever is excited at its resonant frequency and oscillates with an amplitude of approximately 100 nm, getting in close proximity to the surface. During the scan, varying forces between surface and tip (van der Waals, electrostatic, dipole-dipole interaction, etc.) perturb the cantilever oscillation, determined by an alternating surface topography. A feedback loop compensates the cantilever perturbation and calculates the sample topography. For a detailed review on AFM measurements, the reader is referred to Giessibl [218].

6 Highly Transparent Metal Top Electrodes

The following chapter discusses the realization of ultra-thin, highly transparent, and conductive metal top electrodes for top-emitting OLEDs. The application of a high surface energy gold wetting layer, also in combination with molybdenum trioxide, improves the growth of silver films on organics, allowing to reduce the silver thickness in comparison to a neat film. Thereby, the transmittance is increased, while a low sheet resistance of the ultra-thin metal top electrodes is maintained.

In state-of-the-art top-emitting OLEDs, transparent top electrodes with thicknesses in the range of 15 nm are usually applied to realize white emission in top-emitting OLEDs.[124, 125] Even silver films of such a low thickness show only an average transmittance in the range of 50 %, which is by far lower than for TCO electrodes used in bottom-emitting OLEDs. The lower transmittance of the transparent electrode in top-emitting devices leads to prominent microcavity effects, which adversely affect the device efficiency, as well as the spectral emission in comparison to bottom OLEDs. To overcome these limitations, highly transparent metal top electrodes are required.

To use a thin metal film as top electrode, not only a high transmittance, but further a high conductivity is required. Investigations on the growth of thermally evaporated silver on glass by Sennett *et al.* [219] showed that silver starts to grow from isolated nucleation sites as isolated grains, which connect with further material deposition (*percolation threshold*). Typically, the percolation threshold is reached for thicknesses significantly larger than 10 nm [219] and thus only moderate transmittance can be achieved. Furthermore, surface roughness and isolated metal grains strongly reduce the transmittance of the metal electrodes, due to the excitation of LSP modes (Section 4.3.1). Hence, the main requirements for highly transparent metal electrodes are the reduction of the percolation threshold and the formation of smooth, ultra-thin metal films.

Metal Thin Film Growth

In general, three different mechanisms of layer growth, not restricted to metals, can be distinguished: *Frank-van der Merwe*, *Stranski-Krastanov*, and *Volmer-Weber* growth, illustrated in Fig. 6.1. The actual growth mechanism of a material depends on the relation between the adhesive force to the layer underneath and the cohesive force of the deposited material.[220] Volmer-Weber growth occurs if the cohesive force is stronger than the surface adhesive force. This leads to clustering, as a smooth coverage of the layer underneath is not energetically favorable.[220, 221] Such films, e.g. silver on glass, form isolated grains with high roughness and the percolation threshold is reached for comparably large film thicknesses.

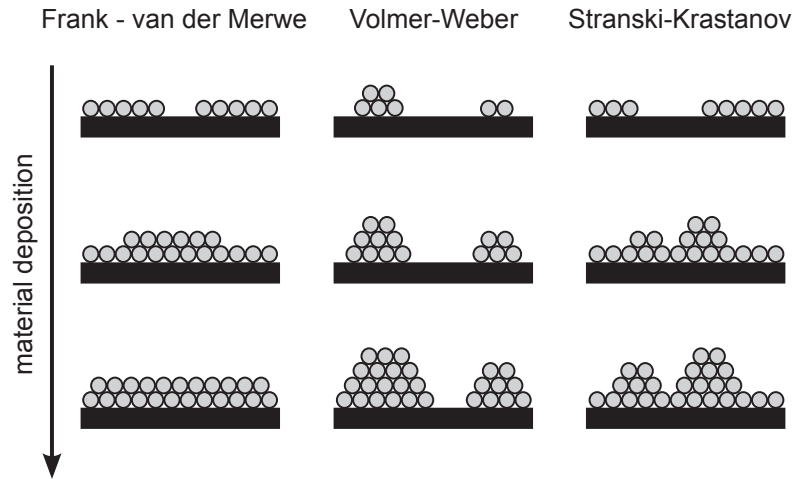


Figure 6.1: Illustration of the fundamental film growth types from physical vapor deposition, depicted from [220]. Thin, closed, and smooth layers are obtained if the cohesive force between the single particles is smaller than the surface adhesive force (Frank-van der Merwe growth). The opposite case is described by Volmer-Weber growth, leading to isolated grains and a rough surface. Stranski-Krastanov growth forms a closed first monolayer on the substrate, while the material tends to agglomerate for further deposition.

Due to the excitation of LSP modes and the large thickness of metal which is required to form the electrode, the transmittance of Volmer-Weber grown metal films will be comparatively low. In contrast, Frank-van der Merwe growth, which occurs if the surface adhesive force between the particles is larger than the cohesive force [220, 221], results in smoothly closed planar layers and a low percolation threshold. This film growth mechanism is desired, as the absent LSP absorption and the thin layer thickness ensure a high transmittance and the closed layer guarantees a low resistance. Stranski-Krastanov growth occurs when a concentration of strain forces leads to an accumulation of deposited material, according to a Volmer-Weber growth, after the first layers followed the Frank-van der Merwe type. In order to realize ultra-thin transparent metal electrodes, the surface adhesive force has to be larger than the cohesive force between the silver atoms, which is not the case for most organic- and oxide materials (e.g. SiO_2). [220, 222] The desired Frank-van der Merwe growth can be realized by several methods, e.g. the use of surfactant or *wetting layers* [223–225], substrate variation [220], thermal processing [226], as well as the optimization of the deposition rate [219]. As the organic underlayer is fixed and thermal post-treatment might harm the organic material, the focus of this work is on the wetting layer approach.

Reports on wetting layers of Sr [227], Ca [152, 162], Ba [163] or Yb [228] have not resulted in a decrease of the silver film thickness below 15 nm, what is required to maintain a sufficient conductivity. Metal oxide layers like MoO_3 [164], WO_3 [165], or CaO [229] increase the transmittance of the top electrode system, but the metal thickness remained still larger than 15 nm. Furthermore, no improvement of white top-emitting OLEDs compared to bottom-emitting OLEDs has been achieved with these electrodes.

Recently, Schubert *et al.* [224, 225] have shown top-illuminated organic solar cells using highly transparent silver films of only 7 nm thickness, on top of a high surface energy gold

wetting layer and a MoO₃ film. Based on this report, a high surface energy wetting layer of gold, as well as the use of MoO₃, is investigated to improve the electrode performance of silver top electrodes in top-emitting OLEDs.

6.1 Au/Ag Top Electrodes on N-Doped Layers

To improve white top-emitting OLEDs highly transparent metal top electrodes have to be realized on top of BPhen:Cs (ETL material). According to the requirements of the surface adhesive and the cohesive force of the material, in order to achieve Frank-van der Merwe growth, a high surface energy wetting layer of gold is introduced beneath the silver film. While reports also suggested the application of MoO₃ to improve the silver growth, it is not applied here, as the cathode of a pin-OLED demands on an efficient electron injection, while MoO₃ is known as an efficient hole injection material [95, 96].

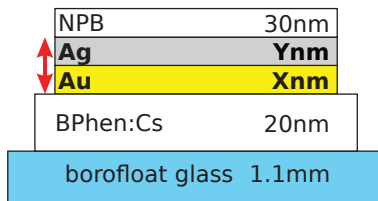
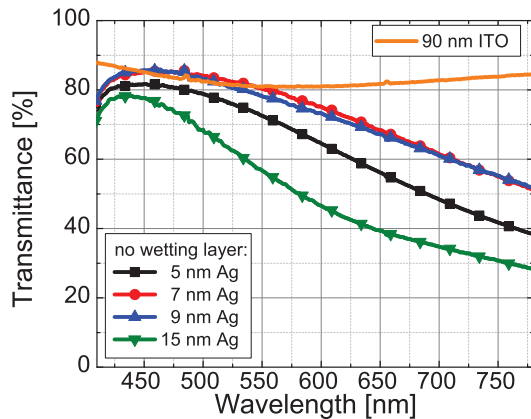


Figure 6.2: Electrode architecture for the characterization of Au/Ag metal electrodes, guaranteeing equivalent metal film growth as in the pin-OLED.

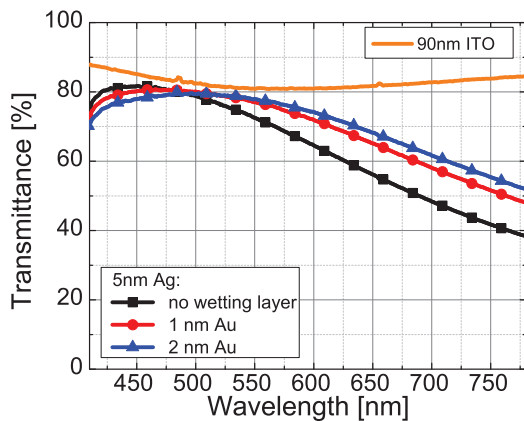
Figure 6.2 shows the layer structure for the investigation of Au/Ag wetting layer electrodes on BPhen:Cs. The 20 nm thick ETL layer provides a comparable thin film growth as in the OLED, while the 30 nm thick NPB capping layer is deposited to optimize the transmittance of the layer stack. Hence, the layer sequence represents the upper most part of a top-emitting OLED. In Fig. 6.3, the spectral transmittance and sheet resistance of neat silver layers on the ETL are shown.



Electrode	R_S [Ω/\square]
5 nm Ag	1672
7 nm Ag	18.0
9 nm Ag	6.7
15 nm Ag	2.8
ITO	32.0

Figure 6.3: Spectral transmittance and sheet resistance of neat silver top electrodes on 20 nm BPhen:Cs in comparison to an ITO electrode. Down to 7 nm of silver, the transmittance increases and broadens compared to 15 nm, applied as standard. For 5 nm thick Ag films, the transmittance decreases again. The ITO reference is reached for wavelengths between 430 nm and 540 nm, using 7 nm or 9 nm of Ag. The sheet resistance remains lower than ITO for silver films down to 7 nm.

The 15 nm thick state-of-the-art reference film reaches a sheet resistance of $2.8 \Omega/\square$, lower than the lab standard ITO. The transmittance continuously decreases as the wavelength increases, reaching values from 81 % at 440 nm to 28 % at 780 nm, which is always lower as for ITO. The reduction of the silver film thickness yields a transmittance increase and spectral broadening for layers down to 7 nm. Furthermore, the sheet resistance remains lower than $20 \Omega/\square$. For 5 nm of silver, the transmittance decreases slightly, while the sheet resistance is higher than $1000 \Omega/\square$. These results show that even without the gold wetting layer, the percolation threshold has to be in a range between 5 nm and 7 nm. The absence of spectral narrowing by LSP modes at metallic grains suggests a Frank-van der Merwe-like film growth even without gold wetting layer. Reports on the silver growth on cesium containing organic layers support this conclusion.[230] However, silver electrodes with thicknesses below 11 nm have so far not been reported in top-emitting OLEDs using BPhen:Cs.[11] This might be attributed to a potential damage of the thin film electrode during the encapsulation of the OLEDs, as the electrode itself shows a sufficient performance to guarantee electrical operation for thinner layer thicknesses. Hence, a 40 nm thick silver film is deposited underneath the encapsulation glass to protect the top electrode from mechanical damage, while the OLED performance is not affected. In order to reduce the percolation threshold of the silver further, gold wetting layers of 1 nm and 2 nm have been deposited on BPhen:Cs prior to the evaporation of 5 nm Ag. With gold wetting layer, the transmittance for wavelengths up to 500 nm is slightly reduced, while a prominent increase is detected for larger wavelengths (Fig. 6.4). For 2 nm of Au, 80 % transmittance are reached in a spectral range from 480 nm to 570 nm, close to the ITO reference and the sheet resistance is decreased to $28.8 \Omega/\square$. For 1 nm of gold, the improvements in transmittance and sheet resistance are not that prominent as for the 2 nm thick film.



Wetting Layer	R_S [Ω/\square]
none	1672
1 nm Au	58.8
2 nm Au	28.8
ITO	32.0

Figure 6.4: Spectral transmittance and sheet resistance of 5 nm thick silver films on 20 nm BPhen:Cs including gold wetting layers, in comparison to an ITO electrode. With gold wetting layer a slight transmittance decrease is observed below 500 nm, while a strong increase is detected for larger wavelengths. The overall transmittance increases and the dispersion is reduced, while the sheet resistance significantly decreases.

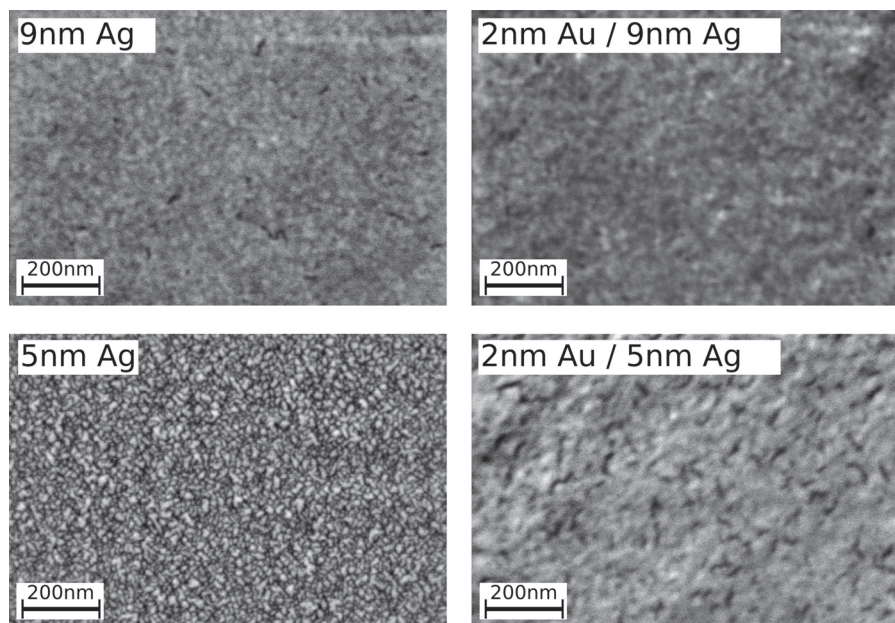


Figure 6.5: SEM images of silver films with and without an Au wetting layer on BPhen:Cs, without NPB capping layer (cf. Fig. 6.2). Homogeneously closed Ag films can be observed for 9 nm even without a wetting layer. 5 nm of silver shows a granular film morphology. Including the gold wetting layer, the growth homogeneity of the 5 nm thick silver layer is strongly improved and the grains almost completely vanish.

In order to investigate the silver morphology with and without gold wetting layer in more detail, SEM images of the silver films have been recorded (see Fig. 6.5)^[1].

The SEM image of the neat silver film of 9 nm thickness shows a homogeneous, closed, and smooth silver surface. This corresponds to the measured low sheet resistance and high spectral transmittance in Fig. 6.3. Since 9 nm of Ag already form a homogeneous closed metal film on BPhen:Cs, the introduction of the gold wetting layer does not result in a further improvement of the film morphology. For a silver layer of only 5 nm, a morphological form consisting of a granular film with grain diameters below 20 nm can be found. Thus, the increase in sheet resistance as well as the decrease in transmittance can be associated to the granular silver film. With a 2 nm thick Au wetting layer, the film morphology for 5 nm of silver is significantly improved and an almost completely closed layer is formed, where only a few isolated cracks below 80 nm in length remain. The transmittance improves as absorption from LSP modes is less prominent, whereas the formed conductive paths through the silver film result in a decrease of the sheet resistance of the wetting layer electrode, as shown in Fig. 6.4.

A crucial point related to the Ag morphology is given by the optical optimization of top-emitting OLEDs with ultra-thin metal top electrodes. The simulation demands an accurate description of the thin film optics, based on the thicknesses and refractive index of the layers. In order to verify a reliable device optimization of top-emitting OLEDs using ultra-thin Au/Ag top electrodes, optical simulation results of the spectral transmittance are shown in Fig. 6.6.

^[1] The support of Ellen Hieckmann in the SEM measurements is gratefully acknowledged.

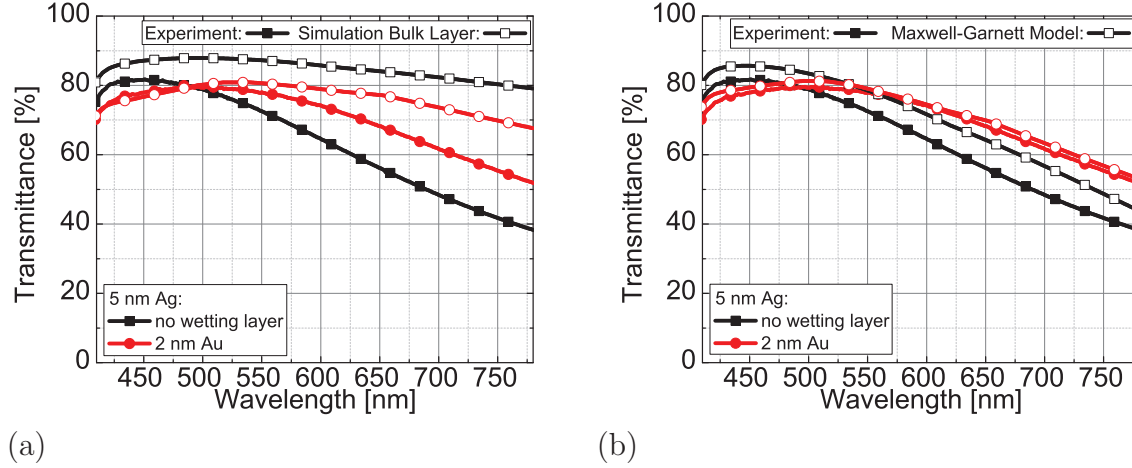


Figure 6.6: Comparison of the measured spectral transmittance and optical simulation results of 5 nm thick silver films with and without gold wetting layer, assuming smooth bulk layers of the materials (a) or introducing an effective medium of silver/NPB according to the Maxwell-Garnett model (b). Assuming bulk layers in the simulation, the measured transmittance cannot be fitted. The Maxwell-Garnett model instead is able to qualitatively reproduce the measured transmittance.

The simulation based on the assumption of bulk layers cannot reproduce the correct transmittance trend for 5 nm thick silver films with and without gold wetting layer, as neither one of both films are completely closed (Fig. 6.6(a)).

This mismatch in the predicted electrode transmittance would result in completely different optimization results of the OLED architecture, compared to real top-emitting OLEDs. An approach to qualitatively describe the transmittance of granular films is the Maxwell-Garnett model, describing granular metal films with an effective refractive index and including a further simplification of spherical metal particles, here.[159, 231] An effective refractive index n_{eff} of the agglomerated metal film, as a mixed layer of metallic spheres surrounded by a matrix material has been calculated according to [159]:

$$n_{\text{eff}}^2 = n_{\text{D}}^2 \frac{n_{\text{M}}^2 + 2n_{\text{D}}^2 + 2q \cdot (n_{\text{M}}^2 - n_{\text{D}}^2)}{n_{\text{M}}^2 + 2n_{\text{D}}^2 - q \cdot (n_{\text{M}}^2 - n_{\text{D}}^2)}. \quad (6.1)$$

For the layer architecture investigated, the refractive index of the metal n_{M} is given by Ag, while the dielectric matrix material (n_{D}) is given by NPB. The parameter q describes the volume fraction of the metal in the mixed layer, with $q=1.0$ representing a neat metal film. For the simulation of the transmittance spectra, a single granular Ag/NPB layer has been included in the device architecture, while the further layers are described as neat films. The Maxwell-Garnett model shows an excellent agreement between simulated and measured transmittance of the wetting layer electrode, where a volume fraction of $q=0.95$, extrapolated from the SEM surface image, has been used (Fig. 6.6(b)). The transmittance of the neat 5 nm thick silver film can be reproduced with a slightly smaller volume fraction of $q=0.93$. Granular metal electrodes can therefore be accurately described in terms of optical properties, using the Maxwell-Garnett model, allowing for the optical optimization of top-emitting OLEDs.

Overall, the investigations on the silver film formation on BPhen:Cs show that highly transparent metal top electrodes can be realized for thicknesses down to 7 nm without an additional wetting layer. Introducing 2 nm of gold, the silver thickness can be further decreased, while the transmittance increases and the sheet resistance is significantly reduced. Furthermore, the optical properties of the ultra-thin wetting layer electrodes have been accurately described applying the Maxwell-Garnett model, assuming spherical metal particles.

In addition to the improvement of silver top electrodes as cathode in pin-OLEDs, the following section will focus on the realization of highly transparent metal electrodes for inverted devices, which are of interest, e.g. in display applications and require a highly transparent and conductive anode.

6.2 $\text{MoO}_3/\text{Au}/\text{Ag}$ Top Electrodes on P-Doped Layers

The wetting layer concept can be further applied to reduce the percolation threshold of silver films on p-doped organic layers as represented by MeO-TPD doped with 4 wt.% of F6-TCNNQ. Here, the use of MoO_3 is not contradictory to the electrical properties of the inverted OLEDs, as an efficient injection of holes is desired. Thus, combinations of MoO_3 and the high surface energy gold wetting layer are investigated. Again, 20 nm of the organic material are deposited on a glass substrate, in order to provide similar growth conditions to that of the metal electrode as in final OLEDs. A 30 nm thick capping layer of NPB on top of the electrode is used to improve the transmittance of the layer architecture (see Fig. 6.7).

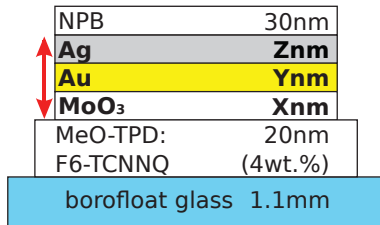


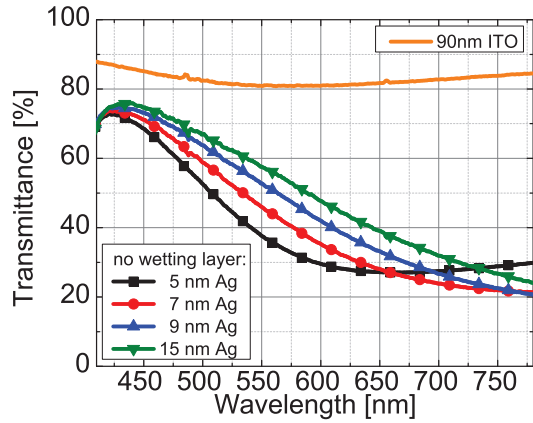
Figure 6.7: Electrode architecture for the characterization of $\text{MoO}_3/\text{Au}/\text{Ag}$ metal electrodes, guaranteeing equivalent metal film growth as in the nip-OLED.

In Fig. 6.8, the spectral transmittance and sheet resistance of neat silver films between 5 nm and 15 nm deposited on the HTL material are shown. The state-of-the-art 15 nm thick silver film reaches a sheet resistance of $3.9 \Omega/\square$, which is almost one order of magnitude lower than for the lab standard ITO reference (see Fig. 6.8). However, the spectral transmittance shows a continuous decrease from 75.7% at 435 nm to 24% at 780 nm, significantly lower than for ITO. A reduction of the silver layer thickness leads to a further decrease of the transmittance, forming a dip at 630 nm for 5 nm Ag. The sheet resistance is greatly increased to $100 \Omega/\square$ for 9 nm Ag thickness, while for thinner films no conductivity is detected ($R_S > 10^8 \Omega/\square$).

It is concluded that the percolation threshold is in the range of 7 nm to 9 nm for silver on MeO-TPD:F6-TCNNQ.

The reduced transmittance for lower silver film thickness contradicts the trend observed for the silver electrodes on BPhen:Cs, as well as the bulk layer simulations shown in Section 4.2.2. Thus, a formation of non-closed layers, even for a silver thickness of 9 nm, is expected, while the observed transmittance tendencies are correlated to plasmonic absorptions in granular silver films. Overall, the thickness of a neat silver top electrodes on MeO-TPD:F6-TCNNQ has to be larger than 9 nm, in order to maintain a comparable electrical operation of inverted top-emitting OLEDs. Since the electrode transmittance cannot be improved by reducing the thickness of the neat silver

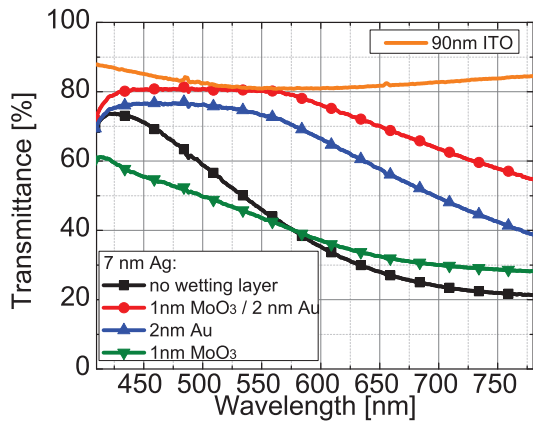
film, microcavity effects remain and thus the disadvantages in the optical properties of such top-emitting OLEDs compared to bottom-emitting devices.



Electrode	R_S [Ω/\square]
5 nm Ag	$>10^6$
7 nm Ag	$>10^6$
9 nm Ag	122.8
15 nm Ag	3.9
ITO	32.0

Figure 6.8: Spectral transmittance and sheet resistance of neat silver top electrodes on top of 20 nm MeO-TPD:F6-TCNNQ, in comparison to an ITO electrode. A reduction in silver thickness leads to a decrease in transmittance and the formation of a broad dip with peak at around 630 nm for the 5 nm Ag sample. The transmittance of the ITO reference is not reached for any Ag thickness in the range investigated. Furthermore, no conductivity is detected for silver films below 9 nm thickness.

In order to improve the performance of silver films on MeO-TPD:F6-TCNNQ, wetting layers have to be applied. In Fig. 6.9, the influence of different wetting layers beneath a 7 nm thick silver film on the spectral transmittance and sheet resistance is shown.



Wetting Layer	R_S [Ω/\square]
none	$>10^6$
1 nm MoO ₃ / 2 nm Au	9.0
2 nm Au	15.7
1 nm MoO ₃	$>10^6$
ITO	32.0

Figure 6.9: Spectral transmittance and sheet resistance of a 7 nm thick silver top electrode for different wetting layers on top of 20 nm MeO-TPD:F6-TCNNQ. 1 nm of MoO₃ as wetting layer, shows only slight changes of the transmittance and the film remains non-conductive. The transmittance is strongly increased introducing 2 nm of Au, while the sheet resistance drops below 20 Ω/\square . The MoO₃/Au wetting layer decreases the sheet resistance and improves the transmittance further, reaching the ITO benchmark in a spectral range between 430 nm and 575 nm.

As wetting layer, either a single layer of gold and MoO₃, or a combination of both is investigated to improve the performance of a 7 nm Ag film. Using 1 nm of MoO₃, the transmittance is decreased for wavelengths below 575 nm, while for larger wavelengths only slight improvements are observed in comparison to the neat silver film. The sheet resistance of the silver electrode remains larger than 10⁶ Ω/□, representing a non-conductive film.

From these results it can be concluded that a single layer of MoO₃ cannot serve as wetting layer for silver on p-doped organics. By introducing 2 nm of Au, the transmittance can be increased over the entire spectral range between 420 nm and 780 nm. A transmittance of 76 % is reached between 430 nm and 575 nm, which gradually decreases for larger wavelengths. In comparison to the sample without wetting layer, this represents a transmittance enhancement by a factor of 2 for wavelengths larger than 550 nm. The strong improvement of the transmittance suggests a beneficial change in the silver layer morphology, suppressing parasitic absorption by LSP modes at metallic nano-particles. Furthermore, the 2 nm Au wetting layer decreases the sheet resistance to 15.7 Ω/□. In a further step, the MoO₃ and the Au layer are combined, according to the reports by Schubert *et al.* [224], to improve the silver films in terms of both, transmittance and sheet resistance. The MoO₃/Au wetting layer indeed leads to a further improvement of the transmittance up to 81 % in the spectral range between 420 nm and 780 nm, while the sheet resistance is reduced to 9.0 Ω/□. These results show that ultra-thin silver electrodes with a transmittance comparable to ITO and an even lower sheet resistance can be realized using suitable wetting layers.

In Fig. 6.10, SEM images of silver films with and without a MoO₃/Au wetting layer on top of 20 nm MeO-TPD:F6-TCNNQ are shown^[2]. Again, no organic capping layer has been deposited on the silver film for these investigations. For 7 nm of neat silver, a granular film is detected, indicating Volmer-Weber growth, where the percolation threshold is not reached. Furthermore, the isolated metal grains suggest that the observed absorption dip in the transmittance measurement is induced from LSP modes.

For a neat silver film of 15 nm thickness, the layer is almost completely closed, except for various cracks smaller than 200 nm in length. Hence, a conductive electrode is formed, while the comparably large film thickness allows only for moderate transmittance.

Including the MoO₃/Au wetting layer, the film morphology of the silver is dramatically affected. Even for a 7 nm thin silver film, a homogeneously closed, smooth electrode is formed. These results prove that the high surface energy gold layer ($\gamma_{\text{Au}} = 1.5 \text{ J/m}^2$) underneath the silver ($\gamma_{\text{Ag}} = 1.25 \text{ J/m}^2$), in combination with MoO₃ ($\gamma_{\text{MoO}_3} = 0.06 \text{ J/m}^2$) [224], can turn the initial Volmer-Weber growth of the silver film into a Frank-van der Merwe-like growth.

Furthermore, the MoO₃ layer with its low surface energy is expected to assist the silver film formation by decoupling the metal film growth from the organics underneath. The gold particles tend to form isolated and distributed nucleation sites on the MoO₃. Thus, the deposited silver atoms can accumulate at the gold sites, homogeneously wetting the surface, forming smooth and closed layers following a Frank-van der Merwe-like growth. Figure 6.11 shows simulated transmittance spectra of metal top electrodes with and without wetting layer.

^[2] The assistance of Vera Hoffmann in the SEM measurements is gratefully acknowledged.

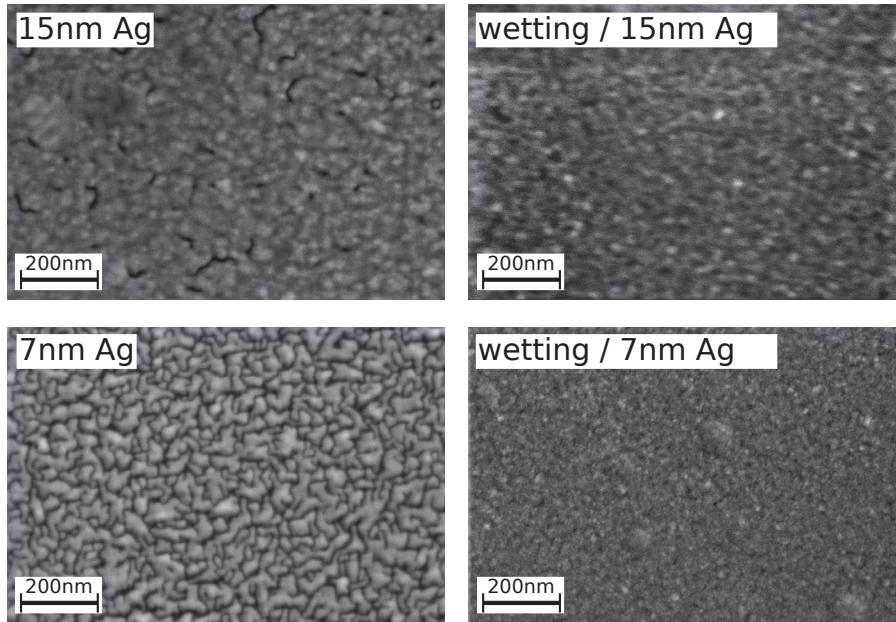


Figure 6.10: SEM images of silver films with and without MoO_3/Au wetting layer on MeO-TPD:F6-TCNNQ , without NPB capping layer (cf. Fig. 6.7). Neat silver films show isolated cluster growth for a nominal thickness of 7 nm. Even a 15 nm thick Ag layer shows remaining cracks in the surface and is not homogeneously closed. Including the MoO_3/Au wetting layer, smooth and closed silver layers are formed even for 7 nm thickness.

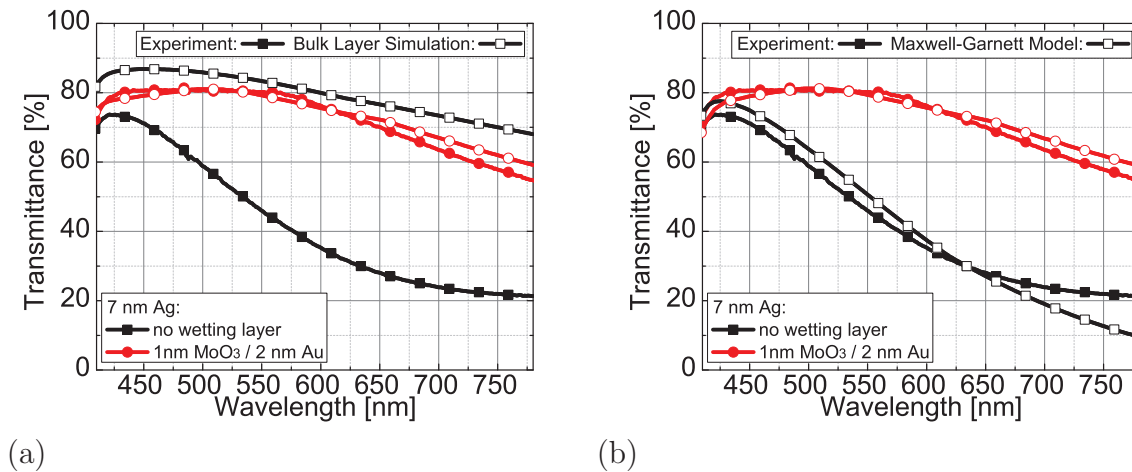


Figure 6.11: Comparison of the measured spectral transmittance and optical simulation results of 7 nm thick silver films with and without wetting layer, assuming smooth bulk layers of the materials (a) or an effective medium of silver/NPB according to the Maxwell-Garnett model (b). The bulk layer simulation can only be used to fit the transmittance of homogeneously closed films, while the transmittance for the granular silver film cannot be reproduced. Introducing the metal volume fraction ($q=0.85$), determined from the SEM image in Fig. 6.10, the transmittance of the granular silver layer can sufficiently be reproduced by the Maxwell-Garnett model.

As for the Au/Ag electrode system, the transmittance spectra of the wetting layer electrodes are simulated by either a bulk layer simulation or the Maxwell-Garnett model. Again only assuming an effective medium of spherical metallic Ag particles dispersed in the surrounding medium NPB is present. For the wetting layer electrode, which is a homogeneously closed film, an accurate fit of the transmittance is obtained, assuming bulk layers (Fig. 6.11(a)). In contrast, the granular film cannot be described by this approach at all. In Fig. 6.11(b), the measured and simulated transmittance for the Maxwell-Garnett model are shown.

As expected, for the wetting layer electrode ($q = 1.0$) the results of the Maxwell-Garnett model are in accordance to the bulk layer simulation. From the SEM surface image of the granular silver film without wetting layer, a volume fraction of $q = 0.85$ has been extrapolated. The simulated transmittance of the granular film predicts the trend of the spectral transmittance in the range between 420 nm and 660 nm accurately, while for larger wavelengths the curves deviate. Despite the strong simplifications made by the Maxwell-Garnett model, assuming spherical metal particles and a single effective medium of Ag/NPB here, the simulation shows a good agreement to the measurement. Thus, it can be concluded that top-emitting OLEDs can be optimized with optical simulation for homogeneously closed wetting layer electrodes as well as granular neat silver films, as long as the film morphology has been determined.

Chapter Summary

In summary, highly transparent and ultra-thin metal top electrodes have been realized through the application of wetting layers. Using a high surface energy gold layer, as well as MoO_3 on p-doped organics, Frank-van der Merwe-like layer growth of the silver can be realized. Hence, homogeneously closed silver films with a percolation threshold below 7 nm on MeO-TPD:F6-TCNNQ and below 5 nm on BPhen:Cs can be deposited. These electrodes outperform the state-of-the-art 15 nm thick Ag electrodes regarding transmittance, while a comparable sheet resistance is reached. In addition to this, the transmittance of the ITO reference has almost been reached. These results deliver promising methods to overcome the limitations of white top-emitting OLEDs, arising from microcavity effects introduced by reflective metal top electrodes, applying wetting layer electrodes.

7 White Top-Emitting OLEDs with Optimized Microcavity Effects

This chapter focuses on the optimization of top-emitting OLEDs for efficient, angularly color-stable, and high quality white light emission. Therefore, highly transparent wetting layer electrodes are applied for white top-emitting OLEDs, to improve the emission by a reduction of microcavity effects. The impact of the silver layer thickness as well as the wetting layer on the device performance is investigated in detail. In addition, experimental results on TCO-free transparent, bi-directional white light-emitting OLEDs are shown.

A general approach to optimize top-emitting OLEDs regarding white light emission is presented in the following. While monochrome top-emitting OLEDs benefit from the microcavity effects introduced by the reflective metal electrodes, efficient and high quality white emission is difficult to achieve. When compared to white bottom-emitting OLEDs, the top-emitting devices show lower efficiency and poor color rendering. As top-emitting OLEDs allow for the application of opaque substrates, e.g. display back planes or metal foils, which cannot be used for bottom-emitting devices, the optimization of these device architecture is highly desired. Furthermore, top-emitting OLEDs are compatible with R2R processing, while bottom-emitting OLEDs often use brittle TCO electrodes. Another aspect of top-emitting OLEDs is the lack of substrate light modes, which might be beneficial to achieve a higher efficiency as in bottom-emitting devices.

Even though the introduction of an organic capping layer on top of the semitransparent metal electrode improves the device performance of white top-emitting OLEDs (cf. Section 4.2.2), efficiency and color rendering remain low.[124, 125] Replacing the metal top electrodes by more transparent materials like TCOs or carbon based compounds is often limited due to the associated deposition techniques (see Section 3.3.3).

Analysis of the optical properties of microcavities in Chapter 4 showed that the microcavity effects can be reduced with increasing top electrode transmittance. Hence, the application of highly transparent, ultra-thin, and conductive metal top electrodes has been one particular focus of this thesis. As improvements based on the optimized device optics are not correlated to a specific organic material, this approach is expected to be beneficial for white top-emitting OLEDs in general.

First, the impact of a top electrode variation on the white top-emitting OLEDs is investigated in detail (Section 7.1). The full potential of the wetting layer concept is then shown for a tandem OLED architecture with a comparably large cavity length, increasing the impact of microcavity effects on the device performance (Section 7.2). Transparent, bi-directional emitting OLEDs using two metal electrodes are shown in Section 7.3.

7.1 Hybrid White Top-Emitting OLEDs

The following experiments focus on the application of highly transparent top electrodes used to compensate the microcavity effects introduced by state-of-the-art silver electrodes with a thickness in the range of 15 nm and having only moderate transmittance. The aim is to improve the color rendering, the angular color-stability, and finally the efficiency of white top-emitting OLEDs. For that purpose, hybrid white top-emitting pin-OLEDs are investigated, analyzing the influence of the silver top electrode thickness and the application of a gold wetting layer on the device performance. Finally, optimized white top-emitting OLEDs are compared to state-of-the-art bottom-emitting reference devices, to highlight the enormous potential of the wetting layer concept.

7.1.1 Optimization of the Silver Thickness

A hybrid white OLED architecture, as shown in Fig. 7.1, has been used for the investigation of the silver top electrode thickness on the white emission. Neat silver top electrodes deposited on BPhen:Cs are investigated in a thickness range between 15 nm and 5 nm, according to the electrodes on partial OLED stacks presented in Section 6.1.

NPB	50nm
Ag	Xnm
BPhen:Cs	35nm
BPhen	10nm
MADN:TBPe	10nm (1wt.%)
TCTA:TPBi	2nm
TCTA:Ir(ppy) ₃	3nm (5wt.%)
NPB:Ir(MDQ) ₂ (acac)	10nm (5wt.%)
NPB	10nm
Spiro-TTB:F6-TCNNQ	20nm (4wt.%)
Ag	40nm
Al	40nm
borofloat glass	1.1mm

Figure 7.1: Hybrid white top-emitting OLED architecture with varied neat silver layer top electrode.

4.9 V. Even for only 5 nm of silver without a wetting layer, a luminance onset at only 2.5 V is observed. The detected leakage current offsets below 2.5 V cannot be associated to specific electrode characteristics and have not been observed in comparable devices in a statistically relevant extent. For potentials larger than 2.5 V, only small deviations between the electrodes with thicknesses between 15 nm and 7 nm are observed, which is in accordance to the measured sheet resistances, which are all below $30 \Omega/\square$ (see Fig. 6.3).

The hybrid white OLED architecture is based on the pin-concept, while an emission layer system using the fluorescent blue emitter system MADN:TBPe and the phosphorescent emitters Ir(ppy)₃ (green) and Ir(MDQ)₂(acac) (red) is applied. The incorporated organic materials have been chosen in accordance to a report on hybrid white top-emitting OLEDs by Freitag *et al.* [125]. Furthermore, the device structure in Fig. 7.1 has been optimized by optical simulation, adjusting the EML positions, the cavity length, and the capping layer thickness for the reference silver electrode of 15 nm thickness.

According to the simulation, an OLED with an HTL thickness of 20 nm and a total cavity length of 100 nm provides a broad cavity emission, comparable to the reported thicknesses by Freitag *et al.* [125], for a top electrode of 15 nm Ag on 1 nm Al. In the following, the organic layer sequence is kept constant to neglect an impact of an organic layer variation on the results, even though the devices with a thinner top electrode might not be prepared in the optical maximum.

Figure 7.2(a) shows the current-voltage-luminance characteristics of the devices for a positive bias between 1.9 and

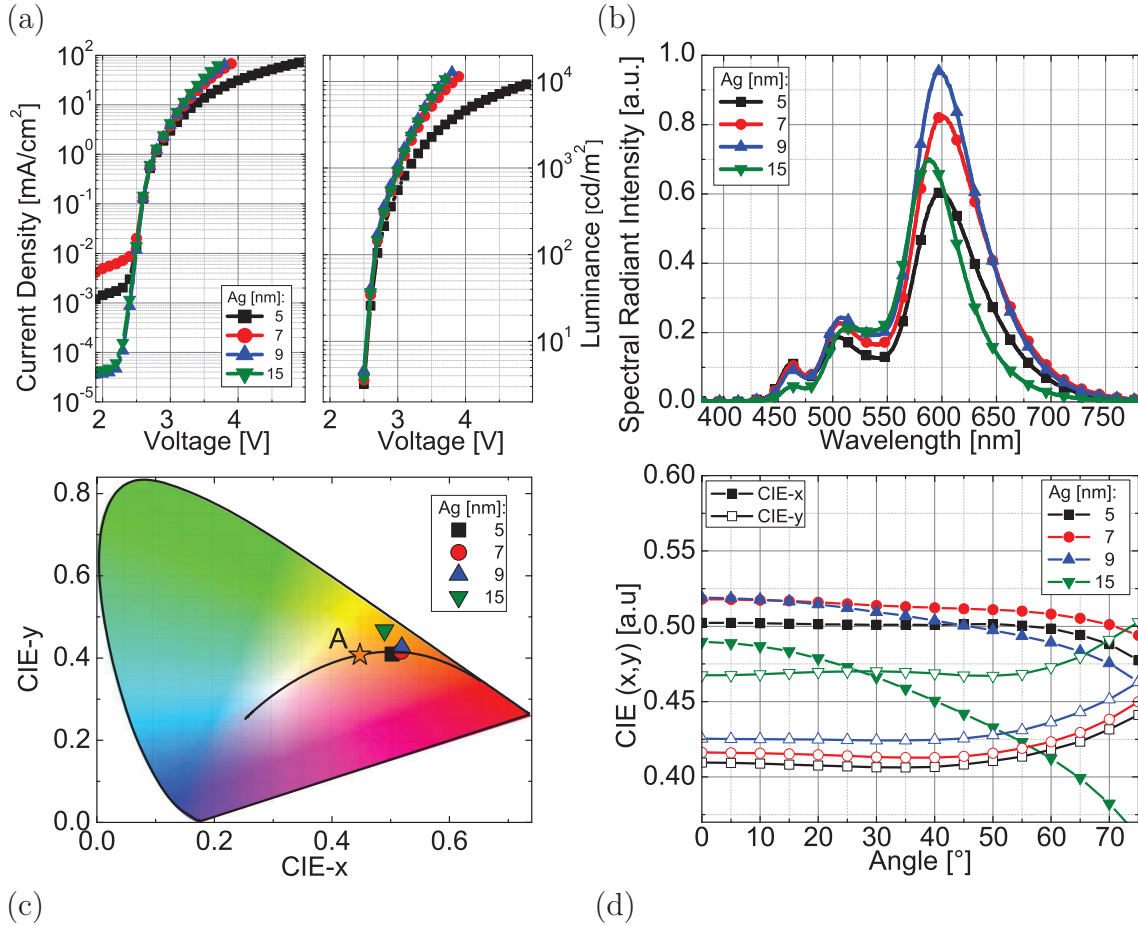


Figure 7.2: Influence of the silver top electrode thicknesses between 5 nm and 15 nm on the *j*V characteristics (a), the spectral emission in normal direction at a current density of $14.8 \text{ mA}/\text{cm}^2$ (b), the color coordinates in normal direction (c), as well as the angular dependent color coordinates (d). Even without wetting layer, neat silver electrodes down to 7 nm thickness show a comparable electrical performance on the Cs doped ETL.

The slope of the *j*V characteristic is significantly reduced for the 5 nm thick silver electrode, due to the high sheet resistance of more than $1000 \Omega/\square$. This limitation of the 5 nm thick electrode can also be detected in the luminance-voltage dependence. While the required additional potential at a brightness of $1000 \text{ cd}/\text{m}^2$ is 0.2 V, it is increased to 0.45 V for a brightness of $3000 \text{ cd}/\text{m}^2$. The spectral emission in normal direction at a current density of $14.8 \text{ mA}/\text{cm}^2$ (current of 1 mA) is shown in Fig. 7.2(b). It is worth to note that a comparison of device spectra at a constant applied current allows for a direct comparison of the generated emission intensities from an identical amount of charge carriers. Furthermore, all white top-emitting OLEDs reach relevant brightness levels of more than $1000 \text{ cd}/\text{m}^2$ at the reported current density.

The devices show a broad emission with an onset at approximately 450 nm corresponding to the PL emission off the blue emitter system MADN:TBPe up to 750 nm which is the red emitter NPB:Ir(MDQ)₂(acac). All spectra show three prominent peaks according to the blue ($\approx 470 \text{ nm}$), green ($\approx 515 \text{ nm}$), and red ($\approx 600 \text{ nm}$) emitter spectra. The blue emitter shows the lowest contribution to the device spectrum for all devices, while the

red emitter is the most intense (cf. Fig. 7.2(b)). In comparison to the device with a 15 nm silver electrode, the reduction of the top electrode thickness broadens the spectra and increases the emission intensities for wavelengths smaller than 500 nm and larger than 600 nm. The spectral changes are a result of the broadened emission affinity as presented in Section 4.2.2. While the spectral deviations between the 7 nm and 9 nm thick top electrode are quite small, the 5 nm silver electrode shows a reduced green and red emission. As a higher voltage is required to reach a certain current density in this device, a shift of the recombination zone to the blue EML might be induced, contributing to the detected spectral deviations. Furthermore, the transmittance of the 5 nm Ag electrode is lower when compared to electrodes with 7 nm and 9 nm, which also has an impact on the emission affinity.

The emission in normal direction (0°) is close to the Planckian locus for all devices (Fig. 7.2(c)), except for the 15 nm silver electrode and a maximum CRI of 68.7 is obtained for 7 nm of Ag (5 nm CRI: 67.5, 9 nm CRI: 65.6). The Planckian locus is reached at lower correlated color temperatures (CCTs) compared to the warm white reference point A and rather corresponds to "candle light" white emission (CCT 1850 K). In order to reach the warm white color point A, the OLED architecture has to be optimized for increased blue emission, e.g. from thickness variations of the doped transport layers or variations of the EML system. For a detailed optimization of device emission at the warm white color point, the reader is referred to Appendix A.

In Fig. 7.2(d), the angular dependent color coordinates are shown for an angle range between 0° and 75° . The restriction to angles up to 75° is given by the increasing contribution of background noise during the measurement of the device spectra, which could negatively affect the determination of the color coordinates. The OLED with the 15 nm thick Ag electrode shows a prominent shift of the CIE-x coordinate even for small deviations from the normal direction. The velocity of the color-shift is further increased with increasing viewing angle. In comparison, the CIE-y coordinate shows only slight variations up to 60° . The reduction of the top electrode thickness has a significant impact on the angular dependency of the emission color. Even a top electrode of 9 nm thickness improves the color-stability, to be completely stable between 0° and 20° . A further reduction to 7 nm or even 5 nm enables angular color-stabilities up to viewing angles of almost 60° , at which a shift of the CIE-y coordinate sets in for all devices. The angular color-shift (Δ CIE), calculated in the CIELAB space, for a 15 nm, 9 nm, 7 nm, and 5 nm Ag electrode is 1.0, 0.42, 0.34, and 0.34, respectively. The remaining high angular color-stability of the 5 nm device allows to conclude that the observed spectral deviations in Fig. 7.2(b) might be induced by differences in the device optics and a shift of the recombination zone, while microcavity effects seem not to be prominent.

In Fig. 7.3, the efficiency-current dependencies of the devices are presented. The OLEDs with a 9 nm, 7 nm, and 5 nm Ag electrode show increased EQEs compared to the 15 nm sample. At a current density of 3 mA/cm^2 , corresponding to approximately 1000 cd/m^2 , the device with the 9 nm silver electrode reaches 9.1 % EQE, almost twice as high as the device with a state-of-the-art 15 nm thick top electrode (4.7 % EQE). Furthermore, the device with 7 nm silver electrode reaches a comparable EQE (8.8 %) as the 9 nm device, while the OLED with 5 nm thick top electrode reaches 6.5 %.

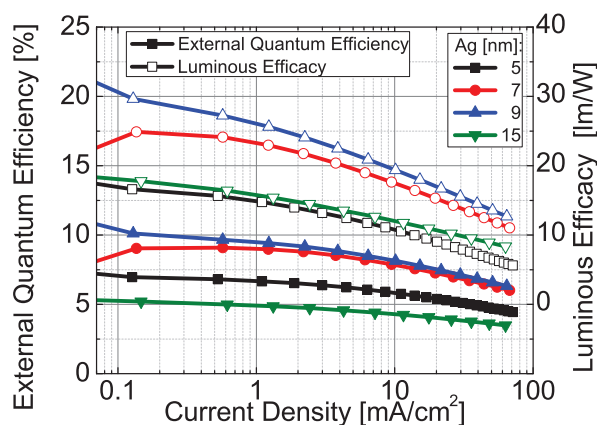


Figure 7.3: Influence of the silver top electrode thicknesses between 5 nm and 15 nm on the efficiency-current dependency. A reduction of the silver top electrode thickness down to 7 nm results in a significant increase of the device efficiency, while the poor electrical performance for 5 nm Ag restricts a further improvement.

The poor electrical performance of the 5 nm top electrode device reduces the LE compared to the other devices, reaching only 13.2 lm/W at 3 mA/cm². This is lower than for the 15 nm thick Ag top electrode (14.0 lm/W), even though the EQE has been significantly higher. In contrast, the LE of the devices with 7 nm (21.7 lm/W) and 9 nm (24.0 lm/W) Ag thickness show a rather large efficiency enhancement compared to the state-of-the-art device. It is worth to note that the reference OLED with 15 nm thick Ag electrode reaches a comparable performance as reported in literature for a similar device layout [124, 125], validating the shown results.

In summary, the deposition of ultra-thin, highly transparent top electrodes on white top-emitting OLEDs allowed for a reduction of the angular color-shift, typically introduced by the only moderate transmittance of state-of-the-art metal top electrodes. Overall, the color-shift has been reduced by a factor of 2.88. In addition, the spectral emission broadens, which is beneficial to achieve white emission with high color rendering, especially desired for solid-state lighting applications. Here, CRIs of up to 68.7 have been achieved, even though blue emission below 450 nm and red emission above 700 nm has only merely been achieved by the chosen emitter materials. Most important, the external quantum efficiency and luminous efficacy of white top-emitting OLEDs have been enhanced by a factor of up to 1.9 compared to state-of-the-art devices, while the previously mentioned benefits are maintained.

7.1.2 Gold Wetting Layer for Ultra-Thin Metal Top Electrodes

The beneficial growth conditions for silver films on Cs doped organics have enabled the fabrication of ultra-thin and highly transparent top electrodes down to 5 nm thickness even without a wetting layer. However, a top-emitting OLED with 5 nm thick silver electrode suffered from a sheet resistance of over 1000 Ω/□, potentially introducing a shift of the recombination zone and reducing the luminous efficacy, while further the transmittance of the film decreases. In Chapter 6, it has been shown that the percolation threshold of silver films can be further reduced by introducing suitable wetting layers. Furthermore, the spectral transmittance of the top electrode increases, broadens, and the

sheet resistance decreases. In the following, the effects on the device performance introducing gold wetting layers underneath 5 nm thick silver top electrodes are shown. The other layers of the OLED architecture are the same as in the previous section (Fig. 7.4).

NPB	50nm
Ag	5nm
Au	Xnm
BPhen:Cs	35nm
BPhen	10nm
MADN: TBPe	10nm (1wt.%)
TCTA:TPBi	2nm
TCTA: Ir(ppy) ₃	3nm (5wt.%)
NPB: Ir(MDQ) ₂ (acac)	10nm (5wt.%)
NPB	10nm
Spiro-TTB: F6-TCNNQ	20nm (4wt.%)
Ag	40nm
Al	40nm
borofloat glass	1.1mm

Figure 7.4: Hybrid white top-emitting OLED architecture with gold wetting layer underneath a 5 nm thick silver top electrode.

In Fig. 7.5(a), the current-voltage-luminance dependency for a positive bias between 1.9 and 4.9 V is shown. All devices show an identical luminance onset of 2.5 V. This shows that the injection of electrons into the Cs doped ETL is not affected by the higher work function of the gold wetting layer (5.1 eV) compared to neat silver (4.3 eV), which is attributed to the tunnel injection of charge carriers. For most devices, leakage currents in the range of 10^{-5} mA/cm² have been observed with and without gold wetting layer, which is approximately five orders of magnitude lower than the current contributing to the light generation in the EML at typical brightnesses of 1000 cd/m². The slope of the current-voltage is increased, due to the reduced sheet resistance of the electrodes with gold wetting layer. As a consequence, the operating voltages to reach comparable brightness levels are reduced by up to 1.0 V at 10,000 cd/m² for both wetting layer thicknesses.

The spectral radiant intensity in forward direction for a current density of 14.8 mA/cm² is shown in Fig. 7.5(b). Introducing the gold wetting layer, the emission in the green and red spectral range is increased, while 2 nm of gold show a slightly broader and more intense red emission. With respect to the previous results in Section 7.1.1, the increase of red and green emission can be attributed to a shift of the recombination zone back to the IL/ green EML interface, as the sheet resistances of the wetting layer electrodes is again reduced below $30 \Omega/\square$. Furthermore, the transmittance of the electrodes increases when introducing the gold wetting layer and a more homogeneous transmittance characteristic is observed in the visible spectral range (cf. Fig. 6.4), which also effects the spectral emission. Emission from 440 nm to approximately 750 nm is detected and the peak positions of the three incorporated emitter materials MADN:TBPe (≈ 470 nm), Ir(ppy)₃ (≈ 515 nm), and Ir(MDQ)₂(acac) (≈ 600 nm), remain nearly constant.

In Fig. 7.5(c), the color coordinates in normal direction are shown in the CIE1931 color space. In accordance to the nearly conserved spectral shape, the emission remains close to the Planckian locus for all devices. The slight spectral deviations result in a shift of the color along the Planckian locus to lower CCTs. Again, the achieved white emission is more a "candle light" white, than a warm white emission from a light bulb. However, CRIs of up to 70.3 are reached for 2 nm of Au (1 nm Au: CRI: 68.8, 0 nm Au: CRI: 67.5) at CCTs in the range of 2200 K. All investigated devices maintain the excellent angular color-stability up to viewing angles of almost 60° (not included here), comparable to the result shown in Fig. 7.2(d).

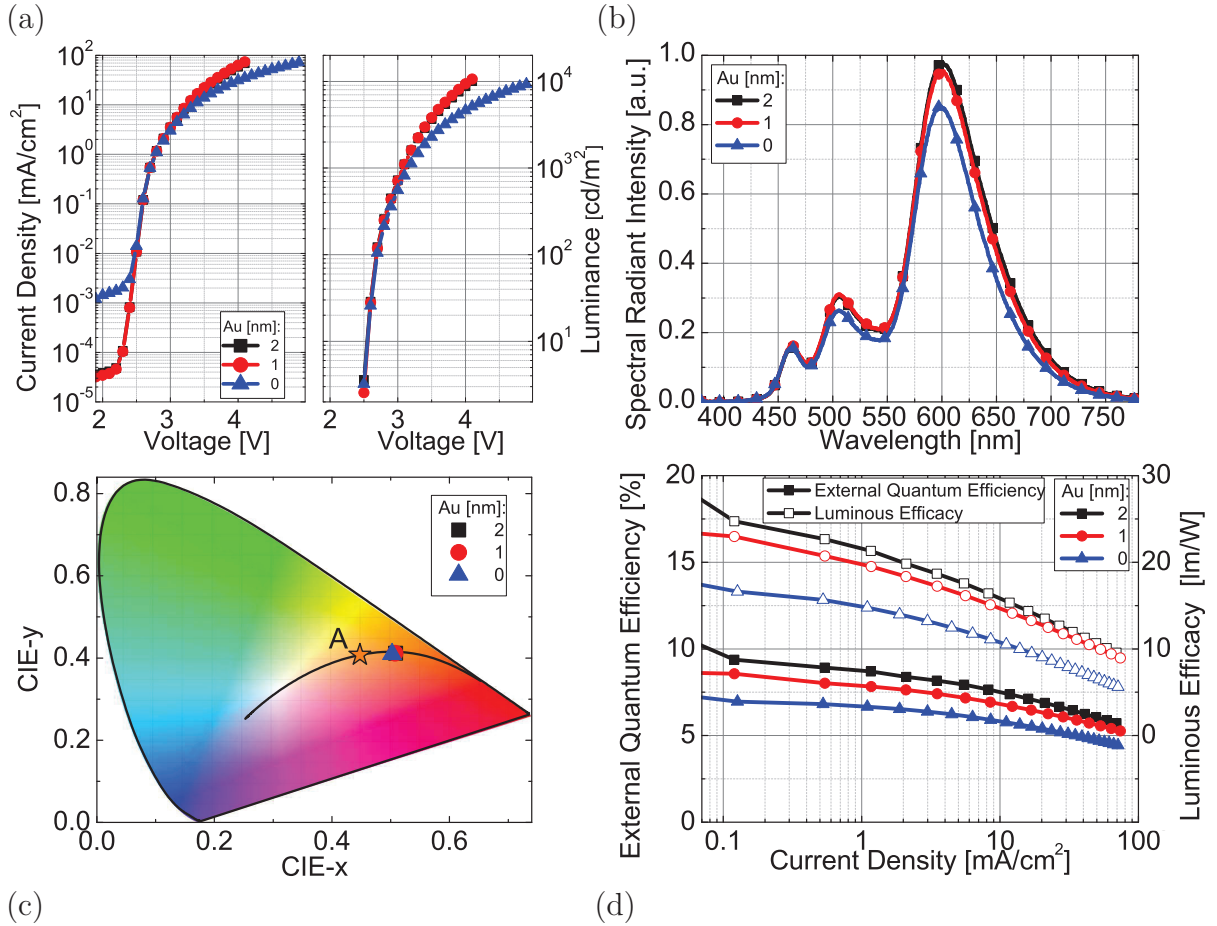


Figure 7.5: Influence of the gold wetting layer on the j VL characteristics (a), the spectral emission in normal direction at a current density of 14.8 mA/cm^2 (b), color coordinates in normal direction (c), as well as the efficiency-current dependency (d). The introduction of gold wetting layers of 1 nm or 2 nm thickness improves the electrical characteristic and leads to increased spectral emission in the green and red spectral range, which results in a higher device efficiency.

Even though the total metal thickness of the top electrode is increased by up to 40 %, the angular color-stability can be improved (ΔCIE : 1.0 (0 nm Au), 0.96 (1 nm Au), and 0.86 (2 nm Au), normalized to the device without wetting layer). This finding is attributed to the increase and spectral broadening of the top electrode transmittance by the gold wetting layer (cf. Fig. 6.4). In Fig. 7.5(d), the efficiency-current dependencies of the devices are shown. The enhanced emission in the green and red spectral range of the samples with the gold wetting layer increases the EQE of these devices.

At a current density of 3 mA/cm^2 , corresponding to approximately 1000 cd/m^2 , the device with 2 nm gold wetting layer reaches 8.3 % EQE, 28 % higher than for the device without wetting layer (6.5 % EQE). The device with 1 nm Au reaches an EQE of 7.6 %, which is slightly lower than for the device with 2 nm thick wetting layer. As the operating voltages of the wetting layer devices decreased, the improvement in luminous efficacy is even larger than for the EQE. The wetting layer OLEDs reach 19.0 lm/W (2 nm Au) and 17.5 lm/W (1 nm Au) at 3 mA/cm^2 , while the reference device without Au wetting layer has only reached 13.2 lm/W , due to the worse electrical performance. Hence, the device

performance of top-emitting OLEDs using only 5 nm of silver as top electrode can be significantly improved by introducing a gold wetting layer. The wetting layer allows the reduction of the silver layer thickness, while a low sheet resistance is maintained and the transmittance of the top electrode is increased (cf. Chapter 6).

The maintained electrical performance of the wetting layer electrodes preserves the charge balance and the exciton recombination in the top-emitting OLEDs, neglecting a potentially negative impact on the photon generation. Furthermore, the improved device optics in combination with the preserved electrical performance allow the fabrication of angularly color-stable and highly efficient white top-emitting OLEDs.

Comparing the performance of 5 nm Ag electrodes with a 2 nm wetting layer to state-of-the-art 15 nm silver top electrodes, the EQE is improved by a factor of 1.76 and the angular color-shift is reduced by a factor of 3.36, referring to the results presented in Fig. 7.2. In addition, the devices with ultra-thin wetting layer electrodes clearly outperform the literature standard on white top-emitting OLEDs with comparable layer architectures [124, 125], regarding the reported figures of merit.

7.1.3 Comparison to Bottom-Emitting Reference OLEDs

In addition to the investigation of the effects of silver layer thickness and the introduction of a wetting layer on the device performance of white top-emitting OLEDs, the potential of the ultra-thin metal top electrodes is now demonstrated in comparison to a bottom-emitting reference device, which so far gives the benchmark regarding efficiency, color rendering and angular color-stability. Furthermore, the efficiency and angular color-stability of white top-emitting OLEDs with varied silver top electrode thickness is summarized.

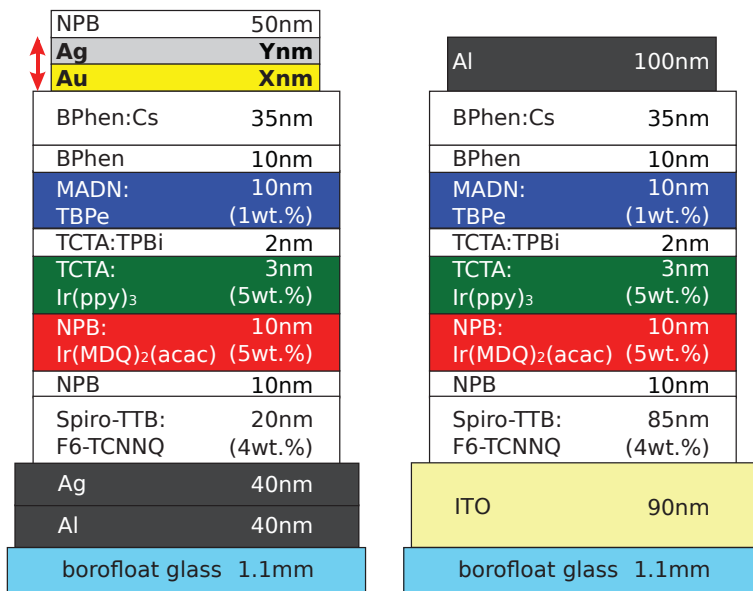


Figure 7.6: Top- and bottom-emitting OLED architectures with identical hybrid white EML system. Both optimized devices are compared regarding electrical performance, efficiency, emission, and angular color-stability.

In order to compare the performance of top- and bottom-emitting OLEDs accordingly, pin-architectures of identical organic materials have been used. In addition, the intrinsic layers EBL, EML, and HBL have been deposited with comparable process parameters (e.g. deposition rate, base pressure), in the same sequence, as well as with identical thickness (see Fig. 7.6) in two sample runs. The anode material of the bottom-emitting device is 90 nm ITO on top of a glass substrate, and 100 nm of Al is used as cathode, according to literature reports.[89]

The doped transport layers have been optimized in preliminary performed experiments, not shown here. For the bottom-emitting device an HTL thickness of 85 nm has been found (20 nm for the top-emitting devices), while the ETL thickness can be kept constant at 35 nm. It is worth to mention that the different optical properties of the transparent electrode materials result in different transport layer thicknesses in the optimized devices. The top-emitting OLEDs are varied regarding the metal top electrodes, with and without 2 nm thick gold wetting layer. The only exception is a device with a 2 nm Au/7 nm Ag wetting layer electrode referred to as "balanced white", which uses an IL with 2.5 nm thickness and HTL of 25 nm thickness in order to reach warm white emission. Figure 7.7(a) shows the current-voltage-luminance dependencies for a small selection of devices, including the bottom-emitting reference, a state-of-the-art top-emitting device with a 15 nm neat Ag electrode, an OLED with an ultra-thin 5 nm wetting layer electrode, and the balanced white device.

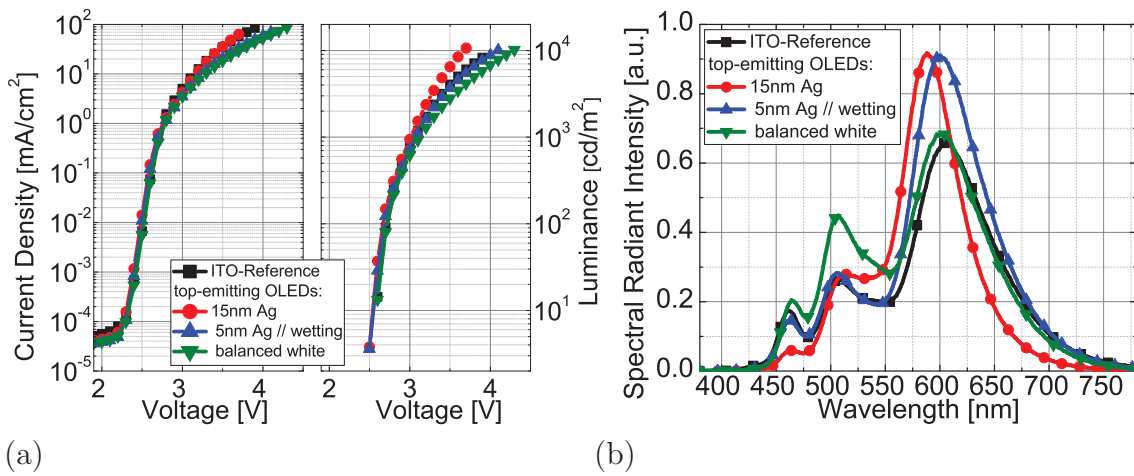


Figure 7.7: Current-voltage-luminance characteristics (a) and spectral radiant intensity in normal direction at a current density of 14.8 mA/cm^2 (b) for top-emitting white OLEDs with different top electrodes and for a bottom-emitting reference with an ITO anode. All devices show comparable leakage currents and operating voltages within a range of 0.3 V for brightnesses up to 3000 cd/m^2 . Wetting layer top OLEDs reach a similar spectral width, while showing more intense emission compared to the bottom-emitting reference device.

The bottom-emitting reference reaches comparable leakage currents in the range of 10^{-5} mA/cm^2 as the top-emitting samples, provided by the smooth ITO bottom electrode. Furthermore, the luminance onset can also be found at 2.5 V like for the top-emitting devices, determined by the tunnel injection into doped organic layers independent from the electrode work function. The current-voltage dependence of the bottom-emitting device shows a nearly identical characteristic as for the top-emitting OLED with a 15 nm silver top electrode, while the wetting layer devices have slightly reduced currents at the same voltage. However, the operating voltages for a brightness up to 3000 cd/m^2 are within a range of 0.3 V.

The spectral radiant intensity in normal direction at a current density of 14.8 mA/cm^2 is shown in Fig. 7.7(b). Except for the top OLED with a 15 nm silver electrode, all devices show broad and intense emission in the spectral range from 450 nm to 750 nm. In addition, the increased transmittance of the transparent ITO electrode compared

to the wetting layer electrode does not lead to a spectral broadening for the investigated OLEDs. This emphasizes that the ultra-thin wetting layer electrode reaches sufficiently high transmittance that top-emitting OLEDs can compete with the optimized bottom-emitting OLEDs using a rather thick ITO anode. The spectral composition of the bottom-emitting device shows a reduced red contribution and similar green and blue emission, compared to the 5 nm wetting electrode top OLED. The balanced white OLED shows a more intense blue and green emission with respect to the ITO reference and the wetting layer device, which is desired to reach the Planckian locus close to the warm white color point A.

Figure 7.8 illustrates the angular color dependencies of the devices from Fig 7.7 in an angle range from 0° to 75° each 5° in the CIE 1931 color space. The top-emitting OLED with a 15 nm state-of-the-art top electrode shows a strong shift of the emission color with the viewing angle. The color is not approaching the Planckian locus, but is situated in the yellowish-green region. The emission colors of all other devices are in proximity to the Planckian locus. The bottom-emitting reference and the 5 nm wetting layer electrode top-emitting OLED show emission at lower CCTs, whereas the balanced white device emits close to the warm white color point A.

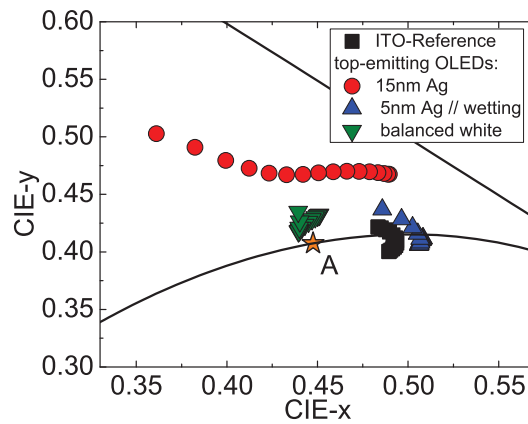


Figure 7.8: CIE 1931 diagram showing the angularly dependent emission of white top-emitting OLEDs with different top electrodes and for a bottom-emitting reference with ITO anode in a range from 0° to 75° . Except for the state-of-the-art 15 nm silver top electrode, the devices show emission close to the Planckian locus and only minor angular color dependence.

In comparison to the 15 nm Ag top-emitting OLED, the bottom-emitting reference shows only a slight variation of the perceived color with increasing viewing angle, corresponding to a high color-stability of this device. Also the top-emitting OLED with 5 nm Ag wetting layer electrode represents a highly color-stable device with only slight change in emission color over the viewing angle, comparable to the bottom-emitting reference. This holds for the balanced white device close to color point A, as well.

In Fig. 7.9, the angular color-shift Δ CIE for silver thicknesses between 5 nm and 15 nm, with and without gold wetting layer are summarized and normalized to the bottom-emitting reference. Furthermore, the luminous efficacy and the external quantum efficiency at a brightnesses of 1000 cd/m^2 for top-emitting OLEDs in comparison to the bottom-emitting reference are shown. The bottom OLED reaches an EQE of 6.7% and a LE of 15.1 lm/W , both higher than for the state-of-the-art top-emitting OLED using

15 nm of Ag as top electrode (EQE: 4.7%, LE: 13.4 lm/W), which is in agreement to previous reports [124, 125].

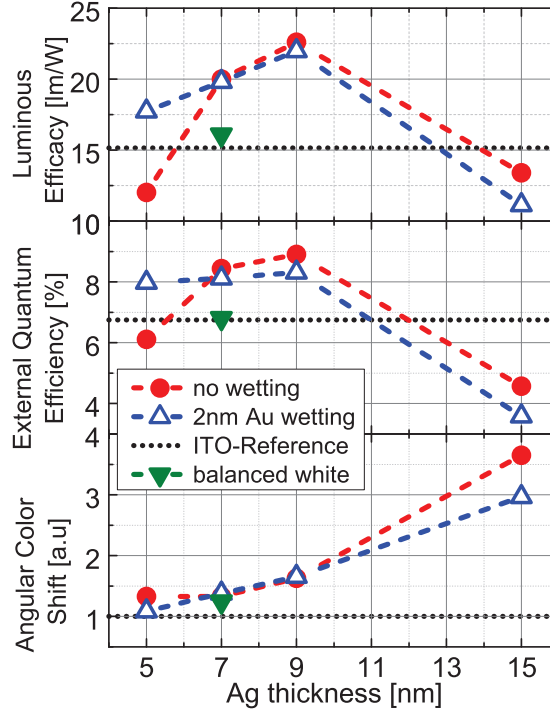


Figure 7.9: Luminous efficacy, external quantum efficiency, and angular color-shift as a function of the silver thickness for samples with and without a 2 nm gold wetting layer. The performance of the bottom-emitting reference is given as dotted line. All OLED performance data are taken at 1000 cd/m^2 .

In Section 7.1.1, the efficiency characteristics of top-emitting OLEDs without a wetting layer and for several Ag layer thicknesses have been investigated. The LE and EQE increased for an Ag reduction from 15 nm to 9 nm to an EQE of 9.0% and a LE of 23.0 lm/W, clearly outperforming the state-of-the-art top-emitting device and the bottom-emitting reference. For a 5 nm Ag electrode, the poor electrical performance has led to a reduction in luminous efficacy to 12.0 lm/W, which is lower than the bottom-emitting reference as well as the top-emitting OLED with a 15 nm Ag electrode.

Introducing 2 nm of gold as wetting layer, the electrode performance is improved, thus increasing the LE, as well as the EQE. The 5 nm Ag electrode with wetting layer shows a similarly high EQE of 8.0%, comparable to the wetting layer devices with 7 nm and 9 nm Ag thickness. The balanced white OLED reaches a LE of 16.2 lm/W and an EQE of 6.8%, comparable to the ITO reference emitting, while warm white emission has been achieved. The IL variation increases the contribution of the fluorescent blue emitter to the spectral emission, while the red emission decreases. Therefore, the EQE of the balanced white device is reduced in comparison to the top-emitting OLEDs with identical top electrode, which further affects the LE. The broadened transmittance characteristics of the wetting layer electrodes lead to comparable or improved angular color-stability for Ag thicknesses in the range from 5 nm to 9 nm, even though the total metal thickness is increased by the wetting layer. In comparison to the 3.5 fold enhanced color-shift of the 15 nm Ag top electrode to the bottom-emitting reference, a reduction to 7 nm Ag

thickness decreases the shift, resulting in an only 30% increased instability. The top-emitting OLED with 5 nm Ag wetting layer electrode reaches an angular color-stability comparable to the bottom-emitting reference device, even though the transmittance of the wetting layer electrode is lower than for ITO. Moreover, the efficiency of the top-emitting OLED remains higher in comparison to the bottom-emitting reference.

Finally, these results illustrate that highly transparent wetting layer electrodes on top-emitting OLEDs enable the fabrication of angularly color-stable devices, comparable to the bottom-emitting benchmark, even though the transmittance is not completely reached by the wetting layer electrodes. In addition, such top-emitting OLEDs can at least compete with bottom-emitting references in terms of device efficiency.

Overall, the findings emphasize the potential of the wetting layer electrodes to be established as a new standard for highly efficient white top-emitting OLEDs, as devices using silver electrodes with 15 nm thickness are outperformed regarding both, the angular color-stability and the device efficiency.

7.2 Stacked Inverted White Top-Emitting OLEDs

For display applications, inverted top-emitting OLED architectures are preferred, as they provide benefits in regard to the electrical circuit integration in comparison to non-inverted structures, while both would allow for a direct fabrication on a display back plane.[232] The application of n-doped TFTs, which usually outperform p-TFTs, in combination with inverted OLEDs is expected to additionally improve the overall display performance. However, inverted OLED designs often exhibit lower electrical performance in comparison to non-inverted OLEDs, which has been associated with deficits in the charge carrier injection, even though doped charge transport layers have also been applied.[63] Furthermore, a charge carrier unbalance can reduce the internal quantum efficiency, as well as imply a shift of the exciton recombination zone.

In the following, inverted white top-emitting OLEDs using MoO₃/Au wetting layers are investigated in order to improve the optical properties and the electrical performance of inverted OLEDs. As shown in Chapter 6, the application of such a wetting layer results in highly transparent, ultra-thin, and conductive silver top electrodes on p-doped organics. To demonstrate the full potential of the wetting layer concept, improving the optical properties of top-emitting OLEDs, investigations of tandem white top-emitting OLED architectures are presented.

A tandem OLED architecture consists of two OLEDs connected in series via a pn-junction. They often reach higher EQE and LE values compared to single unit devices, as a charge generation pn-junction between both sub-units generates an additional charge carrier pair to the injected one. The generated charge carriers do not only improve the device efficiency, but further reduce the required current density needed to reach a certain brightness level, which increases the device lifetime.[233] Tandem OLEDs are therefore often preferred in terms of solid-state lighting applications. However, such OLEDs are rather complex and require a large number of organic layers. In addition, the increased cavity length improves the impact of microcavity effects on the emission characteristics. To overcome the limitations introduced by prominent microcavity effects, an excellent top electrode performance is required, whereas the beneficial properties of tandem OLED architectures can be used to obtain highly efficient top-emitting OLEDs.

Figure 7.10 shows a state-of-the-art bottom-emitting tandem OLED, which sets the benchmark in terms of the efficiency and angular color-stability [81, 105], as well a top-emitting OLED using a MoO₃/Au wetting layer based on the same architecture but with inverted organic layer sequence. The tandem layout consists of a full phosphorescent green/yellow unit, as well as a triplet-harvesting blue/red unit. Again, doped charge transport layers are applied to reduce the operating voltage and to optimize the device optics without drawbacks on the electrical performance. The charge generation contact is formed by a pn-junction of MeO-TPD:F6-TCNNQ and BPhen:Cs, including a 0.5 nm thick Ag layer. The optimization of the bottom-emitting tandem architecture regarding the incorporated organic materials, doping concentrations, as well as layer thicknesses have been investigated in detail by Rosenow [234] and Hofmann [88]. The optimization of the inverted top-emitting devices has been performed in several preliminary experiments, including the variation of the transport layer thicknesses to optimize the cavity length and EML positions, but are not shown in detail here.

MeO-TPD is deposited instead of the previously used Spiro-TTB, in order to compare the results to the bottom-emitting reference device reported, without an impact from an HTL variation. The inverted top-emitting OLEDs further uses an electron injection layer of BPhen:Cs doped with Ag, according to reports by Thomschke *et al.*[63].

Al	100nm	Spiro-TAD	60nm
BPhen:Cs	60nm	Ag	Ynm
TPBi	10nm	Au	2nm
TPBi:Ir(dhfpv) ₂ (acac): 5nm Ir(ppy) ₃ (91:1:8wt.%)		MoO ₃	1nm
TCTA:Ir(dhfpv) ₂ (acac): 5nm Ir(ppy) ₃ (91:1:8wt.%)		MeO-TPD:	Xnm
Spiro-TAD	10nm	F6-TCNNQ	(4wt.%)
MeO-TPD:	75nm	Spiro-TAD	10nm
F6-TCNNQ	(4wt.%)	4P-NPD:	5nm
Ag	0.5nm	Ir(MDQ)₂(acac)	(10wt.%)
BPhen:Cs	90nm	4P-NPD	4nm
BPhen	10nm	BPhen	10nm
4P-NPD	4nm	BPhen:Cs	110nm
4P-NPD:	5nm	Ag	0.5nm
Ir(MDQ)₂(acac)	(10wt.%)	MeO-TPD:	65nm
Spiro-TAD	10nm	F6-TCNNQ	(4wt.%)
MeO-TPD:	30nm	Spiro-TAD	10nm
F6-TCNNQ	(4wt.%)	TCTA:Ir(dhfpv) ₂ (acac): 5nm Ir(ppy) ₃ (91:1:8wt.%)	
ITO	90nm	TPBi:Ir(dhfpv) ₂ (acac): 5nm Ir(ppy) ₃ (91:1:8wt.%)	
borofloat glass 1.1mm		TPBi	10nm
		BPhen:Cs	40nm
		BPhen:Cs:Ag	5nm
		Ag	40nm
		Al	40nm
		borofloat glass 1.1mm	

(a)

(b)

Figure 7.10: Bottom-emitting tandem OLED containing a fully phosphorescent green/yellow and a triplet-harvesting blue/red emitting sub-unit according to literature reports [81, 88] (a). Top-emitting OLED architecture with fully inverted organic layer sequence compared to (a), using a highly transparent MoO₃/Au/Ag top electrode as investigated in Section 6.2 (b). Both devices have been optimized by optical simulation for efficient white emission.

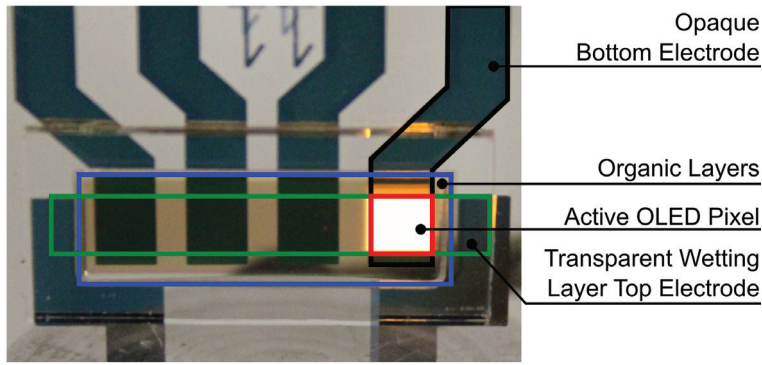


Figure 7.11: Photo of an inverted tandem white top-emitting OLED using a highly transparent $\text{MoO}_3/\text{Au}/\text{Ag}$ electrode.

In Fig. 7.11, a photograph of the top-emitting tandem architecture is shown. The area covered by the wetting layer top electrode can only barely be distinguished from the organic layers, emphasizing its high transmittance. The doped organic layers show absorption in the blue spectral range and thus introduce a reddish color appearance.

In Fig. 7.12(a), the current-voltage and luminance-voltage curves of the bottom OLED and the inverted top-emitting tandem OLEDs are compared for positive bias. The bottom OLED shows a luminance onset at 5.0 V, while the inverted top-emitting devices require a voltage of 5.5 V. Considering the fact that a tandem OLED design is used and the voltages are given by the sum of the potential which drops over each single unit, these voltages are remarkably low. The introduction of the MoO_3/Au wetting layer increases the slope of the jV characteristics compared to the inverted top-emitting OLED with a neat 15 nm thick Ag electrode.

and the inverted top-emitting tandem OLEDs are compared for positive bias. The bottom OLED shows a luminance onset at 5.0 V, while the inverted top-emitting devices require a voltage of 5.5 V. Considering the fact that a tandem OLED design is used and the voltages are given by the sum of the potential which drops over each single unit, these voltages are remarkably low. The introduction of the MoO_3/Au wetting layer increases the slope of the jV characteristics compared to the inverted top-emitting OLED with a neat 15 nm thick Ag electrode.

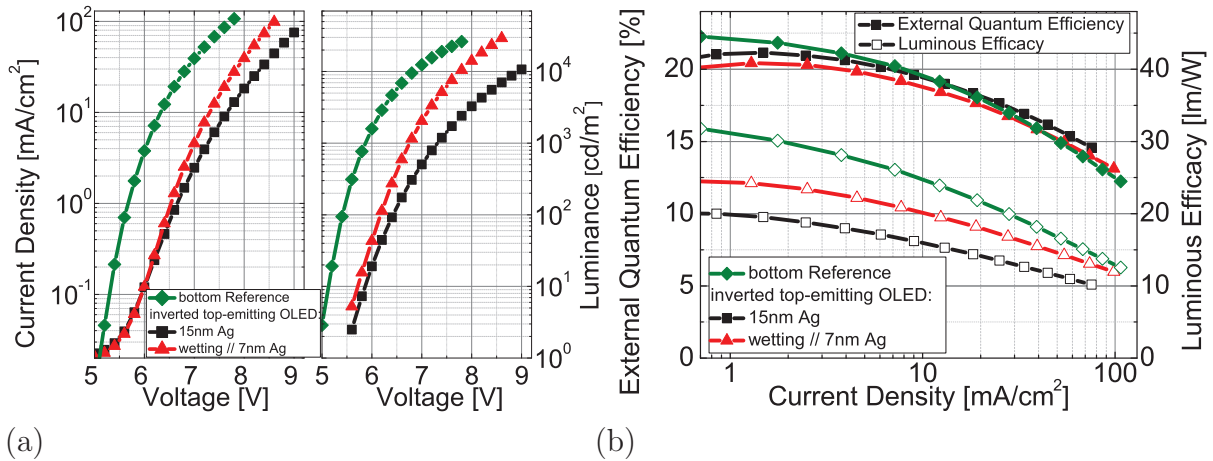


Figure 7.12: Current-voltage and luminance-voltage (a), as well as the efficiency-current dependency (b) of a bottom-emitting OLED and two inverted top-emitting OLEDs with a 15 nm Ag electrode, or a wetting layer top electrode. The inverted top-emitting OLED with a neat silver electrode has a smaller slope of the jV characteristic compared to the bottom-emitting reference. Including the MoO_3/Au wetting layer, the slope of the jV -curve increases and the operating voltage is reduced by up to 1 V compared to the device with a conventional 15 nm thick Ag top contact.[154] EQEs of 20 % are reached by all devices, while the LE of the inverted OLED with wetting layer can be enhanced by 25 % due to the improved jV characteristic.

This finding is attributed to an improved injection of holes by the MoO₃ layer.[95, 96] The improvement of the electrical characteristics applying MoO₃ in inverted OLEDs is further validated by results presented in Appendix B. The operation voltage in the inverted OLEDs using a MoO₃/Au wetting layer is reduced by 0.6 V at 1000 cd/m², and by more than 1 V for brightnesses higher than 6000 cd/m². However, at 1000 cd/m², the operation voltage is still about 0.7 V lower for the bottom OLED compared to the inverted wetting layer device. The remaining voltage off-set is likely to be attributed to remaining differences in the interface formation, as well as potentially affected charge injection, transport, and recombination for the inverted tandem OLEDs, even though the jVL characteristics have been improved by the wetting layer. It is expected that by further optimizing the inverted OLED stack, e.g. including MoO₃ at the charge generation contact between both units, the present limitations can be overcome.

All devices reach EQEs of approximately 20 % for a brightness of 1000 cd/m² ($\approx 2 \text{ mA/cm}^2$) (Fig. 7.12(b)). These results demonstrate that inverted white top-emitting OLEDs can achieve efficiencies comparable to optimized bottom-emitting OLEDs.[154] According to the results in Section 7.1.3, it is assumed that the EQE of the inverted top-emitting OLEDs can also surpass the efficiency of the non-inverted bottom-emitting devices, benefiting from a remaining Purcell effect and the lack of trapped light modes in the glass substrate and the ITO electrode. So far, it cannot be excluded that the inversion of the organic layer sequence had an adverse impact on the internal quantum efficiency, limiting the EQE in the inverted devices. The bottom-emitting reference reaches a LE of 30 lm/W for 1000 cd/m². The inverted top-emitting OLED with standard 15 nm thick Ag electrode reaches 20 lm/W in the same brightness range.

Including the wetting layer electrode, the LE improves by 25 % to 25 lm/W, which represents the highest reported value for inverted top-emitting white OLEDs so far (13.6 lm/W by Thomschke *et al.* [124]). The spectral radiant intensity in normal direction has been recorded at a current density of 14.8 mA/cm² and is shown in Fig. 7.13(a).

The incorporated deep blue emitter 4P-NPD enables emission of the devices starting from 400 nm. Contributions of the three other emitters generate a broad spectral emission almost covering the entire visible spectral range. Compared to the bottom-emitting reference, the top-emitting OLEDs show reduced emission ratios in all spectral ranges except for the red and is most prominent for the low blue emission. Thus, also the lower emission in the green and yellow spectral regime has contributed to the reduced luminous efficacy of the inverted top-emitting devices with respect to the bottom-emitting reference. These differences are expected to be mainly attributed to the different optical properties of the bottom and top-emitting OLEDs, even though the microcavities have been optimized for broad emission. The top-emitting OLED with a 15 nm thick Ag top electrode shows a narrowing and shift of the red peak emission ($\approx 653 \text{ nm}$), compared to the bottom-emitting OLED and the wetting layer device ($\approx 610 \text{ nm}$). The prominent microcavity effects in this device also reduce blue, green, and yellow emission compared to the wetting layer OLED. In order to increase the spectral emission of top-emitting OLEDs in these spectral regimes, several variations of the OLED architecture can be performed and are exemplary shown in Appendix A. Here, the HTL thickness in the blue/red unit of a wetting layer device has been increased from 40 nm to 50 nm to control the emission spectrum. This device is labeled as "balanced white".

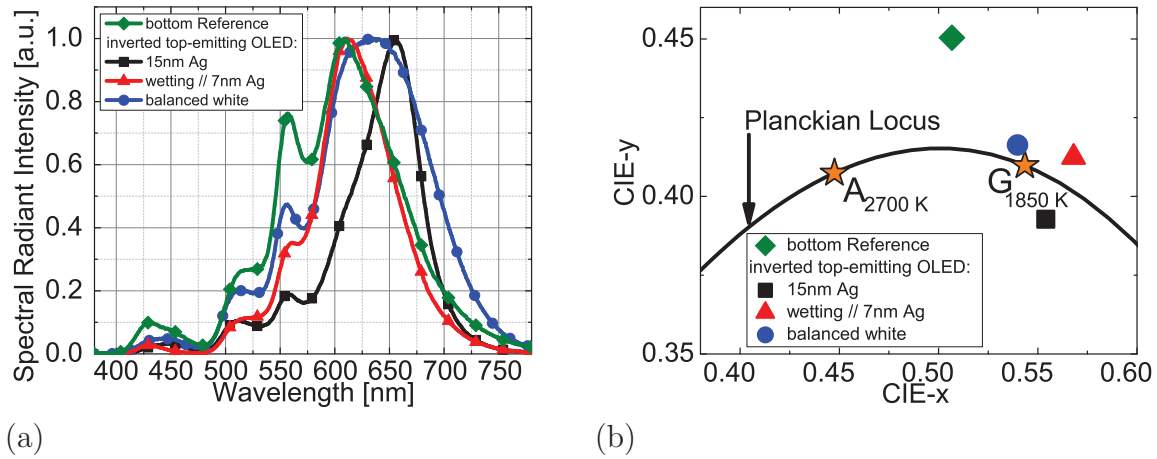
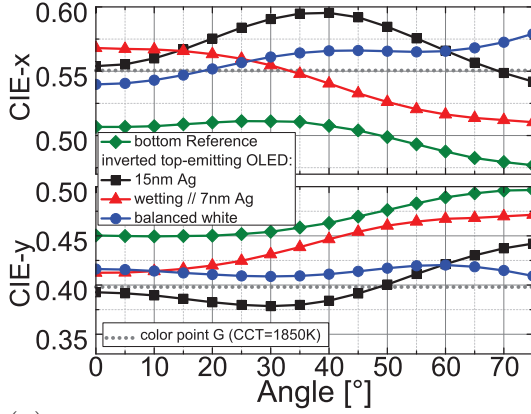


Figure 7.13: Normalized spectral radiant intensity in forward direction (a) and correlated CIE coordinates (b) of the devices from Fig. 7.12 and a balanced white top-emitting OLED. For all devices, emission of the four emitters included, almost covering the entire visible spectral range, is detected. Emission close to the Planckian Locus at a candle light white "G" (CCT: 1850 K) color is detected for the top-emitting devices.

The modified top-emitting OLED shows more intense emission contributions in the green/yellow spectral regime, while only minor changes of the blue emission are detected. The red emission shows a large broadening of the emission with prominent contributions even for wavelengths larger than 700 nm. As a variation of a doped transport layer only affects the device optics, the spectral change can be directly attributed to an emission affinity increase at larger wavelengths.

The overall low contribution of blue emission leads to color coordinates at lower CCTs compared to the warm white color point A (see Fig. 7.13(b)). Here, a "candle light" white emission with a CCT of 1850 K is achieved by the balanced white top-emitting OLED. Attributed to the spectral changes in the modified device, the LE decreases to 17.5 lm/W, even though the EQE remains at 20.2% at 1000 cd/m². The emission of the bottom-emitting reference is shifted to larger CIE-y coordinates, as expected by the intense yellow emission. The broad emission, which covers almost the entire visible spectral range, results in excellent color rendering of the balanced white top-emitting OLED (CRI: 94), sufficient for all applications requiring high quality white light.[154]

In addition, the balanced white inverted top-emitting OLED shows a superior angular color-stability (Δ CIE: 0.78) compared to the other top-emitting OLEDs, as well as the bottom-emitting reference device (Δ CIE: 1.0), in an angle range of 0° to 75° (Fig. 7.14(a)). As expected, microcavity effects of the top-emitting OLED with 15 nm thick Ag top electrode lead to a large deviation of the perceived color with the viewing angle (Δ CIE: 2.73), not desired for lighting applications. Introducing the highly transparent wetting layer electrode, the angular color-shift is significantly reduced (Δ CIE: 2.19), but still prominent compared to the bottom-emitting reference, as long as the microcavity is not carefully adjusted. In Fig. 7.14(b), the CRI and the angular color-shift Δ CIE of the devices are summarized.



(a)

Sample	CRI	Δ CIE
bottom reference	73	1.0
inverted top-emitting OLEDs		
15 nm Ag	86	2.73
wetting // 7 nm Ag	73	2.19
balanced white	94	0.78

(b)

Figure 7.14: CIE-x and CIE-y coordinates as a function of the observation angle (a). Introducing the wetting layer, the angular color-shift, even compared to the bottom-emitting reference can be reduced. Summary of the color rendering index (CRI) and color-stability (Δ CIE) of the different tandem OLEDs (b).

In conclusion, the microcavity effects of tandem inverted white top-emitting OLEDs have been reduced by ultra-thin and highly transparent $\text{MoO}_3/\text{Au}/\text{Ag}$ top electrodes. Hence, these devices show improved color rendering and angular color-stability compared to an optimized bottom-emitting white OLED with an ITO electrode and a standard top-emitting OLED with a neat silver electrode of 15 nm thickness. These results emphasize that the wetting layer concept is also suitable to overcome the limitations of stacked top-emitting OLEDs, preferred for solid-state lighting applications, as microcavity effects are significantly reduced.

In addition, the MoO_3/Au wetting layer improves the current-voltage characteristics, resulting in a reduction of the operating voltage of up to 1 V, compared to inverted OLEDs with a neat silver top electrode. This consequences an increase in luminous efficacy of the inverted OLEDs with wetting layer electrode. Even though the inverted top-emitting OLEDs reaches comparable EQE values to the bottom-emitting reference, the remaining increased operation voltage results in lower luminous efficacies in comparison to non-inverted device architectures. This emphasizes the demand on the further analysis and optimization of inverted nip-OLED designs, in order to be competitive to pin-OLEDs. Nevertheless, an improvement of the luminous efficacy by 25% has been achieved in this work.

Overall, the wetting layer concept showed for the first time the applicability of top-emitting tandem OLED architectures for the realization of angularly color-stable and high color quality white emission suitable for solid-state lighting applications.

7.3 ITO-Free Transparent White OLEDs

A further application of the ultra-thin and highly transparent wetting layer metal electrodes are bi-directional emitting transparent OLEDs. Transparent OLEDs are of special interest, e.g. for the integration in windshields as a head up display, or in windows for lighting applications. In its off-state, the device should be as transparent as possible, while bright emission should be achieved during operation. The used organic materials addressed in this thesis are almost completely transparent in the visible spectral range, while only the dopants show little absorption. Therefore, the total transmittance of a transparent OLED is mainly determined by the two transparent electrodes.

In the following section, experiments on bi-directional emitting transparent OLEDs using two wetting layer electrodes are presented. The focus is set on maximum device transmittance with maintained electrical characteristics. Furthermore, the device efficiency and spectral emission through both transparent electrodes is investigated.

7.3.1 Total Transmittance of ITO-Free Transparent OLEDs

For experiments on transparent OLEDs, ITO-free samples containing a $\text{MoO}_3/\text{Au}/\text{Ag}$ electrode on the glass substrate and an Au/Ag electrode on top of the organic layer sequence have been prepared (see Fig. 7.15). Reference devices use a 90 nm thick ITO bottom electrode, replacing the $\text{MoO}_3/\text{Au}/\text{Ag}$ electrode, while all other parameters remain constant.

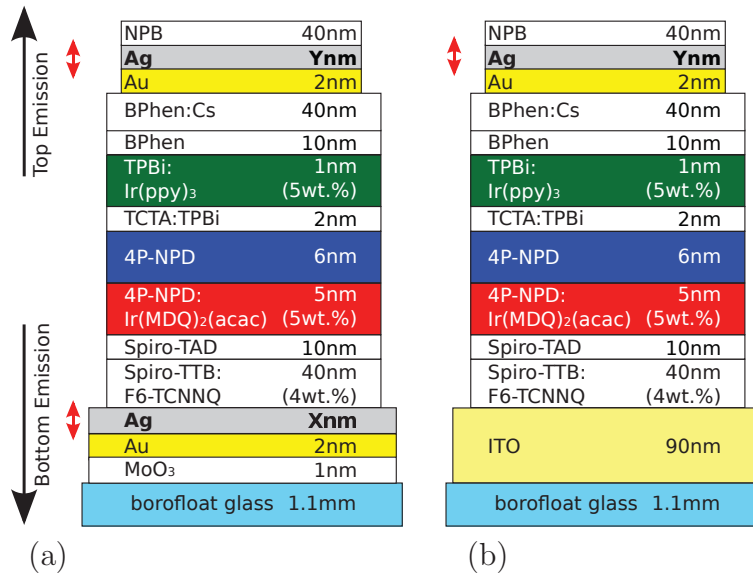


Figure 7.15: Architectures of transparent OLEDs using Au/Ag wetting layer top electrodes and $\text{MoO}_3/\text{Au}/\text{Ag}$ (a) or ITO (b) bottom electrodes. A triplet-harvesting blue/red unit and a phosphorescent green EML are deposited for white emission.

For white light generation, blue and red emission is obtained from a triplet-harvesting unit using 4P-NPD and $\text{Ir}(\text{MDQ})_2(\text{acac})$, while green emission is generated by the phosphorescent emitter $\text{Ir}(\text{ppy})_3$. For the optimization of the ITO-free devices, the silver thickness of either the bottom or top electrode is varied, while the other electrode is kept constant. In Fig. 7.16(a), the total transmittance of the entire transparent OLED

including the glass substrate is shown for a variation of the bottom electrode. The top wetting layer electrode has a silver thickness of 7 nm. With decreasing silver thickness of the bottom electrode, the total transmittance increases, reaching approximately 66% in a spectral range between 450 nm and 675 nm using 3 nm of Ag in the bottom electrode. To my best knowledge, these results represent the highest total transmittance of transparent OLEDs without the application of TCO electrodes.[235] Furthermore, the ITO benchmark reaches only slightly increased transmittance of 70.1% in a wide spectral range.

The results of the ITO reference are comparable to literature reports where two TCO electrodes have been used [236], instead of a TCO and metal electrode, which emphasizes the extraordinarily high transmittance of the Au/Ag top electrode. In addition, all samples with a silver bottom electrode thickness between 3 and 15 nm show an almost dispersion free transmittance in a spectral range between 450 nm and 675 nm.

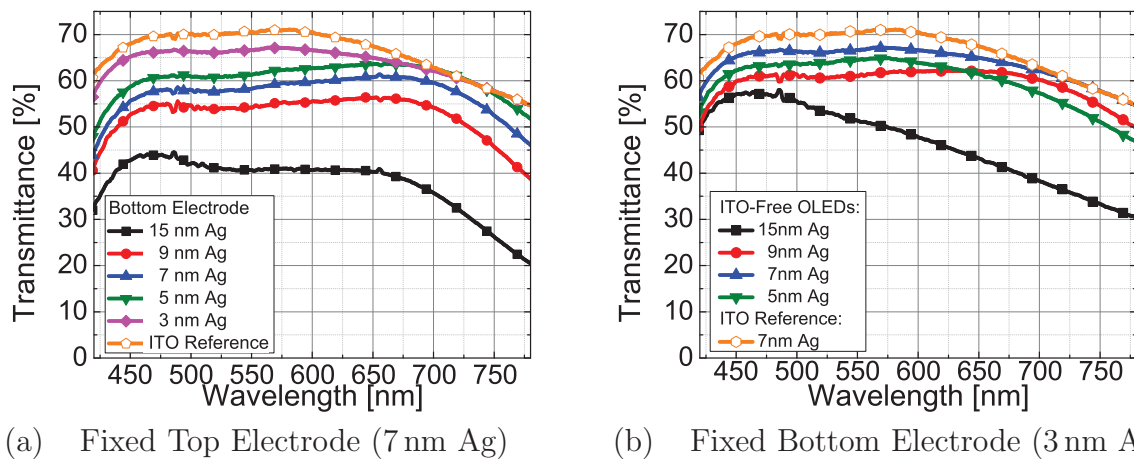


Figure 7.16: Spectral transmittance of the OLEDs for varied bottom electrode thickness and a fixed wetting layer top electrode (a), as well as varied top electrode and fixed wetting bottom electrode (b). In contrast to the top electrode variation, the dispersion of the spectral transmittance remains nearly unaffected for a variation of the bottom electrode. The combination of 3 nm bottom and 7 nm top Ag thickness yields in a remarkable transmittance of 66% between 450 nm and 675 nm, nearly approaching the ITO reference.

An increase of the top electrode silver thickness up to 9 nm, while the bottom electrode is fixed at 3 nm of silver, results in an almost unaffected transmittance (see Fig. 7.16(b)). For a 15 nm thick top electrode, the transmittance is significantly reduced, while a steady decrease for increasing wavelengths is detected. This trend is comparable to the transmittance of the single electrode. A maximum total transmittance is found for a combination of a 3 nm silver bottom electrode and a 7 nm top electrode, both using wetting layers. Figure 7.17 shows a photograph of the transparent OLED architectures with a 3 nm bottom electrode or an ITO electrode, both using a 2 nm Au/ 7 nm Ag top electrode, respectively. Even though the ITO reference device is slightly more transparent, the ITO-free OLED allows an excellent readability of the IAPP logo in the background. The current-voltage characteristics of the transparent, bi-directional emitting OLEDs are shown in Fig. 7.18. For a variation of the bottom electrode, the current-voltage characteristics show comparable electrical performance in the investigated silver thickness

range from 3 to 15 nm with a diode onset at 2.5 V (see Fig. 7.18(a)). These results prove that the MoO₃/Au wetting layer can further be used to grow ultra-thin, transparent, and conductive silver films directly on glass substrates as well.

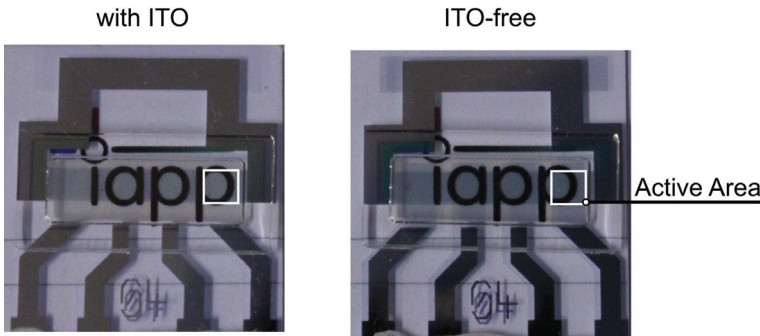


Figure 7.17: Image of an ITO-free and an ITO containing transparent OLED. Excellent visibility of the background IAPP logo is given for both devices.

The use of ITO as bottom electrode shows no beneficial effects on the electrical characteristics, as the operational voltages and leakage currents are similar to the ITO-free devices (see Fig. 7.18(a)). In Fig. 7.18(b) the influence of the top electrode silver thickness on the jV characteristics is shown. The ITO-free devices use a bottom electrode with a 3 nm thick Ag film. Again, comparable jV-curves are reached by the ITO con-

taining devices. It is noted that all devices with the 3 nm thick Ag bottom electrode show an excellent electrical performance, emphasizing the reliability of such thin wetting layer electrodes.

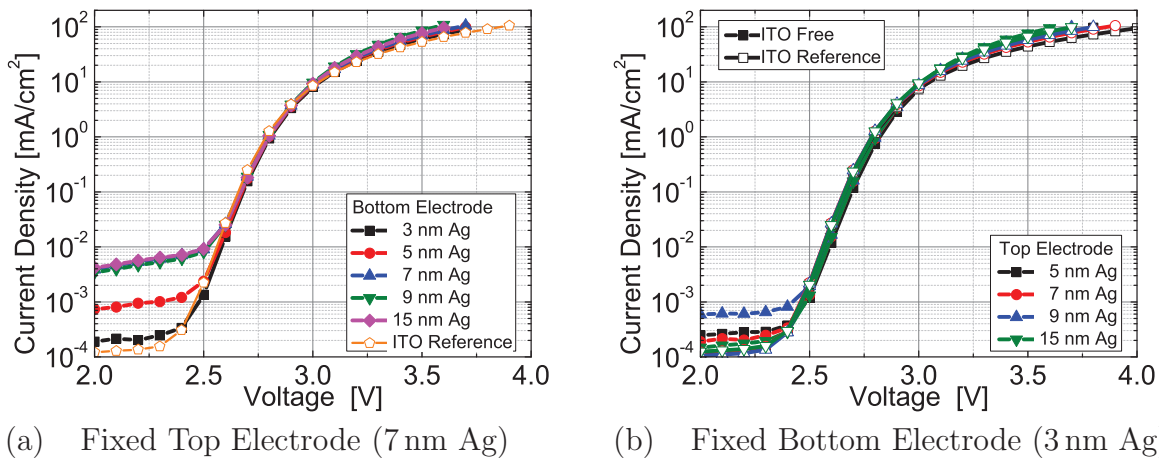


Figure 7.18: Current-voltage curves of transparent OLEDs for a varied bottom electrode thickness and a fixed Ag wetting top electrode (a), as well as a varied top electrode and fixed wetting bottom electrode (b). All devices show a comparable onset voltage of 2.5 V. Only small deviations between ITO references and ITO-free wetting layer OLEDs are observed. The impressively thin bottom electrode of MoO₃/Au and 3 nm of Ag shows an almost identical jV performance as the ITO reference.

7.3.2 Performance of Transparent OLEDs with Fixed Top Electrode

Investigations on the bi-directional characteristics of transparent OLEDs with a fixed top electrode of 2 nm Au and 7 nm Ag are shown in the following. In dependence on the final application, balanced emission with identical color through both electrodes is

desired, e.g. as partition elements in indoor architecture. Figure 7.19 shows a series of images of transparent ITO-free OLEDs for several current densities.

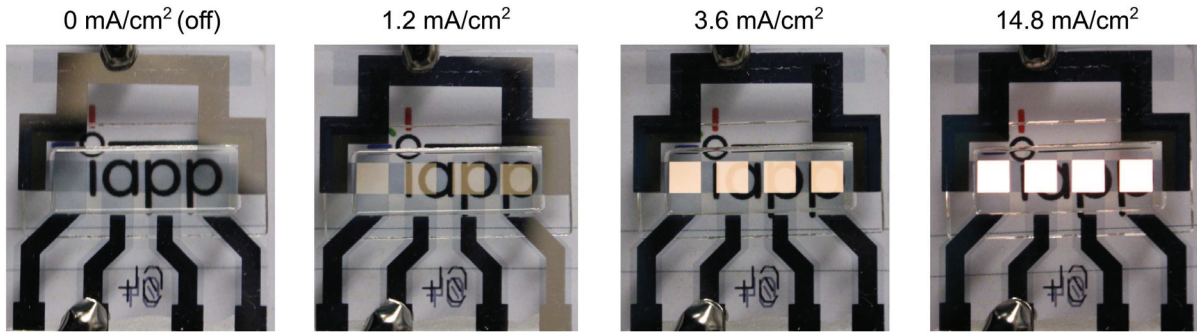


Figure 7.19: Images of a transparent ITO-free OLED for different current densities. For increasing current density values, the emission turns the initially transparent device in a bright white light-emitting OLED.

In the off-state, the background can be perfectly seen. For increasing currents, the brightness increases so that at a certain level, it is not possible to see through the transparent OLEDs. Emission spectra of the transparent OLEDs have been recorded in normal direction at a current density of 14.8 mA/cm^2 . In Fig. 7.20(a), the emission for a variation of the bottom electrode are shown in bottom direction. With a reduction of the silver layer thickness, and thus an increase of the transmittance, the emission intensity increases in the entire spectral range, but most prominent in the red. Overall, the spectral shape remains very similar for the investigated silver thicknesses between 3 nm and 15 nm. All samples show broad emission from 400 nm to 780 nm, while for the ITO-free OLEDs the intensity of the green emission is comparably weak.

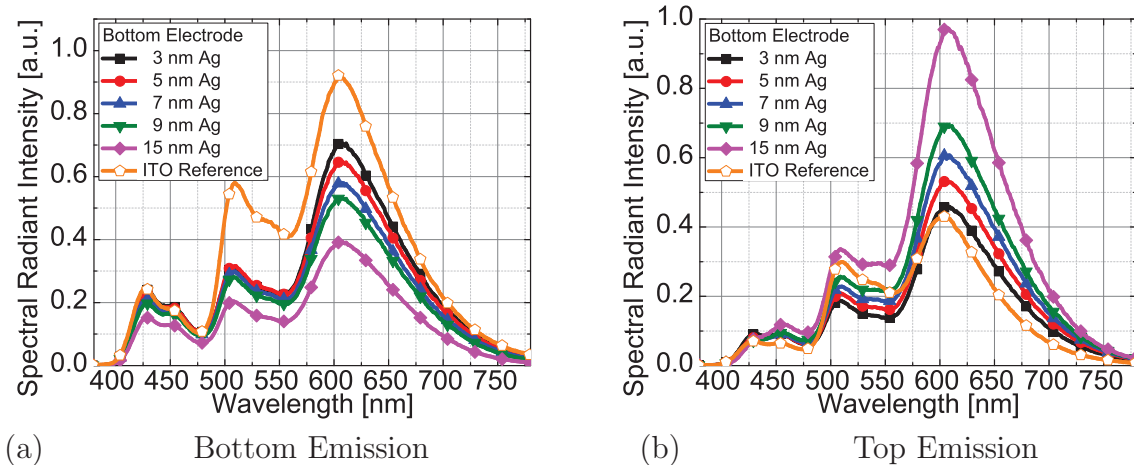


Figure 7.20: Spectral radiant intensity in normal direction at a current density of 14.8 mA/cm^2 in bottom (a) and top (b) emission geometry for a variation of the bottom electrode, while the top electrode is kept constant at 2 nm Au and 7 nm of Ag. The emission between top and bottom direction can be balanced by the bottom electrode. Emission through the top electrode shows pronounced red emission, while the blue emission contribution is significantly reduced compared to the bottom emission.

The ITO reference shows the most intense emission, especially in the green and red spectral region. The spectral differences can be caused by different device optics, as an identical organic layer sequence has been used for ITO-free and ITO containing devices, but the ITO electrode is by far thicker than the metal electrode. However, the significant increase in green emission might also be attributed to other effects, e.g. a slightly shifted charge balance by the different electrodes.

For top emission (see Fig. 7.20(b)), the opposite trend in emission intensity is observed. With increasing bottom silver thickness, the transmittance of the bottom electrode is decreased and more light is reflected, which leads to increased top emission. Again, the increase is most prominently in the red and green spectral regime. Here, the ITO reference reaches a comparable intensity as the ITO-free device with a 3 nm thick Ag film, while the green emission remains increased. Comparing the emission spectra in bottom and top direction, a significant reduction of the blue emission is observed in top emission, while the red emission becomes more prominent. This finding is in agreement with the spectral emission detected for the top-emitting OLEDs investigated in the previous sections, which also lack in blue emission. Even for a device with a comparable wetting layer electrode on both sides (7 nm of silver), the spectral differences are prominent. Hence, the emission colors in bottom and top direction differ and the color to the top is shifted to the red region of the CIE color space and thus to lower CCTs, as shown in Fig. 7.21. The smallest color difference between both directions of the ITO-free devices is obtained for a 3 nm thick silver bottom electrode.

Even though the color difference is smaller for the ITO reference, a prominent shift of the color coordinate with the emission direction can still be observed. As these emission differences cannot be induced by the electrics, the optical properties have to determine the changes between top and bottom emission. Potentially, the asymmetric layer architecture regarding the two transparent electrodes causes the observed deviations in the spectral emission.

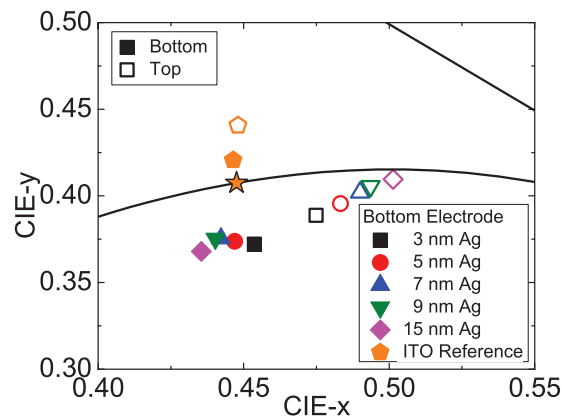


Figure 7.21: CIE color coordinates in normal direction in top and bottom emission for a variation of the bottom electrode, while the top electrode is kept constant at 2 nm of gold and 7 nm of silver. Different emission colors in bottom and top emission are detected for all devices, including the ITO reference. The ITO-free transparent OLEDs show a red shift of the emission color in top emission compared to the bottom direction.

Figure 7.22(a) shows the simulated spectral radiant intensity in normal direction of the bi-directional OLEDs according to the architectures in Fig. 7.15, normalized to the maximum value.

While the top electrode is kept constant at 2 nm Au and 7 nm Ag thickness, the bottom electrode is varied. For the simulation of the transparent OLEDs, the optical properties of the wetting layer electrodes has been described in accordance to the investigations in Chapter 6, using either bulk layers for homogeneously closed metal films or the Maxwell-Garnett model for granular films. It is worth to note that for silver thicknesses of 7 nm on the MoO₃/Au wetting layer, a bulk layer assumption yields good agreement with the measured transmittance.

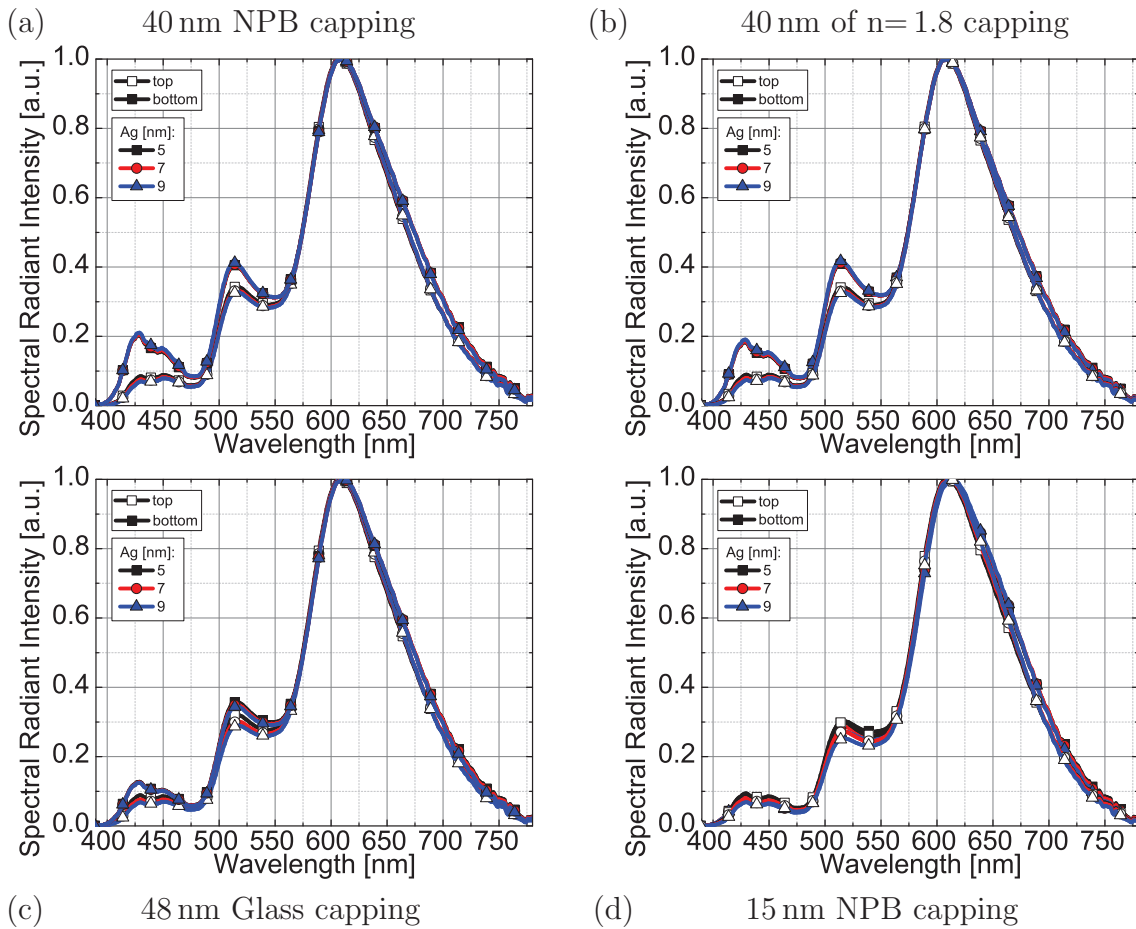


Figure 7.22: Simulated spectral radiant intensity in normal direction and normalized to the maximum value. The top electrode is kept at thicknesses of 2 nm Au and 7 nm Ag. In order to analyze the origin of the spectral deviations in bottom and top emission, the NPB capping layer is varied. In (a), a NPB layer as in the real device architecture is used, while it is replaced by a layer of constant refractive index of 1.8 (b), or by glass (c) with identical optical thicknesses. Neglecting the refractive index dispersion does not significantly affect the spectral emission, a replacement by glass, reduces the spectral deviations, while the overall amount of blue emission decreases. A readjustment of the NPB layer to 15 nm thickness leads to comparable emission in both directions (d), even though the blue emission is lower than in (a).

The emission intensities of the single EMLs has been arbitrary fixed to reproduce the observed intensity distribution of the measured spectra. The simulations reproduce the observed deviations in spectral emission for top and bottom direction from Fig. 7.20. This proves that the differences are associated to the device optics. Furthermore, the simulation results indicate that a lower blue contribution might also be observed in the device spectra of white top-emitting OLEDs in comparison to a bottom-emitting reference device, resulting in lower CCTs.

In bottom emission, the light is extracted from glass, with an almost dispersion free refractive index of 1.54, into air. For top emission, the light is extracted from NPB into air, which has a larger refractive index with a much more pronounced dispersion. Hence, the impact of the refractive index and its dispersion of the organic capping layer material is investigated.

A first attempt to analyze the emission deviations is therefore based on the replacement of the NPB capping layer by an arbitrary organic material with a refractive index of 1.8. This corresponds to the refractive index of NPB at 600 nm wavelength, but neglects any dispersion effects, which influence the spectral reflectance according to Eq. 4.12.

In Fig. 7.22(b), the simulated spectra for this sample set are shown. The spectra do not show significant changes compared to the results for the capping layer of NPB. Thus, an impact of the dispersive characteristics of the organic capping layer in comparison to glass can be excluded to cause the spectral deviations. Another attempt is based on the replacement of the NPB capping layer by a capping layer of glass. Hence, for both directions light is transferred from the metal electrodes into glass and finally extracted to air. Therefore, the impact of the total refractive index can be investigated, while the optical thickness of the capping layer is maintained. The simulated spectra for bottom and top emission direction are shown in Fig. 7.22(c). In comparison to the previous results, the spectral deviations are reduced. The emission to the top remains nearly constant, while the blue and green contribution is reduced for bottom emission. The simulation results emphasize that the spectral changes might occur due to the affected refractive index jump at the capping layer/air interface, even though the optical thickness remains constant.

Independently from a potential impact of the material properties, the NPB capping layer has been varied in thickness, in order to achieve symmetrical emission from the bi-directional transparent OLEDs. The best agreement for emission in both directions has been achieved for a thickness reduction of NPB from 40 nm to 15 nm. Overall, the thickness optimization of the OLED architecture either by a material variation, or just a readjustment of the capping layer material, leads to similar spectral emission to both sides, desired in most devices. As a sputtering deposition of SiO₂ as capping layer potentially harms the organic layers underneath, an optimization of the NPB capping layer is assumed to be favorable. However, a suppressed blue emission is now present for both emission directions, which is disadvantageous for reaching the warm white color point A. Figure 7.23 shows the EQE and LE for the transparent OLEDs for bottom and top direction, as well as for the overall emission. The efficiency values have been recorded at a brightness of 1000 cd/m². In bottom direction, the EQE shows a continuous decrease for increasing bottom Ag thickness, while the efficiency in top direction increases. This trend is predicted by the affected transmittance of the bottom electrode, which leads to a redistribution of the emission.

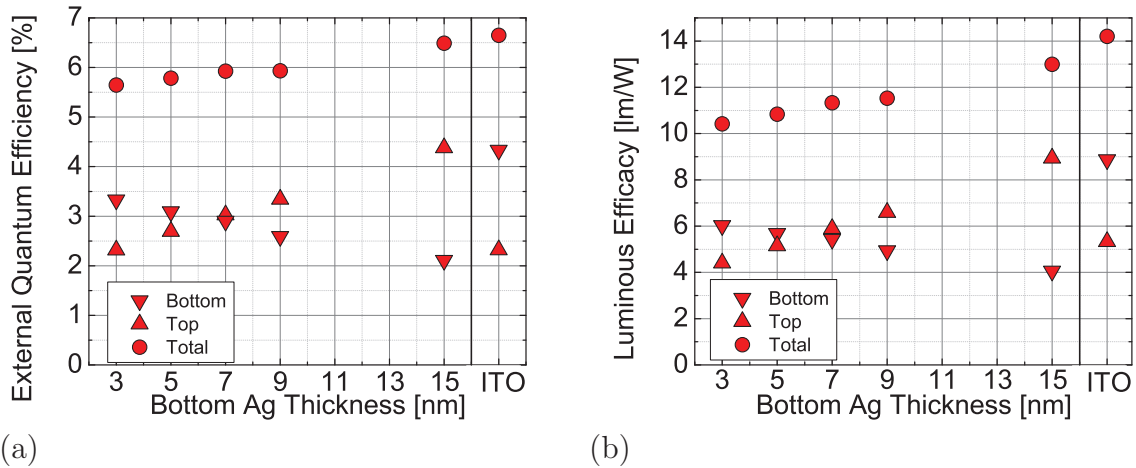


Figure 7.23: EQE (a) and LE (b) for top, bottom, and total emission as a function of the bottom electrode thickness at 1000 cd/m^2 , while the top electrode is kept constant at 2 nm Au and 7 nm of Ag . According to the spectral radiant intensities, the bottom electrode can be used to balance the emission in top and bottom emission, while a comparable efficiency is reached for 7 nm thick silver layers in both directions. The overall efficiency of the ITO-free transparent OLEDs reach the ITO reference for 15 nm of Ag .

For identical silver film thickness in both electrodes, showing also comparable transmittance, the bi-directional OLED reaches nearly identical efficiencies in both emission directions.

Increasing the silver thickness to 15 nm , the top emission (EQE: 4.4%) is twice as efficient as the bottom emission (EQE: 2.1%), while further the total efficiency increases to 6.5% , which is higher than for the other ITO-free samples. This increase in total efficiency can be assigned to the significantly more intense emission in the red spectral regime, determined by the affected device optics. Furthermore, the Purcell effect has an increasing impact on the radiative efficiency, introduced by a stronger microcavity of the reflective metal electrodes. The ITO reference device reaches a slightly higher efficiency compared to the ITO-free OLEDs.

As the spectral shape is almost constant for a variation of the bottom Ag thickness, the detected development of the EQE is also present in the luminous efficacy. The bottom-emitting reference devices show slightly higher efficiencies of 14.2 lm/W in total. The total luminous efficacy of the ITO-free devices reaches values between 10.6 and 13.2 lm/W , which is far below the performance white top-emitting OLEDs have achieved with identical EML concept (cf. Appendix A in Fig. A.6). Here, the lack of at least one highly reflective electrode is expected to cause the lower efficiencies. However, a balanced efficiency for both emission directions has been achieved, whereas the optimization of the emission color has been shown by optical simulation.

In the following, investigations on the long-term stability of transparent OLEDs are presented, intended by the fact that the introduction of wetting layers provided homogeneously closed metal films, which might result in an improved barrier for oxygen and moisture. In Fig. 7.24, the luminance of ITO-free and ITO containing transparent OLEDs is shown for a long-term operation at a current density of 10 mA/cm^2 . The ITO-free OLEDs use a 9 nm thick Ag film on a MoO_3/Au wetting layer, while a 90 nm

thick ITO film is applied in the references. For both device architectures, top electrodes of 5 nm and 15 nm thick silver layers on top of 2 nm Au have been analyzed.

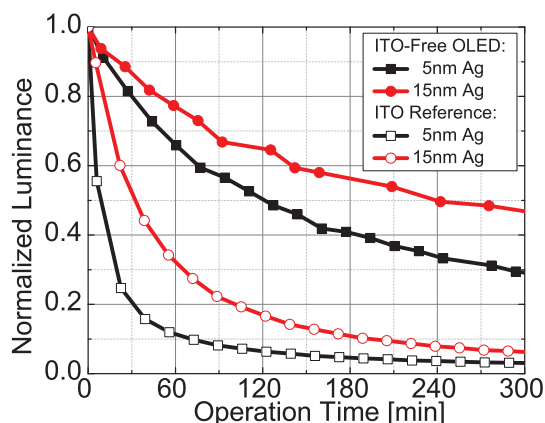


Figure 7.24: Luminance-operation time dependencies for ITO-free transparent OLEDs with a 9 nm thick Ag bottom electrode on a MoO₃/Au wetting layer and for ITO references. All devices are operated at a current density of 10 mA/cm². The ITO-free OLEDs show an increased device lifetime for both top electrode thicknesses compared to the ITO references.

It is found that for thicker silver top electrodes, the luminance decay is reduced in both, ITO-free and ITO-containing devices. In addition, the luminance decay in the ITO-free OLEDs is significantly reduced and thus the lifetime increased, in comparison to ITO references using an identical top electrode. These findings are very promising, as they emphasize an improved barrier effect of the thin MoO₃/Au/Ag electrode in comparison to the rather thick ITO. Schubert *et al.*[225] have shown that the lifetime of organic solar cells with thin silver top electrodes increases if they are sandwiched between two MoO₃ layers, stabilizing the thin metal film from chemical degradation. Such an effect might also contribute to the improved lifetime for the ITO-free OLEDs. Furthermore, the investigations in Chapter 6 have proven that the film morphology of the grown silver is improved by the wetting layer and closed metal films without cracks are formed. Hence, the closed metal films are expected to represent a sufficient barrier for oxygen and water. This argument is supported by the increased lifetimes in both device types for the thicker top electrodes. However, the overall lifetime of these devices is not that long, based on the decay of the deep blue emitter 4P-NPD. Thus, further experiments with long-term stable materials are planned to validate the observed trend for long-term stable materials.

Nevertheless, the detected increase in the device lifetime of the ITO-free OLEDs emphasizes the application of the wetting layer concept in general, as one remaining challenge of the OLED technology is addressed, which is the increase of the long-term stability [237]. Further investigations to validate the barrier function of the wetting layer metal electrodes, also in context of the application of flexible substrates, are in the focus of further experiments.

Overall, the wetting layer concept proves its applicability for transparent OLEDs. Here, MoO₃/Au wetting layers on glass enabled electrodes with only 3 nm of silver. Total device transmittance of 66 % for TCO-free OLEDs have been firstly achieved, comparable to a reference with an ITO anode. In addition, a transparent OLED with balanced

brightness and efficiency has been shown. Simulations revealed that comparable emission color to both sides can be obtained from a thickness optimization of the capping layer, which is highly desired for the use of transparent devices in solid-state lighting applications. Results on the long-term stability show an increased barrier of the wetting layer metal electrodes against oxygen and moisture in comparison to non-closed metal films and ITO, increasing the device lifetime.

Chapter Summary

The application of the ultra-thin and highly transparent wetting layer electrodes on top-emitting OLEDs reduces the impact of microcavity effects for high quality white emission with significantly improved angular color-stability and efficiency. Hybrid white top-emitting OLEDs have shown an improved performance in comparison to bottom-emitting reference devices, using an identical EML concept, while further a comparable angular color-stability has been reached. This emphasizes that prominent limitations of top-emitting OLEDs regarding white emission can be overcome introducing highly transparent wetting layer top electrodes. In Appendix A, the application of another EML concept including the deep blue emitter 4P-NPD is demonstrated, reaching a CRI of 89.5 and a LE of up to 23.0 lm/W.

In inverted device designs, the introduction of MoO₃ as wetting layer results in an improvement of the electrical characteristics, based on the improved injection of holes. Thus, the luminous efficacy is enhanced by 25 % and drawbacks of inverted devices compared to non-inverted designs are reduced, which is beneficial for the realization of top-emitting OLED displays on n-channel transistors. Further experiments, presented in Appendix B, show that an usually used thermal post-annealing procedure to improve the electrical characteristics of inverted OLEDs can become obsolete applying wetting layers of MoO₃ and gold.

Top-emitting tandem OLEDs using wetting layer top electrodes showed a color-stability improved by 22 % compared to optimized bottom-emitting reference devices and an excellent color rendering of 94. These findings further emphasize the applicability of top-emitting OLEDs for solid-state lighting applications, where tandem architectures are usually favored, but also typically cause prominent microcavity effects. The wetting layer electrodes further demonstrated their enormous potential on bi-directional emitting transparent OLEDs. Here, the bottom wetting layer electrode, directly deposited on the glass substrate, has shown remaining electrical performance for Ag thicknesses down to 3 nm. A total transmittance of up to 66 % has been reached by applying two metal electrodes, which is almost comparable to the OLEDs containing an ITO bottom electrode. A further aspect of the wetting layer electrodes is their compatibility with R2R processing, in contrast to most TCO materials. In addition, a beneficial effect on the device lifetime is found for the TCO-free transparent OLEDs, which might be attributed to the homogeneously closed metal film, providing an improved barrier function for water and oxygen.

8 Extraction of Internally Trapped Light Modes

In this chapter, investigations on the extraction of internally trapped light modes from top-emitting OLEDs are presented. First, the preparation of periodically corrugated light extraction structures with a low surface roughness is demonstrated. Then, highly efficient red top-emitting OLEDs are deposited on top of the corrugated substrates, showing an unchanged electrical performance. The efficiency can be enhanced in comparison to optically optimized planar reference devices, as Bragg scattered internal light modes contribute to the far-field emission. Finally, an analytical approach to describe the emission of corrugated OLEDs is provided.

The investigation of efficient OLED device designs, reaching IQEs close to unity [6] has been presented in Chapter 3. Even though the light generation in OLEDs has been optimized to be remarkably efficient, total internal reflection traps the major amount of the emission inside the OLEDs and the EQEs do typically not exceed 30%. [10, 11] Therefore, the extraction of internal waveguided modes and SPP modes remains a key challenge in improving the efficiency of OLEDs in general.

In Section 4.3.3, common techniques to extract the internally trapped light from OLEDs have been shown. The application of outcoupling structures such as half-sphere lenses and microlens foils to a planar OLED architecture is often used in bottom-emitting devices, as the substrate protects the organic layers from mechanical damage or other harmful effects during the structure mount. In contrast, mechanical damage is often observed in top-emitting OLEDs, when these structures are attached, which significantly decreases the device yield. Moreover, the introduction of periodically corrugated light extraction structures beneath the organic layer can be used to extract internal light modes by Bragg scattering from OLEDs. [150, 199, 203, 238] However, the deposition of the OLED on top of the light extraction structure has so far yielded adverse effects on the electrical performance, e.g. an increase of the leakage currents, deviations in the jV -curve slope, or the formation of electrical shorts. Hence, the preservation of the electrical performance of corrugated OLEDs remains challenging. Deviations between the electrical characteristics of the planar reference OLEDs and the corrugated devices indicate affected internal processes, which contribute to the light generation, and thus, the IQE. This restricts direct conclusions on the effect of a structure on the light extraction efficiency from an EQE measurement, as the IQE is not constant.

This work focuses on the integration of 1D periodically corrugated light extraction structures beneath top-emitting OLEDs, in order to extract the internal waveguided and SPP modes by Bragg scattering from these devices, while maintaining the electrical performance. In addition, an analysis as well as a quantitative description of the scattering

effects for such rather simple light extraction structures is intended, to serve as basis for the optimization of more complex extraction structures.

Adverse effects on the leakage currents and the IQE of corrugated OLEDs are supposed to be suppressed by a low surface roughness of the applied structure. Processes which yield such high quality light extraction structures of photoresist layers will be shown in Section 8.1, while Appendix C presents the processing of metal gratings. In Section 8.2, the influence of shallow photoresist gratings with an aspect ratio ($r_h = h/\Lambda$) smaller than 0.1 on 2nd cavity order red top-emitting OLEDs will be investigated. In addition, the impact of a sub- μm grating with a larger aspect ratio ($r_h \approx 0.2$), leading to a stronger corrugation of the layer sequence is shown (Section 8.3), which results in further scattering effects in corrugated top-emitting OLEDs.

8.1 Preparation of a Periodically Corrugated Top-Emitting OLED

In the following, the fabrication of periodically corrugated photoresist layers is discussed in detail. Two techniques have been applied in order to obtain 1D periodic gratings with a high homogeneity of the line structures and a low surface roughness. Photolithography has been used to structure a planar spin coated layer from exposure through a contact mask, where the desired grating structure is introduced from the transparent and opaque sections of the mask. The development process of the exposed photoresist then either removes the exposed or the non-exposed regions, in dependence on the applied photoresist (cf. Section 5.1.2). Nanoimprint lithography instead introduces a corrugation to a photoresist film by molding a corrugated master stamp into the pristine, wet layer. The exposure of the entire molded photoresist film, including the imprint master on top, results in a long-term preservation of the structure.

8.1.1 Fabrication and Characterization of Photoresist Gratings

Figure 8.1 shows AFM images of corrugated photoresist layers obtained from lithography and nanoimprint^[3]. Both techniques yield gratings with periods down to the sub- μm range with a strictly periodic surface regarding the line height, the line width, and the line contour. Figure 8.1(a) shows a line pattern with a period of $0.75\ \mu\text{m}$ and a height of $11.2\ \text{nm}$ obtained from the imprint procedure. The imprint master has been molded with a pressure of $0.5 \pm 0.1\ \text{MPa}$ into a layer of AZnLOF 2020. An increase of the molding pressure to $1.0 \pm 0.1\ \text{MPa}$ yields deeper gratings of approximately $40\ \text{nm}$ depth, which will be used in the investigations of corrugated top-emitting OLEDs. In addition to the shallow imprint master with a period of $0.75\ \mu\text{m}$, a set of master stamps with grating periods of 0.8 , 1.0 , and $1.6\ \mu\text{m}$ has been available, where the gratings can yield depths larger than $100\ \text{nm}$. Hence, a stronger corrugation would be introduced to the organic layer sequence on top of the structures. In Fig. 8.1(b), an AFM scan of an imprint grating with a period of $0.8\ \mu\text{m}$ and a depth of $117\ \text{nm}$ is shown, where also an excellent grating quality is observed.

^[3] The supply of the nanoimprint masters by Wallace Choy, Benjamin Schumm, and Florian Wisser is gratefully acknowledged.

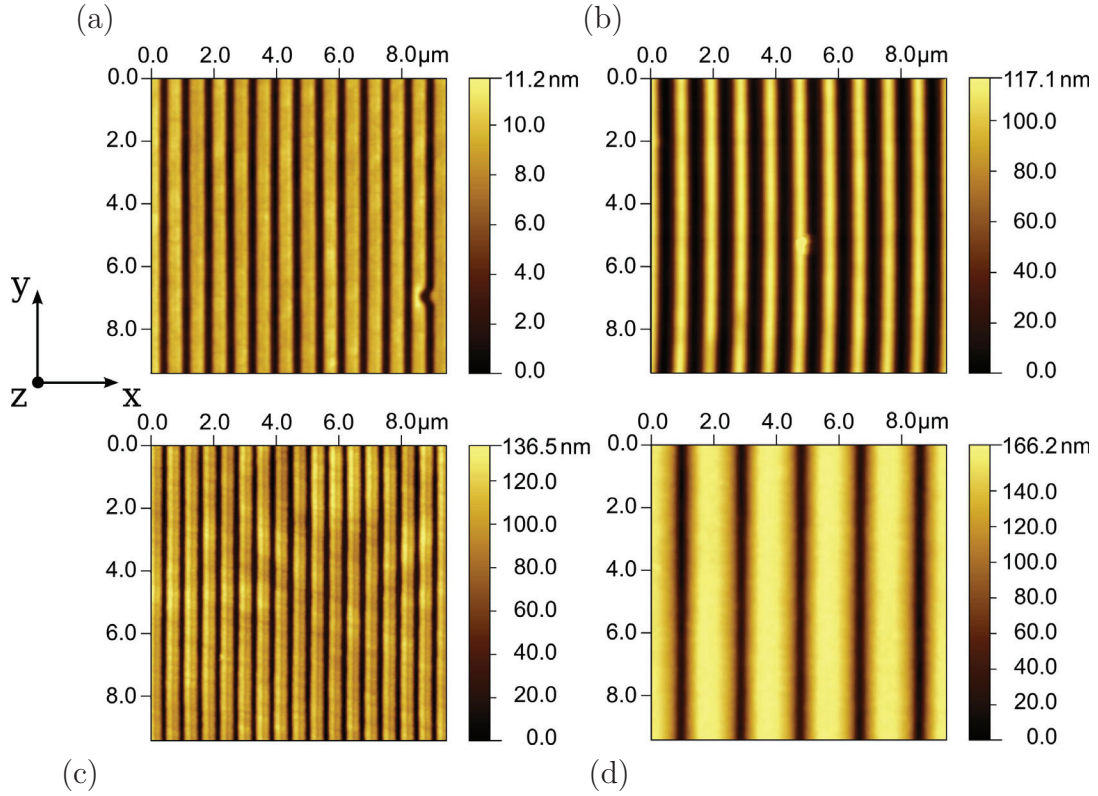


Figure 8.1: AFM series of periodically corrugated photoresist layers processed with nanoimprint (a), (b) and photolithography (c), (d). The imprint gratings have periods of $0.75\ \mu\text{m}$ (a) and $0.8\ \mu\text{m}$ (b), while the periods of the lithography patterns are $0.6\ \mu\text{m}$ (c) and $2.0\ \mu\text{m}$ (d). Both techniques allow for the fabrication of 1D gratings with homogeneous line contours and heights, while prominent surface roughness or a larger number of defects are absent.

Gratings produced by photolithography are presented for a period of $0.6\ \mu\text{m}$ (Fig. 8.1(c)) and $2.0\ \mu\text{m}$ (Fig. 8.1(d)). Also for this procedure, highly periodic gratings with periods in the μm range have been achieved. For a period of $0.6\ \mu\text{m}$, the applied AZ nLOF 2020 photoresist approaches its resolution limit as stated by the supplier and slight inhomogeneities in the grating height are detected. By increasing the corrugation period to $2.0\ \mu\text{m}$, broad and uniform photoresist lines are observed in the AFM scan, which validates that the photolithographic process is suitable for the production of high quality grating structures, as well. In Fig. 8.2, profile scans of single photoresist lines for a period of $0.8\ \mu\text{m}$ from the nanoimprint- and $2.0\ \mu\text{m}$ from the photolithography process are compared. The profiles have been normalized in distance and height in order to illustrate the line profile more clearly. For the nanoimprint grating, a \sin^2 -like profile is observed, while the line produced from photolithography shows a slight plateau and a more pronounced rectangular shape with rounded edges. The flanks of both photoresist lines show comparable slopes.

Overall, the corrugated photoresist patterns obtained from nanoimprint and lithography show an absence of sharp edges and yield high quality line structures with a low surface roughness. Moreover, gratings with periods in the sub- μm range, which is supposed to be the relevant period range for efficient extraction of the internal light modes from

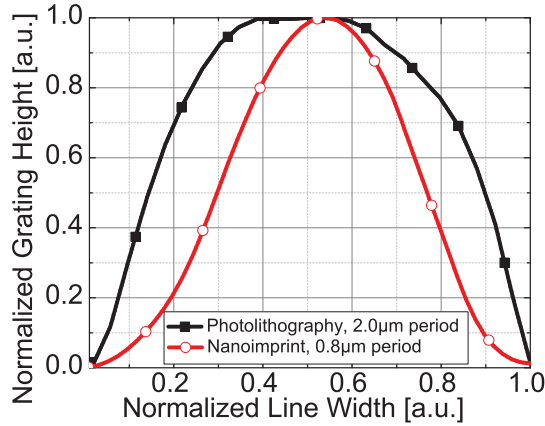


Figure 8.2: Normalized line profiles of single photoresist stripes of gratings produced by photolithography- and nanoimprint. For both, a profile with low roughness and smooth flanks is detected.

development-, and baking time, whereas a reliable control on the grating height and quality is difficult to achieve, especially on areas larger than the mm^2 scale. However, for the imprint process, the availability of master stamps with different grating periods and depths determines the processable gratings, in which the parameters cannot be significantly varied from the process. Experiments on the control of the grating height from the molding pressure have resulted in drawbacks in the long-term preservation of the gratings, reducing the pressure below 0.5 ± 0.1 MPa. This is supposed to be associated with a fusing of the wet photoresist beneath the imprint master in the time gap between the molding and the exposure.

8.1.2 Corrugation of the Organic Layer Sequence

In order to extract internal light modes from an OLED on top of the structure by Bragg scattering, at least the opaque bottom electrode has to show a non-planar topography, leading to a periodic variation of the refractive index. Investigations on the topography of the upper most layer of a top-emitting OLED have been performed by AFM measurements.

Figure 8.3(a) shows the AFM measurement of the neat nanoimprint grating with a period of $0.75 \mu\text{m}$ and a depth of 11.2 nm . Even though a top-emitting OLED with a thickness of 515 nm has been deposited on top of the rather shallow grating, the corrugation introduced by the photoresist layer is well preserved (Fig. 8.3(b)), whereas a slight increase in the grating height is observed. Therefore, interfaces with a prominent refractive index contrast are present at the metal electrode/organic interfaces, as well as the capping layer/air interface, causing light mode diffraction in the corrugated OLEDs. Comparable results for the preservation of the topography are found for the corrugated photoresist layer with a period of $0.8 \mu\text{m}$ and 117 nm depth (Fig. 8.3(c & d)). In addition to the preserved corrugation period, a prominent surface roughness of the capping layer has not been detected in the AFM measurements, which suggests that interfaces with low roughness might also be formed inside the layer architecture.

OLEDs [203, 239], can be obtained from both techniques. In Appendix C, an alternative approach used to obtain periodic gratings with an extend control of the grating period and height is presented, based on the wet chemical etching of metal films. However, remaining challenges in improving the quality of metal gratings limited an application of such structures in corrugated OLEDs so far.

For the grating fabrication, the rather simple nanoimprint process is preferred. It allows for a reproducible grating preparation with a high yield and an extremely high quality of the patterns on large areas. In contrast, a large variety of parameters has to be controlled in the photolithographic process, e.g. exposure-,

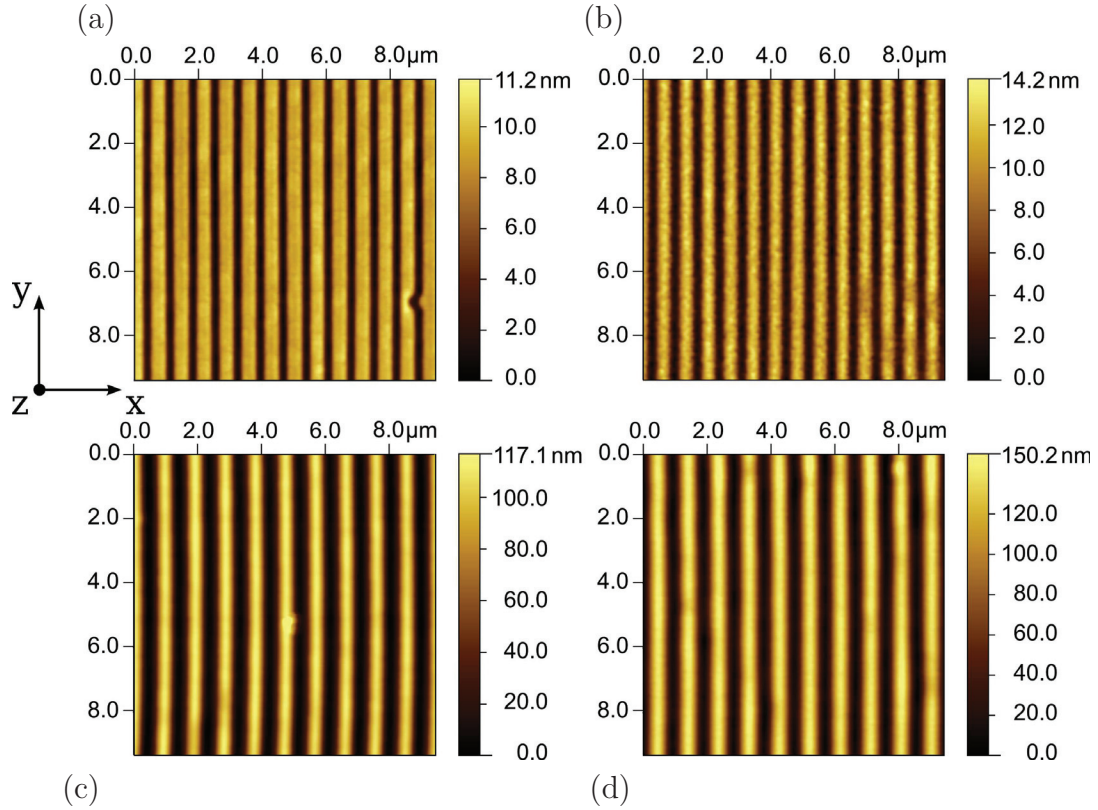


Figure 8.3: AFM series of nanoimprint gratings before and after processing of a top-emitting OLED on top. Even a shallow photoresist grating with a period of $0.75\ \mu\text{m}$ and $11.2\ \text{nm}$ depth (a) is perfectly preserved from an OLED architecture of $515\ \text{nm}$ thickness (b). Also for the deeper grating with $0.8\ \mu\text{m}$ period and $117.1\ \text{nm}$ depth (c) a pronounced corrugation with a low surface roughness is observed for the OLED (d).

It is worth to note that the observed increase in the modulation height for the upper most layer of the OLED in comparison to the neat photoresist film has not been validated with a statistical relevance. It is suggested that this observation might be attributed to variations in the grating height resulting either from inhomogeneities of the imprint master stamp, or from deviations in the molding pressure, which are locally detected by the AFM measurement.

Profile scans of single grating lines of the bare photoresist layer and the corrugated OLED are presented in Fig. 8.4. Both gratings show a smooth \sin^2 -like profile after the OLED deposition. For the grating with a period of $0.8\ \mu\text{m}$, the line profile is accurately preserved through the entire OLED architecture (Fig. 8.4(a)). The shallow grating with a period of $0.75\ \mu\text{m}$ shows a slight variation in the profile, resulting in a smoother shape after the layer deposition (Fig. 8.4(b)).

These results show that the high quality grating patterns of the corrugated photoresist are almost perfectly adopted from the entire organic layer sequence, maintaining the grating period and the line contour. Furthermore, no prominent surface roughness, sharp edges, or defects in the topography of the upper most organic layer are detected. This suggests a smooth film growth of all layers in the OLED architecture, which is supposed to allow for a reliable electrical operation.

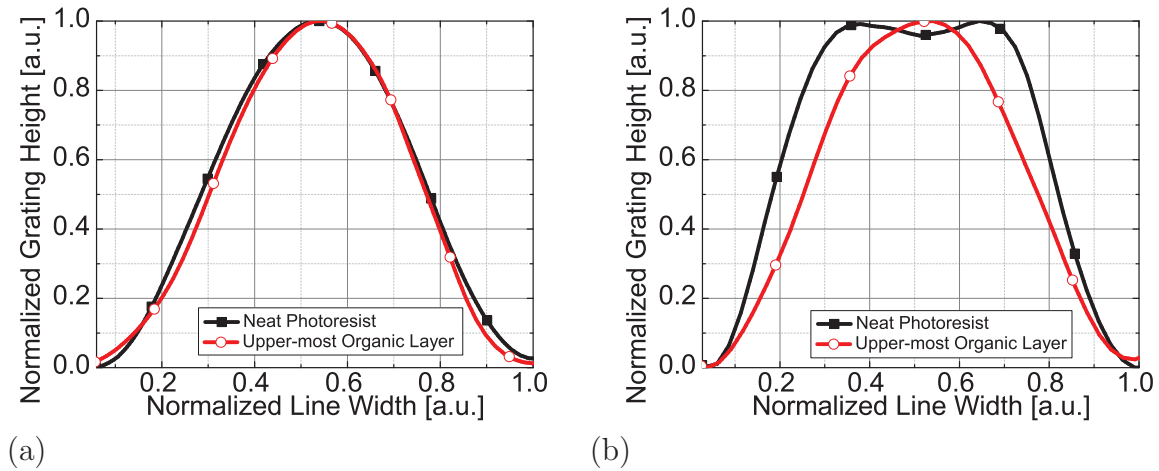


Figure 8.4: Profile scan of single grating lines, comparing the neat photoresist pattern to the upper most layer of a top-emitting OLED structure, normalized in width and height. For both, the deep grating with $0.8\ \mu\text{m}$ period (a), as well as the shallow grating with a period of $0.75\ \mu\text{m}$ (b), a smooth \sin^2 -like corrugation profile is found after the deposition of the organic layer sequence.

8.2 Extraction of Internal Light Modes from Corrugated Top-Emitting OLEDs

Investigations on the extraction of internally trapped light modes by Bragg scattering at 1D periodically corrugated substrates will be shown for state-of-the-art red phosphorescent top-emitting OLEDs. Previous investigations on corrugated bottom-emitting OLEDs deposited on top of 1D gratings have already yielded promising results regarding the electrical operation of corrugated devices, using rather thick charge transport layers [239]. Corrugated top-emitting OLEDs in the second optical maximum have been investigated in detail in this work. Experiments on corrugated 1st order microcavity OLEDs are presented in Appendix C. These devices often showed a poor electrical performance, while only minor scattering effects have been observed.

In order to analyze the scattering effects in corrugated microcavity OLEDs, grating structures with varied grating period as well as grating depth are applied for the investigations shown in this chapter. In Chapter 9, further optimizations of the grating-OLED system will be shown, with focus on the efficiency increase.

Even though several reports on the numerical simulation of corrugated OLEDs based on *rigorous coupled-wave analysis* (RCWA) and *finite difference time domain* (FDTD) algorithms [199, 240] have been reported, none of these simulation tools have been available for the investigations in this work. Hence, optical simulations of the OLEDs investigated are performed to optimize the planar reference for a maximum light extraction efficiency, whereas Bragg scattering of the internal light modes should allow for an increased efficiency of the corresponding corrugated OLEDs with identical layer architecture.

8.2.1 Efficiency Enhancement of Corrugated Top-Emitting OLEDs

To optimize red top-emitting OLEDs from optical simulation, the top electrode thickness has been arbitrarily set to 20 nm, since it is expected that electrodes of such thickness allow for electrical operation of the corrugated devices (Fig. 8.5(a)). For the simulation, a dipole orientation factor of $\theta_{\text{Dipole}} = 0.24$ for $\text{Ir}(\text{MDQ})_2(\text{acac})$ doped in NPB has been used, according to reports by Schmidt *et al.*[181]. The optimized planar layer architecture, starting from the substrate, is given by:

Al (40)/Ag (40)/HTL (228)/EBL (10)/EML (20)/HBL (10)/ETL (77)/Ag (20)/CAP (70).

However, the device fabrication yields different layer thicknesses in the OLEDs, as desired from the simulation. Figure 8.5(a) shows the layer thickness of the fabricated OLEDs, which has been determined through the optical simulation based on the measured emission of the devices. Significant differences in the layer thicknesses are found in the doped charge transport layers as well as the capping layer, deviating up to 20% (HTL: 251 nm vs. 228 nm, ETL: 91 nm vs. 77 nm, and capping layer: 60 nm vs. 70 nm) which is supposed to be attributed to deviations in the thickness control of the deposition tool. Furthermore, it has been shown that thickness inhomogeneities of up to 10% can occur on a 6×6 inch substrate wafer.[241] This affects the comparability of OLEDs which have been deposited at different positions on the substrate wafer. To ensure a high comparability of the corrugated OLEDs and the planar references, a side by side preparation of both samples on a single 1×1 inch substrate has been used.

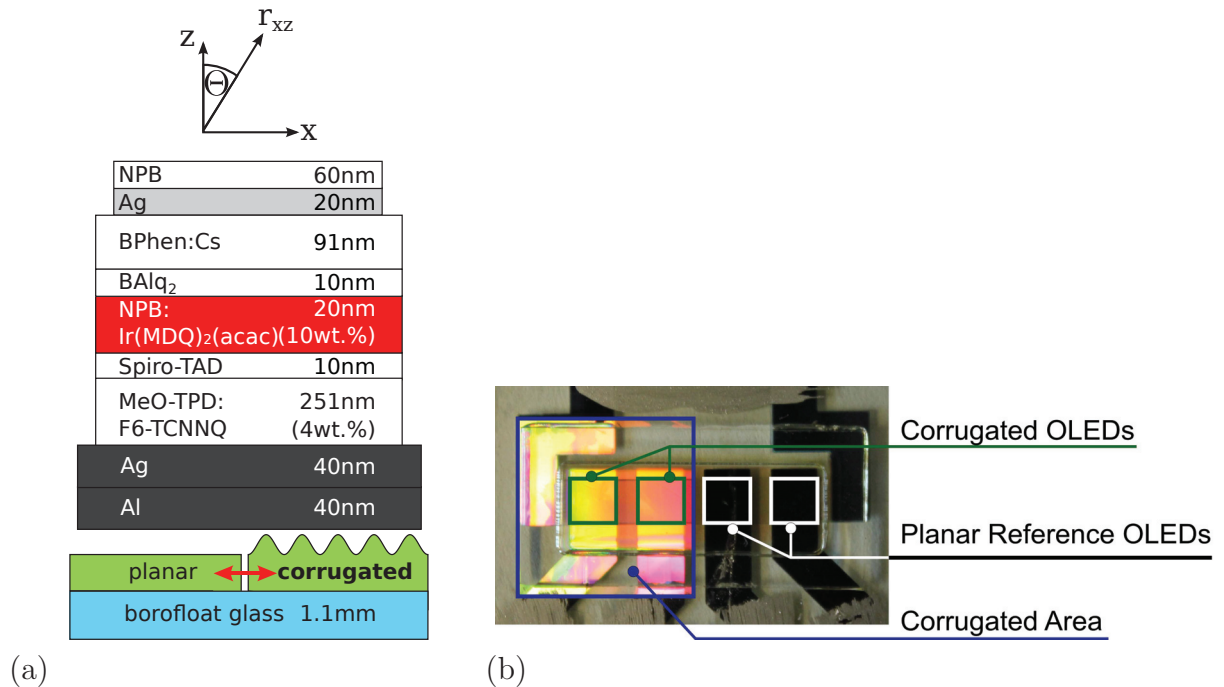


Figure 8.5: Device architecture of a red top-emitting OLED in 2nd cavity order used for the corrugated and the planar devices (a). Both are prepared side by side on a single 1×1 inch substrate, ensuring identical layer sequences and thus the comparability of both devices (b).

The geometrical device layout illustrated in Fig. 8.5(b) depicts the corrugation which covers the active area of two of the four OLEDs. Here, a nanoimprint grating with a

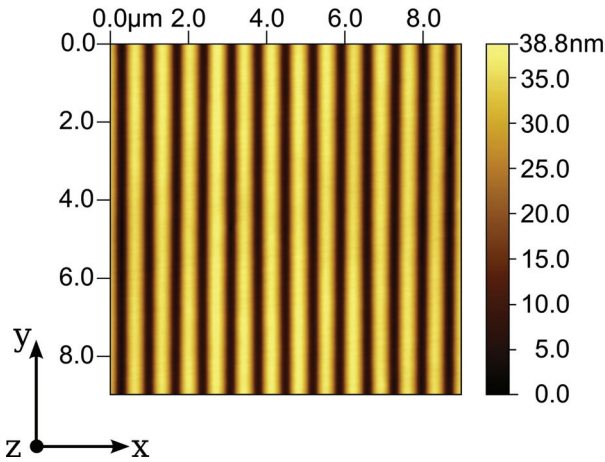


Figure 8.6: AFM image of the extremely homogeneous and shallow 1D line grating with a period of $0.75\ \mu\text{m}$ and a depth of $38.8\ \text{nm}$, prior to the OLED deposition.

period of $0.75\ \mu\text{m}$ has been fabricated with a molding pressure of $1.0 \pm 0.1\ \text{MPa}$, which yields a depth of $38.8\ \text{nm}$ and an aspect ratio of 0.05 (Fig. 8.6)^[4]. In the following, gratings with an aspect ratio < 0.1 will be referred to “*shallow gratings*”, which introduce a “*weak corrugation*” of the organic layer architecture on top. Gratings with an aspect ratio > 0.1 are referred to “*deep gratings*”, resulting in a “*strong corrugation*” of the OLED.

The current-voltage-luminance curves of the planar and the corrugated red top-emitting OLEDs are shown in Fig. 8.7(a). The corrugated OLED shows a comparable current-voltage characteristic to the planar reference device in the entire voltage range and the leakage current remains reasonably low at $10^{-2}\ \text{mA}/\text{cm}^2$. For the first time, the electrical performance is preserved after the introduction of a corrugated substrate for top-emitting OLEDs. This finding is attributed to the shallow surface modification of the grating with an aspect ratio of only 0.05 and the absence of defects or prominent surface roughness. Further experiments will show that leakage currents in the range of $10^{-4}\ \text{mA}/\text{cm}^2$ can also be obtained for top-emitting OLEDs on corrugated photoresist films. In accordance to the maintained electrical performance of both devices, it is suggested that the IQE of the planar and corrugated OLEDs also remain comparable. Thus, effects of the corrugation on the EQE can directly be attributed to an influence of the grating on the light extraction efficiency. Although the current-voltage characteristics of both devices are comparable, the corrugated OLED shows a significant increase in forward luminance.

Figure 8.7(b) shows the spectral emission in normal direction at a current density of $14.8\ \text{mA}/\text{cm}^2$. The cavity emission of the planar reference shows its peak at a wavelength of $724\ \text{nm}$, which is rather large in comparison to the peak of the PL spectrum of the red emitter at $610\ \text{nm}$. In accordance to an optical simulation of the planar device, the increase in the transport layer thicknesses has been found to cause the cavity emission in the deep-red spectral range. However, the corrugated OLED shows a similar cavity mode emission regarding the intensity, the width, and the wavelength, resembling the cavity emission of the planar reference. In normal direction, additional emission from two narrow modes is found in the corrugated top-emitting OLED at wavelengths of $644\ \text{nm}$ and $671\ \text{nm}$ (Fig. 8.7(b)). An increase of the observation angle to 40° results in a shift of the cavity mode emission to smaller wavelengths, which is well-known from the optical properties of resonators (cf. Section 4.1), while the emission intensity increases.

^[4] Nanoimprint master provided by Wallace Choy.

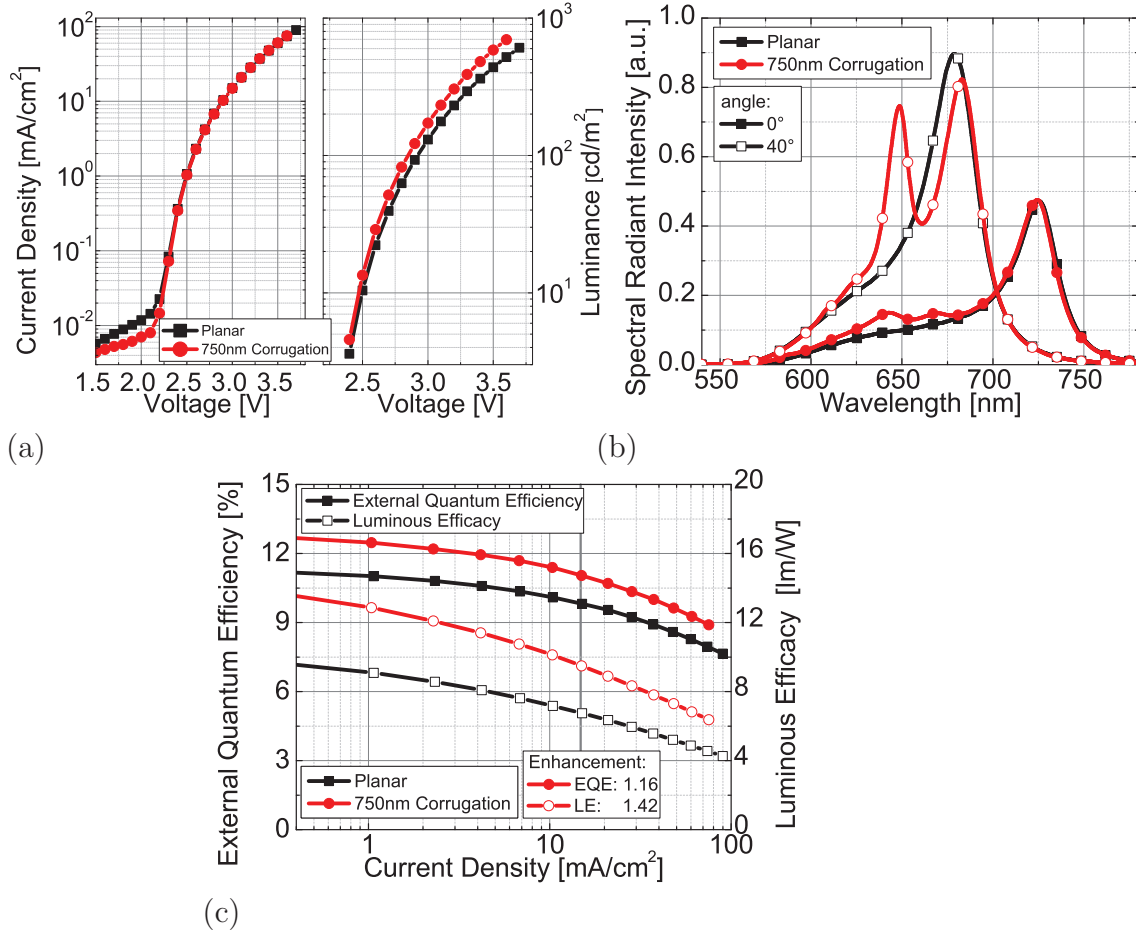


Figure 8.7: Comparison of planar and corrugated OLEDs regarding current-voltage-luminance curves (a), spectral radiant intensity measured at a current density of $14.8 \text{ mA}/\text{cm}^2$ in normal direction and at an angle of 40° (b), as well as the efficiency-current dependencies (c). The electrical operation of the corrugated OLED remains unaffected from the grating, while the luminance is increased in comparison to the planar reference. Additional emission, occurring in the corrugated device, results in an increased device efficiency.

For an observation angle of 40° , the corrugated device shows a prominent second peak at smaller wavelengths compared to the cavity emission, which indicates a significant influence of scattering effects in the top-emitting OLED (Fig. 8.7(b)).

It is noteworthy that the angular dependent spectra have been recorded perpendicular to the grating lines in order to detect the Bragg scattering effects, as shown in Fig. 5.4. The efficiencies of the corrugated OLEDs have been measured in an integrating sphere, detecting the far-field emission, whereas the unwanted emission to the substrate edges and the backside is covered.

At a current density of $14.8 \text{ mA}/\text{cm}^2$, the EQE increases from 9.8% for the planar device to 11.4% for the corrugated OLED, which represents an EQE enhancement of 16%, and remains constant for the entire current range. These results show for the first time that the efficiency of a phosphorescent red top-emitting OLED can be improved by the application of a periodic grating, while the electrical performance remains unaffected. In contrast to literature reports on corrugated top-emitting OLEDs, where significant

changes of the electrical characteristics between planar and corrugated devices have been observed, the EQE enhancement can here be directly attributed to an increase of the light extraction efficiency η_{out} .

The luminous efficacy of the corrugated top-emitting OLED is enhanced by 42%, due to the more intense emission of the Bragg scattered modes in spectral ranges with higher sensitivity to the human eye. Even though the results on corrugated top-emitting OLEDs are promising, an EQE enhancement factor of 1.16 is smaller than for common light extraction techniques, such as half-sphere lenses or microlens foils, which reach enhancement factors of approximately 1.8. Moreover, EQEs of 17% have been shown for a comparable top-emitting OLED architecture [11], which has not been reached by these devices. Hence, the grating-OLED system has to be optimized, improving the extraction efficiency of internally trapped modes and optimizing the cavity thickness of the fabricated OLEDs. In the following section, the identification of the Bragg scattered internal light modes will be demonstrated. Based on the insights gained, an efficient and controlled extraction of the internal light modes is intended for further experiments on corrugated top-emitting OLEDs.

8.2.2 Identification of Bragg Scattered Modes

Figure 8.8 shows the angle and polarization resolved spectral emission of the planar and the corrugated device from Fig. 8.7. All spectra in the observation angle range of $\sin \theta$ between 0 and 1 have been recorded at a current density of 14.8 mA/cm^2 and are normalized to the maximum intensity. As expected, the planar device shows only emission from the fundamental cavity mode with a prominent parabola-like dispersion. The corrugated OLED has a comparable cavity mode dispersion as the planar device for a wide angular range, as already indicated in the spectra shown in Fig. 8.7(b). The results prove that for the applied shallow grating, the cavity mode of the top-emitting OLED is conserved. In addition, sharp spectral features of Bragg scattered modes can be detected across the entire air light-cone, increasing the extracted amount of light from the OLED architecture. The linear dispersions of the scattered modes suggests that these can be associated to extracted internal light modes of the microcavity, since the scattered cavity mode would also show a parabola-like dispersion.

However, the Bragg scattered light modes do not only beneficially contribute to the emission of corrugated top-emitting OLEDs, as partial intensity decreases of the cavity mode have been observed most prominent for the p-polarized emission (cf. Fig 8.8). Furthermore, the interaction of a Bragg scattered mode with the cavity mode in s-polarization results in a significant splitting of the cavity mode into two separated branches for a $\sin \theta$ range between 0.45 and 0.8. An *anti-crossing* effect indicates the interaction of light modes in corrugated top-emitting OLEDs, even though only a shallow grating with an aspect ratio of 0.05 has been applied. In previous analysis of corrugated bottom-emitting OLEDs [239], no evidence for the interaction of light modes, e.g. mode anti-crossing, has been detected. There, Bragg scattered modes have been observed as a weak perturbation to the emission of the planar bottom-emitting reference, superposing their intensities to the planar device emission. With respect to the rather complex effects observed in the corrugated microcavity OLEDs, a treatment of the corrugation as a weak perturbation might not be valid anymore.

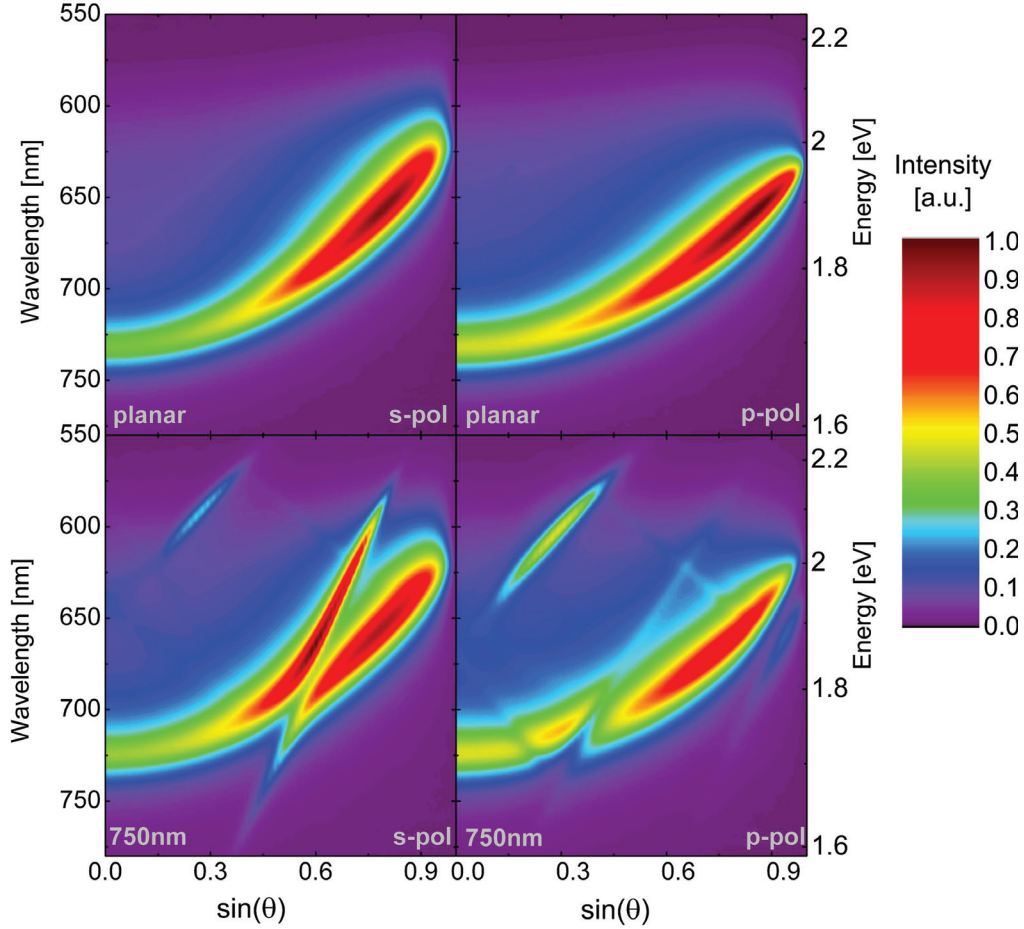


Figure 8.8: Measured angle and polarization resolved spectra at a current density of 14.8 mA/cm^2 of the planar and the corrugated top-emitting OLED from Fig. 8.7. While the planar reference shows only emission from the radiative cavity mode, additional sharp spectral features to the cavity mode are found in the corrugated OLED. Thereby, interactions of the light modes also yield a splitting and a partial intensity decrease of the cavity mode.

In terms of the efficiency enhancement, the splitting of the cavity mode as well as scattered light modes which lead to a decrease of the cavity mode emission are unfavorable. A decrease of the radiative cavity mode emission in the corrugated OLED emphasizes either a more efficient scattering from the air light-cone into the organic layers, as suggested by Hauss *et al.* [238] for bottom-emitting devices, or the presence of light mode interference. In the latter one, destructive interference would account for an emission decrease inside the air light-cone.

In order to investigate the scattering mechanism in the corrugated top-emitting OLEDs, the origin of the Bragg scattered modes is investigated first. In accordance to Rigneault *et al.* [190], Bragg scattered modes of a shallow corrugated device ($h_{\Lambda}/d_{\text{opt}} < 1$) can be obtained from geometrical considerations of the internal light modes from the planar reference device with identical layer architecture (cf. Section 4.3.4). It is worth to mention that this procedure corresponds to the application of the Laue equation to the internal

modes of the reference device, in order to obtain the position of the Bragg scattered modes in the corrugated OLED. It is assumed that this approach is valid for the corrugated top-emitting OLEDs as well, since the shallow grating introduces only a weak modulation of the microcavity ($h_\Lambda/d_{\text{opt}} = 0.09 \ll 1$). This assumption is supported from the comparable position and intensity of the cavity mode emission (cf. Fig. 8.7(b)) and a comparable angular dependency of the cavity mode shown in Fig. 8.8. Hence, the power dissipation spectrum of the planar reference OLED has been calculated, in order to obtain the internally trapped waveguided and SPP modes of the OLED architecture, as this region is not experimentally accessible (Fig. 8.9).

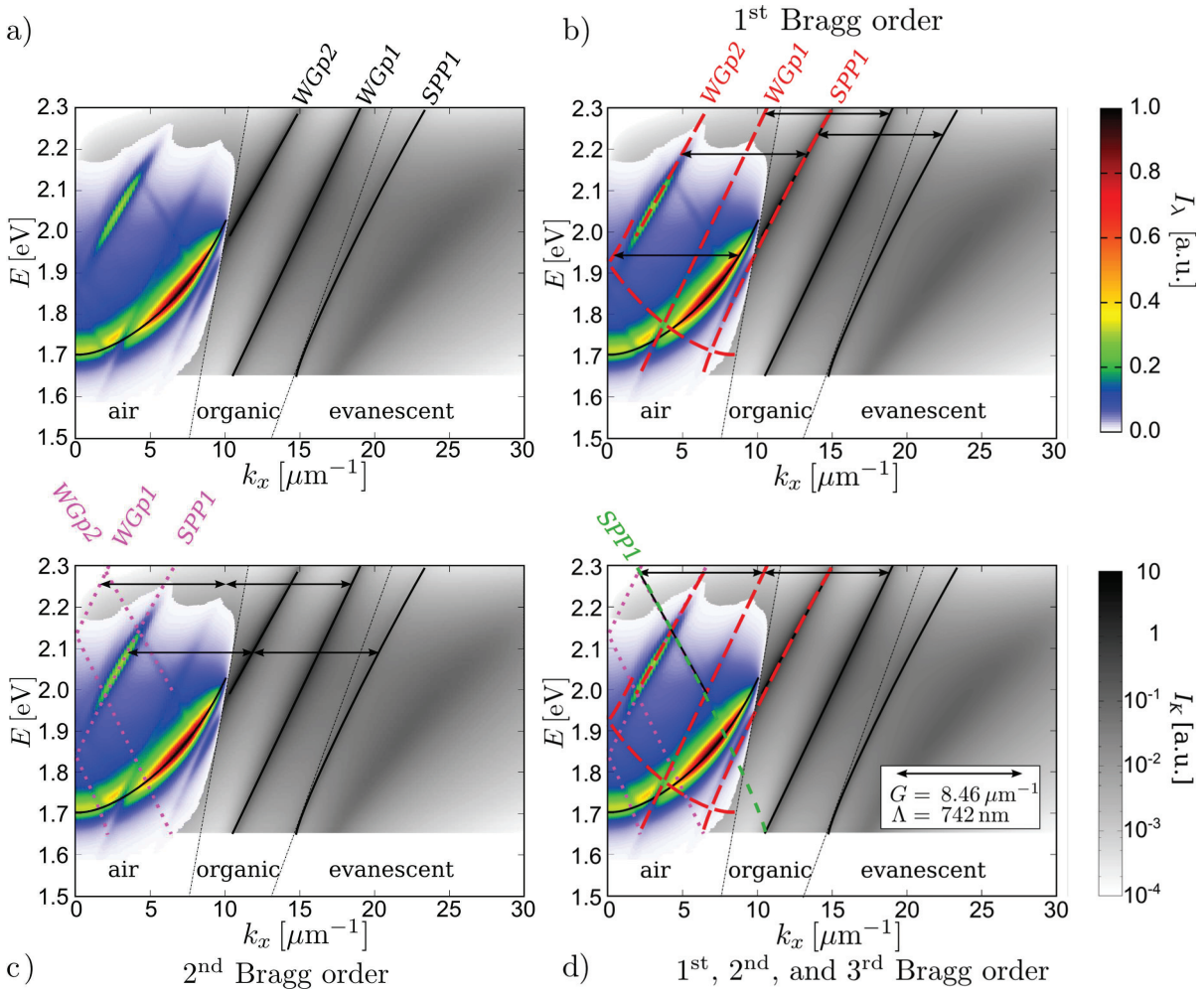


Figure 8.9: Measured p -polarized spectral radiant intensity (I_λ) of the corrugated OLED (color scale). The simulated power dissipation spectra (I_K) of the planar reference with identical layer sequence is shown in grayscale, visualizing the internal light modes outside the experimentally accessible region (black compact lines) (a). Black arrows indicate the reciprocal lattice vector \vec{G} . Bragg scattering features are highlighted by red dashed (1st) (b), purple dotted (2nd) (c) and green dashed lines (3rd) (d) according to their order. All measured scattering features can be identified accounting for the first three Bragg orders (d).

Figure 8.9(a) shows the simulated power dissipation spectrum of the planar reference in p-polarization in grayscale, whereas the experimentally determined spectral emission of the corrugated device inside the air light-cone is superimposed in color scale.^[5] Therefore, the observation angle has been converted into the in-plane wavenumber k_x ($k_x = \sin \theta \cdot k_0$, k_0 : wavenumber in air) and the wavelength has been converted into the photon energy E .

It has been found that the calculated and measured dispersion of the radiative cavity mode accurately overlap, validating that the simulation is based on the correct optical parameters (n_i, d_i) of the layer architecture. Furthermore, the calculation predicts two internally trapped waveguided modes (WGp1 and WGp2), as well as the dissipation of power into two evanescent modes. As only the SPP mode close to the organic light-line shows a sharp and intense mode (SPP1), the analysis of the Bragg scattering effects will be limited to this mode, while the other mode would only contribute as a broad background. Furthermore, for a 2nd cavity order top-emitting OLED, the dissipation of power into SPP modes is not as prominent as for 1st order devices, since the emitters are located in larger distance to the metal electrodes. Hence, the impact of their Bragg scattered modes might be only barely detectable in the measured spectra.

In Fig. 8.9(b), the 1st order ($m = 1$) Bragg scattered modes of the planar reference device are introduced as red dashed lines to the air light-cone. Excellent agreement of the measured scattering effects in the corrugated device and the obtained mode positions from the calculated power dissipation of the planar reference is observed for various features. It is found that the significant increase to the device emission in the air light-cone can be associated to the scattered WGp2 mode, while a decrease of the emission is found at the position of the Bragg scattered WGp1 mode. Moreover, emission of the SPP1 mode is observed in the air light-cone. By taking only the second scattering order into account ($m = 2$), shown in Fig. 8.9(c), further spectral features of the corrugated emission spectra can be identified. For the given corrugated top-emitting OLED, an overlap of the 2nd Bragg scattering order SPP1 mode with the 1st Bragg scattered WGp2 mode is observed, which holds for all higher scattering orders and complicates the association of the measured scattering effect to one distinct mode. However, for the 1st scattering order, the contribution of the SPP1 mode can be observed independently from the WGp2 mode, in which only a slight contribution to the far-field emission has been found. Hence, it is expected that the SPP mode contributes only to a minor part to the detected emission of the scattered modes, where an overlap with the WGp2 mode hinders an association. For the 3rd Bragg scattering order, only the emission of the SPP1 mode would be observable, as the other scattered modes are distributed at higher in-plane wavenumbers outside the air light-cone.

The superposition of the 1st, 2nd, and SPP1 mode in 3rd order yields the identification of all spectral features of the corrugated OLED (Fig. 8.9(d)), in which an excellent agreement to all measured spectral features can be observed. For the analysis, best agreement to the scattering effects has been found for a reciprocal lattice vector G_{p-pol} of $8.46 \mu\text{m}^{-1}$, corresponding to a grating period of Λ_{p-pol} of 742 nm. This is in good agreement with the experimentally determined grating period of $0.75 \mu\text{m}$ from AFM measurement.

^[5] The contribution of Cornelius Fuchs in programming a tool to convert the measurement data for the plot is gratefully acknowledged.

In Fig. 8.10, the s-polarized emission is analyzed by the same procedure. Again, an excellent agreement of the calculated cavity mode dispersion of the reference and the measured corrugated OLED is detected (Fig. 8.10(a)). Due to the absence of evanescent modes in s-polarization, the observed scattering features have to be caused by Bragg scattering of the two internal waveguided modes (WGs1 and WGs2). By considering the first two Bragg scattering orders (1st: red dashed lines, 2nd: purple dotted lines), all spectral features of the corrugated OLED can be well reproduced. Here, the best agreement has been obtained for a reciprocal lattice vector of $G_{s\text{-pol}}$ of $8.56 \mu\text{m}^{-1}$, corresponding to a grating period of $\Lambda_{s\text{-pol}}$ of 734 nm, in order to reproduce the scattering effects. This is still in good agreement to the grating period of $0.75 \mu\text{m}$ ($\Delta\Lambda/\Lambda < 3\%$) and to the grating period applied for the analysis of the p-polarized emission ($\Delta\Lambda/\Lambda \approx 1\%$).

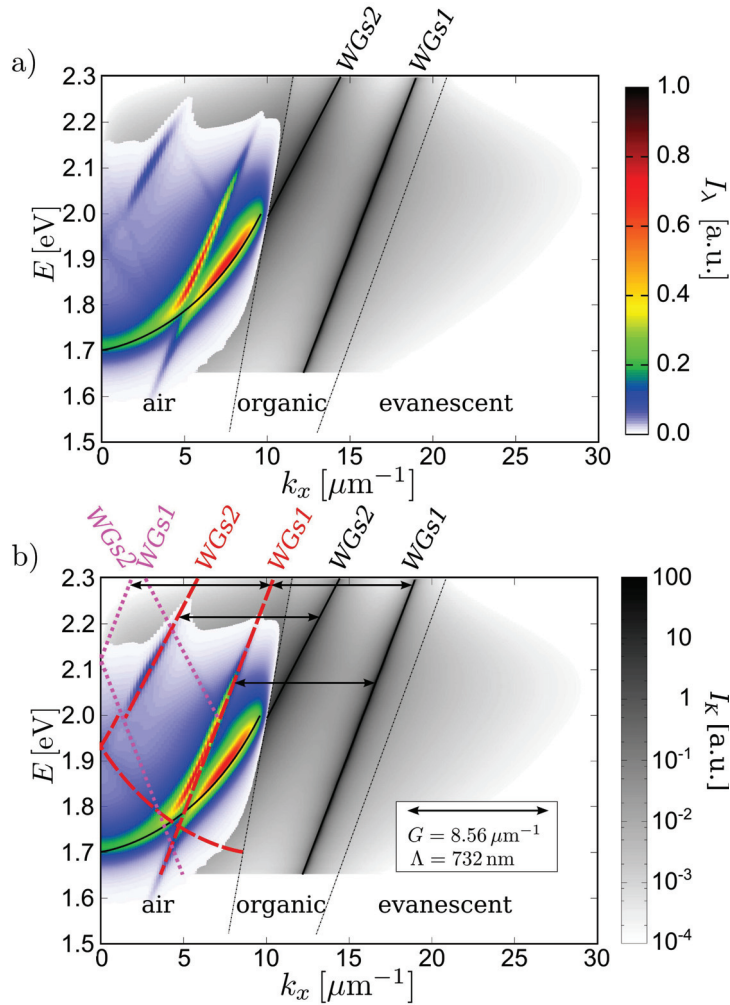


Figure 8.10: Measured s-polarized emission (I_λ) of the corrugated OLED (color scale). The simulated power dissipation spectra (I_K) of the planar reference with identical layer sequence is shown in grayscale, visualizing the mode dispersions as black compact lines (a). Black arrows indicate the reciprocal lattice vector \vec{G} . Scattering features are highlighted by red dashed (1st) and purple dotted lines (2nd) lines according to their order (b). All measured spectral features can be identified accounting for the first two Bragg scattering orders.

Overall, the results have shown that the identification of Bragg scattering effects in corrugated top-emitting OLEDs on shallow gratings is possible, using the approach suggested from Rigneault *et al.* [190]. Moreover, additional emission in the corrugated 2nd cavity order top-emitting OLEDs is introduced from extracted waveguided modes, which mainly contribute to the observed efficiency enhancement. In contrast, only slight effects of Bragg scattered SPP modes are observed in the 2nd order microcavity OLEDs. This might be attributed to a lower scattering efficiency of these modes, as significant contributions of extracted SPP modes have also not been observed in corrugated 1st order cavities (cf. Appendix C), while also the intensity of SPP modes in 2nd order cavity OLEDs are comparably low.

In corrugated top-emitting OLEDs, Bragg scattered modes cause additional emission phenomena, not observed in previous investigations on bottom-emitting OLEDs [239]. For s-polarized emission, the interaction of the Bragg scattered WG_{s1} mode with the radiative cavity mode results in a splitting of the cavity mode into two separate branches. With respect to this observation, Wedge *et al.* [202] reported on the cross-coupling of SPP modes for light emitted through corrugated metal films. Even though an anti-crossing behavior has not been reported in their work, they emphasized the occurrence of such an effect could be the result for an increased coupling interaction of the light modes in the system.

However, anti-crossing phenomena are well-known for various interacting photonic systems, such as for planar microcavities operating in the so-called *strong-coupling regime* [242–245] or planar microcavities containing thin metal films [246, 247]. Anti-crossing phenomena in devices operating in the strong-coupling regime are typically found for interactions between excitons and the photonic modes, resulting in cavity polariton modes.[244] The interaction of both modes can be described with coupled oscillators, which allows for a sufficient characterization of the observed anti-crossing effect when the frequencies of both modes are approaching each other.[242] For the corrugated top-emitting OLEDs, an operation in the strong-coupling regime is excluded, as by far higher Q-factors and small exciton linewidths are fundamental requirements to operate in this regime.[245]

Reports on microcavities comprising a thin metal layer close to the active medium sandwiched between two periodic dielectric Bragg mirror showed that a so-called optical *Tamm plasmon polariton* mode can be formed at the interface of the metal and the adjacent dielectric.[248] In contrast to SPP modes, Tamm plasmons can be excited in TE as well as TM polarization and dissipate power to the far-field.[247–249] Brückner *et al.* [250] have shown for a planar microcavity with varied metal layer thickness that instead of a single cavity mode, two coupled Tamm plasmons are excited and contribute to the far-field emission. Furthermore, the eigenenergies of the Tamm plasmons could be controlled by the metal layer thickness and the cavity thickness, while an anti-crossing behavior of the coupled Tamm plasmons has been observed.[250] Also in these reports, the quality factors of the microcavities have been approximately two orders of magnitude higher than for top-emitting OLEDs. Furthermore, the formation of Tamm plasmons has not been validated in corrugated top-emitting OLEDs so far.

However, since an anti-crossing effect has not been observed in corrugated bottom-emitting OLEDs [239], it is indicated that the light mode interaction might be correlated

to the thin transparent metal top electrode in the corrugated microcavity OLEDs, or to increased microcavity effects, resulting in the observed interaction of a waveguided and the cavity mode. In Chapter 9, further experiments to analyze the anti-crossing phenomenon in corrugated top-emitting OLEDs are shown.

Moreover, a partial decrease of the cavity emission has also been observed as a result from the scattered modes in the corrugated top-emitting OLEDs, which further limits the potential efficiency gain from Bragg scattering. For corrugated bottom-emitting OLEDs, Hauss *et al.* [238] have suggested that the transfer rates for scattering from the organics into the air light-cone, or vice versa, determine if light can be extracted from the organics or is transferred into them. The shown results for corrugated top-emitting OLEDs suggest that other processes might be relevant to explain the scattering effects and the emission spectra. In the next section, Bragg scattering effects in corrugated top-emitting OLEDs will be investigated in more detail, in which also a model to describe the emission spectra of corrugated devices is presented.

8.3 Coherent Mode Coupling in Strongly Corrugated Microcavities

Investigations into corrugated microcavity OLEDs have also been extended to the description of scattering effects in strongly corrugated devices. Therefore, corrugated photoresist patterns produced by photolithography are used, since gratings with larger aspect ratios as for the available imprint masters could be achieved. The device layout, preparing the planar reference and the corrugated OLED on the identical substrate, is preserved. Furthermore, red top-emitting OLEDs in the second optical maximum are deposited on top of the corrugation patterns, in order to analyze the scattering effects.

8.3.1 OLED Performance on Strongly Corrugated Substrates

The layer thicknesses of the processed OLEDs are shown in Fig. 8.11(a), which obtain again prominent deviations, e.g. in the HTL thickness (255 nm vs. 228 nm) as well as the top electrode thickness (24 nm vs. 20 nm) in comparison to the optimized device from optical simulation, which has been mentioned in the previous section.

In order to yield a weakly corrugated OLED comparable to the device investigated in the previous section, the exposure time of the photolithography process has been reduced from a few seconds to 0.2 s, resulting in a rather small cross-linking of the photoresist film. A shallow grating with a period of 1.0 μm and a depth of 69.3 nm ($r_h = 0.07$) has been obtained (Fig. 8.11(b)). However, the decrease of exposure time also reduces the homogeneity in the line formation of the grating, which is supposed to adversely affect the intensity of Bragg scattering reflexes. In order to realize a strongly corrugated OLED, the exposure time has been extended to 3 s. For a grating with a period of 0.6 μm , a depth of 144.4 nm ($r_h = 0.24$) has been found (Fig. 8.11(c)).

Even though the grating depth is increased by more than a factor of 3 in comparison to the shallow grating (0.75 μm period and 40 nm depth) investigated before, the corrugated top-emitting OLED on top of the deep grating will also represent a weakly corrugated device ($h_\Lambda/d_{\text{opt}} = 0.33 < 1$), according to Rigneault *et al.* [190].

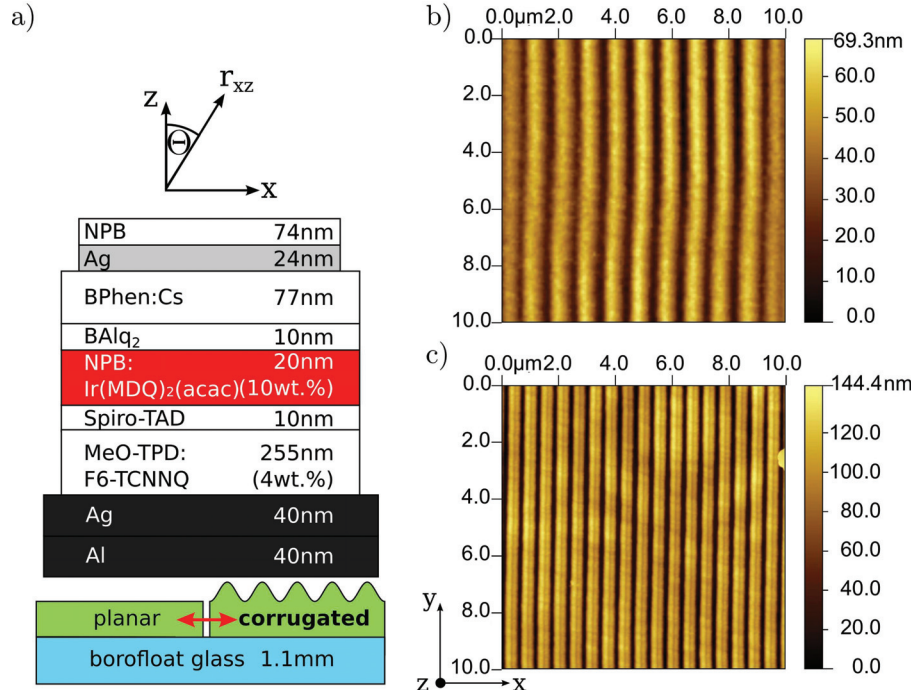


Figure 8.11: Layer architecture of top-emitting OLEDs prepared on gratings with a varied period and depth, in order to analyze the impact on the light extraction (a). AFM scans of gratings with a period of $1.0\ \mu\text{m}$ and $69.3\ \text{nm}$ depth, introducing a shallow corrugation ($r_h=0.07$) (b) and with a period of $0.6\ \mu\text{m}$ and $144.4\ \text{nm}$ depth, introducing a strong corrugation ($r_h=0.24$) (c).

Further extending the exposure time in an attempt to increase the aspect ratio has either resulted in entirely cross-linked resist films which cannot be used as gratings, or in collapsing line structures. However, as a maintained electrical performance of the corrugated OLEDs is the fundamental basis of the investigations, a further increase in the aspect ratio might not be desirable. The electrical performance of the planar reference and the corrugated OLEDs are shown in Fig. 8.12(a). For the weakly corrugated OLED, a comparable electrical performance as for the planar device is observed in the entire voltage regime, while further a slight increase of the forward luminance is detected. In contrast, the strongly corrugated OLED shows an increase of the leakage currents, whereas also the slope of the jV -curve slightly decreases. Even though these differences are not that prominent, they indicate changes in the internal processes of the strongly corrugated devices, e.g. charge carrier transport and blocking, which account to the IQE. Furthermore, the strongly corrugated OLED reaches a lower EQE as the planar reference device, even though the luminance in normal direction is significantly increased (Fig. 8.12(b)). While the luminance increase in normal direction can be associated to the highly intense emission at lower wavelengths compared to the planar reference (Fig. 8.12(c)), the decrease in the EQE has to result from a reduced emission into the entire far-field. As the deviations in the jV -curves of this corrugated OLED restricts a conclusion on the light extraction efficiency, it remains unclear whether the grating itself or other processes lead to the EQE decrease. In contrast, the corrugated OLED on the shallow grating shows an increase of the EQE by a factor of 1.13, which can be associated to the light extraction efficiency.

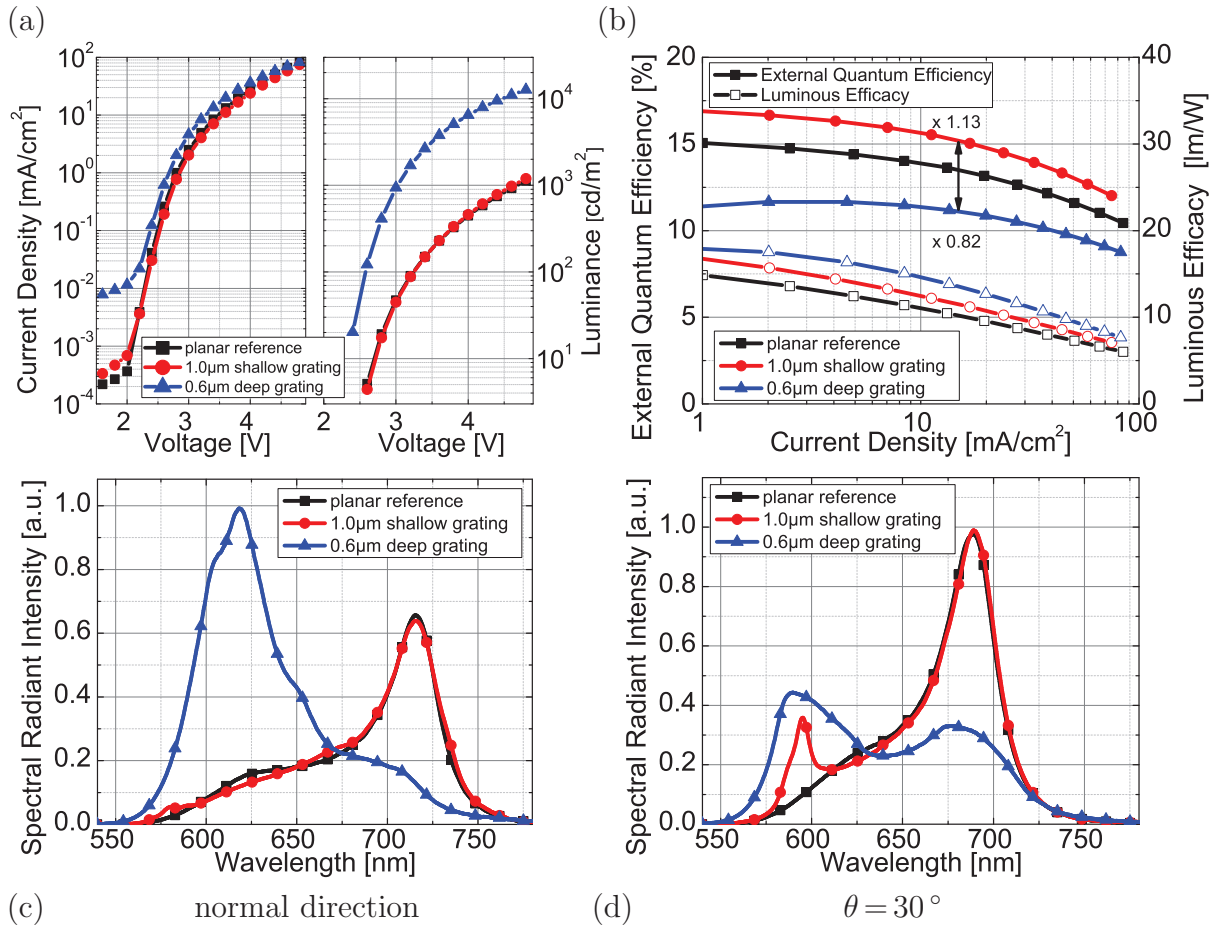


Figure 8.12: Comparison of planar and corrugated OLEDs regarding current-voltage-luminance (a) and efficiency-current characteristics (b), as well as spectral radiant intensity measured at a current density of 14.8 mA/cm^2 in normal direction (c) and at an angle of 30° (d). The strongly corrugated OLED shows an adversely affected jV -curve, while prominent deviations of the spectral emission from the planar reference are also observed. However, an efficiency increase is only detected for the weakly corrugated OLED, in which the electrical performance is maintained.

In addition, the observed EQE enhancement is similar to the result for the shallow grating with $0.75 \mu\text{m}$ period (factor of 1.16) discussed before. For both corrugated devices, the luminous efficacy is enhanced compared to the planar reference. This result is correlated to more intense emission of the corrugated OLEDs at wavelengths with higher sensitivity to the eye. For the weakly corrugated top-emitting OLED, a preservation of the cavity mode in position, width, and intensity, resembling the planar device is again observed.

Extracted internal light modes from Bragg scattering are superimposed to the cavity mode, increasing the extracted amount of light in comparison to the planar reference for the shallow grating. In contrast, the strongly corrugated OLED shows an almost completely vanished cavity mode emission in normal direction, which can be observed as a shoulder around 700 nm wavelength. Furthermore, the emission peaks of the strongly corrugated OLED are broadened in comparison to the planar and the weakly corrugated

device. For an observation angle of 30° (Fig. 8.12(d)), a less intense cavity mode emission as for the planar device is observed for the strongly corrugated device, whereas a prominent second mode is detected at lower wavelengths. The partial vanishing of the fundamental cavity mode for certain angles in the strongly corrugated OLED indicates a significantly increased impact of the deep grating on the far-field emission in comparison to a shallow grating.

In order to gain further insight on the scattering effects, the angle and polarization resolved spectral emission of the devices have been measured in a $\sin \theta$ range from 0 to 1 at a current density of 14.8 mA/cm^2 (Fig. 8.13). The planar device shows only the cavity mode emission with the well-known parabola-like dispersion in s- and p-polarization.

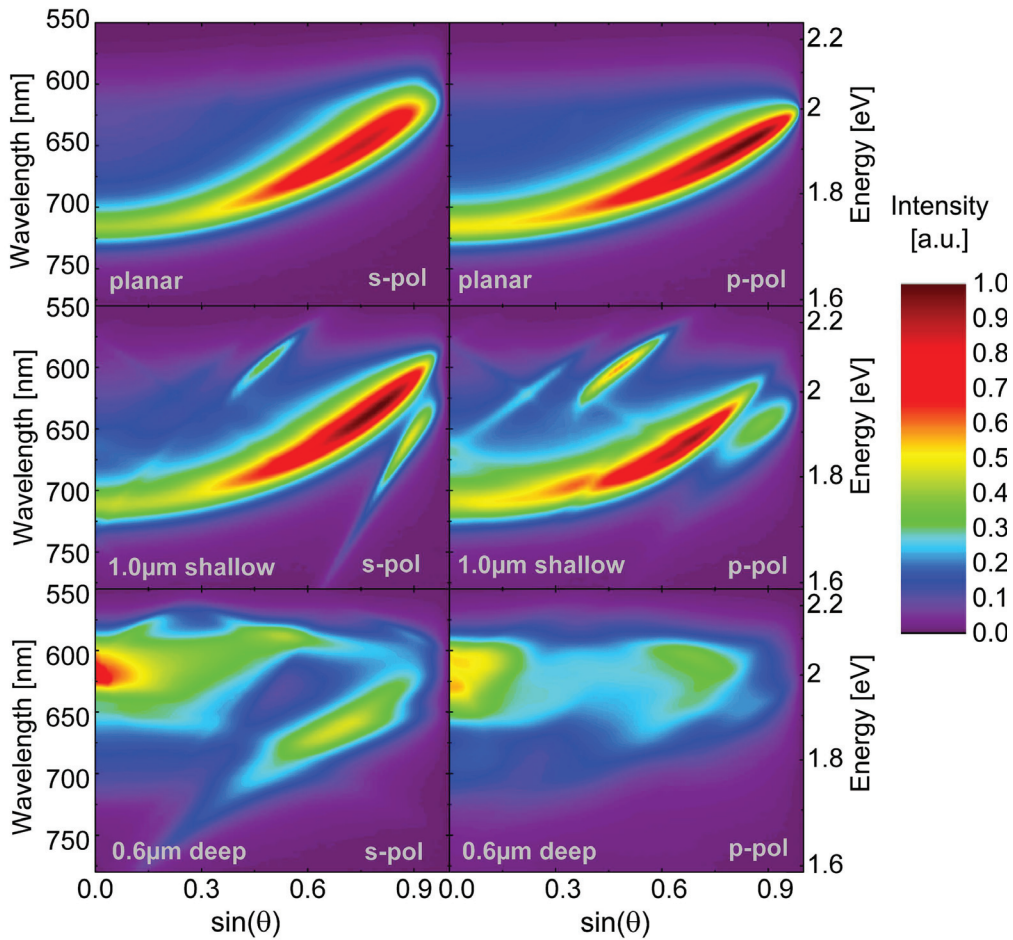


Figure 8.13: Measured angle and polarization resolved emission at a current density of 14.8 mA/cm^2 of the planar and the corrugated OLEDs from Fig. 8.12. Again, the shallow grating introduces additional sharp spectral features to the radiative cavity mode, which is maintained from the planar reference. The deep grating leads to a strongly affected spectral emission without the prominent parabola-like dispersion of the cavity mode. This indicates an increased impact of the perturbation on the far-field emission of the microcavity OLED.

For the corrugated OLED on the shallow grating with $1.0\ \mu\text{m}$ period, the preservation of the cavity mode with comparable intensity is proven for the entire angular range, as indicated in Fig. 8.12(c&d). The observed EQE enhancement can be associated to the additional sharp spectral features in the shallow corrugated OLED, which are detected across the air light-cone.

In contrast, the corrugated OLED on top of the deep grating with a period of $0.6\ \mu\text{m}$ shows a significant decrease in the emission intensity within the air light-cone, resulting in the decrease of the EQE.

Moreover, the parabola-like dispersion of the fundamental cavity mode is not observed in this device for both polarizations. Overall, the emission spectra of the strongly corrugated OLED show significant deviations from weakly corrugated top-emitting devices, as not only sharp spectral features are absent, but also since the cavity mode is not preserved. These findings indicate interactions of the light modes inside the strongly corrugated microcavities, leading to pronounced new effects and significantly altered emission spectra. For the optimization of the OLED-grating structure, a detailed analysis of the scattering effects and its fundamental mechanisms is required, and will be the focus of the further sections.

8.3.2 Analysis of Bragg Scattered Modes

First, geometrical considerations will be used to associate the measured Bragg scattering effects to the internal light modes of the planar reference devices and thus to identify the scattering features, as for both corrugated OLEDs the condition $h_{\Lambda}/d_{\text{opt}} < 1$ is still fulfilled [190]. Figure 8.14 shows the identification of the Bragg scattering effects according to the approach discussed in Section 8.2, for the shallow grating with period of $1.0\ \mu\text{m}$ ^[6]. The measured spectra of the weakly corrugated OLED (color scale) are superimposed to the calculated power dissipation spectra of the reference device (grayscale), covering the entire air light-cone. The measured and calculated cavity mode yields again an accurate agreement in both polarizations (Fig. 8.14). Introducing the reciprocal lattice vector \vec{G} , all scattering features in s-polarization can be assigned to the Bragg scattered WGs1 and WGs2 modes of the 1st and the 2nd Bragg scattering order, where a reciprocal lattice vector of $G_{\text{s-pol}} = 6.41\ \mu\text{m}^{-1}$ ($\Lambda_{\text{s-pol}} = 0.98\ \mu\text{m}$) has been found. For p-polarized emission, the identification of all scattering effects is also achieved, respecting the first two Bragg scattering orders (Fig. 8.14(b)). The best analysis is obtained for a reciprocal lattice vector of $G_{\text{p-pol}} = 6.54\ \mu\text{m}^{-1}$ ($\Lambda_{\text{p-pol}} = 0.96\ \mu\text{m}$), which is in excellent agreement with the grating period measured by AFM ($\Lambda = 1.0\ \mu\text{m}$).

Figure 8.15 shows the application of this method to the s-polarized emission of the strongly corrugated OLED with a period of $0.6\ \mu\text{m}$ ^[6]. Several spectral features coincide with certain confidence to the predicted mode positions obtained from the planar reference. It is found that the scattered WGs1 modes lead to a significant reduction of the emission in the air light-cone. Emission at the predicted position of the cavity mode is only observed at larger in-plane wavenumbers in comparison to the 1st order Bragg scattered WGs1 mode, suggesting an interaction of these two modes. Furthermore, the intense emission at $\approx 600\ \text{nm}$ ($2.0\ \text{eV}$) can be associated to the 1st Bragg scattered WGs2 mode, back folded at $k_x = 0$.

^[6] The power dissipation spectrum of the planar reference has been calculated by Cornelius Fuchs.

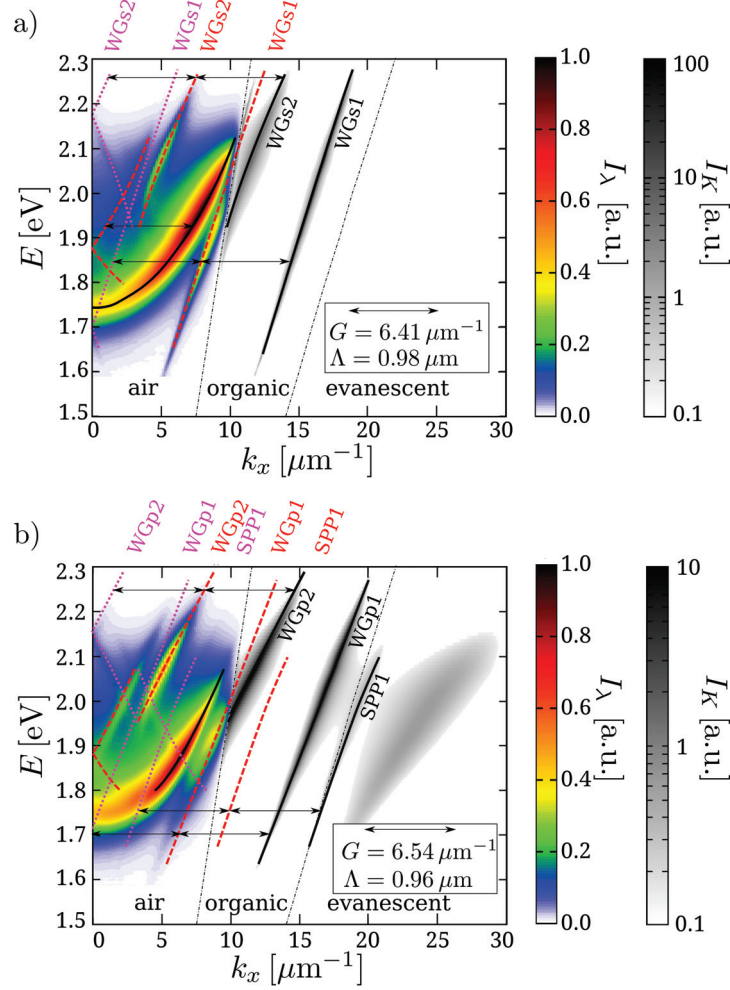


Figure 8.14: Measured spectra (I_λ) of the weakly corrugated top-emitting OLEDs on a 1D grating with period of $1.0 \mu\text{m}$ (color scale) for s -polarized (a) and p -polarized emission (b). The simulated power dissipation spectra (I_K) of the planar reference with identical layer sequence is shown in grayscale. Bragg scattering features are highlighted by red dashed (1st) and purple dotted lines (2nd) lines according to their order. All measured features can be identified accounting for the first two Bragg scattering orders.

In addition, the results suggest that the thickness criterion, obtained from the characterization of corrugated slab waveguide without metallic layers ($h_\Lambda/d_{\text{opt}} < 1$) [190], seems not to be sufficiently applicable for corrugated microcavity OLEDs. The findings indicate a failure of the criterion at even lower ratios of $h_\Lambda/d_{\text{opt}} \lesssim 0.33$ for microcavity OLEDs, as several detected scattering features cannot be associated to internal modes from the planar reference, by using this approach. In order to identify all scattering features in (strongly) corrugated top-emitting OLEDs and to calculate the emission of such devices, a further model will be applied.

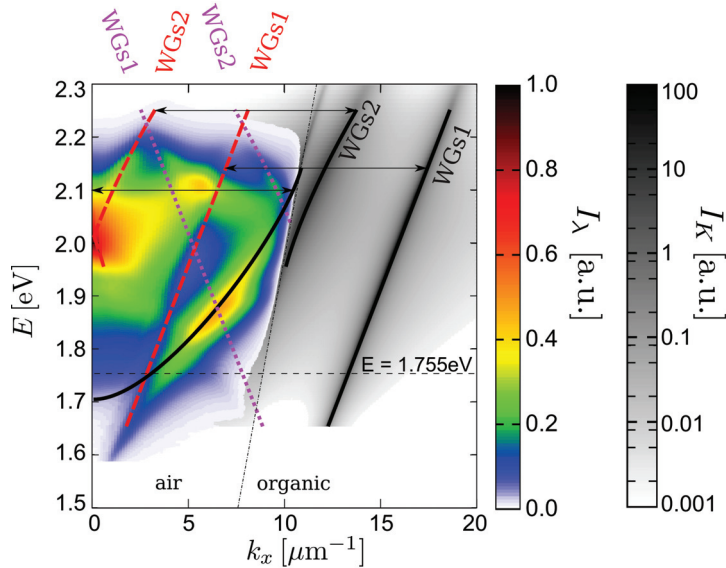


Figure 8.15: Measured s -polarized spectra (I_λ) of the strongly corrugated OLED on the $0.6 \mu\text{m}$ grating (color scale). The simulated power dissipation spectra (I_K) of the planar reference with identical layer sequence is shown in grayscale. Bragg scattered modes determined from the planar reference are highlighted by red dashed (1^{st}) and purple dotted lines (2^{nd}) lines. Even though some spectral features can be assigned to Bragg scattered modes of the planar reference, several effects are not sufficiently reproduced.

8.3.3 Mode-Coupling Effects in Strongly Corrugated OLEDs

This section focuses on the analysis of the spectral emission in (strongly) corrugated top-emitting OLEDs. In order to evaluate the rather complex effects in the emission spectra, an approach is presented, based on the description of radiative far-field modes as damped electromagnetic waves. Therefore, waves of the type:

$$\vec{E}(\vec{r}) = \vec{E}_0 e^{i(\hat{k}_x x + k_z z)}, \quad (8.1)$$

are considered [251], based on the orientation of the 1D grating structures, where \hat{k}_x is smaller than k_0 . For the sake of simplicity, the time dependent factor $e^{-i\omega t}$ has been dropped. The radiative character of the modes inside the air light-cone leads to a decrease in the amplitude E_0 as the wave propagates. Hence, the in-plane wavenumber \hat{k}_x of the resonance can be represented by the complex quantity $\hat{k}_x = k'_x + ik''_x$, with k''_x as damping coefficient. The Fourier transformed representation in dependence of the in-plane wavenumber k_x is given by a Lorentzian-like resonance of the type:

$$E(k_x) = E_0 \left(\frac{e^{-i\phi}}{k'_x - k_x + ik''_x} + \frac{e^{i\phi}}{k'_x + k_x - ik''_x} \right), \quad (8.2)$$

gathering up phase ϕ while propagating. The mode propagation in real space is indicated by the sign of the in-plane wavenumber. As the damping of the radiative mode is associated to the light extraction from the microcavity, it can be correlated to the

reflectivity r of the top "+" and bottom "-" interface of the microcavity:

$$r_+r_- = \exp\{-2d_{\text{opt}}k_x'' \tan \theta\}, \quad (8.3)$$

where d_{opt} describes the total optical thickness of the microcavity and while neglecting absorption losses [251]. Furthermore, the dependence of the phase shift originating from the propagation with an angle θ with respect to the normal direction on the reflection coefficients is respected. Hence, the damping coefficient is also correlated to the real part k_x' of the in-plane wavenumber. In order to validate this approach, an accurate description of a radiative mode from a planar microcavity is shown first.^[6] In Fig. 8.16(a), the s-polarized emission of the planar reference from Fig. 8.13 is fitted by a single resonance of the type described in Eq. 8.2.

The resulting center positions of the Lorentzian mode (k_x') are depicted by black crosses and match well the mode dispersion. For spectra at fixed energies of 1.75, 1.85, and 1.95 eV, the simulation results of the single Lorentzian fit are provided in Fig. 8.16(b). Excellent agreement in mode position, width, and intensity are observed for all energies, evidencing the reliability of this approach.

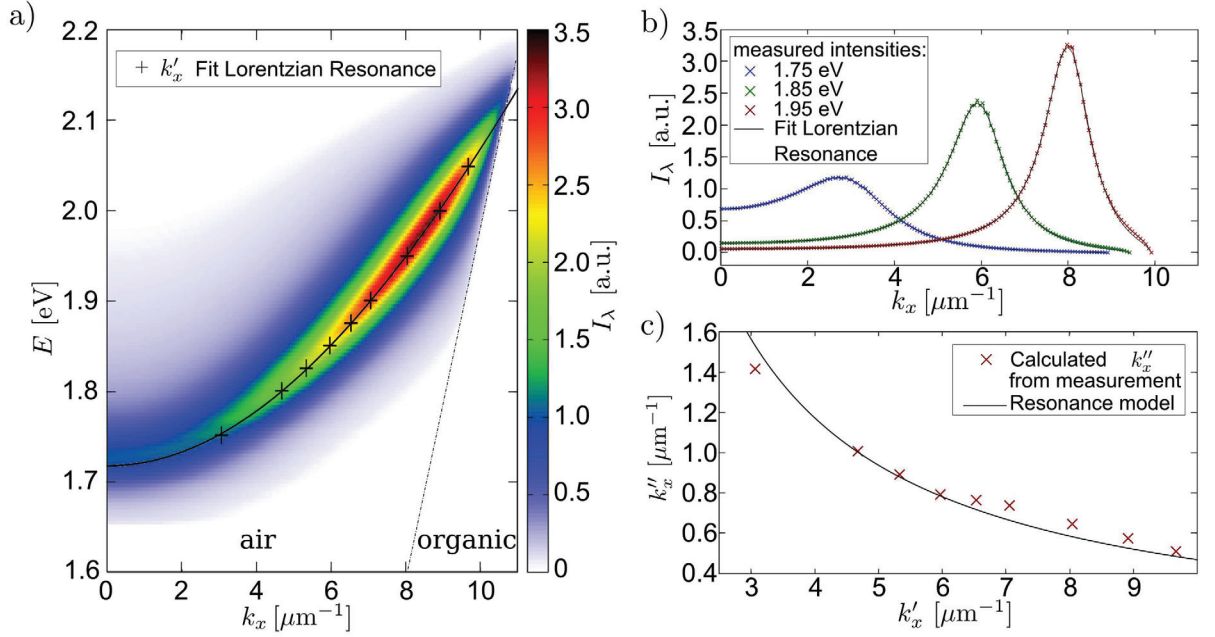


Figure 8.16: S-polarized spectral emission (I_λ) for the planar reference of Fig. 8.13. The emission has been fitted by a single Lorentzian-like resonance, highlighting its center position (k_x') by black crosses (black line as guide to the eye). For fixed energies of 1.75, 1.85, and 1.95 eV, the correspondence between the fitted resonance and the cavity emission is depicted (b). Furthermore, the damping parameter k_x'' of the measured and fitted cavity mode in dependence on the resonance position k_x' is shown (c). The fit proves an accurate description of a single radiative mode of a microcavity by a single Lorentzian-like resonance.

^[6] The contribution of Cornelius Fuchs and Reinhard Scholz in the investigation of this model is gratefully acknowledged.

In order to validate the description of the damping parameter k_x'' by Eq. 8.3, the values obtained from the fit of the cavity mode are correlated to the calculated ones from the spectral emission (Fig. 8.16(c)).

Even though an energy dependence of the reflection coefficients has been neglected in the calculation, a good agreement between the predicted and the fitted values has been observed. Overall, the results show that the emission of a single radiative mode from a microcavity can be well described by a single Lorentzian-like resonance. Furthermore, the calculated damping coefficients in the range of $1 \mu\text{m}^{-1}$ represent a very large damping of the light modes inside microcavity OLEDs with propagation lengths of only a few wavelengths, which reveals an intense light extraction instead of light mode confinement. In order to describe the emission spectra of corrugated devices with this approach, the number of resonances for each energy has to be determined. Even though this number can be chosen as a free parameter in the simulation, the number of modes has been determined from the previously presented analysis of the measured emission spectra (cf. Fig. 8.15). This is based on the assumption that the measured spectra of the corrugated OLED originates from the interaction of the fundamental cavity mode with the Bragg scattered modes of the microcavity inside the air light-cone. Hence, the number of resonances is determined by the power dissipation spectrum of the OLED and the according Bragg scattered modes.

In Fig. 8.17, the measured spectrum of the corrugated device for an energy of 1.755 eV (705 nm) is shown. According to the previously mentioned analysis, three interacting modes (WGs1 ($m = 1$), WGs1 ($m = -1$), and the cavity mode) contribute to the measured spectrum at this energy (cf. Fig. 8.15). For the analysis of the spectrum, a complex summation of the single Lorentzian-like modes has been applied, while only the number of resonances is supplied to the simulation and the parameters: E_0 , k_x' , k_x'' , and ϕ are starting from arbitrary numbers. In Table 8.1, the parameters obtained for each resonance are summarized.

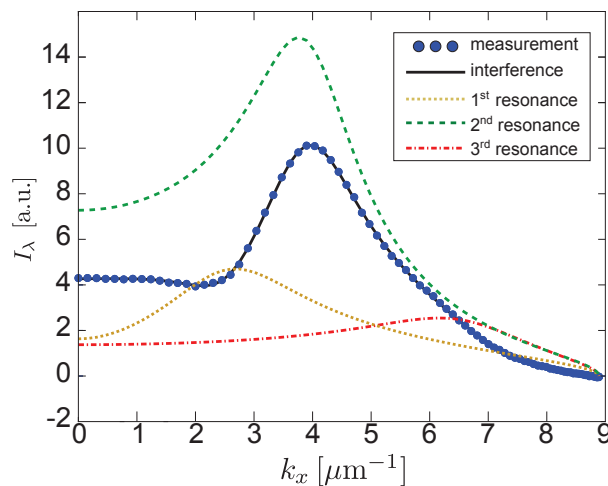


Figure 8.17: The measured s -polarized spectrum for a photon energy of 1.755 eV (705 nm) extracted from Fig. 8.15 and the obtained fit based on the interference of three Lorentzian-like resonances is shown. The measured spectrum can be reproduced by the complex sum of the three resonances. Furthermore, the intensity of the individual resonances is depicted.

Table 8.1: Summary of the parameters of each Lorentzian-like resonance for the analysis of the measured spectrum of a strongly corrugated OLED shown in Fig. 8.17.

Resonance	k'_x [μm^{-1}]	k''_x [μm^{-1}]	ϕ
1	2.53	1.22	1.49π
2	3.92	0.96	0.95π
3	6.64	1.57	1.15π

The complex sum of the three simulated modes, shown as black line in Fig. 8.17, yields excellent agreement with the measured spectrum. The first resonance shows a pronounced phase-shift to the second mode ($\Delta\phi > \pi/2$), while the second and third resonance are almost carrying the same phase ($\Delta\phi \approx 0.2\pi$).

Again, damping parameters in the range of $1.0 \mu\text{m}^{-1}$ have been found for the corrugated device, which are similar to the values for the planar reference, mainly attributed to the identical microcavity layout. However, the impact of Bragg scattered modes can have a significant influence on the calculated damping coefficients according to Eq. 8.3, as the spectral reflectance is affected, and might rather serve as an indicator for a reasonable damping parameter of the fitted resonance, instead of an accurate measure.

Accordingly, the shown results prove that the measured spectrum of a corrugated OLED can be described by a complex summation of interfering Lorentzian-like resonances. Furthermore, the accurate description is based on a simulation with identical number of resonances as experimentally determined radiative modes. For this energy, the measured resonances can be attributed to an interference of the 1st order WGs1 mode, the cavity mode, and the -1st WGs1 mode. The comparison of the individual resonance intensities with the complex sum proves the mainly destructive interference of the first resonance (1st order WGs1 mode) with the other two resonances, most prominent at k'_x of approximately $2.4 \mu\text{m}^{-1}$ (cf. Fig. 8.17). In Fig. 8.18(a), the obtained positions of the three resonances for an energy of 1.755 eV are superimposed to the measured s-polarized emission of the planar device.

Based on the presented model, the mode positions obtained from the fit of the measured spectra over the entire energy range are included in Fig. 8.18(b)^[7]. According to the modes determined in Fig. 8.15, up to five resonances have been required to accurately describe the measurement spectra. It is worth to note that the application of a different number of resonances than the predicted one from the experimental data typically does not allow to reach a sufficient convergence with the experimental results.

The analysis confirms that destructive interference of the Bragg scattered WGs1 mode in the air light-cone causes the partial decrease of light mode intensities in the air light-cone, while a model based on rate considerations of the Bragg scattering processes, suggested by Hauss *et al.* [238], is not required. It is found that the intense emission in normal direction at 2.0 eV results from the constructive interference of the -1st and 1st Bragg order WGs2 mode. Moreover, several obtained positions of the resonances coincide with the positions of the scattered internal modes from the planar reference. Therefore, they are again represented by colored lines, shown in Fig. 8.18(c). The absence of the radiative cavity mode is confirmed by the resonance positions determined from the interference model.

^[7] Simulation data calculated by Cornelius Fuchs.

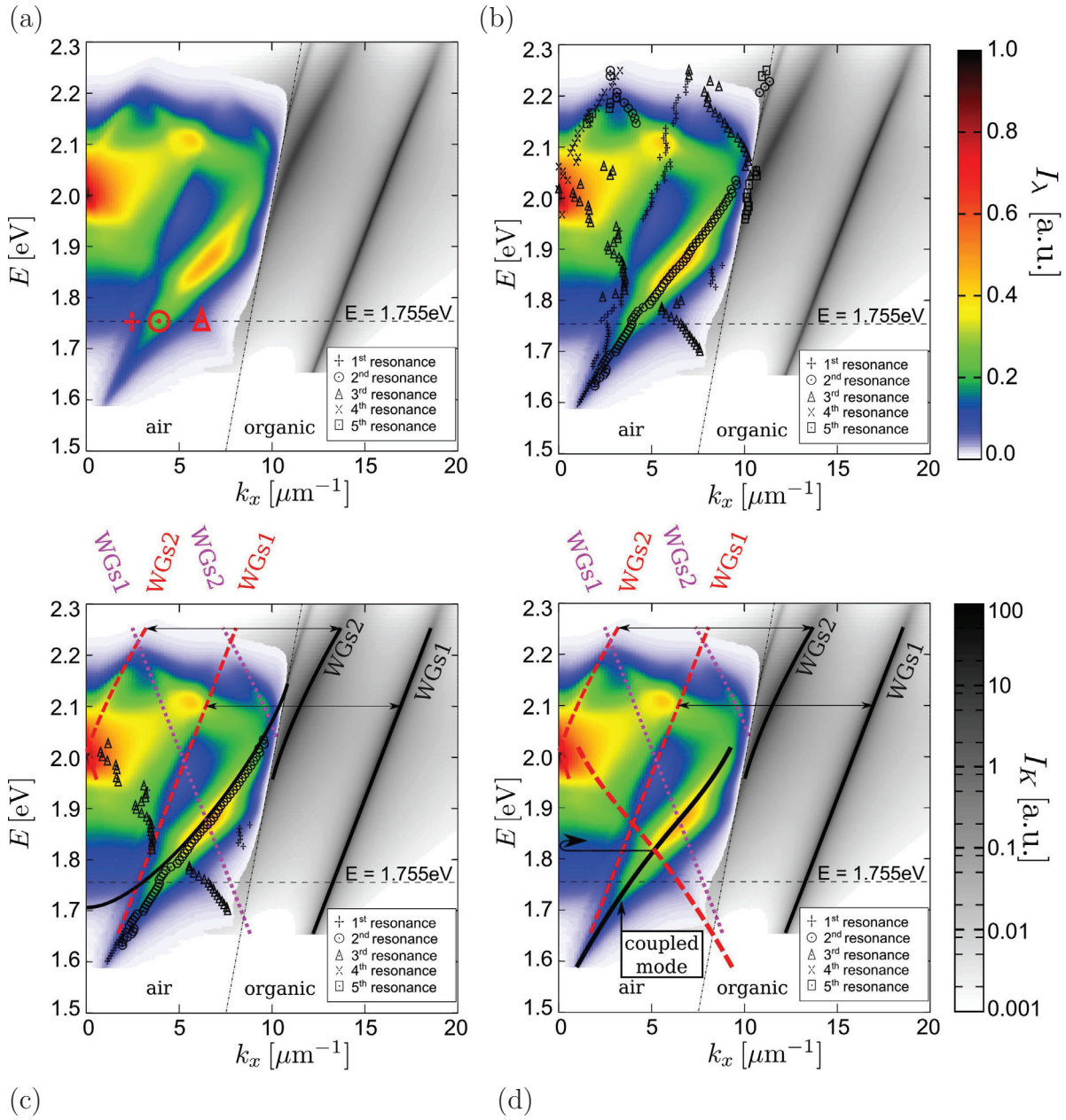


Figure 8.18: Fitted center position (k'_x) of resonances for the s -polarized emission spectrum of the strongly corrugated OLED for an energy of 1.755 eV (a) as well as for the entire energy range (b). According to the analysis in Fig. 8.15, up to five interfering resonances have been allowed at each energy. The resonances obtained coincide with the observed absence of the cavity mode (c), while the formation of a coupled mode pair of the cavity mode and the WGs1 mode is emphasized (d), allowing to identify all spectral features of the strongly corrugated top-emitting OLED.

In an interval of in-plane wavenumbers from 2.0 to $3.9\ \mu\text{m}^{-1}$ and energies from 1.7 to $1.85\ \text{eV}$, pronounced destructive interference of the cavity mode and the first Bragg order WGs1 mode is found in the phase information of the interfering resonances. Furthermore, it is detected that these two interacting modes form a coherently coupled mode pair, visualized in Fig. 8.18(c & d), while the initial cavity mode partially vanishes. The coupled mode pair finally allows for the association of the remaining measured spectral effects to its 1st Bragg scattering replica, which could not yet been identified by scattered modes from the planar reference device.

Overall, the suggested model has provided convincing results, describing the spectral emission of strongly corrugated top-emitting OLEDs by a complex summation of interfering Lorentzian-like resonances. The information obtained on the local phase, position, and amplitude of the individual resonances further allows to gain a detailed insight into the processes predicting the observed emission patterns from mode interference. The formation of a coherently coupled mode pair in a strongly corrugated top-emitting OLEDs has been observed for the first time and emphasizes that even in top-emitting OLEDs, having rather low Q-factors in comparison to microcavities using DBR mirrors [252], complex scattering phenomena are present.

Chapter Summary

In this chapter, the experimental realization of periodically corrugated top-emitting OLEDs, employing state-of-the-art device architectures, has been presented. For the first time, the preservation of the electrical characteristics and hence the IQE has been achieved, while introducing the corrugation. This allows for the direct correlation of changes in the EQE to the light extraction efficiency. The conservation of the electrical performance is associated to the application of photoresist gratings with a low surface roughness and the absence of defects. It has been shown that photolithography as well as nanoimprint can be used to produce high quality 1D photoresist gratings with periods down to $0.6\ \mu\text{m}$ and depths of only $11.2\ \text{nm}$. The surface modulation of the corrugated photoresist is almost perfectly maintained from the entire layer sequence of the top-emitting OLED deposited on top. In contrast to photolithography, the nanoimprint approach allows also for an easy up-scaling of the process, while being compatible with the preferred R2R processing.

In weakly corrugated top-emitting OLEDs, Bragg scattered modes have been identified from geometrical considerations in the wave vector diagram, associating the measured effects to Bragg scattered modes of the planar reference OLED. For a shallow grating of $0.75\ \mu\text{m}$ period (aspect ratio 0.05), the interaction of a Bragg scattered waveguided mode and the cavity mode results in the splitting of the cavity mode into two branches. Such an anti-crossing phenomenon has so far not been observed in corrugated OLEDs and the detailed mechanism of the coupling has still to be identified, whereas further investigations on the mode interaction in corrugated top-emitting OLEDs will be shown in Chapter 9. The deposition of top-emitting OLEDs on a grating with an aspect ratio of 0.24 results in dramatically altered spectral effects, including the partial vanishing of the fundamental cavity mode. Here, the identification of all spectral features has not been possible, only using the Bragg scattered modes of the planar reference device.

In order to describe the emission spectra of corrugated OLEDs and to identify all scattering effects in strongly corrugated devices, a model which describes the radiative modes inside the air light-cone by damped resonant waves, propagating along the microcavity and interfering with each other, has been presented. This simulation model has yielded excellent agreement with the experimental results, providing the number of resonances in accordance to the measured spectral emission. These findings show that interference of the light modes inside the air light-cone determines the spectral emission of corrugated top-emitting OLEDs, instead of a simple superposition/ transfer of mode intensities. With this approach, the absence of the cavity mode could be associated to the formation of a coupled mode pair consisting of the Bragg scattered WGs1 mode and the cavity mode. Furthermore, contributions of the 1st order Bragg scattered replica of this mode have been detected in the spectral emission, which finally allowed for the identification of all scattering effects in the strongly corrugated top-emitting OLED.

For red top-emitting OLEDs on 1D shallow gratings with 0.75 μm period, an EQE enhancement factor of 1.16 has been detected with respect to the planar reference device, slightly larger than that for a shallow grating with 1.0 μm period ($\text{EQE} \times 1.13$). Analysis of the spectral emission of the corrugated OLEDs reveal that the efficiency increase is mainly attributed to additionally extracted waveguided modes, whereas SPP modes only slightly contribute to the far-field emission and remain mostly trapped within the OLED. Furthermore, the EQE of corrugated top-emitting OLEDs exceeds values of 17 %, which is comparable to the highest values reported for 2nd cavity order red top-emitting OLEDs so far.[11] However, the corrugated 2nd order microcavity OLEDs shown have not reached the efficiency benchmark of top-emitting devices, which is represented by planar 1st order OLEDs reaching EQEs of up to 29 %.[11] The identified destructive interferences of the Bragg scattered modes and the cavity mode suggest that the efficiency of corrugated OLEDs could be increased if constructive interference can be realized. On the one hand, the optical properties of the microcavity OLED can be tuned by the variation of layer thicknesses, in order to optimize the phase relations of the interfering modes and thus to allow for constructive interference. On the other hand, the parameters of the light extraction structure, especially the grating period, can be varied to affect control the interference of the light modes, such as the grating period to avoid a scattering of the 1st Bragg order WGs1 mode into the air light-cone and thus hindering the destructive interference with the cavity mode.

Hence, further optimizations of the grating-OLED system are necessary to improve the efficiency. In addition, further investigations on the anti-crossing phenomenon in corrugated top-emitting OLEDs, will be presented in the following chapter.

9 Optimization of the Grating-OLED System

This chapter focuses on the optimization of the grating-OLED system, in order to improve the extraction efficiency of internally trapped light modes by applying 1D periodically corrugated photoresist films. First, red top-emitting OLEDs are investigated with regard to the impact of microcavity effects on the mode interference inside the air light-cone. Then, these findings are applied to increase the efficiency of corrugated white top-emitting OLEDs, using ultra-thin and highly transparent wetting layer electrodes.

In the previous chapter, the efficiency of optimized planar red top-emitting OLEDs has been increased by extracting internally trapped light modes via Bragg scattering at 1D periodically corrugated photoresist layers. An analysis of the scattering effects has shown that the emission of corrugated microcavity OLEDs is predicted from the interference between Bragg scattered modes and the radiative cavity mode. Thereby, effects of destructive interference as well as the formation of a coherently coupled mode pair from interfering modes have been found, where the radiative cavity mode partially vanished. Both effects limit the efficiency gain from extracted light modes, in comparison to a constructive interference of all light modes inside the air light-cone.

In this chapter, experiments to increase the efficiency of corrugated top-emitting OLEDs are presented. The focus is set on the evaluation of a distinct approach which maintains the initial cavity mode and suppresses destructive interference between light modes. Since a large variety of parameters of the grating as well as the OLED architecture have an impact on the occurring scattering effects, the presented experiments can only provide a preliminary insight into the parameter space. For instance, the grating can be varied in period, height, aspect ratio, and profile, while parameters for an OLED optimization are for example the charge transport layer thicknesses, EML positions, top electrode thickness, capping layer thickness, as well as the materials, e.g. the application of oriented emitters.

Corrugated red top-emitting OLEDs are investigated in Section 9.1, optimizing the microcavity for constructive mode interference. Based on the insights obtained for the monochrome devices, white top-emitting OLEDs on top of 1D grating structures are investigated in Section 9.2.

9.1 Microcavity Optimization for Constructive Mode Interference

Investigations on the scattering effects in corrugated monochrome microcavity OLEDs using rather thick silver top electrodes of ≈ 20 nm thickness have been shown in Chapter 8. For a weak corrugation of the microcavity from a shallow grating (aspect ratio < 0.1), an efficiency enhancement of up to 16% has been achieved, whereas the introduction of a strong layer modulation using a deep grating (aspect ratio ≈ 0.24) has not yielded an efficiency improvement so far.

Based on the previous findings, shallow gratings of $0.75 \mu\text{m}$ period and a depth of ≈ 40 nm are investigated in this section^[8], so that the cavity mode is preserved and an efficiency enhancement can be expected. In order to increase the light extraction efficiency, the impact of the metal top electrode thickness as well as the capping layer thickness are investigated, since both can be used to control the quality factor (Q) and thus the spectral emission from the microcavity. On the one hand, the optimization is supposed to optimize the phase correlation between the interfering modes, enabling constructive interference. On the other hand, it allows for a detailed investigation of the anti-crossing phenomenon in s-polarized emission of weakly corrugated top-emitting OLEDs (cf. Section 8.2), requiring a coupling interaction of light modes in the microcavity.

9.1.1 Variation of the Top Electrode Thickness

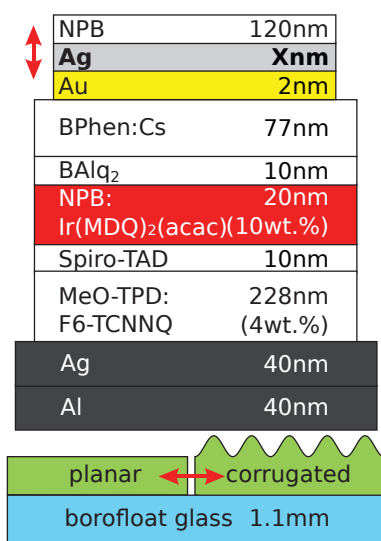


Figure 9.1: Device architecture for the investigation of the influence of a top electrode variation on the light extraction efficiency in corrugated top-emitting OLEDs.

The impact of the top electrode thickness on the light extraction from corrugated top-emitting OLEDs is analyzed in the following. Therefore, the silver thickness is varied between 20 nm and 9 nm. A gold wetting layer of 2 nm is deposited underneath the silver, allowing to maintain a reliable device operation for such thin silver films (cf. Chapter 6). A NPB capping layer with a thickness of 120 nm confines the cavity emission for an increased impact of the cavity effect on the light mode interaction. Figure 9.1 shows the planned device architecture being the same as for the devices presented in Chapter 8, except for the gold wetting layer and the capping layer thickness.

Even though a top electrode of only 2 nm Au/ 9 nm Ag is deposited on top of the corrugated layer sequence, a comparable electrical device operation as for the corrugated OLEDs with 15 nm and 20 nm thick Ag layers is observed (Fig. 9.2(a)). Furthermore, the leakage currents of the corrugated OLEDs on the shallow gratings with approximately 40 nm depth and $0.75 \mu\text{m}$ period remain smaller than 10^{-4} mA/cm^2 . Overall, the jV -curves of the planar references and the corresponding corrugated OLEDs show an excellent comparability for all top electrodes investigated.

[8] Wallace Choy contributed the nanoimprint master.

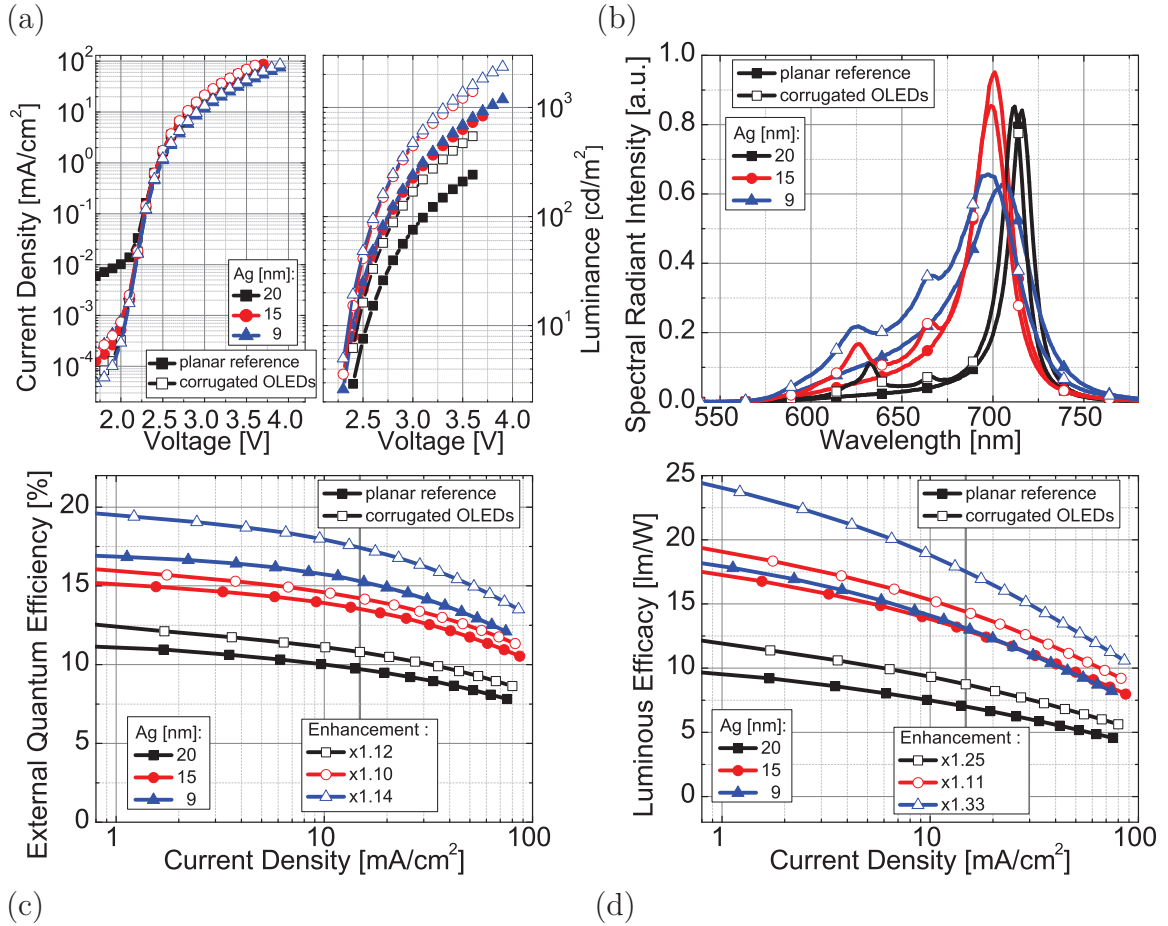


Figure 9.2: Influence of the top electrode thickness on the j VL characteristics (a), the spectral emission in normal direction at a current density of 14.8 mA/cm^2 (b), the EQE (c), and LE-current dependency (d) of planar and corrugated red top-emitting OLEDs. The electrical performance of the corrugated OLEDs, built on a grating of $0.75 \mu\text{m}$ period and 40 nm depth are comparable to the planar references. Additional emission peaks, originating from Bragg scattered internally trapped light modes, increase the efficiency of the corrugated devices.

An increase in the luminance is found for all corrugated OLEDs. Figure 9.2(b) shows the spectral radiant intensity of the planar and the corrugated OLEDs in normal direction, measured at a current density of 14.8 mA/cm^2 . By decreasing the Ag thickness and thus the reflectivity of the top electrode, a spectral broadening of the cavity emission is detected. The corrugated OLEDs show comparable emission of the radiative cavity mode as the planar references, while only slight variations in the peak wavelength are detected. Again, this shows that the optical properties of the planar and the corresponding corrugated device are comparable, as intended from the fabrication on the same substrate. Besides the cavity mode, two additional emission peaks attributed to Bragg scattered light modes are observed in the corrugated devices. A sharp peak at a wavelength of 670 nm is detected in all corrugated OLEDs, independently of the top electrode thickness. Since the grating period is identical in all devices, a remaining position of the scattering peak can only be explained by a similar position of the scattered internal mode for all silver thicknesses. In contrast, the second peak shows a broadening and shift to smaller

wavelengths with a reduced Ag thickness (635 nm to 625 nm). This peak represents the trend of the radiative cavity mode for the electrode variation, while the distance to the initial cavity mode position remains constant. Hence, this peak is assigned to the Bragg scattered radiative cavity mode.

The EQEs of the device set are shown in Fig. 9.2(c). For the planar references, an EQE increase is detected for reduced the top electrode thickness. The planar OLED with a top electrode of 2 nm Au/ 9 nm Ag reaches the highest EQE of 15.4% at a current density of 14.8 mA/cm². Furthermore, the corrugated OLEDs show an increase of the EQE in comparison to their planar reference, which have been attributed to the extracted internal light modes from the cavity. The corrugated OLED with a 9 nm thick Ag layer reaches an EQE of 17.6% at a current density of 14.8 mA/cm², which is slightly higher than the highest reported efficiency (EQE: 17%) of an optimized planar red top-emitting OLED in the second optical maximum by Hofmann *et al.* [11]. It is expected that optimizations of the organic layer sequence for each top electrode can potentially result in higher EQEs, even for the planar references. Especially, the capping layer has not been optimized for maximum photon flux in these devices, but for the strongest mode confinement of the cavity mode in order to investigate the anti-crossing behavior, observed for comparable devices presented in Section 8.2. However, the EQE enhancement factor is only 10-14%, without a prominent dependency on the top electrode thickness so that it is not improved in comparison to the previous results. Thus, the efficiency of the most efficient planar device architectures, represented by 1st order microcavity OLEDs, has not been reached for corrugated devices yet. In terms of luminous efficacy (Fig. 9.2(d)), a comparable trend as for the EQE is found, while changes of the spectral shape alter the explicit enhancement factors. This could be interesting for the application in corrugated white OLEDs, as the LE might be additionally increased to the EQE from the affected spectral emission.

In order to investigate the Bragg scattering effects of the corrugated OLEDs in more detail, the angle and polarization resolved spectral emission is shown in Fig. 9.3, measured at a current density of 14.8 mA/cm². Prominent effects of Bragg scattered modes, introducing sharp spectral features to the parabola-like cavity mode, are observed in all corrugated devices. Thereby, the effects remain comparable to the findings for weakly corrugated OLEDs shown in Section 8.2, where a detailed analysis of the scattering effects has been presented.

For a top electrode of 2 nm Au/ 20 nm Ag, a narrow cavity mode emission is detected, while the Bragg scattered light modes introduce destructive interference effects in s- and p-polarization, partially decreasing the intensity of the cavity mode. The interaction of a Bragg scattered (waveguided) mode and the cavity mode results again in a prominent splitting of the cavity mode in s-polarization. In contrast, the destructive interference observed for p-polarized emission for $\sin \theta < 0.3$ does not result in the formation of two bended emission branches, which suggests that the anti-crossing phenomenon might not only be based on destructive interference of light modes. Decreasing the silver thickness to 15 nm leads to a decrease in the Q-factor, which results in a broadening of the cavity mode emission, while the observed scattering effects remain nearly unaffected. Only slight changes are observed in the anti-crossing behavior as well as in the destructive interference in p-polarized emission. The reduced intensity decrease indicates that the interaction and phase difference between the light modes are affected by the variation of

the metal electrode thickness. Differences in the position of the Bragg scattered modes are associated to changes in the power dissipation of the OLED architectures.

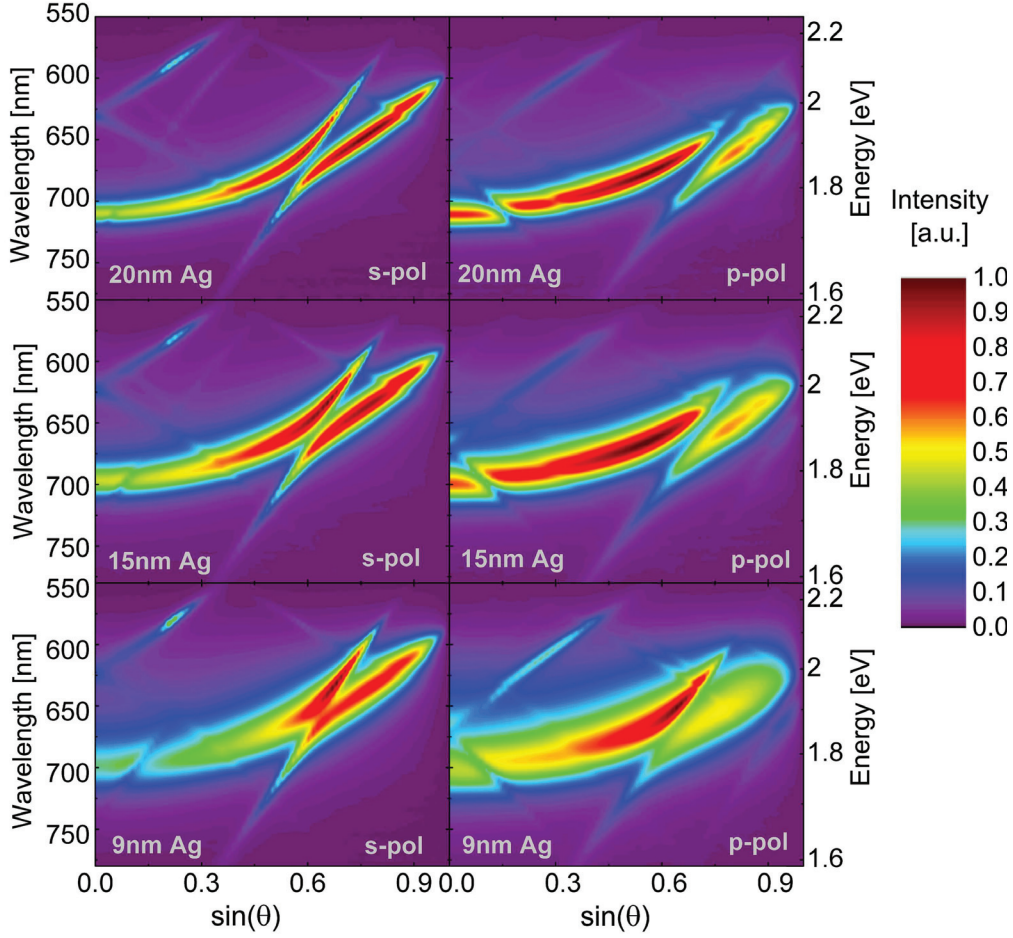


Figure 9.3: Normalized angle and polarization resolved spectral radiant intensity of the corrugated red top-emitting OLED from Fig. 9.1. Prominent destructive interference between the Bragg scattered internal light modes and the cavity mode is observed for all Ag thicknesses in both polarizations. Again, a splitting of the cavity mode is observed in s-polarization for all microcavities. For thinner Ag electrodes, the intensity decrease as well as the energetic separation of the cavity mode branches in s-polarization is reduced.

By further reducing the top electrode thickness to 9 nm Ag, the observed trends increase. The cavity emission is again broadened, corresponding to an even more reduced Q-factor of the microcavity. The interaction of the Bragg scattered mode and the cavity mode results in a smaller relative decrease of the emission intensity compared to the devices with larger Ag thickness, regarding to the destructive interference in p-polarization and the anti-crossing for s-polarized emission. However, an anti-crossing behavior of light modes in s-polarization can still be observed, whereas the separation between the two branches decreases with Ag thickness (cf. Fig. 9.3). Even though several beneficial changes in the interaction of Bragg scattered modes and the cavity mode are found by decreasing of the top electrode thickness, a new destructive interference between Bragg scattered and

cavity mode arises in s-polarization for $\sin \theta < 0.3$ and for wavelengths between 650 nm and 720 nm. Overall, it has been found that the interference of Bragg scattered modes and cavity mode can be influenced by a variation of the metal top electrode, as revealed by different degrees of destructive interference in the angular and spectrally resolved emission. However, the efficiency enhancement remains comparably small ($\text{EQE} \times 1.14$), as prominent constructive interference of the Bragg scattered mode and the cavity mode has not yet been achieved. The anti-crossing modes do not only show a smaller intensity reduction at their intersection, but further a reduced separation of the two branches for a thickness decrease of the top electrode.

These findings suggest a smaller coupling interaction in the system, which might be correlated either to a lower Q-factor of the microcavity, or a thinner metal thickness. For the Purcell effect, which accounts for the impact of the light mode confinement in a cavity structure on the radiative decay of radiative molecules, a correlation between the Q-factor of the microcavity and the emission from these structures has been proven [252]. In order to investigate a possible influence of the Q-factor on the anti-crossing phenomenon detected for corrugated top-emitting OLEDs in more detail, the organic capping layer will be varied, while the metal layer remains unaffected.

9.1.2 Variation of the Capping Layer to Optimize the Microcavity

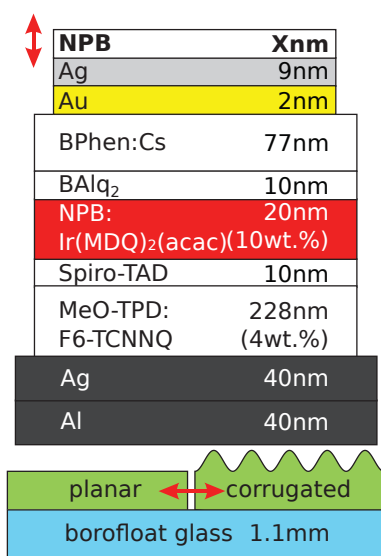


Figure 9.4: Top-emitting OLEDs with varied capping layer thickness to optimize the light extraction for a shallow 1D grating with $0.75 \mu\text{m}$ period.

In the following, the organic capping layer thickness is varied to control the optical properties of the microcavity and to investigate its impact on the light extraction efficiency in corrugated top-emitting OLEDs. As shown in Section 4.2.2, a variation of the capping layer thickness can be used to narrow or broaden the emission from a microcavity OLED, even though the thickness of the metal top electrode is not altered.

Here, a capping layer of 120 nm thickness has been used to achieve a confined cavity emission, representing a device with a "high Q" factor in the experiments (cf. Section 9.1.1). These OLEDs are compared to devices with a capping layer of 60 nm thickness, designed to show broad spectral emission, which represents a cavity with a "low Q" factor. It is worth to note that the Q-factors of the investigated top-emitting OLEDs are much smaller (< 20) than that for resonators which are referred in literature to have a "high quality" factor (> 1000) [252]. Here, the attribute is used to distinguish between the devices. For all devices, the top electrode is a 2 nm Au/ 9 nm Ag wetting layer electrode (Fig. 9.4). A shallow 1D grating of approximately 40 nm depth and $0.75 \mu\text{m}$ period is used to extract the internally trapped light modes. Figure 9.5(a) shows the

electrical performance of the planar and the corrugated OLEDs, which is neither affected by the capping layer nor by the introduction of the corrugation pattern. This behavior is expected, as the capping layer is not included in the electrically active part of the OLEDs. For both corrugated OLEDs, the luminance shows a prominent increase.

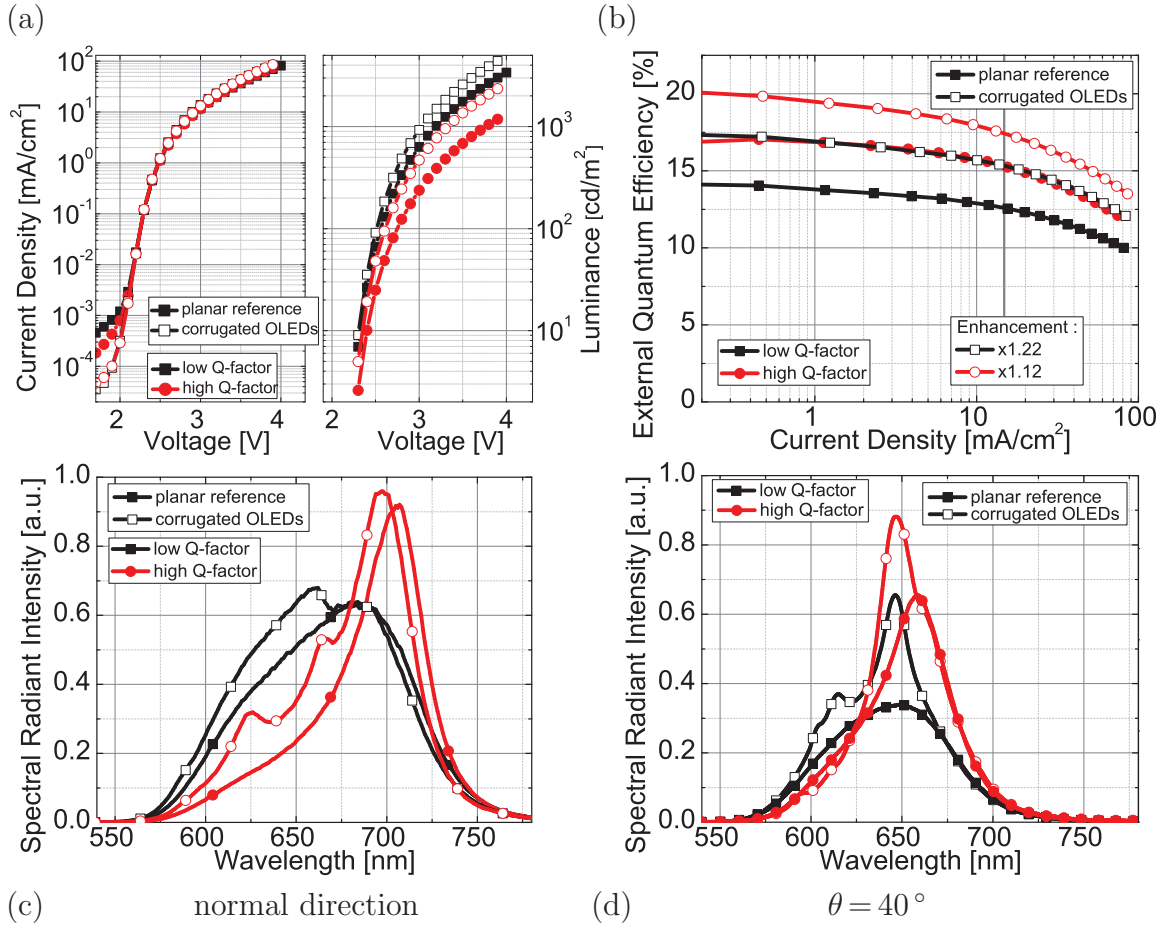


Figure 9.5: Influence of the capping layer thickness on the planar and the corrugated red top-emitting OLEDs, regarding the j VL characteristics (a), the EQE-current dependency (b), as well as the spectral emission in normal direction (c) and for 40° (d) at a current density of 14.8 mA/cm^2 . The electrical performance of all devices remains comparable, as neither the capping layer nor the corrugation introduce adverse effects. The shallow grating efficiently extracts trapped light modes, increasing the EQE by up to 22 %, reducing the Q-factor of the microcavity.

In accordance to the luminance, the grating increases the EQE for both devices. The 1D corrugated OLED with a low Q-factor provides a significant enhancement of the EQE by a factor of 1.22, whereas the device with a high Q-factor has only been improved by a factor of 1.12, but its overall performance remains better than for the cavity with a thinner capping layer (Fig. 9.5(b)). Two effects can cause the higher enhancement factor for the device with a lower Q-factor: either a more efficient extraction of the internally trapped light modes or an increasing contribution from constructive interference of light modes inside the air light-cone. The spectral radiant intensity of the sample set in normal direction, measured at a current density of 14.8 mA/cm^2 , is shown in Fig. 9.5(c). The emission of the cavity mode validates the control on the Q-factor by a capping layer variation. The Q-factors of the microcavity OLEDs have been correlated to the radiative cavity mode and are thus derived from the FWHM of the radiative cavity mode and the resonance wavelength, yielding values of 7.1 and 2.8 for the high-Q device and the low-Q device, respectively. Both corrugated devices show a cavity emission comparable

to the planar references. The observed slight variations in peak wavelength are again attributed to minor thickness variations during the device fabrication. Two narrow peaks of Bragg scattered modes are found in the high-Q device, in contrast to the corrugated OLED with a broad cavity emission, showing an almost homogeneous intensity increase in a spectral range between 570 nm and 670 nm, while distinct features of the scattered modes fade within the broad cavity emission.

For an observation angle of 40° ($\sin \theta = 0.43$) (Fig. 9.5(d)), the relative intensity increase from the Bragg scattered light modes is more prominent for the low-Q device. Since the capping layer does not only affect the Q-factor of the microcavity, but also the resonance conditions, this large intensity increase can be attributed to constructive interference of the modes. In comparison, the relative intensity increase for the high-Q device is not as prominent as in the low-Q device, indicating less suitable phase relations of the interfering modes. More detailed investigations of the scattering effects are shown in the normalized angle and polarization resolved spectra of the corrugated OLEDs in Fig. 9.6. Again, the measurement has been performed under electrical operation at a current density of 14.8 mA/cm^2 . As indicated in Fig. 9.5(c & d), an intense emission contribution of a Bragg scattered mode can be detected for the device with the lower Q-factor. Due to the significant intensity increase, the cavity emission becomes less prominent in the normalized color scale for s-polarized emission. For p-polarization (Fig. 9.6), Bragg scattered modes introduce additional emission in both devices, but the intensity increase is not as significant as it is observed for s-polarized emission in the low Q-device. From the angularly resolved emission, the higher enhancement factor can be associated to prominent constructive interference of Bragg scattered and cavity mode, which has been obtained from an optimization of the capping layer thickness. In addition, the anti-crossing phenomenon vanishes in the s-polarized emission of the low Q-factor device.

Even though the experimental results emphasize an interaction of a waveguided organic and the cavity mode in the corrugated microcavity OLEDs, it has so far not been clearly validated which mechanisms cause the anti-crossing phenomenon. On the one hand, the optical environment has a significant influence on the radiative characteristics of the emitting molecules (cf. Purcell effect), which might contribute to the vanishing anti-crossing for lower Q-factors. On the other hand, the interaction of the dissipated radiation with the microcavity, either by the corrugated layers itself, e.g. the thin metal electrode, or by the periodic modulation of the refractive index, representing a photonic crystal like structure, might also account to the observed anti-crossing.

Detailed investigations on the mode interaction in such OLEDs might lead to advanced device designs, which can benefit from a controlled coupling of light modes for future applications and are in the focus of further studies. With focus on the efficiency enhancement from Bragg scattered internally trapped light modes, a reduction of the metal top electrode thickness as well as an optimization of the capping layer for low Q-factor cavities has yielded a significant increase of the light extraction efficiency up to a factor of 1.22 in corrugated red top-emitting OLEDs. Thereby, the detected anti-crossing behavior vanished, and a mainly constructive mode interference between the Bragg scattered modes and the cavity mode has been observed. The device design concept obtained to increase the efficiency in corrugated monochrome devices is somehow related to the optimization of planar top-emitting OLEDs for efficient white light emission.

Experiments to improve the efficiency of white top-emitting OLEDs from the extraction of internal light modes are presented in next section.

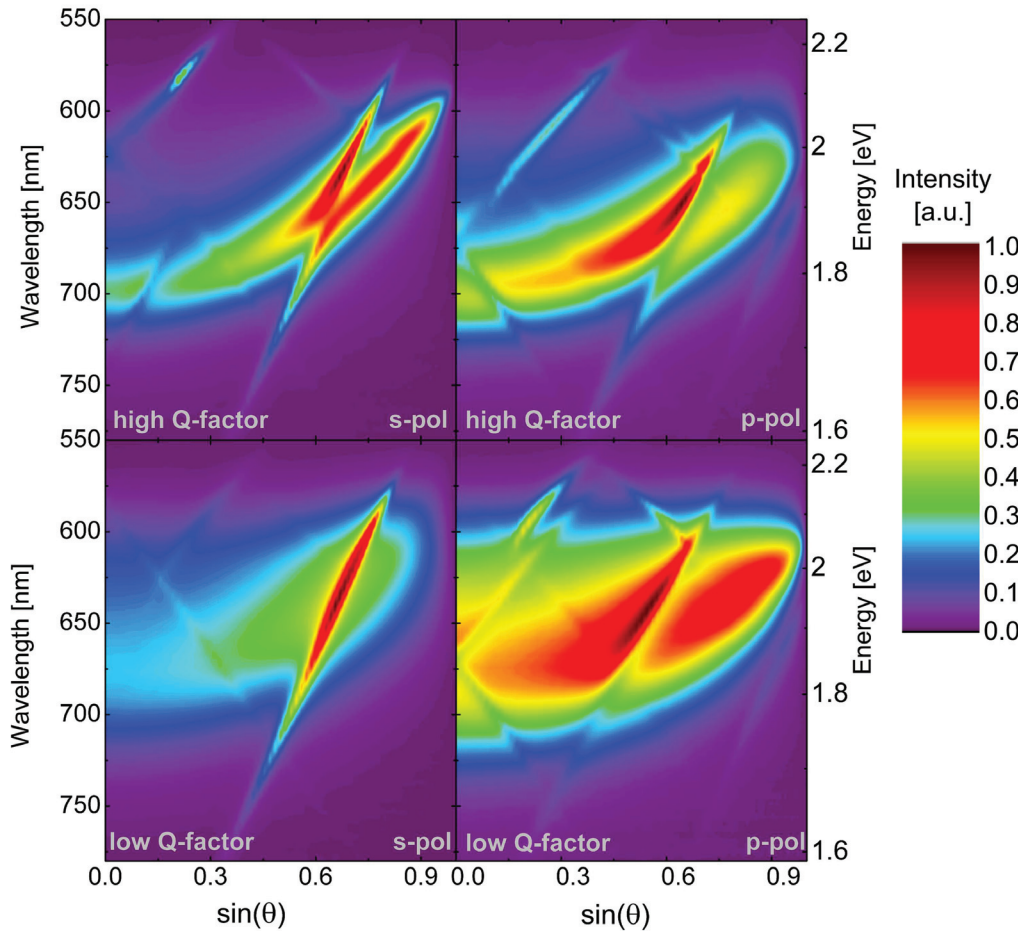


Figure 9.6: Normalized angle and polarization resolved spectral radiant intensity of the corrugated red top-emitting OLEDs from Fig. 9.4, deposited on a shallow 1D grating with a period of $0.75\ \mu\text{m}$. The corrugated device with a low Q-factor shows prominent constructive interference of a Bragg scattered mode and the cavity mode in s-polarization, while an anti-crossing effect is not observed. Overall, contributions of destructive mode interference are significantly reduced, in comparison to the OLED with a higher Q-factor.

9.2 White Top-Emitting OLEDs on Periodically Corrugated Substrates

The investigations on white top-emitting OLEDs presented in Chapter 7 have shown that the application of highly transparent and ultra-thin wetting layer electrodes results in angularly color-stable and efficient devices. The previous section has proven that corrugated red top-emitting OLEDs on shallow corrugated photoresist patterns of 40 nm depth achieve a reliable electrical device operation using wetting layer electrodes down

to 2 nm Au/ 9 nm Ag. In the following, periodic photoresist structures of approximately 150 nm depth and a top electrode silver thickness reduced down to 7 nm will be used to investigate the light extraction of white top-emitting OLEDs, since master stamps to fabricate shallow gratings with different grating period have not been available.

With respect to the previous findings and the results shown in Appendix C, white top-emitting OLED architectures of at least the 2nd cavity order are desired for the extraction of internally trapped light modes. Tandem OLEDs have a complex device architecture consisting of a large variety of layers and their development requires an immense experimental effort to obtain efficient devices. Hence, in the following less complex single unit devices are investigated.

9.2.1 Application of Highly Transparent Wetting Layer Electrodes

This section analyzes the influence of the top electrode thickness on the performance of corrugated white top-emitting OLEDs on gratings with a fixed period of $0.8 \mu\text{m}$ ^[9]. Figure 9.7(a) shows the investigated device structure, where the silver thickness has been varied between 7 nm and 15 nm. In this thickness range, the most efficient planar devices have been realized in the 1st cavity order (cf. Chapter 7).

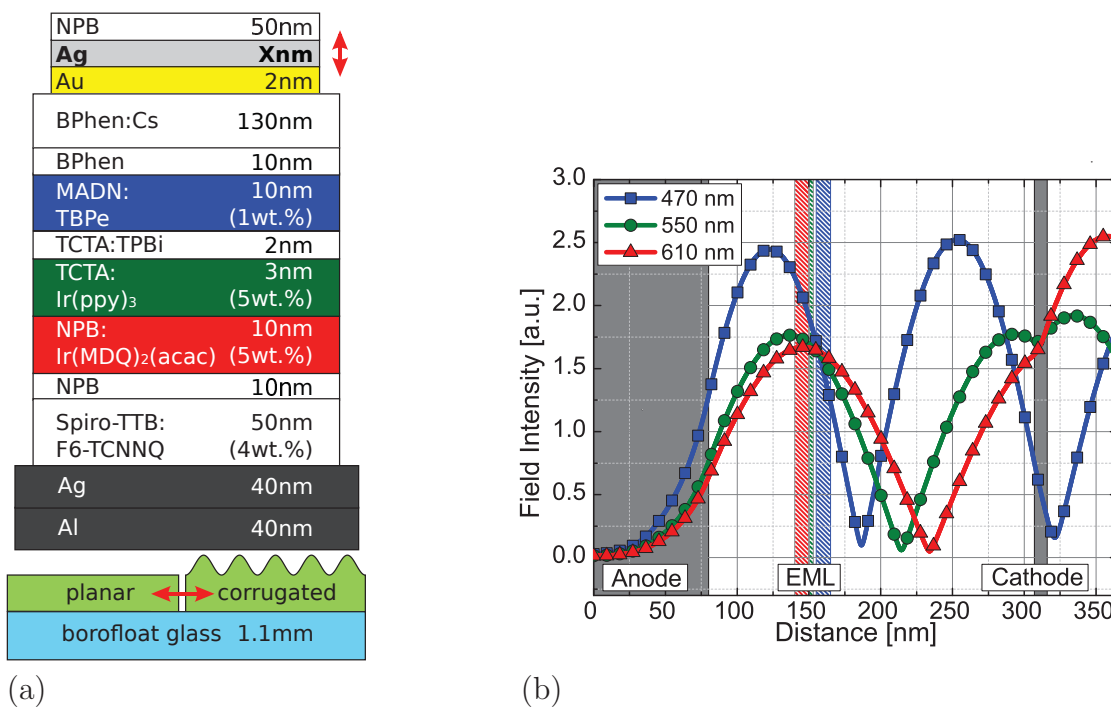


Figure 9.7: Hybrid white top-emitting OLED architecture used to investigate the influence of different top electrode thicknesses on the light extraction, introducing periodically corrugated substrates (a). Optical field distribution inside the microcavity OLED with an Ag thickness of 7 nm for the peak wavelengths of the three emitters (b). The transport layer thicknesses have been adjusted to position the EMLs close to the antinodes of the corresponding fields, which is essential to obtain intense emission.

[9] The nanoimprint master was provided by Benjamin Schumm and Florian Wisser.

The hybrid white EML system is identical to previous investigations in this work, only the doped transport layer thicknesses have been optimized by optical simulation. A broad spectral emission is obtained for an HTL thickness of 50 nm and an ETL thickness of 130 nm. In Fig. 9.7(b), the optical field intensity inside a microcavity OLED with a 7 nm thick Ag layer is shown for the peak wavelengths of the three emitters. Since the field distributions of the resonator modes are dependent on wavelength, but the single EML positions cannot be chosen independently, a compromise has to be found to obtain intense emission from each emitter. While the green and red EML could be placed close to the corresponding field antinode, the blue EML is located at a flank of the field distribution. Thus, the blue EML will not contribute with its highest achievable intensity to the emission. However, the required amount of blue to reach a warm white emission is rather low compared to the other emitters, which warrants the compromise in the EML position in the optimized device.

Figure 9.8(a) shows the current-voltage-luminance characteristics of the planar and the corrugated white top-emitting OLEDs. The leakage currents scatter over a range of almost four orders of magnitude. As such deviations are also found in the planar devices, a parasitic roughness of the photoresist, e.g. due to particle contamination, is expected to cause these deviations. Except for the corrugated OLED with a 15 nm Ag top electrode, the corrugated devices show a current-voltage characteristic comparable to the planar references for voltages larger than the diode onset at 2.5 V. Even though the corrugation has a depth of 150 nm, a reliable electrical device operation is achieved in the corrugated devices using ultra-thin wetting layer electrodes of 2 nm Au/ 7 nm Ag, validating the applicability of the wetting layer concept for corrugated devices. Furthermore, the corrugated white top-emitting OLEDs reach higher luminance values than the planar references.

The increase in luminance can be assigned to a prominent improvement of the emission in the red spectral range, while a slight decrease in the green and nearly unaffected emission in the blue spectral range is detected for the electrically stable corrugated devices (Fig. 9.8(b)). In contrast, the poor electrical performance of the corrugated 15 nm Ag device results in a dramatically decreased emission in comparison to all other devices, indicating an adversely affected photon generation in this device. In the corrugated OLEDs, several sharp spectral features are superimposed to the cavity emission, observed at 545 nm, 600 nm, and 656 nm for silver thicknesses of 7 nm and 9 nm. Since the grating period is identical in the corrugated devices, the results indicate that the dispersion of the scattered internally trapped light modes is comparable for these two silver thicknesses, while also the 15 nm device indicates a scattered mode at 656 nm. The efficiency-luminance dependencies of the sample set are shown in Fig. 9.8(c). The planar references follow the efficiency trend observed for 1st order microcavity OLEDs in Chapter 7, when varying the top electrode thickness. While the reference device with 15 nm Ag top electrode reaches an EQE of 2.9 % at 1000 cd/m², a reduction of the Ag thickness results in an increased EQE of 3.8 % for 9 nm Ag and 5.0 % for 7 nm Ag. However, as predicted from a simulation of the outcoupling efficiency, the planar 2nd order microcavity top-emitting OLEDs do not reach a comparable EQE as the planar 1st cavity order devices, shown in Chapter 7. For the corrugated OLEDs, intense emission in the red spectral range results in an EQE enhancement compared to the corresponding planar reference (15 nm Ag device excluded due to affected electrics).

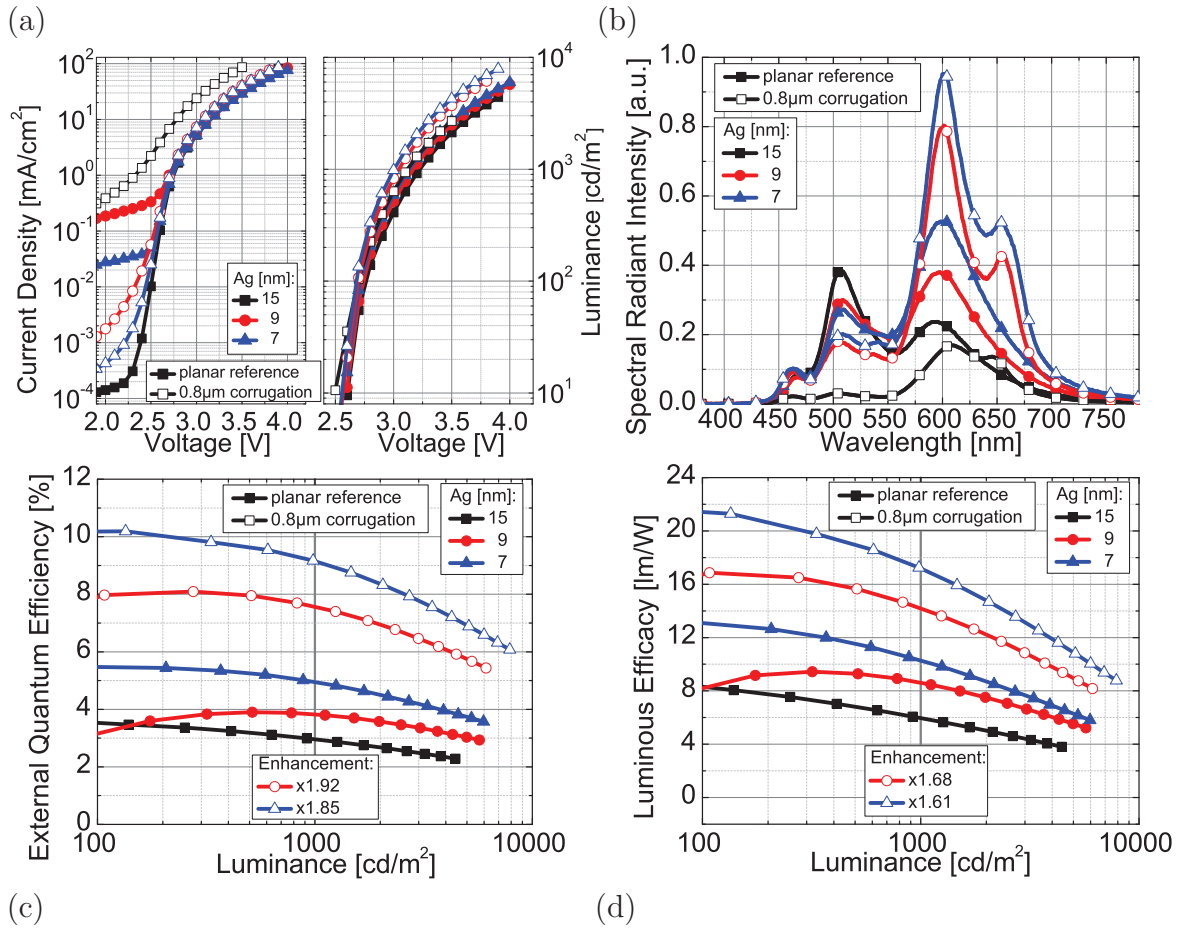


Figure 9.8: Influence of the top electrode thickness variation on the j VL characteristics (a), the spectral emission in normal direction at a current density of 14.8 mA/cm^2 (b), the EQE-luminance (c), and LE-luminance dependencies (d) of planar and corrugated 2nd order white top-emitting OLEDs. Even for the wetting layer electrode of 2 nm Au/ 7 nm Ag, the electrical performance is only weakly affected for the corrugated device, while the emission and efficiency strongly increase. Sharp spectral features in the emission of the corrugated OLEDs indicate that the efficiency increase can be attributed to Bragg scattered (waveguided) light modes.

An EQE enhancement factor of 1.92 is obtained for the device with 9 nm Ag and a factor of 1.85 for 7 nm Ag, which are comparable to state-of-the-art light extraction techniques, e.g. half-sphere lenses or microlens foils [7, 81]. Such large enhancement factors are rather unexpected, as only a 1D grating structure is applied to extract the internally trapped light modes. The low EQE of the planar reference devices might beneficially contribute to the large efficiency enhancement. However, as the electrical characteristics are not affected by the corrugation, the enhancement can be attributed to the increase of the light extraction efficiency. Even though this device architecture does not seem to be advantageous in realizing efficient white emission, the corrugated OLEDs with a period of $0.8 \mu\text{m}$ reach EQEs (7 nm Ag: 9.1%, 9 nm Ag: 7.6%, at 1000 cd/m^2) which are comparable or even slightly higher than for the planar white top-emitting OLEDs in 1st cavity order (7 nm Ag: 8.1%, 9 nm Ag: 8.4%, at 1000 cd/m^2). For the corrugated OLEDs with Ag thicknesses of 7 nm and 9 nm, the LE is increased by approximately

60 %, while the LE trend for the planar as well as the corrugated OLEDs remains comparable to the EQE. Hence, the device with a silver thickness of 7 nm reaches the highest LE of 17.2 lm/W at 1000 cd/m², whereas for 9 nm Ag 14.1 lm/W are obtained. For white OLEDs, the influence of the corrugation pattern on the emission color is of interest, as the Bragg scattered modes cause deviations in the spectral emission compared to the planar references. Figure 9.9(a) shows the emission color of the planar and the corrugated OLEDs in the CIE1931 color space in normal direction.

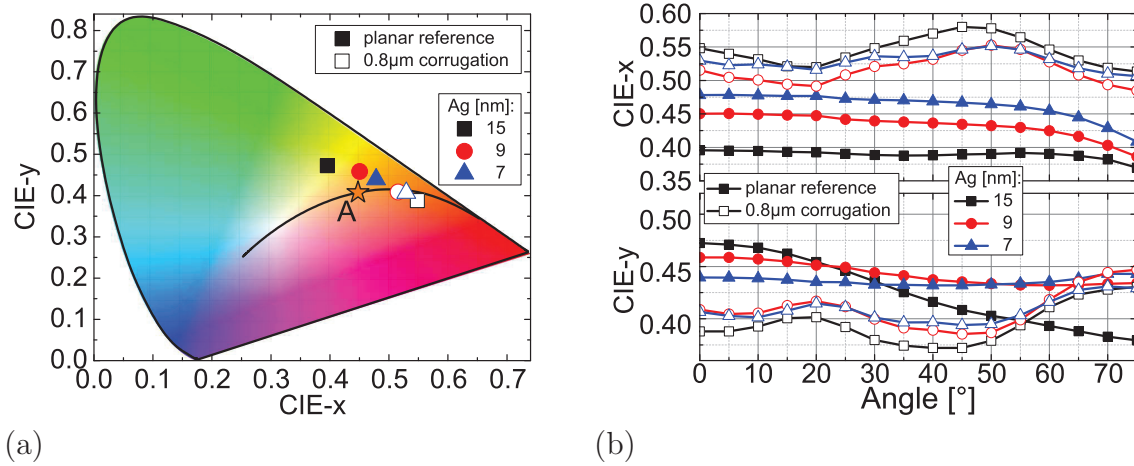


Figure 9.9: CIE color coordinates of the planar and the corrugated white top-emitting OLEDs in normal direction (a) as well as for observation angles between 0° and 75° (b). The reduction of green and the increase in red emission in the corrugated devices results in a color-shift to the red region of the CIE color space. All corrugated devices show comparable color changes within the observation angle which are not correlated to the color dependency in the planar cavities.

The planar reference devices emit in the yellow region of the color space and would require for a more intense blue emission to reach the warm white color point A. The prominent increase in red emission and the slight decrease in green emission in the corrugated devices introduces a shift of the emission color to the red region of the CIE space, while the color coordinates remain in proximity to the Planckian locus. Hence, also the corrugated devices would require an optimized layer architecture with increased blue and green emission to realize warm white emission at color point A, instead of a "candle light" white. In addition to the change in emission color, the angle dependency of the device emission is also affected when the corrugation pattern is introduced (Fig. 9.9(b)). Even though the planar references show an improved angular color-stability over the observation angle for a reduced top electrode thickness, the color-shift of the corrugated devices reveal an angle dependency of the emission color only slightly influenced by the thickness of the top electrode. Instead, the color fluctuations of the corrugated devices can be correlated to Bragg scattered light modes. The similar trend of the emission color in all corrugated devices emphasizes comparable scattering effects, which have been detected in the normal emission already (cf. Fig. 9.8(b)).

It is worth to mention that the investigation of the color dependency is only shown for a scan along the Bragg reflexes (cf. Fig. 5.4), as this is the relevant axis for Bragg scattered mode evaluation, while the shift depends on the rotational axis and can even vanish for

a scan along the lines of the 1D grating structure. For light extraction structures with several symmetry axes (e.g. hexagonal patterns), this orientation dependency will be reduced. Furthermore, as an angularly color-stable emission is desired for most lighting applications, the additional application of random scattering layers might be beneficial if an optimization of periodic structures does not result in sufficiently color-stable emission. In order to investigate the impact of the corrugation patterns in white top-emitting OLEDs, the angle and polarization resolved spectral emission has been measured for electrical operation of the devices. Figure 9.10 shows the emission from the planar and the corrugated top-emitting OLEDs with a fixed top electrode of 2 nm Au/ 7 nm Ag. Bragg scattered light modes are found in the entire air cone for both polarizations, most prominently increasing the red emission. As indicated in normal direction, a decrease of green emission is observed for the entire angle range, even though scattering effects with constructive contributions are detected in s-polarization.

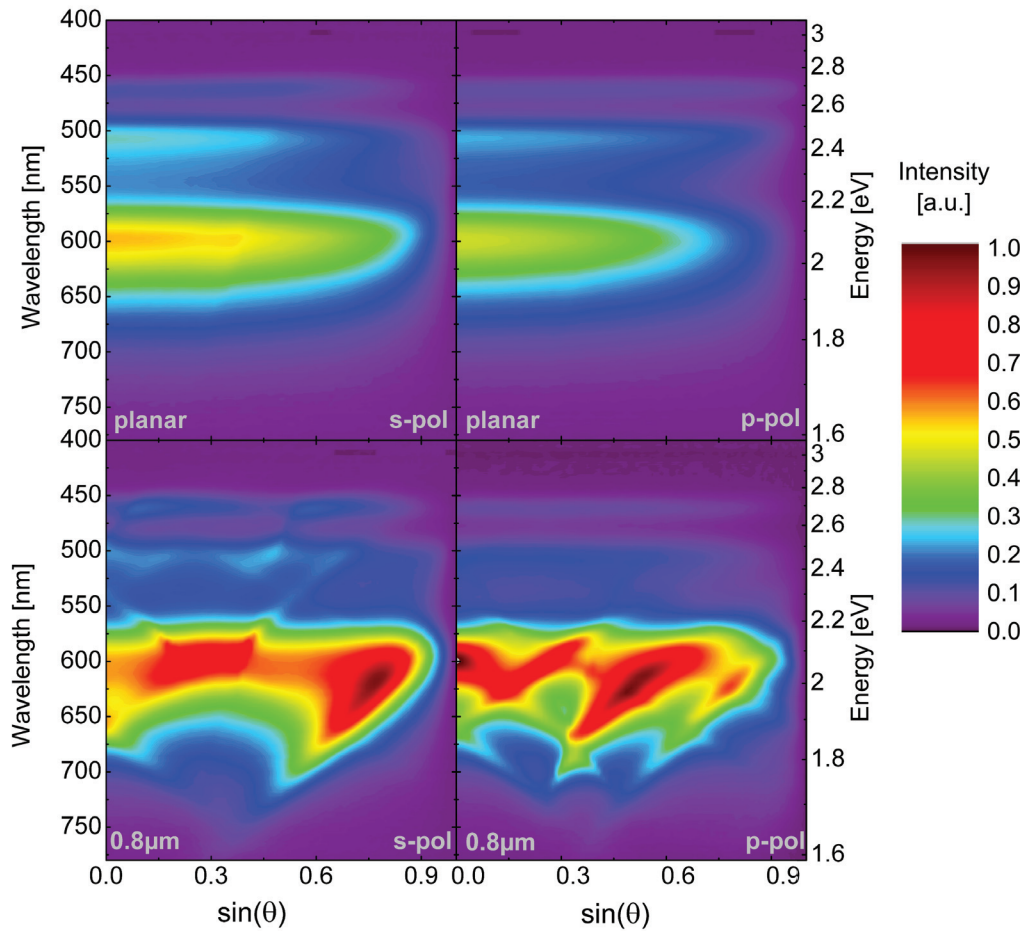


Figure 9.10: Angle and polarization resolved spectral emission of a corrugated and a planar white top-emitting OLED with 2 nm Au/ 7 nm Ag top electrode operated at 14.8 mA/cm^2 . The corrugated OLED shows a prominent emission increase in the red spectral range, while blue and green emission are not beneficially affected. The observed color fluctuations are assigned to the sharp spectral features arising from the Bragg scattered modes.

So far, the decrease in green emission is not completely understood, as the blue emission remains nearly unaffected and thus a shift of the recombination zone to the red emitter is less probable. However, the result highlights the requirement for an improvement of the grating structure to achieve an emission increase in the entire spectral range. Furthermore, the angle dependent emission proves that the sharp spectral features from Bragg scattered modes introduce fluctuations of the color with the observation angle (cf. Fig. 9.9(b)). In Fig. 9.11, the angle and polarization resolved emission spectra of the corrugated devices with varied top electrode thickness are shown, normalized to the maximum intensity. In comparison to the corrugated device with 7 nm Ag thickness, an increase of the top electrode thickness results in a stronger impact of the Bragg scattered mode in s-polarization for $\sin \theta > 0.55$.

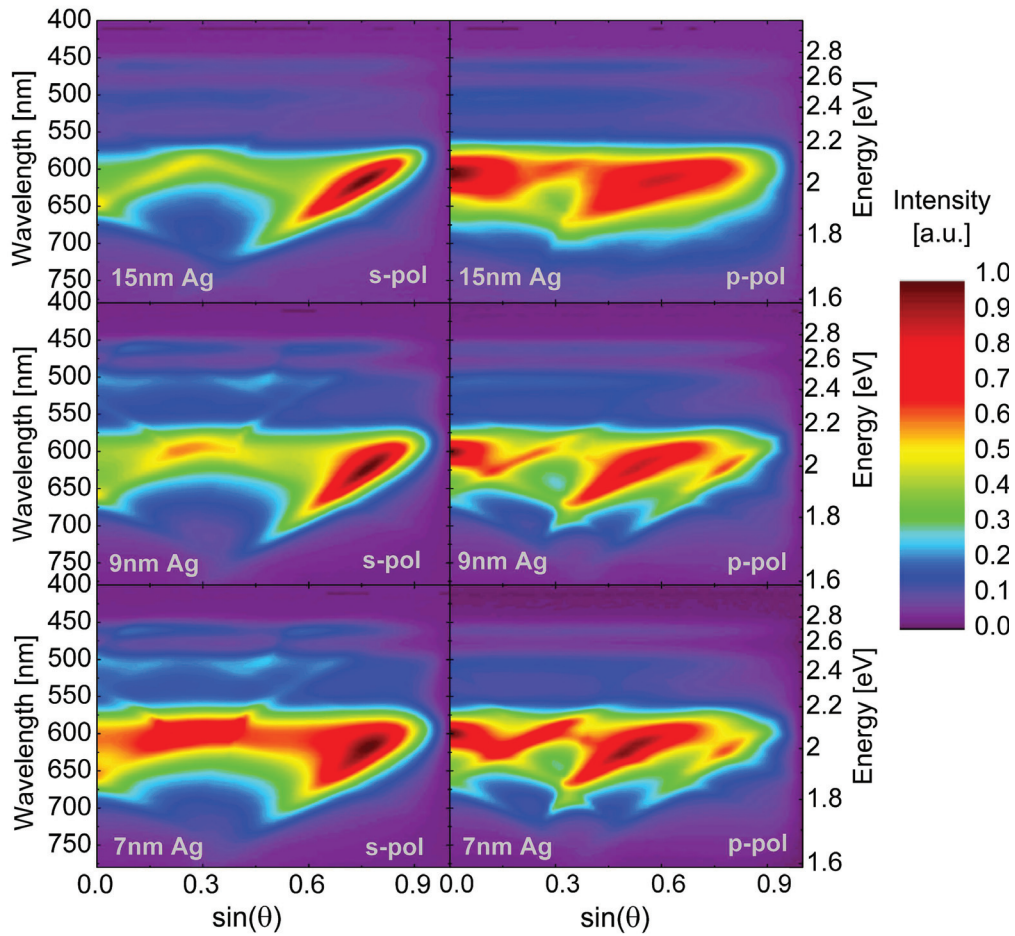


Figure 9.11: Normalized angle and polarization resolved spectral emission of the corrugated white top-emitting OLEDs with different top electrode thicknesses at a current density of 14.8 mA/cm^2 . Comparable Bragg scattered mode patterns are detected for all Ag layers, attributed to the identical grating period of $0.8 \mu\text{m}$ and the only slightly affected power dissipation spectra of the devices. By decreasing the top electrode thickness, increasing contributions from Bragg scattered modes are observed in the air light-cone, which is in good agreement to the trend in the EQE enhancement factors (cf. Fig. 9.8).

Hence, the relative intensities of the cavity emission and the other scattered modes are less significant on the normalized scale. In p-polarization, an increase of the top electrode thickness results in spectrally broadened contributions of the Bragg scattered modes. Furthermore, neither prominent destructive interference nor anti-crossing effects are found in the emission of the corrugated white top-emitting OLEDs, which suggests that these effects can be suppressed in low Q-factor cavities. For all devices, the position and dispersion of the Bragg scattered modes remain similar, indicating comparable dispersions of the light modes in the OLED architectures, because the grating period is kept constant at $0.8\ \mu\text{m}$ in all devices.

As mentioned previously, a variety of parameters can be used to optimize the OLED-grating system for an improved light extraction efficiency. The impact of a grating period variation on the light extraction efficiency is exemplary shown in the following.

9.2.2 Variation of the Corrugation Period

Based on the findings in the previous section, white top-emitting OLEDs with an ultra-thin wetting layer electrode of $2\ \text{nm}\ \text{Au}/7\ \text{nm}\ \text{Ag}$ are used to investigate the influence of the grating period on the efficiency and on the angular color-shift. For this purpose, 1D photoresist gratings with periods of $0.8\ \mu\text{m}$ and $1.6\ \mu\text{m}$ and depths of $\approx 150\ \text{nm}$ have been prepared by nanoimprint lithography^[10].

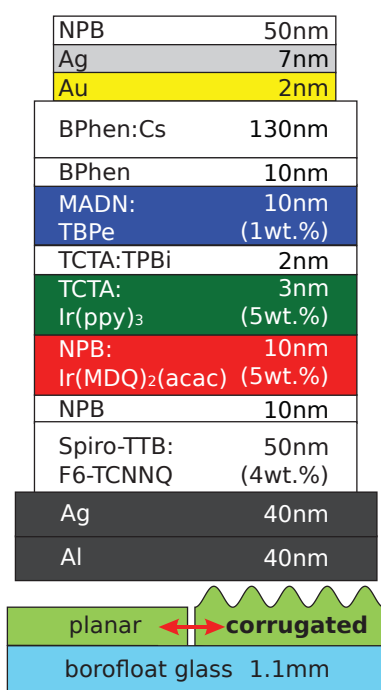


Figure 9.12: White top-emitting OLED architecture including a wetting layer electrode. The influence of the grating period on the device performance is investigated.

The OLED architecture is the same as in the previous section, whereas the top electrode thickness is fixed now (Fig. 9.12). Figure 9.13(a) shows the electrical performance of the planar reference and the corrugated OLEDs with different periods. Even though an identical layer sequence has been deposited for the planar references, the leakage currents show deviations, which are again attributed to defects in the photoresist layer. The corrugated OLEDs reach leakage currents in the range of the planar references, although the leakage is rather large ($10^{-3}\ \text{mA}/\text{cm}^2$ to $10^{-2}\ \text{mA}/\text{cm}^2$) for all devices. The jV -curves of the corrugated OLEDs are similar to the planar reference devices for voltages larger than the diode onset at $2.5\ \text{V}$.

The luminance increase of the corrugated OLEDs can be assigned to the sharp spectral features, originating from Bragg scattered modes, which are superimposed to the emission of the planar reference OLEDs (Fig. 9.13(b)). As expected, the position of the features depends on the grating period, as the reciprocal lattice vector is affected. In addition, also for the larger grating period a prominent emission increase is only detected in the red, while the blue emission remains nearly unaffected and a slight emission decrease is found again in the green spectral range. However, also for the larger grating period, an EQE increase is observed (Fig. 9.13(c)).

^[10] Benjamin Schumm and Florian Wisser prepared the nanoimprint master.

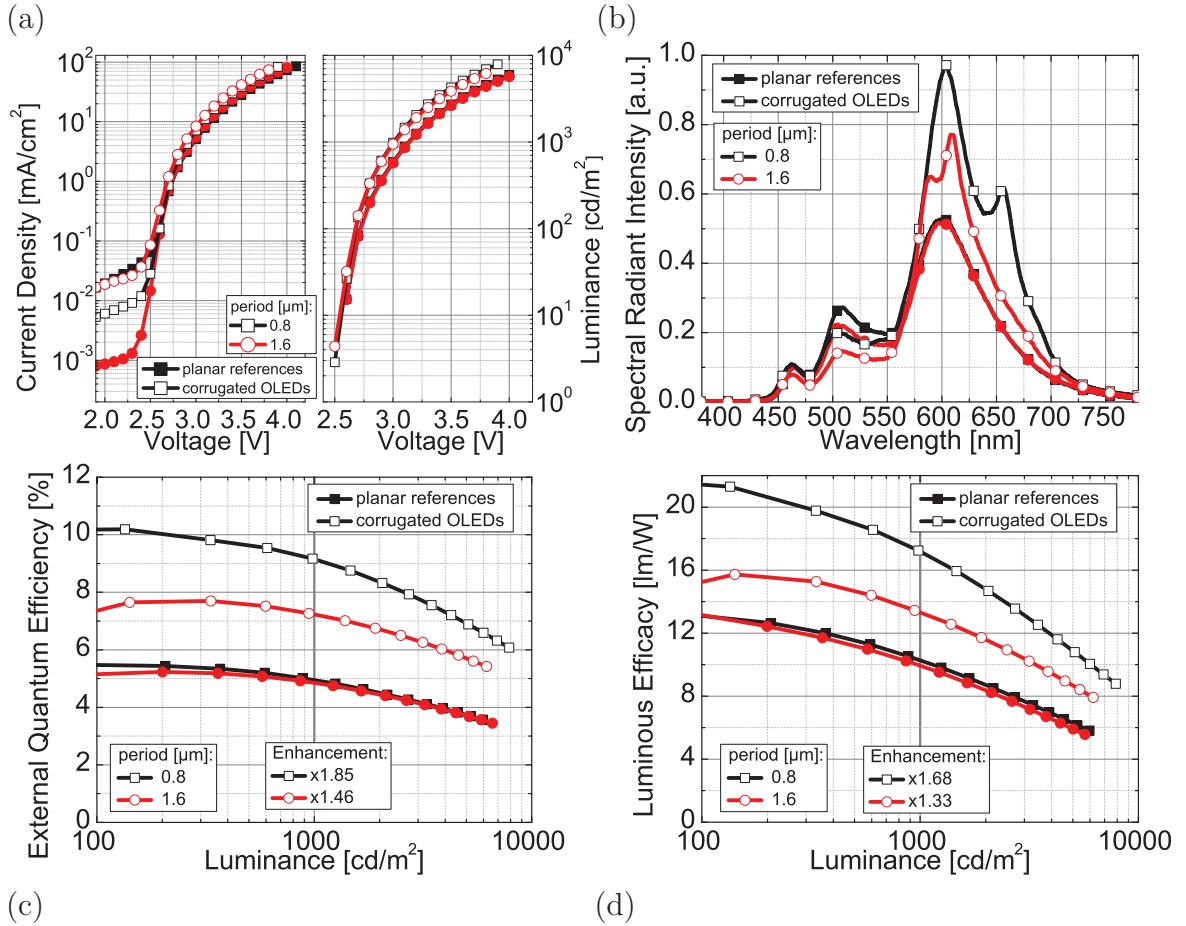


Figure 9.13: Influence of the corrugation period in white top-emitting OLEDs on the jV characteristics (a), the spectral emission in normal direction at a current density of $14.8 \text{ mA}/\text{cm}^2$ (b), the EQE-luminance (c), as well as LE-luminance dependency (d). Even though strong fluctuations in leakage current are detected, the jV -curves remain comparable for voltages above the diode onset at 2.5 V. A strong increase of red emission is observed in the corrugated devices, while the green and blue emission show no increase. Both corrugated devices reach higher efficiencies than the planar references, whereas a period of $0.8 \mu\text{m}$ yields a stronger enhancement compared to $1.6 \mu\text{m}$.

In comparison to the planar references, reaching EQEs of 5.0% at $1000 \text{ cd}/\text{m}^2$, the corrugated OLED with a period of $1.6 \mu\text{m}$ reaches 7.2%, which represents an increase in EQE by a factor of 1.46, while a factor of 1.85 has been found for a grating period of $0.8 \mu\text{m}$ (cf. Section 9.2.1). Furthermore, the corrugated OLED with a grating period of $1.6 \mu\text{m}$ reaches a LE of $13.5 \text{ lm}/\text{W}$ at $1000 \text{ cd}/\text{m}^2$, which is 33% higher compared to the planar reference ($10.2 \text{ lm}/\text{W}$), whereas a corrugation period of $0.8 \mu\text{m}$ yields a LE of $17.2 \text{ lm}/\text{W}$ (Figure 9.13(d)). The observed EQE enhancement factors indicate that grating periods below $1.0 \mu\text{m}$ are beneficial to realize efficient extraction of the trapped light modes from microcavity OLEDs.

An explanation would be that the intensity of the Bragg scattered modes decreases with increasing scattering order, emphasizing the use of sub- μm grating periods, which allow for the extraction of internally trapped modes in the first scattering order. However,

the experiments presented in this work have also shown that other parameters can have a significant impact on the light extraction, which makes a general conclusion on the correlation between the grating period and the light extraction efficiency difficult. Experiments with a larger variation of the grating period are in the focus on further studies. So far, the availability of master stamps required for the nanoimprint technique has been limited and the comparability of the electrical device performance for corrugated OLEDs on gratings produced by photolithography has not allowed to show results on such investigations.

The influence of the grating period on the emission color in normal direction is shown in Fig. 9.14(a). Slight variations in the spectral emission of the planar references result in a small deviation of the perceived color in normal direction. The increased red emission in the corrugated devices results in a shift of the emission color to the red region of the color space, increasing the distance to the warm white color point A, while the emission color remains in proximity to the Planckian locus.

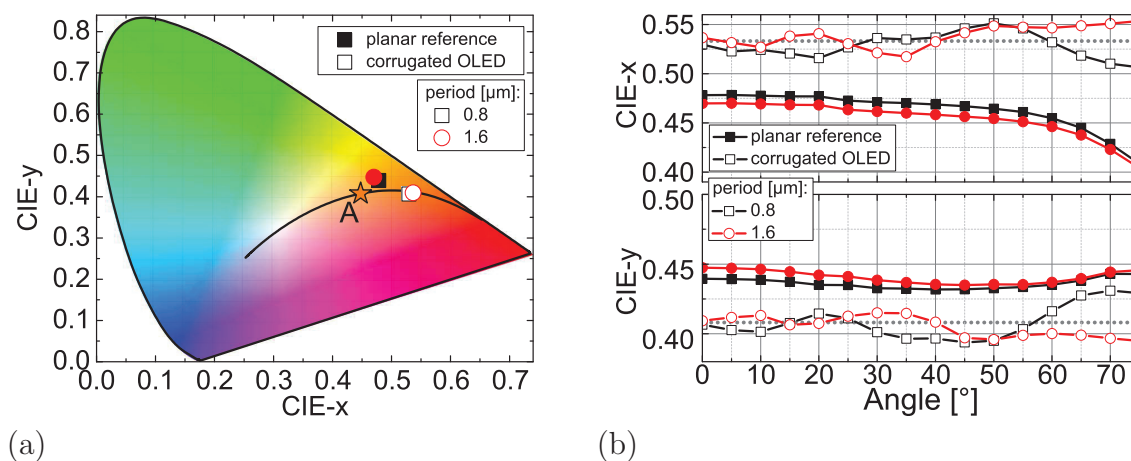


Figure 9.14: CIE color coordinates of the planar and the corrugated white top-emitting OLEDs in normal direction (a) as well as for observation angles between 0° and 75° (b). The extracted light modes in the corrugated devices result in a color-shift to the red region of the CIE color space in comparison to the planar references. While the planar references show a slight and continuous variation of the emission color with the observation angle, Bragg scattered modes introduce prominent color fluctuations.

In addition, fluctuations of the emission color are found for the corrugated devices, when varying the observation angle (Fig. 9.14(b)), where a larger grating period results in a slightly improved color-stability. Presumably, this can be attributed to the smaller reciprocal lattice vector of the structure, leading to a dense superposition of the scattered modes for different Bragg orders to the planar cavity emission, smoothening the influence of each single mode. In addition, the white corrugated OLED with a period of $1.6 \mu\text{m}$ does not show a distinct shift of the CIE-x coordinates for angles larger than 50° , which is the case in the planar microcavities. This indicates that the optimization of periodic light extraction structures might also be beneficial to improve the color-stability in comparison to planar microcavities if the introduced color fluctuations from the Bragg scattered modes can be confined inside a single Mac Adams ellipse. The influence of the grating period on the angle and polarization resolved emission of corrugated OLEDs with

different grating periods is shown in Fig. 9.15 and further compared to the emission of a planar reference. The spectra have been recorded for electrical operation at a current density of 14.8 mA/cm^2 . Bragg scattered modes are detected for both periods in the entire air light-cone, while contributions in the blue and green spectral range are most prominent in s-polarization, but do again not increase the emission in comparison to the planar references. The increase in red emission is significant for both corrugation periods, as shown for the normal direction in Fig. 9.13(b). As for the white corrugated OLEDs with varied top electrode, destructive interference or anti-crossing effects between Bragg scattered light modes and the cavity emission are also not observed for a grating period of $1.6 \mu\text{m}$, which further validates the findings for low Q-factor cavities.

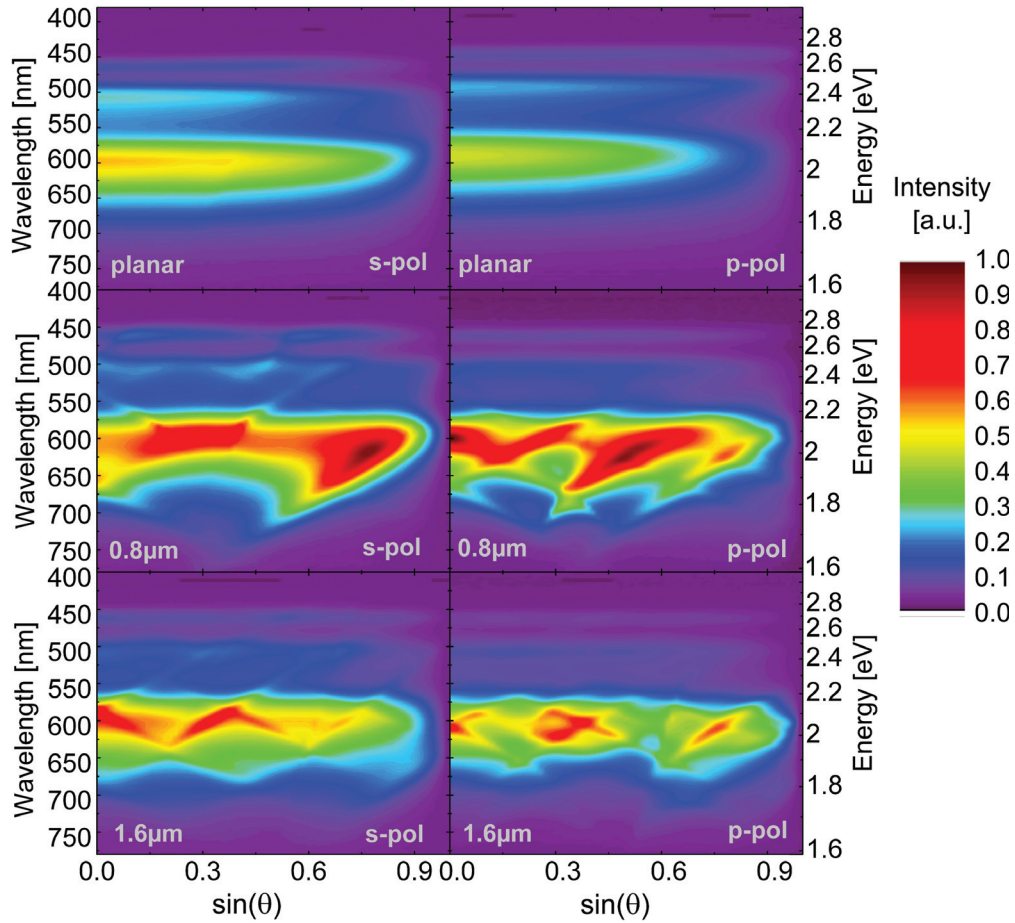


Figure 9.15: Angle and polarization resolved spectral emission of corrugated white top-emitting OLEDs with periods of $0.8 \mu\text{m}$ and $1.6 \mu\text{m}$ operated at a current density of 14.8 mA/cm^2 , in comparison to a planar reference. For both grating periods, Bragg scattered modes are detected across the entire air light-cone, increasing the total emission in comparison to the planar reference, whereas the red emission is increased most strongly. The OLED on top of a $0.8 \mu\text{m}$ grating reaches the highest emission intensities, whereas the device with $1.6 \mu\text{m}$ grating period shows a more homogeneous angle dependent emission, which is beneficial for lighting applications.

Chapter Summary

The experimental studies presented in this chapter have shown that the light extraction efficiency of corrugated top-emitting OLEDs can be significantly increased if the OLED architecture is optimized to allow for constructive interference between Bragg scattered internally trapped light modes and the cavity mode. For corrugated red top-emitting OLEDs on 1D shallow gratings with a period of $0.75\ \mu\text{m}$, the optimization of the metal top electrode as well as the capping layer thickness yield an EQE enhancement factor of up to 1.22. The EQEs of the corrugated devices are increased to maximum values of up to 20%, higher than the highest reported EQEs of 17% for planar OLEDs with comparable device architecture [11]. However, further optimizations will be necessary to outperform optimized 1st cavity order red top-emitting OLEDs. In addition, the detected anti-crossing behavior of a Bragg scattered waveguided mode and the cavity mode has been investigated in more detail by varying the metal top electrode thickness and the capping layer thickness. The decrease of the separation between the two mode branches for a reduced metal electrode thickness and the vanishing of the splitting for a reduced cavity strength provides additional insight on the mode interaction in corrugated micro-cavity OLEDs.

Experiments on 2nd order corrugated white top-emitting OLEDs have shown that internally trapped light modes can be efficiently extracted from the microcavities, applying 1D gratings with periods of $0.8\ \mu\text{m}$ and $1.6\ \mu\text{m}$, and a depth of 150 nm. A reliable electrical operation of the corrugated OLEDs has been shown for top electrode thicknesses down to 2 nm Au/ 7 nm Ag, which again validates the applicability of wetting layer electrodes, adopting the profile of the corrugated layer sequence. The corrugated white top-emitting OLEDs showed a maximum EQE enhancement factor of 1.92 for a wetting layer device with 9 nm Ag (7.6% EQE at $1000\ \text{cd}/\text{m}^2$), whereas the highest EQE of 9.1% at $1000\ \text{cd}/\text{m}^2$ has been achieved for a wetting layer electrode with 7 nm of Ag (EQE $\times 1.85$). Here, corrugated 2nd order OLEDs reach the efficiency benchmark of planar 1st order white top-emitting OLEDs (cf. Chapter 7). To my best knowledge, enhanced emission from corrugated white top-emitting OLEDs has been demonstrated for the first time, while the detected EQE enhancement factors are already comparable to state-of-the-art macroscopic light extraction structures. It is expected that the application of optimized 2D structures, e.g. hexagonal patterns, will result in a further increase of the light extraction efficiency. In addition, these results indicate that white tandem OLED architectures, which also represent higher order microcavity devices, could strongly benefit from the application of periodically corrugated substrates. For their application in solid-state light applications, corrugated white top-emitting OLEDs have to maintain an angularly stable color, even though sharp spectral features from Bragg scattered modes affect the spectral emission. Hence, it might be desirable to combine periodic light extraction structures with a random scattering layer on top of these OLEDs, improving the angular color-stability if an optimization of the periodic structure does not result in a confinement of the color fluctuations inside a single Mac Adams ellipse.

10 Conclusions and Outlook

In this thesis, concepts to optimize top-emitting OLEDs for efficient, angularly color-stable, and high quality white light emission have been investigated. In addition, a strong focus has been put on the extraction of internally trapped light modes from top-emitting devices.

Wetting Layer Metal Top Electrodes

In order to improve the transmittance of the Ag top electrodes, wetting layers of Au and MoO₃ have been deposited beneath the actual electrode, introducing a Frank-van der Merwe growth on the organics. This results in the formation of smooth, homogeneous, and closed Ag films with percolation thresholds below 7 nm on the charge transport materials BPhen:Cs and MeO-TPD:F6TCNNQ, which is significantly thinner in comparison to the neat 15 nm Ag electrodes, representing the state-of-the-art technology so far. Furthermore, the wetting layer electrodes show a strong increase in transmittance and a decreased wavelength dispersion, which can be attributed to the thinner films and the absence of localized surface plasmons, present in granular metal films. A wetting layer electrode of 1 nm MoO₃/ 2 nm Au/ 7 nm Ag obtained a transmittance of 81 % in a spectral range between 430 nm and 575 nm, which is comparable to an electrode of 90 nm ITO that represents a state-of-the-art electrode material for bottom-emitting OLEDs. The sheet resistance of this ultra-thin metal electrode is only 9 Ω/□, lower than for the laboratory standard ITO (32 Ω/□). In addition, the deposition of the wetting layers by thermal evaporation is compatible with the preparation of the OLED materials, while the preparation of ITO or PEDOT:PSS mostly harms the organic layer underneath. The evaluation of SEM images verified the beneficially affected Ag film growth from the wetting layers on the organics. Furthermore, the investigation of the electrode morphology allowed to accurately describe the optical properties, by using either the optical constants of the bulk layers if closed films are present, or calculating the effective refractive index from the Maxwell-Garnett model if granular films are observed.

Finally, the introduction of wetting layers provides a basis for further investigations, in order to optimize planar as well as corrugated top-emitting OLEDs, as a reliable electrical performance and high transmittance for ultra-thin metal electrodes are achieved. In addition, the applied concept of wetting layer metal electrodes is also compatible with roll-to-roll processing.

White Top-Emitting OLEDs Using Wetting Layers

The application of highly transparent wetting layer electrodes in white top-emitting OLEDs allows for the compensation of current drawbacks in the efficiency, the angular color-stability, and the color rendering as compared with their bottom-emitting coun-

terparts. Top-emitting OLEDs with a neat 15 nm Ag electrode reached a comparable performance (EQE: 4.7 %, LE: 13.4 lm/W)^[11] to the literature state-of-the-art [124, 125], but are further improved when reducing the top electrode Ag thickness to 9 nm (EQE: 9.0 %, LE: 23.0 lm/W) or 7 nm (EQE: 8.8 %, LE: 21.7 lm/W), where a performance increase by a factor of up to 1.9 is observed. In addition, the angular color-stability is significantly improved decreasing the top electrode thickness. Both trends are attributed to the increased transmittance of the top electrode, which reduces the impact of micro-cavity effects on the white light emission.

The introduction of a 2 nm thick gold wetting layer beneath Ag electrodes of 7 nm (EQE: 8.1 %, LE: 21.0 lm/W) and 9 nm (EQE: 8.4 %, LE: 22.1 lm/W) thickness results in white top-emitting OLEDs with a performance increased up to 34 % in EQE and 51 % in LE, compared to an optimized white bottom-emitting reference OLED (EQE: 6.7 %, LE: 15.1 lm/W). However, for these wetting layer electrodes, an angular color-shift 30- 50 % larger than for the bottom-emitting device remains, even though a color-stability improvement by a factor of 2.7 has been reached with respect to a top-emitting OLED with a neat 15 nm Ag electrode. Finally, a reduction of the top electrode thickness to 2 nm Au/ 5 nm Ag provides an angular color-stability, which is comparable to the white bottom-emitting reference OLED, while the EQE is still improved by 19 % in the top-emitting device.

These results show for the first time that white top-emitting OLEDs can achieve higher efficiencies than bottom-emitting references with a comparable layer architecture while still reaching a comparable angular color-stability. This is ascribed to the optical properties of the top-emitting OLEDs, using ultra-thin transparent metal electrodes instead of 90 nm ITO and the absence of substrate and ITO guided modes. The application of the deep blue emitter 4P-NPD has yielded high quality white top-emitting OLEDs with CRIs of up to 89.5, higher than that required for solid-state lighting applications. The shown results for top-emitting OLEDs render the wetting layer concept to a promising candidate not only to compensate the drawbacks of white top-emitting OLEDs, but also to replace the brittle TCO electrodes in bottom-emitting devices.

The application of a MoO₃/ Au wetting layer in inverted top-emitting OLEDs has further yielded an improvement in electrical characteristics. The MoO₃ improves the hole injection, resulting in a reduction of the driving voltage by up to 1 V for inverted white tandem top-emitting OLEDs, in comparison to the application of neat Ag top electrodes. Hence, these devices benefit from an improved transmittance and an improved hole injection, using wetting layer top electrodes. Highly efficient inverted white tandem OLEDs with EQEs of 20 % and CRIs of up to 94 have been realized by using four emitters which nearly cover the entire visible spectrum and by applying a wetting layer electrode with 7 nm of Ag. Since the operational voltage is reduced in the wetting layer devices, the LE has been increased by 25 % (to 25 lm/W) in comparison to an OLED with a neat Ag electrode. In addition, the highly transparent wetting layer electrode improves the angular color-stability, whereas an even higher color-stability as that for the bottom-emitting reference device has been measured. These findings validate the compatibility of the wetting layer concept with stacked OLED architectures, which are preferred in solid-state lighting applications.

^[11] Efficiency data reported for a device brightness of 1000 cd/m² if not stated otherwise.

The wetting layer concept has further been investigated in transparent, bi-directional emitting OLEDs, in which the brittle ITO electrode has been replaced. The ITO-free transparent OLEDs reach an almost dispersion free transmittance of up to 66 %, only slightly lower than for the ITO containing devices (70 %). Even though optimizations of the ITO-free OLEDs have yielded the desired balanced brightness and efficiency through both transparent contacts, further optimizations are required to improve the efficiency above the ITO containing references and to obtain an identical emission color in both directions. However, the excellent transparency of the presented ITO-free OLEDs emphasizes the application of the wetting layer concept for flexible and/or transparent OLEDs for solid-state lighting and display applications.

Periodically Corrugated Top-Emitting OLEDs

The extraction of internally trapped light modes from top-emitting OLEDs has been investigated, depositing the OLEDs on top of periodically corrugated light extraction structures, in order to avoid mechanical damage to the organic layers during the structure mount. Several process methods for the fabrication of 1D grating structures have been analyzed, e.g. photolithography, wet chemical etching of metals, and nanoimprint lithography, with a focus on periodic, high quality line structures with a low surface roughness. Thereby, the nanoimprint lithography has yielded the highest grating quality with periods between 0.75 μm and 1.6 μm and depths between 12 nm and 150 nm. However, not only the period, but also the depth of the grating is widely determined by the nanoimprint master stamp and cannot be significantly varied.

In this work, it has been shown for the first time that highly efficient state-of-the-art top-emitting OLEDs, which are deposited on top of grating structures can maintain an electrical performance comparable to planar devices. Since no adverse effects on the internal quantum efficiency are observed, changes in the EQE can be directly associated to the light extraction efficiency, affected from the Bragg scattered light modes. Furthermore, this allows for the evaluation of the influence of grating and OLED parameters on the light extraction efficiency from an EQE measurement, as the IQE is supposed to be constant.

Detailed investigations on the angle resolved emission of corrugated OLEDs have allowed for the assignment of the origin of the observed scattering effects. For shallow gratings with aspect ratios smaller than 0.1, excellent agreement between the measured Bragg scattered modes and the different Bragg scattering orders of the internal light modes from the corresponding planar reference has been shown, allowing for the identification of the Bragg scattered modes. Here, contributions of waveguided modes and SPP modes have been found. By applying gratings with an aspect ratio of $\gtrsim 0.2$, the identification of scattering effects using the power dissipation spectrum of the planar reference has been limited, as additional effects, such as the partial vanishing of the cavity mode, have been observed.

In order to quantitatively describe the scattering effects and to analyze the partial vanishing of the cavity mode, the far-field modes of microcavity OLEDs have been described by damped electromagnetic waves, as they represent leaky modes of the microcavity. It has been shown that the complex summation of the represented far-field light modes yields the emission of the corrugated top-emitting OLEDs and enabled to describe the effects of

Bragg scattered modes in strongly corrugated OLEDs, as well. From this model, it has been proven that the emission of corrugated top-emitting OLEDs can be explained by the interference of light modes inside the air light-cone. Destructive interference of Bragg scattered modes and the cavity mode are associated to an observed emission intensity decrease in corrugated OLEDs. Furthermore, the partial vanishing of the fundamental cavity mode in strongly corrugated devices is found to be caused from the formation of a new coherently coupled mode pair of the initial cavity mode and a Bragg scattered waveguided mode, which has been first observed in corrugated OLEDs. Moreover, the interaction of a Bragg scattered waveguided mode and the cavity mode in weakly corrugated OLEDs has result in a significant splitting of the cavity mode in two branches for s-polarized emission, representing the interaction of both light modes.

The extraction of internally trapped light modes by Bragg scattering results in an increase of the efficiency in comparison to a planar reference device with identical layer architecture. For a 2nd order red top-emitting OLED with 20 nm Ag top electrode, a maximum EQE enhancement of 16 % (EQE: 11.4 % at 14.8 mA/cm²) has been achieved, by applying a grating with 0.75 μ m period and 40 nm depth. In contrast, strongly corrugated OLEDs with \approx 20 nm Ag top electrode showed no EQE enhancement at all, even though prominent scattering effects are observed.

For the efficiency improvement of corrugated top-emitting OLEDs, the application of shallow gratings has therefore been the initial focus. A reduction of the wetting layer electrode Ag thickness from 20 nm to 9 nm Ag is suggested to affect the phase relations of the interfering modes, as the contributions of destructive mode interference on the emission have been reduced. Furthermore, the splitting of the cavity mode in s-polarization becomes less prominent, as the energetic separation of the two separated mode branches decreases. This shows that the thickness of the metal electrode has a significant influence on the light extraction of corrugated top-emitting OLEDs.

Even though the Ag thickness reduction has not yielded a prominent increase of the enhancement factor, as contributions of constructive interference have merely been observed, the EQE of the corrugated OLED continuously increases. A corrugated red top-emitting OLED with 9 nm Ag wetting electrode on a grating with 0.75 μ m period and 40 nm depth reaches a maximum EQE of 20 %, which is higher than the highest reported efficiency of planar top-emitting OLEDs in the 2nd cavity order with comparable OLED architecture (EQE: 17 %) [11]. However, optimizations of the light extraction structures are still required to outperform the performance of the current state-of-the-art in top-emitting OLEDs, which is represented by planar 1st cavity order devices. So far, corrugated 1st cavity order OLEDs have not shown an efficiency increase, as prominent Bragg scattering of SPP modes from the devices has not been achieved.

The optimization of the capping layer thickness, in order to reduce the Q-factor of the microcavity and to obtain a broad spectral emission, has yielded a significant influence on the emission of the corrugated OLEDs. Thereby, a prominent constructive interference of a Bragg scattered waveguided and the cavity mode has been observed. Furthermore, the anti-crossing vanishes with the adjustment of the capping layer for a decrease of the microcavity Q-factor, suggesting that an interaction of light modes in corrugated microcavity OLEDs might be correlated to the mode confinement insight the devices. Overall, the optimization of the capping layer thickness has yielded an increase of the efficiency enhancement factor to 1.22 for 1D grating structures.

The investigated concept to optimize the efficiency of corrugated monochrome OLEDs is similar to the optimization of white top-emitting OLEDs for efficient and angularly color-stable emission. Corrugated 2nd order white top-emitting OLEDs have been investigated, in order to improve the efficiency in these devices. A variation of the wetting layer top electrode thickness between 7-15 nm Ag has shown no adverse effect on the electrical performance of the corrugated OLEDs, even though gratings with a depth of 150 nm and a period of 0.8 μm have been applied. These results emphasize the applicability of the wetting layer concept for corrugated white top-emitting OLEDs on rather deep grating structures, as the electrical performance is maintained even for only 7 nm of Ag. A decrease of the top electrode thickness in corrugated 2nd order white top-emitting OLEDs yields an efficiency increase, whereas a comparable trend has been observed for planar 1st order devices. Here, the corrugated white top-emitting OLEDs reach an EQE of up to 9.1%. This represents an EQE enhancement by a factor of 1.85 in comparison to the planar reference with identical layer architecture, mainly due to a significant increase in red emission. Thus, corrugated 2nd order white top-emitting OLEDs have reached higher EQEs as planar 1st cavity order devices (EQE: 8.1%), applying an identical top electrode of 2 nm Au/ 7 nm Ag. Furthermore, it is worth to note that periodically corrugated white top-emitting OLEDs have been presented for the first time ever.

However, Bragg scattered light modes do not only affect the efficiency of white top-emitting OLEDs, but also introduce fluctuations of the CIE coordinates with the observation angle. Even though the angular color-stability has been slightly improved, by increasing the grating period from 0.8 μm to 1.6 μm , the efficiency decreases to 7.3% and the EQE enhancement factor accounts to 1.46. However, the measurement of such large enhancement factors for 1D grating structures is quite surprising, as Bragg scattering at such structures only occurs along a single axis, whereas 2D structures introduce scattering effects along each symmetry axis, which is supposed to result in larger efficiency enhancements.

In summary, the investigated concepts have compensated present drawbacks of top-emitting OLEDs, regarding white light emission as well as the extraction of internally trapped light modes, in regard to the bottom-emitting counterparts.

Outlook

Even though the presented results validate the applicability and the benefits of the investigated concepts to improve top-emitting OLEDs, further progress has to be achieved in future devices. On the one hand, the combination of the wetting layer concept and the light extraction structures with advanced OLED architectures, materials, and new device concepts is supposed to result in improved efficiencies. For example, the application of wetting layer electrodes in multi-unit OLED architectures [253], where each single unit can be independently driven, has already shown its benefits in terms of device efficiency and the emission color can be controlled. On the other hand, the concepts themselves have to be improved to increase the tackled figures of merit. The investigation of suitable wetting layers, or the replacement of metal electrodes by carbon based materials, e.g. graphene, can yield further optimizations of the transparent electrode for OLEDs, being compatible with the organic layers and R2R processing. Furthermore, progress on the optimization of the grating-OLED system in corrugated devices is supposed to be based

on simulation, predicting the occurring scattering effects, their intensities and the light extraction efficiency of the corrugated devices. In order to validate the simulation results, a procedure to fabricate high quality gratings with a precise control on the grating period, height, and the line profile is required. In addition to the presented nanoimprint process, wet chemical etching of metal gratings has been suggested as a suitable candidate. However, a lower grating quality and an unfavorable OLED performance on the Cr undercoating have not resulted yet in highly efficiency corrugated OLEDs on metal gratings. Moreover, the application and design of more complex 2D light extraction structures is expected to significantly increase the efficiency of corrugated OLEDs.

In order to reduce the influence of Bragg scattered modes on the CIE coordinates for varying observation angles, random scattering layers might be applied on top of the corrugated OLEDs. The deposition of random scattering layers from solution on top of top-emitting OLEDs has been recently shown in the IAPP [254]. There, an improved angular color-stability as well as improved efficiency in comparison to top-emitting OLEDs without scattering layer has been observed, while the solution process has no prominent adverse effect on the electrical characteristics.

Despite the progress in the optimization of the device optics, which has been focused in this work, further challenges are present in OLED research, e.g. the controlled deposition of horizontally oriented phosphorescent or TADF emitters with radiative efficiencies close to unity, the development of long-term stable deep blue emitters, the reduction of annihilation processes at high brightness, as well as the investigation of flexible and thin-film encapsulations, etc. Recent reports emphasize the huge potential of horizontally aligned emitters to increase the efficiency of OLEDs and have introduced a new focus in material research. Progress in these directions is required, in order to gain access to the full potential of the OLED technology, providing unique characteristics for lighting and display applications.

Appendix A

OLED Optimization for Warm White Emission

In Chapter 7, white top-emitting OLEDs with highly transparent wetting layer metal electrodes have been investigated to improve the efficiency, the angular color-stability, and the color rendering in comparison to state-of-the-art bottom- and top-emitting device designs. Here, the optimization of the spectral emission of white top-emitting OLEDs regarding warm white color is discussed. Therefore, variations on the intrinsic layers to affect the exciton distribution and the thickness of the doped charge transport layers used to optimize the emission affinity will be shown.

A.1 Thickness Variation of the Doped Charge Transport Layers

According to the pin-concept, doped charge carrier transport layer thicknesses can be used to optimize the emission affinity of OLEDs without drawbacks on the electrical performance. In Fig. A.1(a), a hybrid white top-emitting OLED architecture, including a fluorescent blue and phosphorescent green and red emitter is shown. The thickness of the doped charge transport layers is varied to reach an emission at the color reference point A.

The normalized spectral emission shows increased emission at smaller wavelengths for reduced transport layer thickness, according to the predicted change of the emission affinity (Fig. A.1(b)). Thus, the emission colors shift along the Planckian locus to lower CCTs, closer to A (Fig. A.2(a)). In Section 4.2.2, it has been shown that the positioning of the emitting dipoles close to maxima of the electric field leads to intense emission. Here, the device with 25 nm HTL and 35 nm ETL shows stronger emission in the blue and green spectral range compared to the device with 30 nm HTL and 30 nm ETL, even though the total layer thickness is not affected. The variation of the EML positions in relation to the field maxima can therefore be used to balance the contributions of the different EMLs, reaching color reference point A for 20 nm HTL and 35 nm ETL thickness (CRI: 78.2, CCT: 2710 K). The efficiencies of the devices are reduced with decreasing cavity length, which is mainly caused from a decrease in the red emission (Fig. A.2(b)). Thus, the LE decreases from 18.2 lm/W to 14.6 lm/W at a current density of 3 mA/cm² (≈ 1000 cd/m²), when reducing the HTL from 30 nm to 20 nm thickness at a fixed ETL thickness of 35 nm. A comparable trend is observed for the EQE. Even though the warm white color is achieved by the variation of the doped transport layers, the assignment of a certain color by a detuning of the device optics is not desired, as the EQE is significantly reduced.

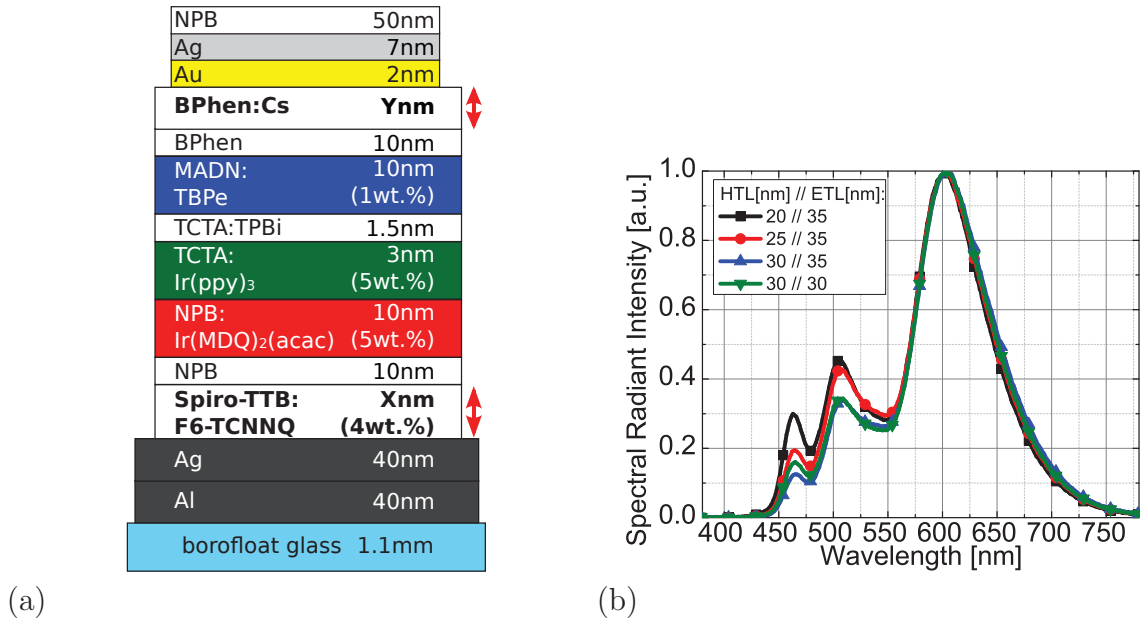


Figure A.1: Hybrid white top-emitting OLED architecture with varied transport layer thicknesses to reach emission at the color reference point A (a) and normalized spectral emission in normal direction (b). A reduction of the total layer thickness increases the contribution of blue and green emission. Furthermore, the positioning of the EML for fixed cavity length is used to control the emission.

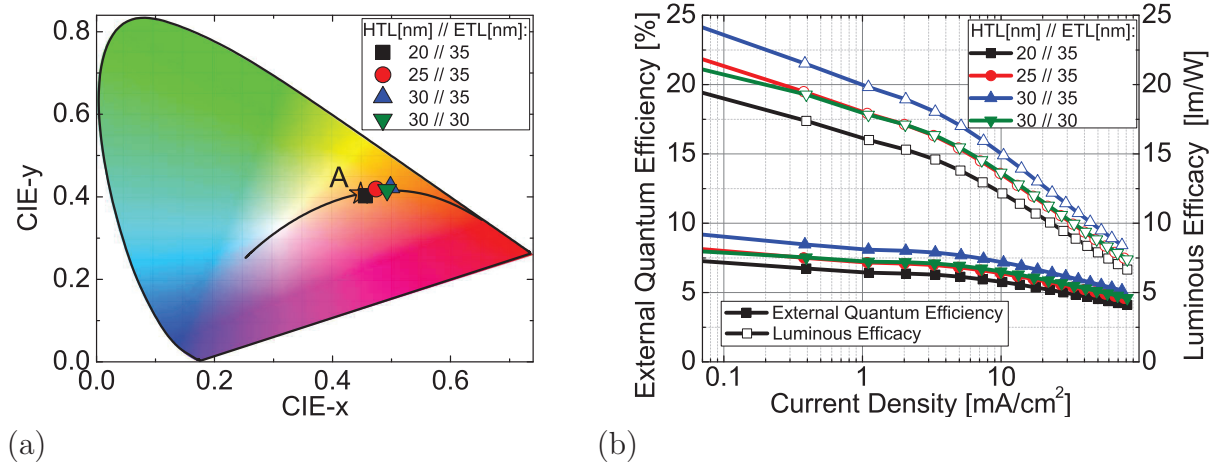


Figure A.2: CIE-1931 color coordinates in normal direction (a) and efficiency-current characteristics (b) for the devices from Fig. A.1. The reduction of the total layer thickness induces a color-shift along the Planckian locus close to the reference point A. For a reduced cavity length, the efficiency of the OLEDs decreases, predicted by a reduced red emission.

A.2 Thickness Optimization of the Emission Layers

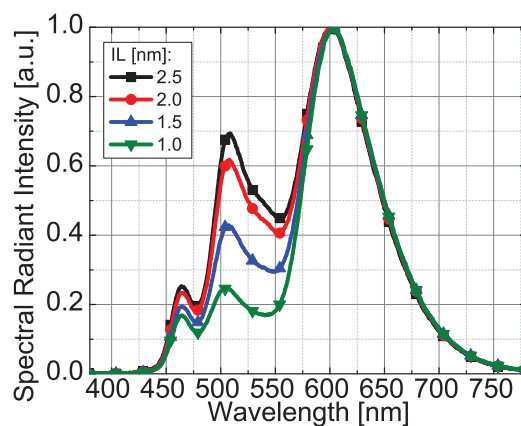
In addition to the optimization of the spectral emission from a variation of the doped charge transport layers, the emission color can be tuned by variations in the emission layer system. Here, the exciton recombination in the devices is directly affected. On the one hand, the thicknesses, the materials, or the doping concentrations of guest emitters in the specific layers can be tuned. On the other hand, an intrinsic interlayer can be applied to control the exciton distribution on the emitters.

Interlayer Thickness Variation

In Fig. A.3(a), a hybrid white top-emitting OLED architecture, according to the previous investigations on the optimization of the doped transport layer thickness is shown (cf. Fig A.1(a)). Here, the thickness of the organic TCTA:TPBi interlayer, embedded between the phosphorescent green and fluorescent blue emitter, is varied to reach a warm white emission. As the overall intrinsic layer thickness is only varied within a 1.5 nm range, no adverse effect on the electrical characteristics or the turn-on voltage of the OLEDs has been observed. In Fig. A.3(b), the normalized spectral emission is shown. An increase of the interlayer thickness enhances the emission of blue and green emission of the devices. Hence, the emission color shifts closer to the blue and green region of the CIE-1931 color space, remaining in proximity to the Planckian locus (Fig. A.4(a)). The OLED with an IL thickness of 2.5 nm reaches a CRI of 83.2 at a CCT of 2997 K, nearly matching the warm white color point A. The observed spectral changes can be directly associated to the affected exciton distribution from the IL variation.

NPB	50nm
Ag	7nm
Au	2nm
BPhen:Cs	35nm
BPhen	10nm
MADN:	10nm
TBPe	(1wt.%)
TCTA:TPBi	Xnm
TCTA:	3nm
Ir(ppy) ₃	(5wt.%)
NPB:	10nm
Ir(MDQ) ₂ (acac)	(5wt.%)
NPB	10nm
Spiro-TTB:	25nm
F6-TCNNQ	(4wt.%)
Ag	40nm
Al	40nm
borofloat glass	1.1mm

(a)



(b)

Figure A.3: Hybrid white top-emitting OLED architecture with varied intrinsic interlayer thickness to reach emission at color reference point A (a) and normalized spectral emission in normal direction (b). Blue and green emission contributions are increased by a thickness increase of the interlayer.

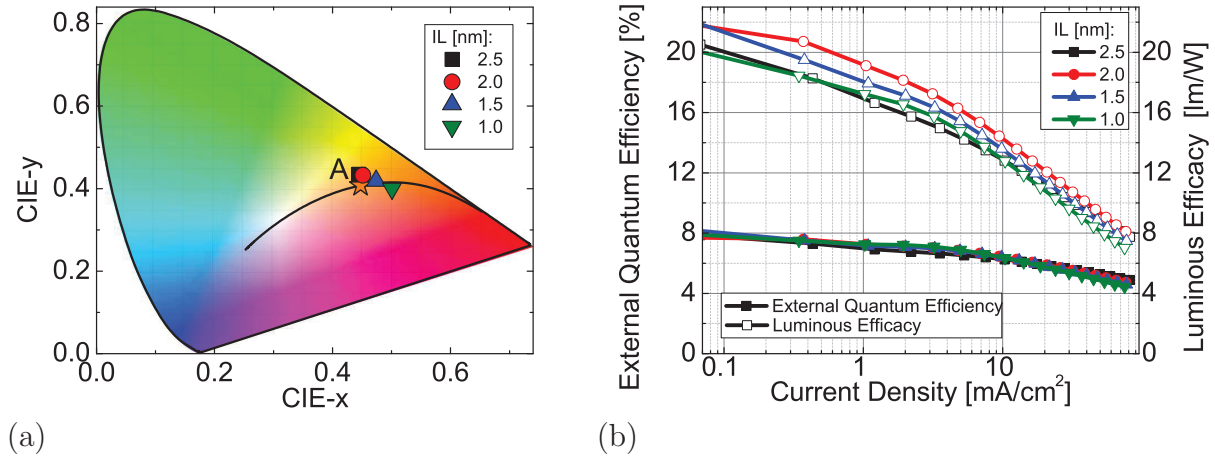


Figure A.4: CIE-1931 color coordinates in normal direction (a) and efficiency-current characteristics (b) for the devices from Fig. A.3. The increase of green and blue contributions to the spectrum for a thicker IL shifts the color point close to warm white emission (IL 2.5 nm). The EQE remains nearly unaffected, while the LE increases by the more intense green emission.

In the specific device design, the exciton recombination zone is expected to be located close at the IL/blue emitter interface or even inside the blue EML, as the matrix materials NPB and TCTA, as well as the IL are mainly hole conductive. An increase of the interlayer thickness would reduce the amount of excitons on the red emitter, as its distance to the exciton generation zone is increased, while the exciton decay on the green emitter is enhanced. The increase of blue emission is correlated to a larger amount of singlet excitons which remain on the blue EML, instead of being transferred to the green EML (Fig. A.3(b)). The EQE of the devices shows only slight decrease with increasing IL thickness, remaining at approximately 7.0% for a current density of 3 mA/cm². As the excitons are mainly redistributed on the different emitters, this approach seems beneficial for the spectral emission optimization, while it can also be combined with a transport layer variation.

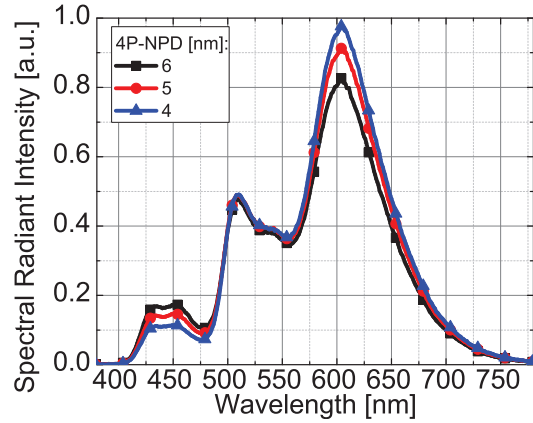
Thickness Optimization of the Emission Layers

In Fig. A.5(a), white top-emitting OLED architectures with a triplet-harvesting blue/red emission layer and a phosphorescent green emitter are shown. The triplet-harvesting concept, which has already been described in Section 3.2.1, conserves the singlet excitons generated on the fluorescent blue emitter, while the triplet excitons have to diffuse to the phosphorescent guest emitters, separated from the exciton generation zone. The exciton formation is expected to be close to the IL/4P-NPD interface, as 4P-NPD is a mainly hole conductive material. Here, the emission color is exemplary controlled by a variation of the 4P-NPD thickness (Fig. A.5(a)).

In Fig. A.5(b), the emission spectra in normal direction are shown for the blue EML thickness variation at a current density of 14.8 mA/cm². An increase of the blue emission layer thickness increases the distance the triplet excitons have to diffuse to the red emitter, reducing the amount of harvested excitons. Hence, the generated emission on the red EML decreases.

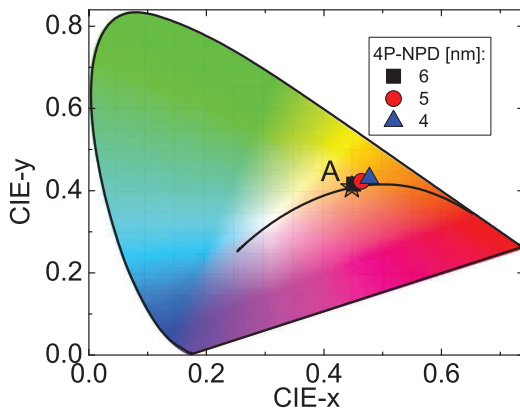
NPB	50nm
Ag	7nm
Au	2nm
BPhen:Cs	30nm
BPhen	10nm
TPBi:	1nm
Ir(ppy) ₃	(5wt.%)
TCTA:TPBi	1.5nm
4P-NPD	Xnm
4P-NPD:	5nm
Ir(MDQ) ₂ (acac)	(5wt.%)
Spiro-TAD	10nm
Spiro-TTB:	30nm
F6-TCNNQ	(4wt.%)
Ag	40nm
Al	40nm
borofloat glass	1.1mm

(a)

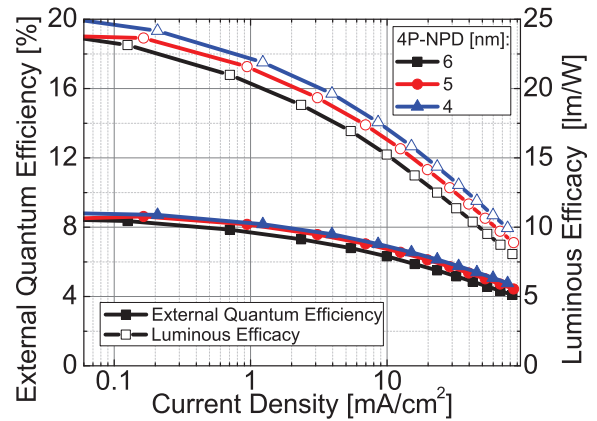


(b)

Figure A.5: Triplet-harvesting white top-emitting OLED architecture with varied blue EML thickness to reach warm white emission (a). Spectra of the devices at a constant current density of 14.8 mA/cm^2 in normal direction (b). An increase of the 4P-NPD thickness leads to a reduction of the red emission, as less triplet excitons reach this EML. Furthermore, undesired transfers of singlet excitons to the red emitter are reduced, increasing the blue emission.



(a)



(b)

Figure A.6: CIE-1931 color coordinates in normal direction (a) and efficiency-current characteristics (b) of the devices from Fig. A.5. The increase in 4P-NPD thickness leads to a color-shift along the Planckian locus to the warm white color point A. While the EQE remains nearly unaffected, the spectral changes result in a decrease of the luminous efficacy for an increased 4P-NPD thickness.

In addition, the unwanted transfer of singlet excitons to the phosphorescent red emitter is reduced, increasing the blue emission. In contrast, the diffusion of excitons to the green EML is not affected and the emission remains unchanged.

Determined by the spectral changes, the emission color shifts along the Planckian Locus to the warm white color point A. For a 4P-NPD thickness of 6 nm, a CRI of 89.5 at a CCT of 2929 K is reached, representing a warm white top-emitting OLED with excellent color rendering (Fig. A.6(a)). The EQE of the devices remains nearly unaffected for the thickness variation of the 4P-NPD, accounting to 7.7% at a current density of 3 mA/cm². Only the OLED with 6 nm thick blue EML shows a slight efficiency decrease to 7.2% EQE and 18.2 lm/W at 3 mA/cm². This decrease is expected to be correlated to triplet excitons, which do not reach the phosphorescent red emitter and decay non-radiatively on the blue EML. The luminous efficacy decreases with the decrease of red, but increase of blue emission, as the eye luminosity function has lower values in the deep blue compared to the red spectral regime.

Appendix B

Post-Processing by Thermal Annealing

Reports reveal that the electrical characteristics of inverted OLEDs can be improved by thermal annealing procedures, reducing energetic barriers and improving the charge injection from the electrodes by an activated diffusion of dopants inside the device.[209, 255, 256] Furthermore, changes of the material morphology can be induced if the annealing temperature is above the glass transition temperature (T_g).

Ag	10nm
Au	2nm
MoO ₃	Xnm
MeO-TPD:	28nm
F6-TCNNQ	(2wt.%)
NPB	10nm
NPB:	20nm
Ir(MDQ) ₂ (acac)	(10wt.%)
BPhen	10nm
BPhen:Cs	65nm
Ag	40nm
Al	40nm
borofloat glass	1.1mm

Figure B.1: Inverted OLEDs with and without a MoO₃ layer to investigate an improvement of the electrical characteristics by thermal annealing.

tion, the thermally induced changes of the jV characteristics in this device are likely to be correlated to morphological changes of the BPhen layers.[209] However, a morphological effect seems to have only a minor impact, as the MoO₃ containing device shows only small change of the jV characteristics, in comparison to the improvement in the device without MoO₃. Hence, a major drawback of the electrical properties of inverted OLEDs has been based on a limited hole injection so far, which is overcome by the MoO₃ wetting layer even without further thermal annealing procedures.

Figure B.1 shows an inverted top-emitting OLED architecture using a red emitter and the MoO₃/Au/Ag wetting layer electrode investigated in Chapter 6 and 7. Results presented in this work have already proven that the electrical characteristics of inverted OLEDs can be improved by the wetting layer electrode, as MoO₃ improves the hole injection. The inverted OLEDs have been annealed for 30 minutes at 70 °C, which is above the T_g of the ETL and HBL material BPhen ($T_g = 62$ °C), according to investigations by Thomschke *et al.* [63], using OLEDs with comparable architecture.

In Fig. B.2(a), the current-voltage dependency of devices with and without a 1 nm thick MoO₃ layer is shown before and after the thermal annealing procedure. The annealing increases the slope of the current-voltage curve of both devices, while the effect is significantly larger for the OLED without MoO₃ layer. Upon annealing, the sample with a MoO₃ layer shows only a slight operating voltage reduction in comparison to the device without MoO₃ (e.g. 0.15 V compared to 0.9 V at 30 mA/cm²). Since inverted OLEDs with MoO₃ show already an improved hole injection,

Appendix B: Thermal Annealing of Inverted OLEDs

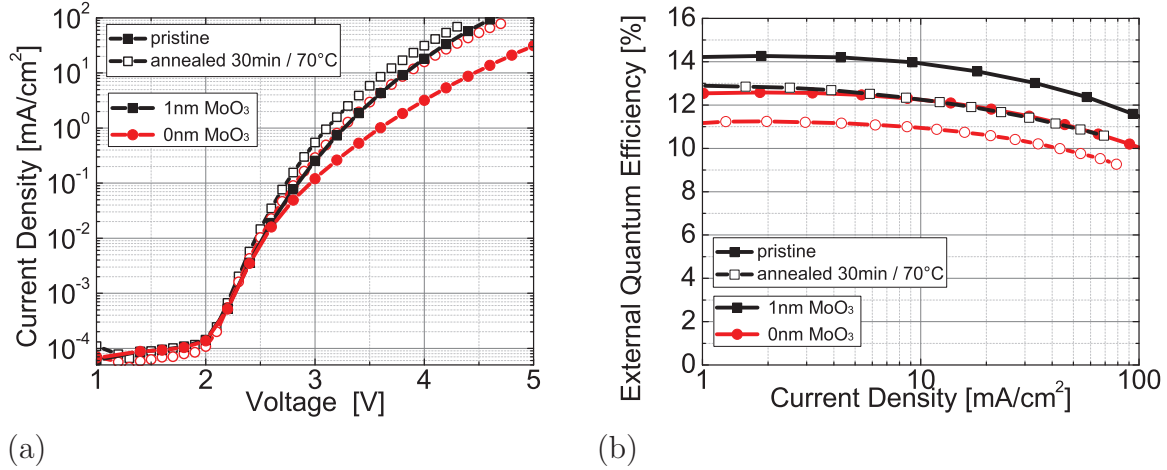


Figure B.2: Current-voltage (a) and EQE-current (b) characteristics of inverted OLEDs from Fig. B.1 with and without a MoO₃ layer. Thermal annealing improves the electrical performances of an OLED without MoO₃, while the EQE significantly decreases. In comparison, the MoO₃ containing device reaches comparable electrical performance and higher EQE without annealing.

Furthermore, the EQE-current dependencies have been evaluated before and after the thermal annealing procedure. For both devices, a reduction of the EQE of approximately 15 to 20 % is found after the annealing procedure (Fig. B.2(b)).

Even though the electrical characteristics are improved by the annealing, the luminous efficacy will decrease, as a consequence from the EQE reduction in the annealed devices (not included here). These observations are in contrast to literature reports for comparable layer architectures under identical thermal treatment, but have already been observed for higher annealing temperatures.[63] On the one hand, the thermal annealing might lead to a diffusion of Cs into the EML, quenching the excitons and increasing the non-radiative decay. On the other hand, thermally induced chemical decomposition of organic materials can cause the efficiency decrease in the annealed devices. Even though the differences in the thermal annealing effects to literature reports are not completely clear, the potential risk of such a procedure to harm OLEDs has clearly been proven evidence.

Overall, the results on inverted OLEDs show that the electrical performance of inverted OLEDs is significantly improved introducing MoO₃ without the need to apply post thermal annealing procedures.

Appendix C

The fabrication of periodically corrugated metal films, based on a wet chemical etching process, is presented in the following section. In comparison to corrugated photoresist layers, which are used in Chapter 8 and 9, the application of metal gratings allows for a more precise control on the grating height and the aspect ratio. In addition, investigations into corrugated 1st order top-emitting OLEDs on top of metal gratings are shown. The experiments highlight basic device design concepts for corrugated top-emitting OLEDs, to extract internally trapped light modes and to maintain the electrical performance.

C.1 Fabrication of Metal Gratings

The processing steps of a periodic grating from wet chemical etching of a neat metal layer is shown in Fig. C.1. First, a corrugated photoresist film is prepared on top of a bulk metal layer. The period of the corrugated photoresist film determines the period of the metal grating. An etchant is applied to dissolve the metal only at the openings of the photoresist film, while the photoresist itself is not affected by the etchant. After the etching process, the photoresist layer is removed, e.g. by acetone, and the bare metal grating with a height of the neat film is obtained. Using PVD for metal deposition, the grating height can be controlled with a higher precision as it is possible for photolithography or nanoimprint techniques, which are used for the preparation of a corrugated photoresist layer in Chapter 8 and 9. Preliminary tests, investigating several combinations of metals (Al, Ag, Au) with negative or positive photoresists, result in a preferred application of gold with a chromium undercoating and the positive photoresist ma-P 1210 to fabricate metal gratings. The positive photoresist layer has been prepared by photolithography, as described in Section 5.1.2. It is worth noting that the chromium undercoating has been introduced to allow for the application of a cleaning procedure of the gratings prior to the OLED deposition. This includes a treatment in an ultrasonic bath, which harms gratings without undercoating.

Figure C.2 shows a series of AFM measurements of metal gratings, which were prepared from a 40 nm thick Au film with 2 nm Cr undercoating for different etching times.

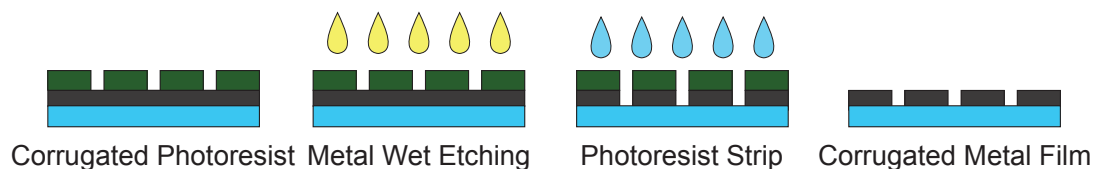


Figure C.1: Illustration of the metal grating preparation from a wet chemical etching procedure. The etchant selectively dissolves the metal film in the regions uncovered from the photoresist. The grating period is determined by the corrugated photoresist, whereas the height is given by the metal film thickness.

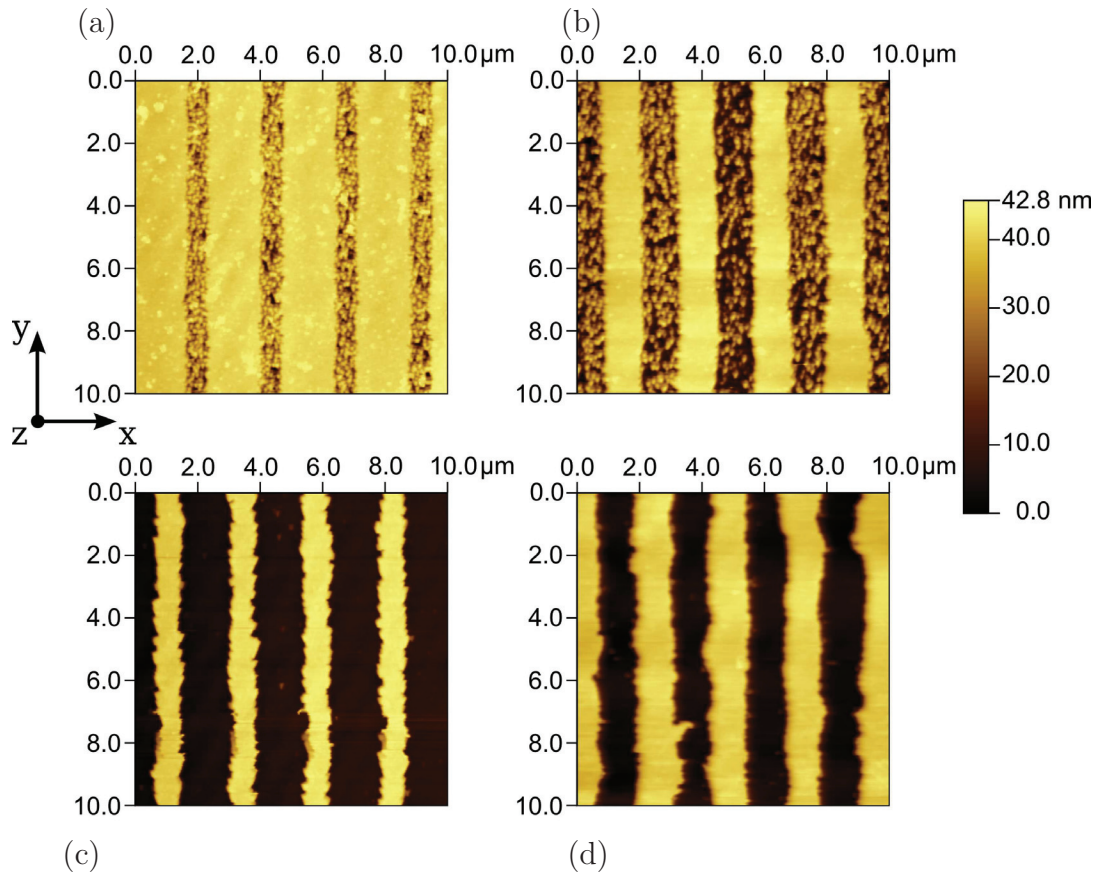


Figure C.2: AFM series of a 40 nm thick gold film for etching times of 1 s (a), 3 s (b), and 15 s (c), respectively. According to the corrugated photoresist, separated gold lines with a period of 2.5 μm are obtained. The contour roughness increases with increasing etching time. O_2 plasma etching of the photoresist, prior to the metal etching, has been found to reduce the etching time (3 s) and to decrease the contour roughness (d).

The corrugated photoresist layer had a period of 2.5 μm and has been stripped prior to the AFM measurement. In Fig. C.2(a), the etching process has been stopped after 1 s. A beginning selective etching of the gold is observed, resulting in broad lines with a period of 2.5 μm and a width of approximately 2.1 μm . Furthermore, isolated gold grains in the space between the gold lines can be seen. By increasing the etching time to 3 s (Fig. C.2(b)), the gold lines narrow to a width of 1.5 μm , while the period is not affected and residual gold grains between the lines remain. For 15 s etching time (Fig. C.2(c)), the line width is reduced to approximately 1.0 μm and the space between the gold lines is free of residual gold grains. Very homogeneous grating heights are observed for all etching times, as the PVD deposition of the metal results in planar films. However, the line contours are very rough and irregularly formed, which becomes more prominent with increasing etching time. A larger contour roughness is supposed to increase the leakage currents of OLEDs deposited on top of these gratings and also electrical shorts become more likely.

In order to reduce the contour roughness, the etching time has to be reduced, while residual metal grains between the grating lines have to be avoided. It is expected that

remaining photoresist causes the preservation of metal grains between the gold lines for etching times in the range of 3 s. For longer etching times, lateral etching from the resist free areas is expected to dissolve the residual grains. Hence, the undesired photoresist has to be removed prior to the etching of the metal. Figure C.2(d) shows an AFM image of a gold grating, where the corrugated photoresist has been treated for 10 minutes with O_2 plasma at a base pressure of 10^{-2} mbar, prior to a 3 s metal etching.

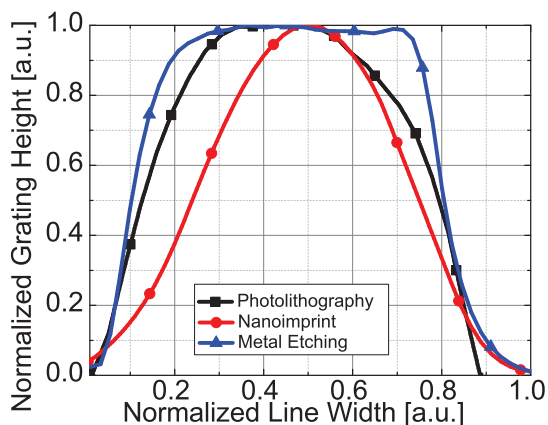


Figure C.3: Comparison of single grating line profiles for the different fabrication methods normalized to width and height.

performance, here. A profile scan of a single metal stripe shows an almost rectangular shape (Fig. C.3). The metal top surface is homogeneously flat, whereas a steeper slope of the grating line would be observed in comparison to photoresist gratings with identical line width. In addition to the rough contour, sharp edges of the metal gratings could also lead to electrical shorts in corrugated OLEDs.

The space between the gold lines remains almost grain free, whereas the contour roughness is reduced in comparison to the grating etched for 15 s without an O_2 plasma treatment of the photoresist. However, the line contours are still not smooth and the grating homogeneity remains lower than for the structures obtained by the nanoimprint procedure, presented in Chapter 8.

The rough contour might be attributed to an anisotropic etching, which depends on the surface orientations in the deposited polycrystalline gold film. In order to produce nano-structures, anisotropic etching is often desired [257], but adverse effects are introduced to the grating per-

C.2 Corrugated OLEDs on Metal Gratings

Investigations of 1st order corrugated red top-emitting OLEDs are presented in the following. Periodic 1D gold gratings with periods of $0.6 \mu\text{m}$ and $2.5 \mu\text{m}$ and 40 nm height on top of a 2 nm thick chromium undercoating have been prepared according to a wet chemical etching procedure and O_2 plasma treatment of the photoresist film. Two planar reference devices are prepared on each 1×1 substrate, one on a non-etched, neat gold film and one on the planar chromium undercoating, where the gold film has been entirely etched. The reference on the Cr is used to detect a potential impact of etching residuals and the undercoating itself on the device performance, as this would also account to the corrugated OLEDs. A rather thick silver top electrode of 20 nm is used, which is comparable to previous reports on highly efficient 1st cavity order red top-emitting OLEDs [11].

Figure C.4 shows the investigated OLED architecture, which represents a state-of-the-art device design using the pin-concept and a red phosphorescent emitter. As in Chapter 8 and 9, the planar references have been optimized by optical simulation for maximum photon flux, respecting the orientation of the red emitter and assuming an exciton recombination at the EML/BPhen interface.

Figure C.5(a) shows the current-voltage and luminance-voltage curves of the planar reference devices as well as for the corrugated OLEDs with periods of 0.6 μm and 2.5 μm .


NPB	70nm	
Ag	20nm	
BPhen:Cs	66nm	
BPhen	10nm	
NPB: Ir(MDQ) ₂ (acac)(10wt.%)	20nm	
Spiro-TAD	10nm	
Spiro-TTB: F6-TCNNQ (4wt.%)	39nm	
Ag	40nm	
Al	40nm	
planar	corrugated	etched
Au		40nm
Cr		2nm
borofloat glass		1.1mm

Figure C.4: 1st cavity order red top-emitting OLEDs on 1D gold gratings of different period.

An increase in leakage current is found for the two corrugated OLEDs, in comparison to the planar devices on top of a compact gold film. As the AFM images of the gratings showed a rough contour of the gold lines, the leakage current increase might be attributed to a prominent roughness introduced by the corrugation. However, the planar OLEDs on the Cr undercoating show an even more prominent increase in leakage current, which cannot be completely explained so far, as the AFM scans (cf. Fig. C.2(d)) revealed a planar surface of the Cr after the etching and cleaning procedure. Eventually, a change of the aluminum growth is introduced by the Cr, resulting in a larger surface roughness.[258] In addition to the leakage current increase, the corrugated OLEDs and Cr references show an increased current in the entire voltage range, more prominent in the planar Cr devices, which indicates further changes in these devices. The luminance of the corrugated OLEDs is comparable to the non-etched planar references for both grating periods, which shows that no prominent changes of the spectral emission have been introduced by the gratings. Figure C.5(b) shows the EQE-current dependency of the devices.

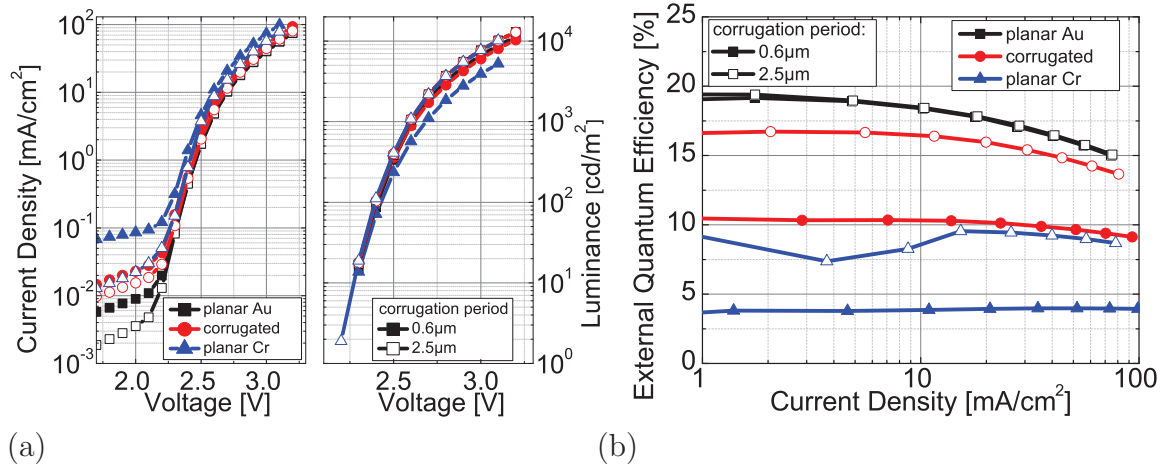


Figure C.5: Comparison of planar and corrugated red top-emitting OLEDs for different grating periods, regarding the j VL characteristics (a) and the EQE-current dependency (b). The corrugated devices show increased leakage currents with respect to the planar references on compact gold films. Planar OLEDs on the Cr undercoating show an even worse electrical performance, indicating an impact on the bottom electrode growth, while also the efficiency is decreased. Furthermore, the corrugated OLEDs show no efficiency increase compared to the non-etched devices.

The non-etched devices reach a comparable performance in the entire current range, which can be assigned to the identical layer sequence and to a reproducible device operation. In comparison to these devices, the references on the Cr layer show a significantly reduced EQE and also a large deviation between the two samples is found. Investigations on top-emitting OLEDs in the 2nd cavity order, which are not included here, have confirmed the observed trend in the electrical performance and the efficiency of devices on a Cr layer, even though a thicker organic layer sequence has been deposited. Based on these findings, a negative impact of the Cr on the performance of top-emitting OLEDs, using an Al/Ag bottom electrode, is indicated. This also holds for the corrugated OLEDs, as a certain amount of the active area is directly deposited on top of the Cr. In Fig. C.5(b), the corrugated OLEDs with periods of 0.6 μm and 2.5 μm , show a lower EQE than the planar references on a compact gold film. Investigations of the spectral emission of the corrugated OLEDs will show that the deviations in the efficiency are not attributed to differences in the emission from Bragg scattering effects. Instead, the differences in the EQE are expected to be caused by an unreliable device operation, induced by the Cr undercoating.

Overall, the experiments of corrugated top-emitting OLEDs on metal gratings, using a Cr layer which is required to allow for the cleaning of the substrates prior to the OLED fabrication, have not yielded a reproducible device performance so far. Hence, these experiments have not been considered in the evaluation of light extraction efficiency enhancements by a periodic grating. As such adverse effects have not been observed in the Au references, an impact on the bottom electrode growth or the formation of etching products with the Cr might be associated to these findings. In future devices, the Cr undercoating should be replaced by another material, in order to maintain a reliable device performance of corrugated OLEDs, whereas a fabrication of gold gratings on glass without undercoating has not been successful, as the structures are washed away during the cleaning procedure.

Extraction of Internal Light Modes from First Order Microcavities

In order to investigate the absent efficiency enhancement in corrugated 1st order top-emitting OLEDs on metal gratings (cf. Fig. C.5(b)), the angle and polarization resolved spectral radiant intensity has been analyzed. Figure C.6 shows the emission of two corrugated OLEDs with periods of 0.6 μm and 2.5 μm , as well as of a planar reference at a current density of 14.8 mA/cm². Only negligible spectral effects are observed in the corrugated OLEDs for s- and p-polarization in comparison to the planar reference device. This finding is in contrast to the results for 2nd cavity order corrugated OLEDs on photoresist films. The absence of Bragg scattered modes in 1st order cavities has to be caused by a lower extraction efficiency of internally trapped light modes from these devices.

As the periods and heights of the metal gratings are comparable to the investigated photoresist gratings, the lower quality of the metal gratings as well as the modified power dissipation of the 1st order microcavities have to contribute to the nearly unaffected device emission of the corrugated OLEDs. In comparison to a 2nd order top-emitting OLED, 1st order cavity devices dissipate more power into SPP modes, and less into waveguided modes.

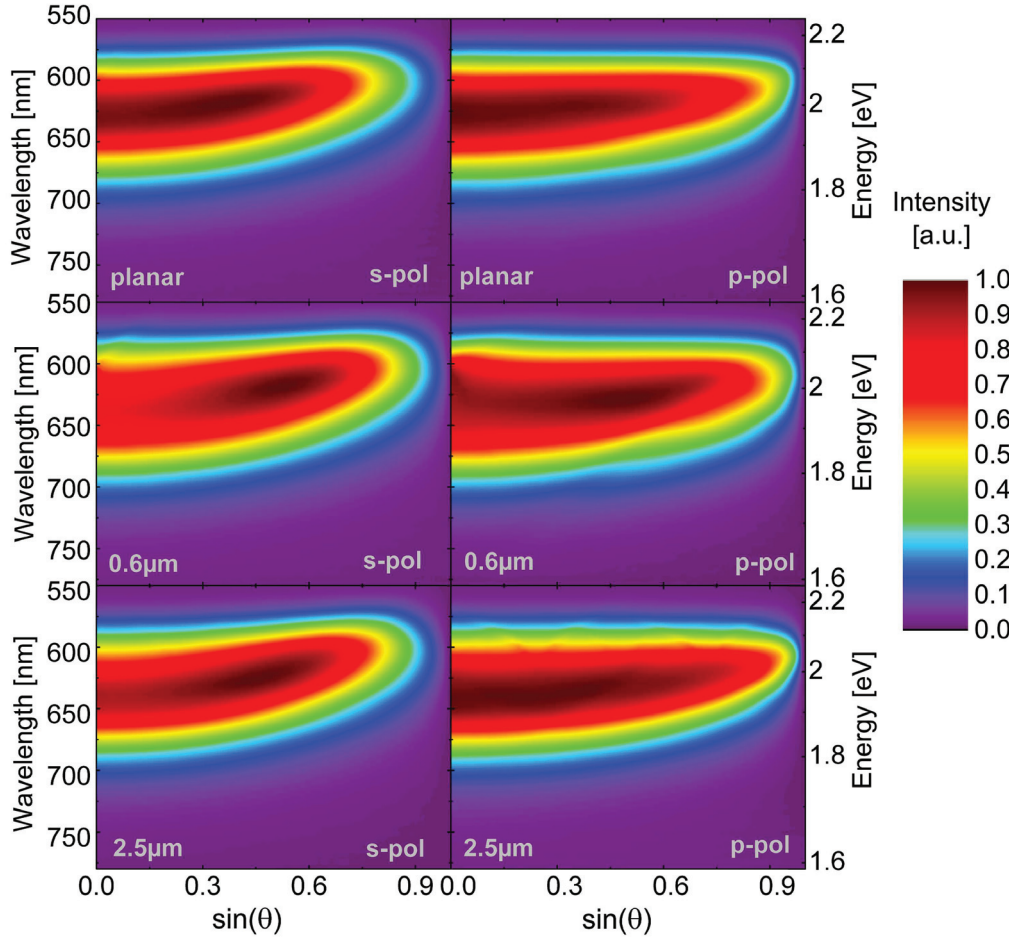


Figure C.6: Measured angle and polarization dependent emission of a planar and two corrugated 1st order top-emitting OLEDs (cf. Fig. C.4) with different metal grating periods for electrical device operation at a current density of 14.8 mA/cm^2 . Both corrugated OLEDs show negligible emission features from extracted internal light modes by Bragg scattering.

In Chapter 8 and 9, it was shown that waveguided modes can be efficiently extracted from a 2nd order cavity, applying 1D gratings with periods in the μm range. Since SPP modes already showed low intensities in the power dissipation spectrum of the planar devices, only small contributions of Bragg scattered SPP modes have been detected in the corrugated 2nd order cavity OLEDs. Referring to the results shown in Fig. C.6, it is indicated that SPP modes might not be efficiently extracted by Bragg scattering at the investigated periodic gratings, in comparison to waveguided modes.

In addition, the grating quality is expected to have a major impact on the Bragg scattering efficiency of light modes. In the Fraunhofer limit, the intensity distribution of the diffracted light is directly correlated to the Fourier transformed representation of the diffracting object (cf. Section 4.3.4). Since a grating with a lower homogeneity of the line contour, width, and height would demand additional terms in the Fourier transformed representation, the intensity of the single scattering reflexes decreases, whereas additional reflexes rise. Investigations of 2nd order top-emitting OLEDs on metal grat-

ings (not included here) showed more prominent scattering effects in comparison to the 1st order cavities, which proves that such metal gratings are in principle applicable to extract internally trapped light modes. However, also in these devices an efficiency enhancement has not been achieved, mainly attributed to the adversely affected electrical performance.

Figure C.7 shows the angle and polarization resolved emission of a corrugated 1st order top-emitting OLED, with an identical layer sequence as the OLEDs in Fig. C.6, on a photoresist grating with 750 nm period and 40 nm depth for a current density of 14.8 mA/cm².

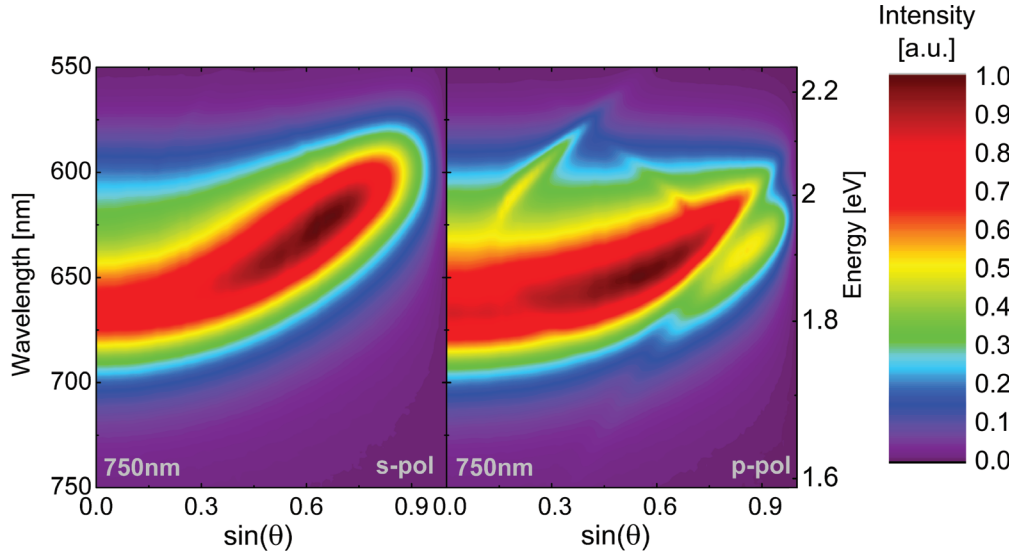


Figure C.7: Measured angle and polarization dependent emission of a corrugated 1st order top-emitting OLED (layer sequence as in Fig. C.4) on a 1D photoresist grating of 750 nm period and 40 nm depth driven at a current density of 14.8 mA/cm². Whereas the s-polarized emission shows only negligible scattering effects, more prominent scattering of internal light modes is observed for p-polarization.

In comparison to the corrugated devices on metal gratings, more prominent scattering effects are observed in this OLED on a high quality photoresist grating, which indicates the impact of the grating quality on the extraction efficiency of light modes. Since scattering effects prominently occur in p-polarized emission, the extracted light modes are supposed to be SPP modes. The absence of scattered modes in s-polarized emission is associated to the less intense power dissipation into waveguided organic modes. Even though the effects are more prominent for the high quality photoresist pattern, whereas grating period and depth of the photoresist grating is roughly comparable to the metal grating with 0.6 μm period, the effects are still not as intense as in 2nd order microcavity OLEDs.

Overall, corrugated 1st order top-emitting OLEDs showed only slight effects of Bragg scattered modes in the emission spectra. This indicates that SPP modes might be scattered with only low efficiency. Furthermore, waveguided modes, which might be scattered more efficiently, are only weakly driven in these OLED architectures. Thus, an efficiency enhancement based on the extraction of internally trapped light modes has so far not been observed in such corrugated devices. A technical aspect concerning corrugated

1st order microcavities is the lower device yield, as the probability of electrical shorts is increased for thinner organic layers, as well as adverse effects on the electrical characteristics. In general, it is expected that 1st order microcavities can benefit from light extraction structures as well if the metal grating quality can be improved by an advanced preparation technique and if SPP modes can be efficiently extracted. *Reactive ion etching* [259] could be a potential candidate to reduce the contour roughness of the metal gratings, as isotropic etch rates with a low sensitivity to surface orientations of the film can be obtained.

Bibliography

- [1] M. Imhoff, W. T. Lawrence, D. C. Stutzer, and C. D. Elvidge, “A technique for using composite DMSP/OLS “City Lights” satellite data to map urban area”, *Remote Sensing of Environment* **61**, 361 (1997).
- [2] M. Imhoff, C. Tucker, W. Lawrence, and D. Stutzer, “The use of multisource satellite and geospatial data to study the effect of urbanization on primary productivity in the United States”, *IEEE Transactions on Geoscience and Remote Sensing* **38**, 2549 (2000).
- [3] European Space Agency (08.04.2014), “http://www.esa.int/spaceinimages/Images/2012/03/Night_lights_in_Europe”.
- [4] E. F. Schubert and J. K. Kim, “Solid-State Light Sources Getting Smart”, *Science* **308**, 1274 (2005).
- [5] C. W. Tang and S. A. VanSlyke, “Organic electroluminescent diodes”, *Applied Physics Letters* **51**, 913 (1987).
- [6] C. Adachi, M. A. Baldo, M. E. Thompson, and S. R. Forrest, “Nearly 100% internal phosphorescence efficiency in an organic light-emitting device”, *Journal of Applied Physics* **90**, 5048 (2001).
- [7] S. Reineke, F. Lindner, G. Schwartz, N. Seidler, K. Walzer, B. Lüssem, and K. Leo, “White organic light-emitting diodes with fluorescent tube efficiency.” *Nature* **459**, 234 (2009).
- [8] Samsung OLED TV KE55S9C (08.04.2014), “<http://www.samsung.com/de/consumer/tv-audio-video/television/oled-tv/KE55S9CSLXZG#>”.
- [9] Siemens AG (08.04.2014), “http://www.siemens.com/innovation/apps/pof_microsite/_pof-spring-2010/_html.en/organic-light-emitting-diodes-2.html”.
- [10] S.-Y. Kim, W.-I. Jeong, C. Mayr, Y.-S. Park, K.-H. Kim, J.-H. Lee, C.-K. Moon, W. Brütting, and J.-J. Kim, “Organic Light-Emitting Diodes with 30% External Quantum Efficiency Based on a Horizontally Oriented Emitter”, *Advanced Functional Materials* **23**, 3896 (2013).
- [11] S. Hofmann, M. Thomschke, P. Freitag, M. Furno, B. Lüssem, and K. Leo, “Top-emitting organic light-emitting diodes: Influence of cavity design”, *Applied Physics Letters* **97**, 253308 (2010).
- [12] M. Fox, *Optical Properties of Solids* (Oxford University Press, Oxford), 1st edition (2001).

Bibliography

- [13] P. Atkins and D. Friedman, *Molecular Quantum Mechanics* (Oxford University Press, Oxford), 4th edition (2005).
- [14] F. Schwabl, *Quantenmechanik* (Springer, Berlin Heidelberg), 6th edition (2002).
- [15] H. Haken and H. C. Wolf, *Molekülphysik und Quantenchemie* (Springer, Berlin Heidelberg), 5th edition (2006).
- [16] M. Pope and C. E. Swenberg, *Electronic Processes in Organic Crystals and Polymers* (Oxford University Press, Oxford), 2nd edition (1999).
- [17] H. Ibach and H. Lüth, *Festkörperphysik* (Springer, Berlin Heidelberg), 6th edition (2002).
- [18] W. Demtröder, *Experimentalphysik 3: Atome, Moleküle und Festkörper* (Springer, Berlin Heidelberg), 3rd edition (2005).
- [19] R. Waser, *Nanoelectronics and Information Technology: Advanced Electronic Materials and Novel Devices* (Wiley-VCH, Weinheim), 1st edition (2003).
- [20] P. Esquinazi, *Tunneling Systems in Amorphous and Crystalline Solids* (Springer, Berlin Heidelberg), 1st edition (1998).
- [21] S. T. Hoffmann, H. Bässler, and A. Köhler, “What determines inhomogeneous broadening of electronic transitions in conjugated polymers?” *The Journal of Physical Chemistry B* **114**, 17037 (2010).
- [22] M. A. Baldo, M. E. Thompson, and S. R. Forrest, “High-efficiency fluorescent organic light-emitting devices using a phosphorescent sensitizer”, *Nature* **403**, 750 (2000).
- [23] E. A. Jares-Erijman and T. M. Jovin, “FRET imaging.” *Nature Biotechnology* **21**, 1387 (2003).
- [24] D. L. Dexter, “A Theory of Sensitized Luminescence in Solids”, *The Journal of Chemical Physics* **21**, 836 (1953).
- [25] J. Wünsche, S. Reineke, B. Lüssem, and K. Leo, “Measurement of triplet exciton diffusion in organic light-emitting diodes”, *Physical Review B* **81**, 245201 (2010).
- [26] S. Hofmann, T. C. Rosenow, M. C. Gather, B. Lüssem, and K. Leo, “Singlet exciton diffusion length in organic light-emitting diodes”, *Physical Review B* **85**, 245209 (2012).
- [27] H. Nakanotani, H. Sasabe, and C. Adachi, “Singlet-singlet and singlet-heat annihilations in fluorescence-based organic light-emitting diodes under steady-state high current density”, *Applied Physics Letters* **86**, 213506 (2005).
- [28] N. C. Giebink and S. R. Forrest, “Quantum efficiency roll-off at high brightness in fluorescent and phosphorescent organic light emitting diodes”, *Physical Review B* **77**, 235215 (2008).

- [29] M. A. Baldo, C. Adachi, and S. R. Forrest, “Transient analysis of organic electrophosphorescence. II. Transient analysis of triplet-triplet annihilation”, *Physical Review B* **62**, 10967 (2000).
- [30] S. Reineke, K. Walzer, and K. Leo, “Triplet-exciton quenching in organic phosphorescent light-emitting diodes with Ir-based emitters”, *Physical Review B* **75**, 125328 (2007).
- [31] C. Murawski, K. Leo, and M. C. Gather, “Efficiency Roll-Off in Organic Light-Emitting Diodes.” *Advanced Materials* (2013).
- [32] S. Reineke, G. Schwartz, K. Walzer, and K. Leo, “Reduced efficiency roll-off in phosphorescent organic light emitting diodes by suppression of triplet-triplet annihilation”, *Applied Physics Letters* **91**, 123508 (2007).
- [33] W. Brütting, *Physics of Organic Semiconductors* (John Wiley & Sons, Weinheim), 1st edition (2006).
- [34] S. M. Sze and K. N. Kwok, *Physics of Semiconductor Devices* (John Wiley & Sons, Hoboken), 3rd edition (2006).
- [35] H. Bässler, “Charge Transport in Disordered Organic Photoconductors A Monte Carlo Simulation Study”, *Physica Status Solidi (b)* **175**, 1 (1993).
- [36] S. Stafström, “Electron localization and the transition from adiabatic to nonadiabatic charge transport in organic conductors.” *Chemical Society Reviews* **39**, 2484 (2010).
- [37] A. Miller and E. Abrahams, “Impurity Conduction at Low Concentrations”, *Physical Review* **120**, 745 (1960).
- [38] J. Simmons, “Poole-Frenkel Effect and Schottky Effect in Metal-Insulator-Metal Systems”, *Physical Review* **155**, 657 (1967).
- [39] P. W. M. Blom, C. Tanase, D. M. de Leeuw, and R. Coehoorn, “Thickness scaling of the space-charge-limited current in poly(p-phenylene vinylene)”, *Applied Physics Letters* **86**, 092105 (2005).
- [40] C. Tanase, P. W. M. Blom, and D. M. de Leeuw, “Origin of the enhanced space-charge-limited current in poly(p-phenylene vinylene)”, *Physical Review B* **70**, 193202 (2004).
- [41] P. Mark and W. Helfrich, “Space-Charge-Limited Currents in Organic Crystals”, *Journal of Applied Physics* **33**, 205 (1962).
- [42] A. J. Campbell, D. D. C. Bradley, and D. G. Lidzey, “Space-charge limited conduction with traps in poly(phenylene vinylene) light emitting diodes”, *Journal of Applied Physics* **82**, 6326 (1997).
- [43] W. Demtröder, *Experimentalphysik 2: Elektrizität und Optik* (Springer, Berlin Heidelberg), 3rd edition (2004).

- [44] M. Mandoc, B. de Boer, G. Paasch, and P. W. M. Blom, “Trap-limited electron transport in disordered semiconducting polymers”, *Physical Review B* **75**, 193202 (2007).
- [45] H. T. Nicolai, M. Kuik, G. A. H. Wetzelaer, B. de Boer, C. Campbell, C. Risko, J. L. Brédas, and P. W. M. Blom, “Unification of trap-limited electron transport in semiconducting polymers.” *Nature Materials* **11**, 882 (2012).
- [46] P. W. M. Blom, M. J. M. de Jong, and J. J. M. Vleggaar, “Electron and hole transport in poly(p-phenylene vinylene) devices”, *Applied Physics Letters* **68**, 3308 (1996).
- [47] R. G. Kepler, P. M. Beeson, S. J. Jacobs, R. A. Anderson, M. B. Sinclair, V. S. Valencia, and P. A. Cahill, “Electron and hole mobility in tris(8-hydroxyquinolinolato-N1,O8) aluminum”, *Applied Physics Letters* **66**, 3618 (1995).
- [48] I. H. Campbell, D. L. Smith, C. J. Neef, and J. P. Ferraris, “Consistent time-of-flight mobility measurements and polymer light-emitting diode current–voltage characteristics”, *Applied Physics Letters* **74**, 2809 (1999).
- [49] M. C. J. M. Vissenberg, “Theory of the field-effect mobility in amorphous organic transistors”, *Physical Review B* **57**, 12964 (1998).
- [50] C. Goldmann, S. Haas, C. Krellner, K. P. Pernstich, D. J. Gundlach, and B. Batlogg, “Hole mobility in organic single crystals measured by a “flip-crystal” field-effect technique”, *Journal of Applied Physics* **96**, 2080 (2004).
- [51] P. E. Burrows and S. R. Forrest, “Electroluminescence from trap-limited current transport in vacuum deposited organic light emitting devices”, *Applied Physics Letters* **64**, 2285 (1994).
- [52] S. Braun, W. R. Salaneck, and M. Fahlman, “Energy-Level Alignment at Organic/Metal and Organic/Organic Interfaces”, *Advanced Materials* **21**, 1450 (2009).
- [53] P. Petelenz, Z. G. Soos, E. Umbach, D. R. Zahn, G. N. Gavrilu, and M. Gorgoi, “The transport gap of organic semiconductors studied using the combination of direct and inverse photoemission”, *Chemical Physics* **325**, 99 (2006).
- [54] J. C. Scott, “Metal–organic interface and charge injection in organic electronic devices”, *Journal of Vacuum Science & Technology A: Vacuum, Surfaces, and Films* **21**, 521 (2003).
- [55] U. Wolf, V. I. Arkhipov, and H. Bässler, “Current injection from a metal to a disordered hopping system. I. Monte Carlo simulation”, *Physical Review B* **59**, 7507 (1999).
- [56] O. W. Richardson, *Emission of Electricity from hot bodies* (Longmans, Green and co., London), 2nd edition (1921).

- [57] H. Ishii, K. Sugiyama, E. Ito, and K. Seki, “Energy Level Alignment and Interfacial Electronic Structures at Organic/Metal and Organic/Organic Interfaces”, *Advanced Materials* **11**, 605 (1999).
- [58] M. Pfeiffer, S. R. Forrest, X. Zhou, and K. Leo, “A low drive voltage, transparent, metal-free n-i-p electrophosphorescent light emitting diode”, *Organic Electronics* **4**, 21 (2003).
- [59] R. H. Fowler and L. Nordheim, “Electron Emission in Intense Electric Fields”, *Proceedings of the Royal Society of London. Series A* **119**, 173 (1928).
- [60] W. Gao and A. Kahn, “Electronic structure and current injection in zinc phthalocyanine doped with tetrafluorotetracyanoquinodimethane: Interface versus bulk effects”, *Organic Electronics* **3**, 53 (2002).
- [61] K. Walzer, B. Maennig, M. Pfeiffer, and K. Leo, “Highly efficient organic devices based on electrically doped transport layers.” *Chemical Reviews* **107**, 1233 (2007).
- [62] S. Scholz, Q. Huang, M. Thomschke, S. Olthof, P. Sebastian, K. Walzer, K. Leo, S. Oswald, C. Corten, and D. Kuckling, “Self-doping and partial oxidation of metal-on-organic interfaces for organic semiconductor devices studied by chemical analysis techniques”, *Journal of Applied Physics* **104**, 104502 (2008).
- [63] M. Thomschke, S. Hofmann, S. Olthof, M. Anderson, H. Kleemann, M. Schober, B. Lüssem, and K. Leo, “Improvement of voltage and charge balance in inverted top-emitting organic electroluminescent diodes comprising doped transport layers by thermal annealing”, *Applied Physics Letters* **98**, 083304 (2011).
- [64] M. Pfeiffer, K. Leo, X. Zhou, J. S. Huang, M. Hofmann, A. Werner, and J. Blochwitz-Nimoth, “Doped organic semiconductors: Physics and application in light emitting diodes”, *Organic Electronics* **4**, 89 (2003).
- [65] R. Schlaf, B. A. Parkinson, P. A. Lee, K. W. Nebesny, and N. R. Armstrong, “Determination of frontier orbital alignment and band bending at an organic semiconductor heterointerface by combined x-ray and ultraviolet photoemission measurements”, *Applied Physics Letters* **73**, 1026 (1998).
- [66] N. Sato and M. Yoshikawa, “Valence electronic structure at the interface of organic thin films”, *Journal of Electron Spectroscopy and Related Phenomena* **78**, 387 (1996).
- [67] I. G. Hill and A. Kahn, “Energy level alignment at interfaces of organic semiconductor heterostructures”, *Journal of Applied Physics* **84**, 5583 (1998).
- [68] V. I. Arkhipov, E. V. Emelianova, and H. Bässler, “Charge carrier transport and recombination at the interface between disordered organic dielectrics”, *Journal of Applied Physics* **90**, 2352 (2001).
- [69] T. Mori, H. Fujikawa, S. Tokito, and Y. Taga, “Electronic structure of 8-hydroxyquinoline aluminum/LiF/Al interface for organic electroluminescent device studied by ultraviolet photoelectron spectroscopy”, *Applied Physics Letters* **73**, 2763 (1998).

- [70] I. G. Hill, A. Kahn, Z. G. Soos, and R. A. Pascal, "Charge-separation energy in films of p-conjugated organic molecules", *Chemical Physics Letters* **327**, 181 (2000).
- [71] A. Bernanose, "Electroluminescence of organic compounds", *British Journal of Applied Physics* **6**, S54 (1955).
- [72] M. Pope, H. P. Kallmann, and P. Magnante, "Electroluminescence in Organic Crystals", *The Journal of Chemical Physics* **38**, 2042 (1963).
- [73] C. W. Tang, S. A. VanSlyke, and C. H. Chen, "Electroluminescence of doped organic thin films", *Journal of Applied Physics* **85**, 3610 (1989).
- [74] M.-H. Lu and J. C. Sturm, "Optimization of external coupling and light emission in organic light-emitting devices: modeling and experiment", *Journal of Applied Physics* **91**, 595 (2002).
- [75] Y. Kawamura, K. Goushi, J. Brooks, J. J. Brown, H. Sasabe, and C. Adachi, "100% phosphorescence quantum efficiency of Ir(III) complexes in organic semiconductor films", *Applied Physics Letters* **86**, 071104 (2005).
- [76] R. Meerheim, M. Furno, S. Hofmann, B. Lüssem, and K. Leo, "Quantification of energy loss mechanisms in organic light-emitting diodes", *Applied Physics Letters* **97**, 253305 (2010).
- [77] T. Schwab, B. Lüssem, M. Furno, M. C. Gather, and K. Leo, *Handbook of organic materials for optical and (opto)electronic devices: Properties and applications - Chapter 18 - Organic light-emitting diodes (OLEDs)* (Woodhead Publishing, Cambridge), 1st edition (2013).
- [78] K. A. Neyts, "Simulation of light emission from thin-film microcavities", *Journal of the Optical Society of America A* **15**, 962 (1998).
- [79] H. Benisty, R. Stanley, and M. Mayer, "Method of source terms for dipole emission modification in modes of arbitrary planar structures", *Journal of the Optical Society of America A* **15**, 1192 (1998).
- [80] M. Furno, R. Meerheim, S. Hofmann, B. Lüssem, and K. Leo, "Efficiency and rate of spontaneous emission in organic electroluminescent devices", *Physical Review B* **85**, 115205 (2012).
- [81] T. C. Rosenow, M. Furno, S. Reineke, S. Olthof, B. Lüssem, and K. Leo, "Highly efficient white organic light-emitting diodes based on fluorescent blue emitters", *Journal of Applied Physics* **108**, 113113 (2010).
- [82] H. Uoyama, K. Goushi, K. Shizu, H. Nomura, and C. Adachi, "Highly efficient organic light-emitting diodes from delayed fluorescence." *Nature* **492**, 234 (2012).
- [83] C. Rothe, C.-J. Chiang, V. Jankus, K. Abdullah, X. Zeng, R. Jitchati, A. S. Batsanov, M. R. Bryce, and A. P. Monkman, "Ionic Iridium(III) Complexes with Bulky Side Groups for Use in Light Emitting Cells: Reduction of Concentration Quenching", *Advanced Functional Materials* **19**, 2038 (2009).

- [84] Y. Kawamura, J. Brooks, J. J. Brown, H. Sasabe, and C. Adachi, "Intermolecular Interaction and a Concentration-Quenching Mechanism of Phosphorescent Ir(III) Complexes in a Solid Film", *Physical Review Letters* **96**, 017404 (2006).
- [85] S.-J. Su, E. Gonmori, H. Sasabe, and J. Kido, "Highly Efficient Organic Blue-and White-Light-Emitting Devices Having a Carrier- and Exciton-Confining Structure for Reduced Efficiency Roll-Off", *Advanced Materials* **20**, 4189 (2008).
- [86] Y. Sun, N. C. Giebink, H. Kanno, B. Ma, M. E. Thompson, and S. R. Forrest, "Management of singlet and triplet excitons for efficient white organic light-emitting devices." *Nature* **440**, 908 (2006).
- [87] G. Schwartz, M. Pfeiffer, S. Reineke, K. Walzer, and K. Leo, "Harvesting Triplet Excitons from Fluorescent Blue Emitters in White Organic Light-Emitting Diodes", *Advanced Materials* **19**, 3672 (2007).
- [88] S. Hofmann, "Exciton Dynamics in White Organic Light-Emitting Diodes comprising Triplet Harvesting", Ph. d. thesis, TU Dresden (2012).
- [89] G. Schwartz, K. Fehse, M. Pfeiffer, K. Walzer, and K. Leo, "Highly efficient white organic light emitting diodes comprising an interlayer to separate fluorescent and phosphorescent regions", *Applied Physics Letters* **89**, 083509 (2006).
- [90] A. Endo, K. Sato, K. Yoshimura, T. Kai, A. Kawada, H. Miyazaki, and C. Adachi, "Efficient up-conversion of triplet excitons into a singlet state and its application for organic light emitting diodes", *Applied Physics Letters* **98**, 083302 (2011).
- [91] J. Huang, M. Pfeiffer, A. Werner, J. Blochwitz, K. Leo, and S. Liu, "Low-voltage organic electroluminescent devices using pin structures", *Applied Physics Letters* **80**, 139 (2002).
- [92] M. L. Tietze, L. Burtone, M. Riede, B. Lüssem, and K. Leo, "Fermi level shift and doping efficiency in p-doped small molecule organic semiconductors: A photoelectron spectroscopy and theoretical study", *Physical Review B* **86**, 035320 (2012).
- [93] Y. Cai, H. X. Wei, J. Li, Q. Y. Bao, X. Zhao, S. T. Lee, Y. Q. Li, and J. X. Tang, "Mechanism of Cs₂CO₃ as an n-type dopant in organic electron-transport film", *Applied Physics Letters* **98**, 113304 (2011).
- [94] J. Blochwitz, T. Fritz, M. Pfeiffer, K. Leo, D. M. Alloway, P. A. Lee, and N. R. Armstrong, "Interface electronic structure of organic semiconductors with controlled doping levels", *Organic Electronics* **2**, 97 (2001).
- [95] T. Matsushima, Y. Kinoshita, and H. Murata, "Formation of Ohmic hole injection by inserting an ultrathin layer of molybdenum trioxide between indium tin oxide and organic hole-transporting layers", *Applied Physics Letters* **91**, 253504 (2007).
- [96] J. Meyer, A. Shu, M. Kröger, and A. Kahn, "Effect of contamination on the electronic structure and hole-injection properties of MoO₃/organic semiconductor interfaces", *Applied Physics Letters* **96**, 133308 (2010).

- [97] M. Kröger, S. Hamwi, J. Meyer, T. Riedl, W. Kowalsky, and A. Kahn, “Role of the deep-lying electronic states of MoO₃ in the enhancement of hole-injection in organic thin films”, *Applied Physics Letters* **95**, 123301 (2009).
- [98] Z. B. Wang, M. G. Helander, J. Qiu, D. P. Puzzo, M. T. Greiner, Z. W. Liu, and Z. H. Lu, “Highly simplified phosphorescent organic light emitting diode with 20% external quantum efficiency at 10.000 cd/m²”, *Applied Physics Letters* **98**, 073310 (2011).
- [99] K. Harada, A. Werner, M. Pfeiffer, C. Bloom, C. Elliott, and K. Leo, “Organic Homojunction Diodes with a High Built-in Potential: Interpretation of the Current-Voltage Characteristics by a Generalized Einstein Relation”, *Physical Review Letters* **94**, 036601 (2005).
- [100] W. S. Jeon, T. J. Park, K. H. Kim, R. Pode, J. Jang, and J. H. Kwon, “High efficiency red phosphorescent organic light-emitting diodes with single layer structure”, *Organic Electronics* **11**, 179 (2010).
- [101] C. W. Joo, S. O. Jeon, K. S. Yook, and J. Y. Lee, “Red phosphorescent organic light-emitting diodes with indium tin oxide/single organic layer/Al simple device structure”, *Organic Electronics* **11**, 36 (2010).
- [102] C. Yun, G. Xie, C. Murawski, J. Lee, F. Ventsch, K. Leo, and M. C. Gather, “Understanding the influence of doping in efficient phosphorescent organic light-emitting diodes with an organic p-i-n homojunction”, *Organic Electronics* **14**, 1695 (2013).
- [103] Z. B. Wang, M. G. Helander, J. Qiu, D. P. Puzzo, M. T. Greiner, Z. M. Hudson, S. Wang, Z. W. Liu, and Z. H. Lu, “Unlocking the full potential of organic light-emitting diodes on flexible plastic”, *Nature Photonics* **5**, 753 (2011).
- [104] G. Schwartz, S. Reineke, T. C. Rosenow, K. Walzer, and K. Leo, “Triplet Harvesting in Hybrid White Organic Light-Emitting Diodes”, *Advanced Functional Materials* **19**, 1319 (2009).
- [105] W. Gaynor, S. Hofmann, M. G. Christoforo, C. Sachse, S. Mehra, A. Salleo, M. D. McGehee, M. C. Gather, B. Lüssem, L. Müller-Meskamp, P. Peumans, and K. Leo, “Color in the Corners: ITO-Free White OLEDs with Angular Color Stability.” *Advanced Materials* **25**, 4006 (2013).
- [106] C. G. Granqvist, “Transparent conductors as solar energy materials: A panoramic review”, *Solar Energy Materials and Solar Cells* **91**, 1529 (2007).
- [107] L. S. Sapochak, A. B. Padmaperuma, X. Cai, J. L. Male, and P. E. Burrows, “Inductive Effects of Diphenylphosphoryl Moieties on Carbazole Host Materials: Design Rules for Blue Electrophosphorescent Organic Light-Emitting Devices”, *Journal of Physical Chemistry C* **112**, 7989 (2008).
- [108] G. Parthasarathy, P. E. Burrows, V. Khalfin, V. G. Kozlov, and S. R. Forrest, “A metal-free cathode for organic semiconductor devices”, *Applied Physics Letters* **72**, 2138 (1998).

- [109] H. Schmidt, H. Flügge, T. Winkler, T. Bülow, T. Riedl, and W. Kowalsky, “Efficient semitransparent inverted organic solar cells with indium tin oxide top electrode”, *Applied Physics Letters* **94**, 243302 (2009).
- [110] G. Gu, B. V., P. E. Burrows, S. R. Forrest, and M. E. Thompson, “Transparent organic light emitting devices”, *Applied Physics Letters* **68**, 2606 (1996).
- [111] H. Kim, C. M. Gilmore, A. Pique, J. S. Horwitz, H. Mattoussi, H. Murata, Z. H. Kafafi, and D. B. Chrisey, “Electrical, optical, and structural properties of indium–tin–oxide thin films for organic light-emitting devices”, *Journal of Applied Physics* **86**, 6451 (1999).
- [112] R. Joshi, V. Singh, and J. McClure, “Characteristics of indium tin oxide films deposited by r.f. magnetron sputtering”, *Thin Solid Films* **257**, 32 (1995).
- [113] W. G. Haines and R. H. Bube, “Effects of heat treatment on the optical and electrical properties of indium–tin oxide films”, *Journal of Applied Physics* **49**, 304 (1978).
- [114] H. Kanno, Y. Sun, and S. R. Forrest, “High-efficiency top-emissive white-light-emitting organic electrophosphorescent devices”, *Applied Physics Letters* **86**, 263502 (2005).
- [115] L. Groenendaal, F. Jonas, D. Freitag, H. Pielartzik, and J. R. Reynolds, “Poly(3,4-ethylenedioxythiophene) and Its Derivatives: Past, Present, and Future”, *Advanced Materials* **12**, 481 (2000).
- [116] D. Zhang, K. Ryu, X. Liu, E. Polikarpov, J. Ly, M. E. Tompson, and C. Zhou, “Transparent, conductive, and flexible carbon nanotube films and their application in organic light-emitting diodes.” *Nano Letters* **6**, 1880 (2006).
- [117] G. Gruner, “Carbon nanotube films for transparent and plastic electronics”, *Journal of Materials Chemistry* **16**, 3533 (2006).
- [118] J. Wu, M. Agrawal, H. A. Becerril, Z. Bao, Z. Liu, Y. Chen, and P. Peumans, “Organic light-emitting diodes on solution-processed graphene transparent electrodes.” *ACS Nano* **4**, 43 (2010).
- [119] S. Bae, H. Kim, Y. Lee, X. Xu, J.-S. Park, Y. Zheng, J. Balakrishnan, T. Lei, H. R. Kim, Y. I. Song, Y.-J. Kim, K. S. Kim, B. Ozyilmaz, J.-H. Ahn, B. H. Hong, and S. Iijima, “Roll-to-roll production of 30-inch graphene films for transparent electrodes.” *Nature Nanotechnology* **5**, 574 (2010).
- [120] T.-H. Han, Y. Lee, M.-R. Choi, S.-H. Woo, S.-H. Bae, B. H. Hong, J.-H. Ahn, and T.-W. Lee, “Extremely efficient flexible organic light-emitting diodes with modified graphene anode”, *Nature Photonics* **6**, 105 (2012).
- [121] X. Li, W. Cai, J. An, S. Kim, J. Nah, D. Yang, R. Piner, A. Velamakanni, I. Jung, E. Tutuc, S. K. Banerjee, L. Colombo, and R. S. Ruoff, “Large-area synthesis of high-quality and uniform graphene films on copper foils.” *Science* **324**, 1312 (2009).

Bibliography

- [122] J. S. Bunch, S. S. Verbridge, J. S. Alden, A. M. van der Zande, J. M. Parpia, H. G. Craighead, and P. L. McEuen, “Impermeable atomic membranes from graphene sheets.” *Nano Letters* **8**, 2458 (2008).
- [123] F. Ostermaier and M. Mertig, “Sorting of CVD-grown single-walled carbon nanotubes by means of gel column chromatography”, *Physica Status Solidi (b)* **250**, 2564 (2013).
- [124] M. Thomschke, R. Nitsche, M. Furno, and K. Leo, “Optimized efficiency and angular emission characteristics of white top-emitting organic electroluminescent diodes”, *Applied Physics Letters* **94**, 083303 (2009).
- [125] P. Freitag, S. Reineke, S. Olthof, M. Furno, B. Lüssem, and K. Leo, “White top-emitting organic light-emitting diodes with forward directed emission and high color quality”, *Organic Electronics* **11**, 1676 (2010).
- [126] Commission Internationale de l’Éclairage, *Proceedings 1931* (Cambridge University Press., Cambridge) (1932).
- [127] R. W. G. Hunt, *The Reproduction of Colour* (John Wiley & Sons, Ltd, West Sussex), 6th edition (2004).
- [128] F. Grum, *Radiometry* (Academic Press, New York), 1st edition (1979).
- [129] W. L. Wolfe, *Introduction to Radiometry* (SPIE - The International Society for Optical Engineering, Bellingham) (1998).
- [130] T. Smith and J. Guild, “The C.I.E. colorimetric standards and their use”, *Transactions of the Optical Society* **33**, 73 (1931).
- [131] W. D. Wright, “The sensitivity of the eye to small colour differences”, *Proceedings of the Physical Society* **53**, 93 (1941).
- [132] D. L. MacAdam, “Visual Sensitivities to Color Differences in Daylight”, *Journal of the Optical Society of America* **32**, 247 (1942).
- [133] D. L. MacAdam, “Projective Transformations of I.C.I Color Specifications”, *Journal of the Optical Society of America* **27**, 294 (1937).
- [134] Commission Internationale de l’Éclairage, *Method of Measuring and Specifying Colour Rendering Properties of Light Sources* (CIE Central Bureau, Vienna) (1995).
- [135] W. Davis and Y. Ohno, “Color quality scale”, *Optical Engineering* **49**, 033602 (2010).
- [136] M. R. Luo, G. Cui, and B. Rigg, “The development of the CIE 2000 colour-difference formula: CIEDE2000”, *Color Research & Application* **26**, 340 (2001).
- [137] P. Freitag, A. A. Zakhidov, B. Lüssem, and K. Leo, “Lambertian white top-emitting organic light emitting device with carbon nanotube cathode”, *Journal of Applied Physics* **112**, 114505 (2012).

- [138] H. Peng, J. Sun, X. Zhu, X. Yu, M. Wong, and H.-S. Kwok, “High-efficiency microcavity top-emitting organic light-emitting diodes using silver anode”, *Applied Physics Letters* **88**, 073517 (2006).
- [139] X. Zhou, M. Pfeiffer, J. S. Huang, J. Blochwitz-Nimoth, D. S. Qin, A. Werner, J. Drechsel, B. Maennig, and K. Leo, “Low-voltage inverted transparent vacuum deposited organic light-emitting diodes using electrical doping”, *Applied Physics Letters* **81**, 922 (2002).
- [140] C.-W. Chen, C.-L. Lin, and C.-C. Wu, “An effective cathode structure for inverted top-emitting organic light-emitting devices”, *Applied Physics Letters* **85**, 2469 (2004).
- [141] S. A. Maier, *Plasmonics: Fundamentals and Applications* (Springer, New York), 1st edition (2007).
- [142] W. Nolting, *Grundkurs Theoretische Physik 3 - Elektrodynamik* (Springer, Berlin Heidelberg), 7th edition (2004).
- [143] C. C. Katsidis and D. I. Siapkas, “General Transfer-Matrix Method for Optical Multilayer Systems with Coherent, Partially Coherent, and Incoherent Interference”, *Applied Optics* **41**, 3978 (2002).
- [144] H. Becker, S. E. Burns, N. Tessler, and R. H. Friend, “Role of optical properties of metallic mirrors in microcavity structures”, *Journal of Applied Physics* **81**, 2825 (1997).
- [145] A. D. Rakic, A. B. Djurišić, J. M. Elazar, and M. L. Majewski, “Optical Properties of Metallic Films for Vertical-Cavity Optoelectronic Devices”, *Applied Optics* **37**, 5271 (1998).
- [146] F. Ma and X. Liu, “Phase shift and penetration depth of metal mirrors in a microcavity structure”, *Applied Optics* **46**, 6247 (2007).
- [147] D. Deppe, C. Lei, C. Lin, and D. Huffaker, “Spontaneous Emission from Planar Microstructures”, *Journal of Modern Optics* **41**, 325 (1994).
- [148] E. F. Schubert, N. E. Hunt, M. Micovic, R. J. Malik, D. L. Sivco, A. Y. Cho, and G. J. Zydzik, “Highly efficient light-emitting diodes with microcavities.” *Science* **265**, 943 (1994).
- [149] W. L. Barnes, “Fluorescence near interfaces: the role of photonic mode density”, *Journal of Modern Optics* **45**, 661 (1998).
- [150] W. Brütting, J. Frischeisen, T. D. Schmidt, B. J. Scholz, and C. Mayr, “Device efficiency of organic light-emitting diodes: Progress by improved light outcoupling”, *Physica Status Solidi (a)* **210**, 44 (2013).
- [151] Q. Huang, S. Reineke, K. Walzer, M. Pfeiffer, and K. Leo, “Quantum efficiency enhancement in top-emitting organic light-emitting diodes as a result of enhanced intrinsic quantum yield”, *Applied Physics Letters* **89**, 263512 (2006).

- [152] R. B. Pode, C. J. Lee, D. G. Moon, and J. I. Han, “Transparent conducting metal electrode for top emission organic light-emitting devices: Ca–Ag double layer”, *Applied Physics Letters* **84**, 4614 (2004).
- [153] T. Schwab, S. Schubert, L. Müller-Meskamp, K. Leo, and M. C. Gather, “Eliminating Micro-Cavity Effects in White Top-Emitting OLEDs by Ultra-Thin Metallic Top Electrodes”, *Advanced Optical Materials* **1**, 921 (2013).
- [154] T. Schwab, S. Schubert, S. Hofmann, M. Fröbel, C. Fuchs, M. Thomschke, L. Müller-Meskamp, K. Leo, and M. C. Gather, “Highly Efficient and Color Stable Inverted White Top-emitting OLEDs with Ultra-thin Wetting Layer Top Electrodes”, *Advanced Optical Materials* **1**, 707 (2013).
- [155] S. Chen and H.-S. Kwok, “Alleviate microcavity effects in top-emitting white organic light-emitting diodes for achieving broadband and high color rendition emission spectra”, *Organic Electronics* **12**, 2065 (2011).
- [156] H. Riel, S. Karg, T. Beierlein, B. Ruhstaller, and W. Rieß, “Phosphorescent top-emitting organic light-emitting devices with improved light outcoupling”, *Applied Physics Letters* **82**, 466 (2003).
- [157] T. Feng, T. A. Ali, E. S. Ramakrishnan, R. A. Campos, and W. E. Howard, “Structure and characterization of a white up-emitting OLED on silicon for microdisplays”, *Proceedings of SPIE* **4105**, 30 (2001).
- [158] S.-F. Hsu, C.-C. Lee, S.-W. Hwang, and C. H. Chen, “Highly efficient top-emitting white organic electroluminescent devices”, *Applied Physics Letters* **86**, 253508 (2005).
- [159] P. L. Clegg, “The Optical Constants of Thin Metallic Films Deposited by Evaporation”, *Proceedings of the Physical Society. Section B* **65**, 774 (1952).
- [160] X.-W. Chen, W. C. H. Choy, S. He, and P. C. Chui, “Comprehensive analysis and optimal design of top-emitting organic light-emitting devices”, *Journal of Applied Physics* **101**, 113107 (2007).
- [161] Q. Wang, Z. Deng, and D. Ma, “Realization of high efficiency microcavity top-emitting organic light-emitting diodes with highly saturated colors and negligible angular dependence”, *Applied Physics Letters* **94**, 233306 (2009).
- [162] D.-G. Moon, C.-J. Lee, and J.-I. Han, “Top emission organic light-emitting devices with CsCl capping layer”, *Thin Solid Films* **518**, 2793 (2010).
- [163] C. J. Lee, R. B. Pode, J. I. Han, and D. G. Moon, “Green top-emitting organic light emitting device with transparent Ba Ag bilayer cathode”, *Applied Physics Letters* **89**, 123501 (2006).
- [164] W. Ji, L. Zhang, M. Liu, J. Wang, G. Liu, W. Xie, and H. Zhang, “High efficiency top-emitting white organic light-emitting devices with a (metal/organic)² cathode”, *Current Applied Physics* **11**, 1410 (2011).

- [165] M. Zadsar, H. R. Fallah, M. H. Mahmoodzadeh, and S. V. Tabatabaei, “The effect of Ag layer thickness on the properties of WO₃/Ag/MoO₃ multilayer films as anode in organic light emitting diodes”, *Journal of Luminescence* **132**, 992 (2012).
- [166] R. Meerheim, R. Nitsche, and K. Leo, “High-efficiency monochrome organic light emitting diodes employing enhanced microcavities”, *Applied Physics Letters* **93**, 043310 (2008).
- [167] X. Zhu, J. Sun, X. Yu, M. Wong, and H.-S. Kwok, “High-Performance Top-Emitting White Organic Light-Emitting Devices”, *Japanese Journal of Applied Physics* **46**, 4054 (2007).
- [168] G. Xie, Z. Zhang, Q. Xue, S. Zhang, L. Zhao, Y. Luo, P. Chen, B. Quan, Y. Zhao, and S. Liu, “Highly efficient top-emitting white organic light-emitting diodes with improved contrast and reduced angular dependence for active matrix displays”, *Organic Electronics* **11**, 2055 (2010).
- [169] Q. Wang, Y. Chen, J. Chen, and D. Ma, “White top-emitting organic light-emitting diodes employing tandem structure”, *Applied Physics Letters* **101**, 133302 (2012).
- [170] S. Hofmann, M. Thomschke, B. Lüssem, and K. Leo, “Top-emitting organic light-emitting diodes”, *Optics Express* **19**, A1250 (2011).
- [171] H. Raether, *Surface Plasmons on Smooth and Rough Surfaces and on Gratings* (Springer, Berlin Heidelberg), 1st edition (1988).
- [172] J. M. Pitarke, V. M. Silkin, E. V. Chulkov, and P. M. Echenique, “Theory of surface plasmons and surface-plasmon polaritons”, *Reports on Progress in Physics* **70**, 1 (2007).
- [173] J. Burke, G. Stegeman, and T. Tamir, “Surface-polariton-like waves guided by thin, lossy metal films”, *Physical Review B* **33**, 5186 (1986).
- [174] E. Economou, “Surface Plasmons in Thin Films”, *Physical Review* **182**, 539 (1969).
- [175] P. Berini, “Plasmon-polariton waves guided by thin lossy metal films of finite width: Bound modes of symmetric structures”, *Physical Review B* **61**, 10484 (2000).
- [176] K. H. An, M. Shtein, and K. P. Pipe, “Surface plasmon mediated energy transfer of electrically-pumped excitons”, *Optics Express* **18**, 4041 (2010).
- [177] W. L. Barnes, A. Dereux, and T. W. Ebbesen, “Surface plasmon subwavelength optics.” *Nature* **424**, 824 (2003).
- [178] K. A. Willets and R. P. Van Duyne, “Localized surface plasmon resonance spectroscopy and sensing.” *Annual Review of Physical Chemistry* **58**, 267 (2007).
- [179] L. J. Sherry, S.-H. Chang, G. C. Schatz, R. P. Van Duyne, B. J. Wiley, and Y. Xia, “Localized surface plasmon resonance spectroscopy of single silver nanocubes.” *Nano Letters* **5**, 2034 (2005).

- [180] K. M. Mayer and J. H. Hafner, “Localized surface plasmon resonance sensors.” *Chemical Reviews* **111**, 3828 (2011).
- [181] T. D. Schmidt, D. S. Setz, M. Flämmich, J. Frischeisen, D. Michaelis, B. C. Krummacher, N. Danz, and W. Brütting, “Evidence for non-isotropic emitter orientation in a red phosphorescent organic light-emitting diode and its implications for determining the emitter’s radiative quantum efficiency”, *Applied Physics Letters* **99**, 163302 (2011).
- [182] M. Thomschke, S. Reineke, B. Lüssem, and K. Leo, “Highly efficient white top-emitting organic light-emitting diodes comprising laminated microlens films.” *Nano Letters* **12**, 424 (2012).
- [183] H.-W. Chang, J. Lee, S. Hofmann, Y. Hyun Kim, L. Müller-Meskamp, B. Lüssem, C.-C. Wu, K. Leo, and M. C. Gather, “Nano-particle based scattering layers for optical efficiency enhancement of organic light-emitting diodes and organic solar cells”, *Journal of Applied Physics* **113**, 204502 (2013).
- [184] T. W. Canzler, S. Murano, D. Pavicic, O. Fadhel, C. Rothe, A. Haldi, M. Hofmann, and Q. Huang, “Efficiency Enhancement in White PIN OLEDs by Simple Internal Outcoupling Methods”, *SID Symposium Digest of Technical Papers* **42**, 975 (2011).
- [185] A. A. Zakhidov, J.-K. Lee, J. A. DeFranco, H. H. Fong, P. G. Taylor, M. Chatzichristidi, C. K. Ober, and G. G. Malliaras, “Orthogonal processing: A new strategy for organic electronics”, *Chemical Science* **2**, 1178 (2011).
- [186] P. Liehm, C. Murawski, M. Furno, B. Lüssem, K. Leo, and M. C. Gather, “Comparing the emissive dipole orientation of two similar phosphorescent green emitter molecules in highly efficient organic light-emitting diodes”, *Applied Physics Letters* **101**, 253304 (2012).
- [187] M. Flämmich, J. Frischeisen, D. S. Setz, D. Michaelis, B. C. Krummacher, T. D. Schmidt, W. Brütting, and N. Danz, “Oriented phosphorescent emitters boost OLED efficiency”, *Organic Electronics* **12**, 1663 (2011).
- [188] K. Saxena, V. Jain, and D. S. Mehta, “A review on the light extraction techniques in organic electroluminescent devices”, *Optical Materials* **32**, 221–233 (2009).
- [189] N. W. Ashcroft and N. D. Mermin, *Festkörperphysik* (Oldenbourg Verlag, München), 3rd edition (2007).
- [190] H. Rigneault, F. Lemarchand, and A. Sentenac, “Dipole radiation into grating structures”, *Journal of the Optical Society of America A* **17**, 1048 (2000).
- [191] H. Peng, Y. Ho, X.-J. Yu, M. Wong, and H.-S. Kwok, “Coupling Efficiency Enhancement in Organic Light-Emitting Devices Using Microlens Array—Theory and Experiment”, *Journal of Display Technology* **1**, 278 (2005).
- [192] H. J. Peng, Y. L. Ho, X. J. Yu, and H. S. Kwok, “Enhanced coupling of light from organic light emitting diodes using nanoporous films”, *Journal of Applied Physics* **96**, 1649 (2004).

- [193] B. Riedel, J. Hauss, M. Aichholz, A. Gall, U. Lemmer, and M. Gerken, “Polymer light emitting diodes containing nanoparticle clusters for improved efficiency”, *Organic Electronics* **11**, 1172 (2010).
- [194] W. H. Koo, W. Youn, P. Zhu, X.-H. Li, N. Tansu, and F. So, “Light Extraction of Organic Light Emitting Diodes by Defective Hexagonal-Close-Packed Array”, *Advanced Functional Materials* **22**, 3454 (2012).
- [195] J. Zhou, N. Ai, L. Wang, H. Zheng, C. Luo, Z. Jiang, S. Yu, Y. Cao, and J. Wang, “Roughening the white OLED substrate’s surface through sandblasting to improve the external quantum efficiency”, *Organic Electronics* **12**, 648 (2011).
- [196] F. Galeotti, W. Mróz, G. Scavia, and C. Botta, “Microlens arrays for light extraction enhancement in organic light-emitting diodes: A facile approach”, *Organic Electronics* **14**, 212 (2013).
- [197] C.-H. Chang, K.-Y. Chang, Y.-J. Lo, S.-J. Chang, and H.-H. Chang, “Fourfold power efficiency improvement in organic light-emitting devices using an embedded nanocomposite scattering layer”, *Organic Electronics* **13**, 1073 (2012).
- [198] T. Bocksrocker, J. B. Preinfalk, J. Asche-Tauscher, A. Pargner, C. Eschenbaum, F. Maier-Flaig, and U. Lemmer, “White organic light emitting diodes with enhanced internal and external outcoupling for ultra-efficient light extraction and Lambertian emission.” *Optics Express* **20**, A932 (2012).
- [199] Y. Bai, J. Feng, Y.-F. Liu, J.-F. Song, J. Simonen, Y. Jin, Q.-D. Chen, J. Zi, and H.-B. Sun, “Outcoupling of trapped optical modes in organic light-emitting devices with one-step fabricated periodic corrugation by laser ablation”, *Organic Electronics* **12**, 1927 (2011).
- [200] J. M. Ziebarth, A. K. Saafir, S. Fan, and M. D. McGehee, “Extracting Light from Polymer Light-Emitting Diodes Using Stamped Bragg Gratings”, *Advanced Functional Materials* **14**, 451 (2004).
- [201] Y. Jin, J. Feng, X.-L. Zhang, Y.-G. Bi, Y. Bai, L. Chen, T. Lan, Y.-F. Liu, Q.-D. Chen, and H.-B. Sun, “Solving efficiency-stability tradeoff in top-emitting organic light-emitting devices by employing periodically corrugated metallic cathode.” *Advanced Materials* **24**, 1187 (2012).
- [202] S. Wedge and W. L. Barnes, “Surface plasmon-polariton mediated light emission through thin metal films.” *Optics Express* **12**, 3673 (2004).
- [203] J. Frischeisen, Q. Niu, A. Abdellah, J. B. Kinzel, R. Gehlhaar, G. Scarpa, C. Adachi, P. Lugli, and W. Brütting, “Light extraction from surface plasmons and waveguide modes in an organic light-emitting layer by nanoimprinted gratings.” *Optics Express* **19**, A7 (2011).
- [204] B. J. Scholz, J. Frischeisen, A. Jaeger, D. S. Setz, T. C. G. Reusch, and W. Brütting, “Extraction of surface plasmons in organic light-emitting diodes via high-index coupling”, *Optics Express* **20**, A205 (2012).

- [205] T. Nakanishi, T. Hiraoka, A. Fujimoto, S. Matake, S. Okutani, H. Sano, and K. Ashakawa, "Improvement of the light extraction efficiency of top-emitting organic light-emitting diodes by a two-dimensional diffraction layer fabricated using self-assembled nanoparticles", *Applied Optics* **48**, 5889 (2009).
- [206] Z. Wang, Z. Chen, L. Xiao, and Q. Gong, "Enhancement of top emission for organic light-emitting diode via scattering surface plasmons by nano-aggregated outcoupling layer", *Organic Electronics* **10**, 341 (2009).
- [207] C.-C. Liu, S.-H. Liu, K.-C. Tien, M.-H. Hsu, H.-W. Chang, C.-K. Chang, C.-J. Yang, and C.-C. Wu, "Microcavity top-emitting organic light-emitting devices integrated with diffusers for simultaneous enhancement of efficiencies and viewing characteristics", *Applied Physics Letters* **94**, 103302 (2009).
- [208] S. Olthof, "Photoelectron Spectroscopy on Doped Organic Semiconductors and Related Interfaces", Ph. d. thesis, TU Dresden (2010).
- [209] M. Thomschke, "Inverted Organic Light Emitting Diodes - Optical and Electrical Device Improvement", Ph. d. thesis, TU Dresden (2012).
- [210] G. Sharma, W. Wu, and E. N. Dalal, "The CIEDE2000 color-difference formula: Implementation notes, supplementary test data, and mathematical observations", *Color Research & Application* **30**, 21 (2005).
- [211] W. H. Press, S. A. Teukolsky, W. T. Vetterling, and B. P. Flannery, *Numerical Recipes* (Cambridge University Press., Cambridge), 3rd edition (2007).
- [212] F. M. Smits, "Measurement of Sheet Resistivities with the Four-Point Probe", *Bell System Technical Journal* **37**, 711 (1958).
- [213] D. S. Perloff, "Four-point sheet resistance correction factors for thin rectangular samples", *Solid-State Electronics* **20**, 681 (1977).
- [214] H. Seiler, "Secondary electron emission in the scanning electron microscope", *Journal of Applied Physics* **54**, R1 (1983).
- [215] G. Kammlott, "Some aspects of scanning electron microscopy", *Surface Science* **25**, 120 (1971).
- [216] G. Binnig and C. F. Quate, "Atomic Force Microscope", *Physical Review Letters* **56**, 930 (1986).
- [217] Q. Zhong, D. Inniss, K. Kjoller, and V. Elings, "Fractured polymer/silica fiber surface studied by tapping mode atomic force microscopy", *Surface Science* **290**, L688 (1993).
- [218] F. J. Giessibl, "Advances in atomic force microscopy", *Reviews of Modern Physics* **75**, 949 (2003).
- [219] R. S. Sennett and G. D. Scott, "The Structure of Evaporated Metal Films and Their Optical Properties", *Journal of the Optical Society of America* **40**, 203 (1950).

- [220] C. T. Campbell, “Ultrathin metal films and particles on oxide surfaces: structural, electronic and chemisorptive properties”, *Surface Science Reports* **27**, 1 (1997).
- [221] W. Kleber, H.-J. Bautsch, and J. Bohm, *Einführung in die Kristallographie*, vol. 18 (Oldenbourg Verlag, München), 18th edition (1998).
- [222] S. H. Overbury, P. A. Bertrand, and G. A. Somorjai, “Surface composition of binary systems. Prediction of surface phase diagrams of solid solutions”, *Chemical Reviews* **75**, 547 (1975).
- [223] S. Olthof, J. Meiss, B. Lüsse, M. Riede, and K. Leo, “Photoelectron spectroscopy investigation of thin metal films employed as top contacts in transparent organic solar cells”, *Thin Solid Films* **519**, 1872 (2011).
- [224] S. Schubert, J. Meiss, L. Müller-Meskamp, and K. Leo, “Improvement of Transparent Metal Top Electrodes for Organic Solar Cells by Introducing a High Surface Energy Seed Layer”, *Advanced Energy Materials* **3**, 438 (2013).
- [225] S. Schubert, M. Hermenau, J. Meiss, L. Müller-Meskamp, and K. Leo, “Oxide Sandwiched Metal Thin-Film Electrodes for Long-Term Stable Organic Solar Cells”, *Advanced Functional Materials* **22**, 4993 (2012).
- [226] S. E. Roark and K. L. Rowlen, “Thin silver films: influence of substrate and post-deposition treatment on morphology and optical properties”, *Analytical Chemistry* **66**, 261 (1994).
- [227] S. Y. Kim, D. G. Moon, C. J. Lee, and J. I. Han, “Sr/Ag semitransparent cathodes for top emission organic light-emitting devices”, *Thin Solid Films* **517**, 2035 (2009).
- [228] W. Xie, K. Lau, C. Lee, and S. Lee, “Transparent organic light-emitting devices with LiF/Yb:Ag cathode”, *Thin Solid Films* **515**, 6975 (2007).
- [229] K. Hong, J. H. Son, S. Kim, B. H. Koo, and J.-L. Lee, “Design rules for highly transparent electrodes using dielectric constant matching of metal oxide with Ag film in optoelectronic devices.” *Chemical Communications* **48**, 10606 (2012).
- [230] H. Cho, J.-M. Choi, and S. Yoo, “Highly transparent organic light-emitting diodes with a metallic top electrode: the dual role of a Cs₂CO₃ layer.” *Optics Express* **19**, 1113 (2011).
- [231] J. C. M. Garnett, “Colours in Metal Glasses and in Metallic Films”, *Philosophical Transactions of the Royal Society A: Mathematical, Physical and Engineering Sciences* **203**, 385 (1904).
- [232] G. Gu and S. R. Forrest, “Design of Flat-Panel Displays Based on Organic Light-Emitting Devices”, *IEEE Journal of Selected Topics in Quantum Electronics* **4**, 83 (1998).
- [233] R. Meerheim, K. Walzer, M. Pfeiffer, and K. Leo, “Ultrastable and efficient red organic light emitting diodes with doped transport layers”, *Applied Physics Letters* **89**, 061111 (2006).

- [234] T. C. Rosenow, “White Organic Light Emitting Diodes”, Ph. d. thesis, TU Dresden (2010).
- [235] Y. H. Kim, J. Lee, S. Hofmann, M. C. Gather, L. Müller-Meskamp, and K. Leo, “Achieving High Efficiency and Improved Stability in ITO-Free Transparent Organic Light-Emitting Diodes with Conductive Polymer Electrodes”, *Advanced Functional Materials* **23**, 3763 (2013).
- [236] P. Görrn, M. Sander, J. Meyer, M. Kröger, E. Becker, H.-H. Johannes, W. Kowalsky, and T. Riedl, “Towards See-Through Displays: Fully Transparent Thin-Film Transistors Driving Transparent Organic Light-Emitting Diodes”, *Advanced Materials* **18**, 738 (2006).
- [237] S. C. Xia, R. C. Kwong, V. I. Adamovich, M. S. Weaver, and J. J. Brown, “OLED Device Operational Lifetime: Insights and Challenges”, *2007 IEEE International Reliability Physics Symposium Proceedings*. **45**, 253 (2007).
- [238] J. Hauss, T. Bocksrocker, B. Riedel, U. Lemmer, and M. Gerken, “On the interplay of waveguide modes and leaky modes in corrugated OLEDs”, *Optics Express* **19**, A851 (2011).
- [239] C. Fuchs, T. Schwab, T. Roch, S. Eckardt, A. Lasagni, S. Hofmann, B. Lüssem, L. Müller-Meskamp, K. Leo, M. C. Gather, and R. Scholz, “Quantitative allocation of Bragg scattering effects in highly efficient OLEDs fabricated on periodically corrugated substrates”, *Optics Express* **21**, 16319 (2013).
- [240] Y.-G. Bi, J. Feng, Y.-F. Li, Y. Jin, Y.-F. Liu, Q.-D. Chen, and H.-B. Sun, “Enhanced efficiency of organic light-emitting devices with metallic electrodes by integrating periodically corrugated structure”, *Applied Physics Letters* **100**, 053304 (2012).
- [241] P. Freitag, “White Top-Emitting OLEDs on Metal Substrates”, Ph. d. thesis, TU Dresden (2010).
- [242] C. Weisbuch, M. Nishioka, A. Ishikawa, and Y. Arakawa, “Observation of the coupled exciton-photon mode splitting in a semiconductor quantum microcavity”, *Phys. Rev. Lett.* **69**, 3314 (1992).
- [243] R. Holmes and S. R. Forrest, “Strong exciton–photon coupling in organic materials”, *Organic Electronics* **8**, 77 (2007).
- [244] M. S. Skolnick, T. A. Fisher, and D. M. Whittaker, “Strong coupling phenomena in quantum microcavity structures”, *Semiconductor Science and Technology* **13**, 645 (1998).
- [245] D. G. Lidzey, D. D. C. Bradley, M. S. Skolnick, T. Virgili, S. Walker, and D. M. Whittaker, “Strong exciton-photon coupling in an organic semiconductor microcavity”, *Nature* **395**, 53 (1998).

- [246] R. Brückner, M. Sudzius, S. I. Hintschich, H. Fröb, V. G. Lyssenko, and K. Leo, “Hybrid optical Tamm states in a planar dielectric microcavity”, *Physical Review B* **83**, 033405 (2011).
- [247] H.-C. Zhou, G. Yang, K. Wang, H. Long, and P.-X. Lu, “Coupled Optical Tamm States in a Planar Dielectric Mirror Structure Containing a Thin Metal Film”, *Chinese Physics Letters* **29**, 067101 (2012).
- [248] M. Kaliteevski, I. Iorsh, S. Brand, R. Abram, J. Chamberlain, A. Kavokin, and I. Shelykh, “Tamm plasmon-polaritons: Possible electromagnetic states at the interface of a metal and a dielectric Bragg mirror”, *Physical Review B* **76**, 165415 (2007).
- [249] M. Kaliteevski, S. Brand, R. A. Abram, I. Iorsh, A. V. Kavokin, and I. A. Shelykh, “Hybrid states of Tamm plasmons and exciton polaritons”, *Applied Physics Letters* **95**, 251108 (2009).
- [250] R. Brückner, “Coherence and Coupling of Cavity Photons and Tamm Plasmons in Metal-Organic Microcavities”, Ph.D. thesis, TU Dresden (2012).
- [251] T. Schwab, C. Fuchs, R. Scholz, A. Zakhidov, K. Leo, and M. C. Gather, “Coherent mode coupling in highly efficient top-emitting OLEDs on periodically corrugated substrates”, *Optics Express* **22**, 7524 (2014).
- [252] K. J. Vahala, “Optical microcavities.” *Nature* **424**, 839 (2003).
- [253] M. Fröbel, T. Schwab, M. Kliem, S. Hofmann, K. Leo, and M. C. Gather, “AC/DC OLEDs: A new Concept for Color-tunable and White Light Sources”, *in preparation* (2014).
- [254] T. Schaefer, “Investigation of Light Scattering Nanoparticles in Top-Emitting Organic Light-Emitting Diodes”, Diploma thesis, TU Dresden (2014).
- [255] G.-T. Chen, S.-H. Su, C.-C. Hou, and M. Yokoyama, “Effects of Thermal Annealing on Performance of Organic Light-Emitting Diodes”, *Journal of The Electrochemical Society* **154**, J159 (2007).
- [256] J. X. Sun, X. L. Zhu, X. Yu, H. J. Peng, M. Wong, and H. S. Kwok, “Improving the Performance of Organic Light-Emitting Diodes Containing BCP/LiF/Al by Thermal Annealing”, *Journal of Display Technology* **2**, 138 (2006).
- [257] P. Nagpal, N. C. Lindquist, S.-H. Oh, and D. J. Norris, “Ultrasoother patterned metals for plasmonics and metamaterials.” *Science* **325**, 594 (2009).
- [258] T. Kingetsu, Y. Kamada, and M. Yamamoto, “Dependence of Al layer growth mode on Cr underlayer thickness in molecular-beam epitaxy of (001) Al/Cr superlattices”, *Journal of Applied Physics* **88**, 1838 (2000).
- [259] F. Marty, L. Rousseau, B. Saadany, B. Mercier, O. Français, Y. Mita, and T. Bourouina, “Advanced etching of silicon based on deep reactive ion etching for silicon high aspect ratio microstructures and three-dimensional micro- and nanostructures”, *Microelectronics Journal* **36**, 673 (2005).

Bibliography

List of Abbreviations

AFM	atomic force microscopy
a.u.	arbitrary unit
CAP	capping layer
CIE	Commission Internationale de l'Éclairage
CRI	color rendering index
DOS	density of states
EBL	electron blocking layer
EL	electroluminescent
EML	emission layer
EQE	external quantum efficiency
ETL	electron transport layer
eV	electron volt
FT	Fourier transformation
FWHM	full width at half maximum
HBL	hole blocking layer
HOMO	highest occupied molecular orbital
HTL	hole transport layer
IAPP	Institut für Angewandte Photophysik, TU Dresden
IQE	internal quantum efficiency
IVL	current-voltage-luminance
LE	luminous efficacy
LSP	localized surface plasmon polariton
LUMO	lowest unoccupied molecular orbital
OLED	organic light-emitting diode
PL	photoluminescence
R2R	roll-to-roll
SEM	scanning electron microscopy
SPP	surface plasmon polariton
TADF	thermally activated delayed fluorescence
TCO	transparent conductive oxide
TE	transversal electric
TM	transversal magnetic
UV	ultraviolet spectral range
WG	waveguided mode
wt.%	weight percent

List of Chemical Names

4P-NPD	N,N'-di-1-naphthalenyl-N,N'-diphenyl- [1,1':4',1'':4'',1''':4''',1''''-quaterphenyl]-4,4'''-diamine
Ag	silver
Al	aluminum
Au	gold
BAlq ₂	bis(2-methyl-8-quinolinolato)-4-(phenyl-phenolato)aluminum(III)
BPhen	4,7-diphenyl-1,10-phenanthroline
Ca	calcium
Cr	chromium
Cs	cesium
F6TCNNQ	2,2'-(perfluoronaphthalene-2,6-diylidene)-dimalononitrile
Ir(dhfp _y) ₂ (acac)	bis(2-(9,9-dihexylfluorenyl)-1-pyridine)(acetylacetonate)iridium(III)
Ir(MDQ) ₂ (acac)	bis(2-methyldibenzo-[f,h]chinoxaline)(acetylacetonate)iridium(III)
Ir(pp _y) ₃	tris(2-phenylpyridine)iridium(III)
ITO	tin-doped indium oxide
MADN	2-methyl-9,10-bis(naphthalene-2-yl)anthracene
MeO-TPD	N,N,N',N'-tetrakis(4-methoxyphenyl)-benzidine
MoO ₃	molybdenum trioxide
NPB	N,N'-di(naphthalene-1-yl)-N,N'-diphenyl-benzidine
PGMEA	propylene glycol monomethyl ether acetate
Spiro-TAD	2,2',7,7'-tetrakis-(N,N-diphenylamino)-9,9'-spirobifluorene
Spiro-TTB	2,2',7,7'-tetrakis-(N,N-di-methylphenylamino)-9,9'-spirobifluorene
TBPe	2,5,8,11-tetra-tert-butylperylene
TPBi	2,2',2''-(1,3,5-phenylene)tris(1-phenyl-1H-benzimidazol)
TCTA	4,4',4''-tris(carbazol-9-yl)-triphenylamine

Acknowledgements

My sincere thanks are dedicated to Prof. Dr. Karl Leo for the opportunity to work on this exciting and challenging topic and for the supervision of this work. His expertise and support allowed for great opportunities in the research on OLEDs in his group at the IAPP.

I gratefully acknowledge the expertise and the effort of Prof. Dr. Wolfgang Brütting in preparing the second review of this thesis.

I would like to thank all people who inspired my research with fruitful discussions and thus had an essential contribution to this thesis. Luckily, there are too many of you to explicitly mention every one, but be sure about my deep gratitude.

Moreover, I gratefully acknowledge the support of:

- Björn Lüssem, Malte C. Gather, and Simone Hofmann, the OLED group leaders who guided me throughout the years.
- Cornelius Fuchs and Reinhard Scholz for the theoretical input, the discussions, and contributions to the analysis of corrugated OLEDs.
- Sylvio Schubert for his work on the wetting layer electrode concept for organic solar cells and the continuous support in establishing this concept for OLEDs.
- Robert Brückner and Vadim Lyssenko for fruitful discussions on light mode interactions in microcavities.
- The “Lesker Team”: Tobias Günther, Caroline Walde, and Andreas Wendel for the accurate sample fabrication. Without your persistent work, a lot of blank pages would have appeared in this thesis.
- Elsa Tesmer, without her no grating structures would have been produced from photolithography.
- Alexander Zakhidov, Hans Kleemann, and Fabian Ventsch for their photolithography expertise.
- Vera Hoffmann and Ellen Hieckmann for their help with the SEM measurements.
- Tobias Mönch and Lars Müller-Meskamp for their expertise and assistance to handle the AFM tool.
- Wallace Choy, Benjamin Schumm, and Florian Wisser for providing the nanoimprint master stamps.

Acknowledgements

- Markus Fröbel for his continuous progress establishing the wetting layer electrodes in new OLED device concepts.
- Cornelius Fuchs and Markus Fröbel for their assistance in programming little helpers for data evaluation.
- The OLED group for their feedback in several talks and discussions.
- For taking care of the everyday worries: Sven Kunze and Daniel Dietrich for technical support, Kai Schmidt and Peter Leumer for IT support, as well as our office team: Johanna Katzschner and Julia Barth for handling “Formular D2.3/32” and all of its fancy friends.
- Charles Gutfleisch and the colleagues at the IAPP for proof-reading this manuscript.

Doch es sind nicht nur die Experimente und fachlichen Diskussionen die mich freudig auf die bisherige Zeit am IAPP zurück blicken lassen. Vielmehr sind es die Erlebnisse und Aktivitäten in der Peripherie der Wissenschaft und außerhalb des Arbeitsgeschehens, u.a. bei Weihnachtsfeiern, sportlichen Teamevents und den Organic Days.

Mit dem ein oder anderen Schmunzeln wird die einmalige Chance des Mitwirkens in der *”Sendung mit der Maus“* in tiefer Erinnerung bleiben, besonders der strahlende Blick von Dr. Hartmut Fröb als die hergestellten OLEDs (selbstverständlich) auch leuchteten.

Besonderer Dank gilt Markus, Paul und Sylvio, weit mehr als nur hervorragende Kollegen, die zusammen mit Frank und Marc das Studentenleben seit dem ersten Semester bereicherten. Danke Jungs, ihr seid exzellent!

Großer Dank gilt Nils, Inbegriff der Kölner Frohnatur und Gefährte auf unzähligen Radtouren, bei denen auch das eine oder andere Karnevalslied die Motivation mal steigerte.

Gedankt sei weiterhin allen die sich dem musikalischen Ausgleich und der sportlichen Ausarbeitung zu Lande, zu Wasser und zur Luft verdient gemacht haben, besonders den Hairy-Metal Gesellen von *”The Garage”* sowie den Vertikal-Heroen von *”Work less, Climb more!”*(n.e.V.) und *”Affenfaust Alarm!”*.

Meiner Familie und ganz besonders meinen Eltern sei für den beständigen Rückhalt sowie die Förderung und Unterstützung auf meinem bisherigem Lebensweg gedankt.

Mit ganzem Herzen danke ich Franzi für Ihre Liebe und unerschöpfliche Geduld in allen Gemütslagen der Promotion sowie Ihre Motivation und Ihren Tatendrang bei der Umsetzung der verrücktesten Ideen und Projekte.

Erklärung

Diese Arbeit wurde am Institut für Angewandte Photophysik der Fakultät Mathematik und Naturwissenschaften an der Technischen Universität Dresden unter der wissenschaftlichen Betreuung von Prof. Dr. Karl Leo angefertigt.

Hiermit versichere ich, dass ich die vorliegende Arbeit ohne unzulässige Hilfe Dritter und ohne Benutzung anderer als der angegebenen Hilfsmittel angefertigt habe; die aus fremden Quellen direkt oder indirekt übernommenen Gedanken sind als solche kenntlich gemacht.

Die Arbeit wurde bisher weder im Inland noch im Ausland in gleicher oder ähnlicher Form einer anderen Prüfungsbehörde vorgelegt.

Ich erkenne die Promotionsordnung der Fakultät Mathematik und Naturwissenschaften der Technischen Universität Dresden vom 23. Februar 2011 an.

Dresden,

Tobias Schwab